Proceedings of:

The 1990 Annual Meeting

The American Society for Precision Engineering

September 23-28, 1990

Riverside Convention Center

Rochester, New York

The American Society for Precision Engineering (ASPE) is a multidisciplinary professional and technical society concerned with research and development, design, manufacture and measurement of high accuracy components and systems. ASPE activities encompass relevant aspects of mechanical, electronic, optical and production engineering, physics, chemistry, and computer and materials science. Membership is open to anyone interested in any aspect of precision engineering.

Founded in 1986, ASPE provides a new focus for a diverse but important community. Other professional organizations have covered aspects of precision engineering, always as a sideline to their principal goals. ASPE is based on the core of generic concepts necessary to achieve precision in any application; independent of discipline, ASPE intends to be the focus for precision technology —and to represent all facets from research to application.

ASPE — The American Society for Precision Engineering
PO Box 7918
Raleigh, NC 27695
(919) 737-7853 Fax: (919) 737-3694

These are exciting times for precision engineering. We see scientific advances in materials, technological advances in devices, metrology, machine design, and controls, and emerging advances motivated by a new emphasis on systems based on nanotechnologies. The 1990s bring an expanded, integrated view of precision engineering. Driven by applications in optical systems, integrated circuit manufacturing, mass data storage, and many other fields, there will be more systems which will depend on precision metrology, machining, machine design, controls, sensors, and materials. We predict a greater exploitation of precision engineering in R/D, manufacturing, and high performance products. In short, we see this decade as one where precision engineering will be truly useful in business, science, and technology.

We are proud to present the Fifth Annual Meeting of the ASPE which is an international forum for the exchange of ideas, for the discussion of solutions to problems, and for the presentation of results involving precision engineering between professionals in universities, government laboratories, and technical corporations. The meeting offers the opportunity for multidisciplinary interaction.

We hope that this program begins to suggest at least some of the vitality of the ASPE and its Annual Meeting.

1990 ASPE Conference Organizing Committee

Carl Zanoni, Chair
Zygo Corporation

Tom Bifano, Boston University
John Byrd, Rank Taylor Hobson, Inc.
Robert Donaldson, LLNL
Thomas Dow, NC State University
Mark Gerchman, Rank Taylor Hobson
Roger Haas, Eastman Kodak Co.
Robert Hocken, UNC-Charlotte
Steven Patterson, Patterson Engr.
Richard Rhorer, LANL
Ronald O. Scattergood, NC State University
Graham Siddall, Tencor Inst.
Irving Stowers, LLNL
Dan Thompson, LLNL

1990 Annual Meeting

Contents

Preface — Organizing Committee ..... *iv*

Corporate Members ..... *iv*

Cooperating Sponsors — Technical Sponsors ..... *v*

Program ..... *vi*

Tutorials *1-4*

Forum/Distinguished Lecturer *4*

Commercial Sessions *5*

Technical Paper Index *6-8*

Poster Paper Index *145-146*

Author Index *240-241*

Preface

This book comprises the proceedings of the 1990 Annual Meeting. The contributions reflect the authors' opinions and are published as presented to ASPE, without change. Their inclusion in this publication does not necessarily constitute endorsement by the ASPE, or its editorial staff.

Individual readers of this book and nonprofit libraries acting for them are permitted to make fair use of the material contained in this book to be used in teaching or research; provided they copy said paper in total, as written by the author. Permission is granted to quote excerpts from the scientific or technical works in this book with proper acknowledgment of the source to include: the author's name, the book name, and the ASPE tag line. Reproduction of figures and tables is likewise permitted from the contents of this book, provided that the same acknowledgment of the same source and content is printed.

Any other type reproduction, systematic copying or multiple reproduction of any material in this book is expressly prohibited except with the written permission of the ASPE editorial staff, addressed to the Society's headquarters.

Printed in the United States of America
AMERICAN SOCIETY FOR PRECISION ENGINEERING

ISBN 1-887706-04-6

Corporate Members of the ASPE

NAME	CONTACT	LOCATION
3M Company	Bill French	St. Paul, MN
Chardon Tool & Supply Co., Inc.	Jack Bennett	Chardon, OH
Digital Instruments	Virgil Elings	Santa Barbara, CA
GCA Tropel	James Scott	Fairport, NY
Moore Special Tool	Ray McClure	Bridgeport, CT
Nissin Machine Works	Mitsuaki Takahashi	Hamamatsu, JAPAN
Professional Instruments Co.	T. J. Arneson	Minneapolis, MN
Rank Pneumo	John Byrd	Keene, NH
Sheffield Measurement Division	Stephen Fix	Dayton, OH
Spindler & Hoyer	Paula Bastiano	Milford, MA
Tencor Instruments	Graham Siddall	Mountain View, CA
Zygo Corporation	Carl Zanoni	Middlefield, CT

Cooperating Sponsors

Rank Pneumo, Inc.

Zygo Corporation

GCA Tropel

Brown & Sharpe

Vickers, Inc.

Cranfield Precision Engineering

Technical Exhibitors

Aerotech, Inc.
A. G. Davis Gage & Engineering Co.
Anorad Corp.
Chapman Instruments
Chardon Tool and Supply Co., Inc.
Cranfield Precision Engineering Ltd.
Digital Instruments
Federal Products Corp.
GCA Tropel
Hewlett Packard Co.
Lunzer
Majestic-Microtool & Instruments, Inc.
NCSU Precision Engineering Center
Norton Company
Optodyne, Inc.
Optra
Park Scientific Instruments
Professional Instruments
Rank Pneumo, Ultra Precision Machining Systems
Rank Taylor Hobson Metrology
Spindler & Hoyer
Surface Finishes Co., Inc.
Tencor Instruments
US Contour Tooling Inc.
UNC Precision Center
Vermont Photonics - Möller - Wedel
Vickers Incorporated
Wilbanks International Inc.
WYKO Corporation
Zygo Corporation

Program

1990 ASPE Annual Meeting

	Sun., Sept. 23	Mon., Sept. 24	Tues., Sept. 25	Wed., Sept. 26	Thurs., Sept. 27	Fri., Sept. 28
7:30						
8:00			Continental Breakfast	Continental Breakfast	Continental Breakfast	
	Tutorials	Tutorials	Session I	Session V	Session VII	Industrial Visits 8:00 - 3:30
9:45						
10:15	break	break	break	break	break	
	Tutorials	Tutorials	Session II	Session VI	Session VIII	
12:00						
1:30				Group Lunch and ASPE Annual Meeting 12:00 - 2:00	Group Lunch	
	Tutorials	Tutorials	Session III		Session IX	
3:15						
3:45	break	break	break		break	
	Tutorials	Tutorials	Session IV	2:00 - 4:00 POSTER SESSION	Session X	
5:30						
7:00				Group Dinner		
		Welcome Reception	Commercial Session	Distinguished Lecturer		
9:00				Open Forum		
			Hospitality Suite	Hospitality Suite		

Guest Tours are 9:00 a.m.-5:00 p.m. on Tues. (Niagara Falls), Wed., (Finger Lakes & Vineyards), Thurs., (Margaret Strong & George Eastman Museum).

Tutorials

Sunday • September 23 and Monday • September 24

Tutorial Schedule

Sunday, September 23
8:00 - 12:00

Control of Precision Mechanical Systems
Thomas A. Dow

Precision Machine Design
Alexander Slocum

Basic Diamond Turning Techniques
Phil Hannah/Richard Rhorer

Surface Finish Metrology
Theodore Vorburger

Dimensioning and Tolerancing to ANSI-Y14.5
Forney Shell

1:30 - 5:30

Computer Systems for Precision Engineering Applications
Robert J. Fornaro

Interferometric Metrology - An Introduction
Robert Smythe

Analyzing the Dynamic Performance of High Precision Machines
M. Weck

Basic Machine Tool Metrology
Robert Hocken

Applied Vibration Isolation
W. Bowie Houghton

Monday, September 24
8:00 - 12:00

Dimensioning and Tolerancing to ANSI-Y14.5
Forney Shell

Classical Grinding and Polishing Techniques
Robert Parks

Axis of Rotation Metrology
James Bryan

Materials for Precision Engineering
Ronald O. Scattergood

1:30 - 5:30

Application of Basic Control Theory
Steven Patterson

Distance Measuring Interferometry
Norman Bobroff

Principles of Grinding
Ranga Komanduri

Temperature Control
K. Blaedel/J. Bryan

9:00 - 4:00

Basic Concepts for Precision Instrument Design
Clayton Teague/Chris Evans

Sunday 8:00-12:00

Control of Precision Mechanical Systems I

Thomas A. Dow, N.C. State University

This tutorial introduces concepts involved in the control of precision mechanical systems, beginning with system identification techniques to define characteristics of the mechanism. These characteristics will be related to equivalent spring/mass/dashpot components that will produce similar response. A model of the system can then be developed and used to design the most appropriate control algorithm. Control strategy will depend on the mechanical systems, actuator, sensor and computer. The design of a control algorithm and the appropriate gains will be discussed in light of the response that different algorithms will produce. Examples of control systems for mechanical structures requiring microinch positioning will be discussed.

Precision Machine Design

Alexander Slocum, CUPE

A brief overview of design considerations for the design of precision machines will be presented (¼ hour). The remainder of the tutorial will focus in detail on the following topics: 1) The use of homogeneous transformation matrices to assemble the error budget for a machine will be discussed and detailed examples will be given (½ hour). 2) Various bearing designs, configurations, and analysis methods for linear motion systems will be discussed in the context of load capacity, accuracy, and manufacturability (2 hours). Design examples will then be discussed and attendees are encouraged to bring their linear motion problems with them for group discussion (1 hour).

Basic Diamond Turning Techniques

Phil Hannah and Richard Rhorer, Los Alamos Nat'l Lab

Many practicing 'precision engineers' started their careers in precision engineering by working with single-point diamond turning. For those who are considering engaging in this relatively new technology, this 'basics' tutorial answers such questions as: What materials should I use? How deep to cut? How high a feed rate? What spindle speed? What tool radius? What tool rake angle? How do I evaluate what I have machined? How do I interpret this interferogram? The class, which includes some 'hands-on' time to learn how to handle and examine diamond-turned parts, how to examine tool bits, and other matters, is divided into four sections: 1) steps to machine a typical part; 2) analyzing the part —geometric surface errors; 3) analyzing the part — surface roughness errors, and 4) determining the sources of the part errors.

Surface Finish Metrology

Theodore Vorburger, NIST

This tutorial emphasizes the wide range of techniques that can be used to characterize surface finish. We discuss the differences between profiling and area methods, and we particularly highlight the techniques of stylus profiling, optical profiling, scanning tunneling microscopy, and light scattering. We also discuss bandwidth limits for these techniques, surface parameters, statistical functions, and document standards.

Dimensioning and Tolerancing to ANSI-Y14.5

Forney Shell, World Class

It is required by the Department of Defense and can increase company profits, yet few industrial issues are understood less than geometric dimensioning and tolerancing. This tutorial discusses geometrics as an engineering and manufacturing language, providing a basic overview of the terminology, symbology and principles of that language.

Sunday 1:30-5:30

Computer Systems for Precision Engineering Applications

Robert J. Fornaro, N.C. State University

This tutorial outlines characteristics of computer systems necessary to implement control strategies developed for precision mechanical systems. Topics covered include architecture of digital systems, multiprocessors, structure of control algorithms, decomposition of algorithms for multiprocessing, digital signal processors and examples.

Interferometric Metrology - An Introduction

Robert Smythe, Zygo Corp.

This two-part tutorial covers the theory and application of interferometry to surface roughness and surface shape metrology.

The first part will address non-contact interferometric metrology of surface roughness. Laser and non-laser based interferometers and systems will be discussed. The main emphasis of interferogram analysis will be on computerized phase measuring interferometry. Sources of error, including geometric, systematic, random and test specific errors will be discussed.

Part two will address non-contact interferometric metrology of surface shape and bulk materials properties. Various interferometric types applicable to surface shape metrology, including some aspheres will be covered. Sources of errors encountered in the interferometer and in the test set-up will be discussed.

Analyzing the Dynamic Performance of High Precision Machines

M. Weck, Fraunhofer-Institut für Produktionstechnologie (IPT)

This tutorial gives a survey of the fundamental principles of machine tool vibration analysis. For a single mass vibrator the mathematical background like characteristic parameters, frequency-response-function, coherence-function, phase-shift-function and locus curve are presented. The modal analysis method for determination of dynamic weak-points is shown.

Basic Machine Tool Metrology

Robert Hocken, UNC-Charlotte

This tutorial will systematically address the subject of machine tool metrology as it is currently practiced with a short introduction on the history of the discipline. It will cover geometric errors, load induced errors, environmental effects, spindle errors, kinematic errors, forced vibrations and the instrumentation and techniques for measuring these errors at several levels of target accuracy. Specific examples taken from the literature will be used for illustrative purposes and an extensive bibliography will be supplied. Whenever possible the lecturer will relate the course to the American National Standard for Coordinate Measuring Machine Performance (B89.1.12) or the developing ASME standard for machining centers (B5 TC52).

Applied Vibration Isolation

W. Bowie Houghton, Newport Corp.

Tutorial topics include establishing vibration requirements for precision work, interpretation of site survey data, and selection of isolation systems. Test data is used to show the applicability of various isolation methods, including active systems, to different applications. Emphasis is on "how to"; theory is used to support practical application. Hardware demonstration will be included.

Monday 8:00-12:00

Dimensioning and Tolerancing to ANSI-Y14.5

Forney Shell, World Class

It is required by the Department of Defense and can increase company profits, yet few industrial issues are understood less than geometric dimensioning and tolerancing. This tutorial discusses geometrics as an engineering and manufacturing language, providing a basic overview of the terminology, symbology and principles of that language.

Classical Grinding and Polishing Techniques

Robert Parks, University of Arizona

The classical procedures for loose abrasive grinding and optical polishing of glass and metals will be discussed, as well as the mechanical metrology of form errors in precision surfaces. Emphasis will be on techniques easily applied to precision engineering problems. This is a 'how to' tutorial but the rationale behind the technique will also be stressed.

Axis of Rotation Metrology

James Bryan, Bryan Associates

This tutorial will cover: 1) Terminology for defining the behavior of spindles used in instruments, measuring machines, machine tools, and rotating equipment of all kinds; 2) Instrumentation available for measuring the various parameters of spindle performance; 3) Relationship of machine tool spindle performance to the roundness, flatness, and surface finish that can be achieved on workpieces; 4) Errors caused by heat generated within spindles; 5) Effect of unbalance on spindle behavior; 6) Roundness errors caused by non-uniform sag of workpiece support fixtures in horizontal spindle machine tools; 7) Performance vs. cost characteristics of hydrodynamic, hydrostatic, aerostatic rolling element, and magnetic bearing spindles.

Materials for Precision Engineering

Ronald O. Scattergood, N.C. State University

Metals, ceramics, glass and polymers have various applications in precision engineering. The important differences in structure between their classes of materials and their chemical, physical and mechanical properties will be covered. Fundamental concepts will be covered along with illustrative examples pertinent to precision engineering design and fabrication processes.

Monday 1:30-5:00

Application of Basic Control Theory

Steven Patterson, Patterson Engineering

The tutorial provides an overview of applied basic control theory with emphasis on motion control applications. Topics discussed will include stability analysis, performance prediction, error rejection and methods of system implementation. The tutorial should be primarily of interest to engineers and technical managers who are working with systems requiring automatic control.

Distance Measuring Interferometry

Norman Bobroff, IBM

The concepts of homodyne and heterodyne interferometry are developed from a historical perspective, beginning with the work of A.A. Michelson. Special attention is given to factors which determine the band width, accuracy, and dynamic range of interferometric metrology. Phase measuring electronics and environmental compensation are treated along with the optical components, light source, and receiver. Techniques by which interferometer systems can be self-evaluated for accuracy and resolution are presented. The tutorial material emphasizes practical considerations in constructing and using interferometers to measure linear and angular displacements to very high accuracy.

Principles of Grinding

Ranga Komanduri, Oklahoma State University

Grinding is an important manufacturing process for producing ultra-precision parts. In fact, for ultra-precision parts made of difficult-to-machine materials, such as, ceramics, glass, ferrites, germanium etc. as well as hardened steels and stainless steels superabrasive (diamond and cBN) grinding is perhaps the only choice. The principles and practices relating to the superabrasive grinding will be covered. Work materials, abrasive materials and their interaction in grinding will be discussed.

Temperature Control

J. Bryan/K. Blaedel, Lawrence Livermore Nat'l Lab

This tutorial will cover the consequences of temperature variation, gradients, and uniform temperatures other than 20 deg. C. Sources of thermal error such as room and coolant temperature variation, mechanical friction, heat from electrical components, heat from the cutting process, and memory from previous environment, will be discussed and solutions presented.

Monday 9:00-4:00

Basic Concepts for Precision Instrument Design

Clayton Teague and Chris Evans, NIST

This tutorial is an effort to begin dialog on the subject of precision instrument design toward the goal of establishing a methodical collection of all the basic design concepts which have come to be accepted by the precision engineering community. We call this collection 'patterns' to indicate their heuristic nature. As applied to precision machine and instrument design, each pattern: 1) identifies a key problem; 2) analyzes historical examples for successes and/or failures; and 3) presents a current best hypothesis which captures the properties of instruments/ machines demonstrating a solution.

Other Technical Sessions

Open Forum Session

Wednesday, September 26, 7:00 - 9:00

Session Chair: Robert Hocken, UNC-Charlotte

This evening session is devoted to short presentations of current problems, results and conclusions in precision engineering. Sign-up sheets for interested presenters will be available at the conference registration table.

Distinguished Lecturer

Wednesday, September 26, 7:00

Professor R.V. Jones

Professor R.V. Jones has led a very distinguished career and has made significant contributions in a number of fields. During World War II he was responsible for Scientific Intelligence in the British armed forces and was awarded the CB and CBE in the U.K. and the Medal of Freedom and Medal for Merit by the President of the United States. In 1946 he became Professor of Natural Philosophy at the University of Aberdeen where he made important contributions in scientific research and education. His work in the field of precision instrument design is world renowned and his editorial comment in the first edition of Precision Engineering in 1979 is a most eloquent description of Precision Engineering.

Professor Jones is a Fellow of the Royal Society and has received many awards, including the Duddel Medal of the Physical Society and the Hartley Medal of the Institute of Measurement and Control. His publications have been numerous and well recognized. Most Secret War *(published as* The Wizard War *in the US), about his experiences during the Second World War, was an international best seller and the subject of a BBC television series. His recent book* Instruments and Experiences *is of particular interest to all workers in the field of Precision Engineering.*

Other Technical Sessions

Commercial Session

Tuesday, September 25, 7:00 - 9:00

Session Chair: Thomas Bifano, Boston University

Company representatives are invited to make brief presentations on products associated with precision engineering during this special evening session. The intent of the Commercial Session is to introduce the ASPE community to new approaches and advances, focusing on actual results, measured product performance and limits to performance.

Intended participation must be confirmed by requesting and submitting a registration form to ASPE by September 1, 1990.

ASPE 1990
Commercial Session Schedule

Tuesday, September 25, 1990

7:00-7:10 pm	**Introduction and Welcome** — Thomas Bifano, Boston University.
7:10-7:15 pm	**North Carolina State University,** "Precision Engineering Research at NCSU," presented by Thomas Alva Dow.
7:17-7:22 pm	**Cranfield Precision Engineering,** "The CNC built for Ultra-Precision Applications: The CUPROC Series 3000 CNC," presented by Geoff Portas.
7:24-7:29 pm	**Norton Company,** "3 Micron Cut Rate Enhanced Lapping Slurry," presented by David Rostoker.
7:31-7:36 pm	**Federal Products Corp.,** "Computer Touch Screen — Efficient User Interface for Gaging," presented by Alexander Tabenkin.
7:38-7:43 pm	**Tencor Instruments,** "High Resolution Profiling for Production Environments," presented by Marc Pasturel.
7:45-7:50 pm	**Moore Special Tool,** "Moore 1200-CPZ Precision Grinding Center," presented by Tom Hannon.
7:52-7:57 pm	**Rank Pneumo (Div. of Rank Taylor Hobson, Inc.),** "Recent Advancements in Ultra-Precision Manufacturing," presented by David H. Youden.
7:59-8:04 pm	**Park Scientific Instruments,** "Applications of Scanning Force Microscopy," presented by Michael Kirk.
8:06-8:11 pm	**Aerotech, Inc.,** "Precision Laser Beam Positioning," presented by Dan Smyers.
8:13-8:18 pm	**WYKO Corporation,** "Non-Contact Profilometry of Precision Machined Surfaces," presented by Larry D'Angelo.
8:20-8:25 pm	**Hewlett Packard,** "Advancements in Interferometry at HP," presented by Charles R. Steinmetz.
8:27-8:32 pm	**Cranfield Precision Engineering Ltd.,** "The NANOCENTRE Range of Ultra Precision Aspheric Generators for Efficient Ductile-Regime Grinding of Complex Profiles," presented by Keith Carlisle.
8:34-8:39 pm	**Optodyne Inc.,** "LDDM for Linear and Angular Measurement," presented by Dr. Charles Wang.
8:41-8:46 pm	**Zygo Corp.,** "A New Interferometer for Abbe Error Compensation," presented by Paul Parise.
8:48-8:53 pm	**Optra Corp.,** "The Nanoscale — Microinch Measurement from Coarse Scales," presented by Donald Mitchell.
8:55-9:00 pm	**Anorad,** "High Speed Submicron Positioning Stages," presented by Tomas Rincon.

Technical Paper Index

The technical program for the 1990 ASPE Annual Meeting contains reports on current research from Europe, Japan and the US. Authors from national laboratories, universities, and industry will share their conclusions on a wide variety of topics ranging from the design of astrophysics facilities to molecular dynamics models of machining.

In addition to ten technical sessions, there will be an open forum where recent results can be discussed, a commercial session where equipment manufacturers will give an update on their recent innovations, and a poster session.

Session I *Tuesday, September 25, 8:00 - 9:45*

Session Chair: Robert Hocken, UNC-Charlotte

1. ***Invited Paper — New Trends and Challenges in Optical Lithography***
   John Bruning (GCA Corp.) ..... *page 9*
2. ***Optically Based Atomic Force Microscope that Adapts to Commercial Scanning Tunneling Microscope Head***
   Robert Day, Lonnie A. Theye (Los Alamos Nat'l Lab) and Phil Russell (NC State Univ.) ..... *page 11*
3. ***Co-Focal Micro-Raman Probe of Residual Stresses and Subsurface Damage in Glass***
   Ronald G. Sparks and M.A. Paesler (NC State Univ.) ..... *page 15*
4. ***Three Dimensional Contouring on a N/C Grinder***
   Dean Ketelsen, W.C. Kittrell and Robert Parks (Univ. of AZ), Lianzhen Shao (Tucson Optical Res. Corp.) ..... *page 19*

Session II *Tuesday, September 25, 10:15 - 12:00*

Session Chair: Kiyoshi Iizuka, Res. Dev. Corp. of Japan

1. ***The Generation of Aspheric Surfaces on Thermal Imaging Materials on a 4-Axis Machining Center***
   Vellore C. Venkatesh and C.P. Tan (Tennessee Tech. Univ.) ..... *page 23*
2. ***Architectures and Algorithms for Computer Control of High Precision Machine Tools***
   Robert Fornaro, K.P. Garrard, and L.W. Taylor (NC State Univ.) ..... *page 27*
3. ***Machining Non-Axisymmetric Optics***
   Dan Luttrell (Rank Taylor Hobson) ..... *page 31*
4. ***Sub-Angstrom, Vertical Resolution, 3D Surface Profiling***
   Frank Demarest and Robert Smythe (Zygo Corp.) ..... *page 35*

Session III *Tuesday, September 25, 1:30 - 3:15*

Session Chair: Irving Stowers, Lawrence Livermore

1. ***Invited Paper — Micro Mechanical Systems***
   William Trimmer (AT&T Bell Labs) ..... *page 38*
2. ***Design of Active Vibration Control System***
   Kazuyoshi Katayama, Yoshinori Takahashi, Nobuyoshi Murai (Takenaka Corp.) ..... *page 39*
3. ***A 0.25 Micrometer Optical Projection Printer for IC Lithography***
   A. Grenville, R.S. Hsieh and R.F.W. Pease (Stanford Univ.), D.A. Markle (Ultratech Stepper) and G. Owen (Hewlett Packard) ..... *page 43*
4. ***The Chemistry of Glass Polishing***
   Lee Cook (Galileo Electro-Optics) ..... *page 47*

Session IV *Tuesday, September 25, 3:45 - 5:30*

Session Chair: Ronald O. Scattergood, NC State University

1. ***An Experimental Procedure for Studying Diamond Turning Chip Mechanics***
   Richard Rhorer (Los Alamos Nat'l Lab), Don A. Lucca (Oklahoma State Univ) ..... *page 51*
2. ***Surface Studies of Diamond Machined Polymers***
   Jeffrey Carr and Claudius Feger (IBM Research) ..... *page 55*
3. ***Diamond Turning of Non-Symmetric Laser Optics***
   M. Weck and M. Pyra (Fraunhofer Inst.) ..... *page 59*
4. ***Step Height Measurements with a Phase-Shifting Interference Microscope***
   A.W. Hartman and Ted Vorburger (NIST) ..... *page 63*

Session V *Wednesday, September 26, 8:00 - 9:45*

Session Chair: Graham Siddall, Tencor Instruments

1. ***Invited Paper — Revolution In X-Ray Optics***
   N.M. Ceglio (Lawrence Livermore) ..... *page 67*
2. ***Mechanics of Material Removal in Diamond Turning***
   Scott Blackley and R.O. Scattergood (NC State Univ.) ..... *page 68*
3. ***Application of Hydrostatic Bearings in Spindle Systems for High Precision Machining***
   M. Weck and U. Bottger (Fraunhofer Institut) ..... *page 72*
4. ***Molecular Dynamics Model of the Orthogonal Cutting Process***
   Irving Stowers and James Belak (Lawrence Livermore) ..... *page 76*

Session VI *Wednesday, September 26, 10:00 - 12:00*

Session Chair: Mark Gerchman, Rank Taylor Hobson

1. ***Recent Developments in the Quality in Automation Project***
   A. Donmez, Ted Vorburger, F. Rudder, K. Yee, and R. Gavin (NIST) ..... *page 80*
2. ***Some Recent Developments in the Analysis and Interpretation of Surface Topography***
   Paul Scott (Rank Taylor Hobson) ..... *page 84*
3. ***Error Modeling and Correction of a Laser Tracker***
   John Patten, John Grant, Paul Tullar and Robert Hocken (UNC-Charlotte) ..... *page 88*
4. ***Diamond Turning of Non-Rotationally Symmetric Surfaces***
   T.A. Dow (NC State Univ.) and P.J. Falter (Westinghouse) ..... *page 92*

Session VII *Thursday, September 27, 8:00 - 9:45*

Session Chair: Alexander Slocum, CUPE

1. ***Invited Paper — Precision Engineering in Mass Data Storage Devices***
   D.B. Bogy (University of CA at Berkeley) ..... *page 96*
2. ***Dynamics Analysis and Control of a Precision Slide with Coulomb Friction and Stiction***
   Paul I. Ro and Roy S. Colby (NC State Univ.) ..... *page 97*
3. ***Computer-Controlled Off-Axis Optical Fabrication***
   Timothy Wilson (Eastman Kodak) ..... *page 101*

Session VIII *Thursday, September 27, 10:00 - 12:00*

Session Chair: Robert Polvani, NIST

1. ***The Specification of Glancing Incidence Mirrors In Terms of System Performance***
   E.L. Church (USA ARDEC) and P.Z. Takacs (Brookhaven Nat'l Lab) ..... *page 103*
2. ***Analytical Photon Scanning Tunneling Microscopy***
   Patrick J. Moyer, C.E. Johnson, M.A. Paesler (NC State Univ.); R.C. Reddick and R.J. Warmack, T.L. Ferrell (Oak Ridge Nat'l Lab) ..... *page 106*
3. ***Comparison of Optical and Mechanical Measurements of Surface Finish***
   Thomas Lettieri, Aaron Kiely, Lin-xiang Cao and Theodore Vorburger (NIST) ..... *page 110*
4. ***Ultra Precision Stylus Profilometry for Large Optical Components***
   Peter B. Leadbeater, W.J. Wills-Moren, P.A. McKeown (Cranfield) ..... *page 114*

Session IX *Thursday, September 27, 1:30 - 3:15*

Session Chair: Thorsten Bispink, Fraunhofer Institut

1. ***Invited Paper — Overview of the Advanced X-ray Astrophysics Facility (AXAF)***
   Leon Van Speybroeck (Smithsonian Astrophysical Observatory) ..... *page 118*
2. ***Scanning Tunneling Microscopy Bit-Making for Use in High Density Memory Chip Applications***
   Jimmie A. Miller and Robert Hocken (UNC-Charlotte) ..... *page 119*
3. ***Cutting and Surface Planing of Diamond Film by YAG Laser***
   Shinichi Tezuka, Naoto Ohtake and Masanori Yoshikawa (Tokyo Inst.) ..... *page 123*
4. ***Optics Fabrication for a Multi-megajoule, Solid State Inertial Confinement Fusion (ICF) Laser***
   J.S. Taylor and John E. Marion (Lawrence Livermore) ..... *page 127*

Session X *Thursday, September 27, 3:45 - 5:30*

Session Chair: Robert Donaldson, Lawrence Livermore

1. ***A Nanometer Digital Interferometric Control for a Stop-Start Grating Ruling Engine***
   Robert Wiley, Semyon Zheleznyak, Jeffrey Olson, Erwin Loewen and John Hoose (Milton Roy Co.) .... *page 131*
2. ***Extension of the 1-D Critical Depth of Cut Model for Brittle Materials to 3-D Contour Grinding***
   Steven Fawcett and T.A. Dow (NC State Univ.) ..... *page 135*
3. ***Implementation of Open Loop Control Techniques for High Speed Micropositioning In a Single Diamond Turning Process***
   Hakan Ozisik and R.F. Keltie (NC State Univ.) ..... *page 139*
4. ***Design of Centerless Grinding Machine for Ductile Mode Grinding of Brittle Materials***
   J. Yoshioka (NUTR KK), M. Miyashita and A. Kanai (Ashikaga Inst. of Tech.), M. Daito (Nissin Machine KK), F. Hashimoto (The Timken Research) ..... *page 143*

NEW TRENDS AND CHALLENGES IN OPTICAL LITHOGRAPHY

John H. Bruning
GCA Tropel
A Unit of General Signal
Fairport, NY

Semiconductor lithography, the patterning process for integrated circuits, is the most costly and highly leveraged technology used in the manufacture of integrated circuits (IC's). The optical "steppers" used in this process have been aptly referred to as the "machine tool" of the semiconductor industry. Optical lithography has continued to evolve to unexpectedly high and exciting new levels of performance primarily through advances in metrology and precision enginering. These developments have made it possible to fabricate significantly more complex reduction imaging lenses while attaining nearly perfect optical correction along with dramatic improvements in image placement accuracies and distortion. These rapid but evolutionary developments have been driven by the phenomenal growth rate of the IC industry, particularly in the area of semiconductor memory (DRAM). This high growth rate, however, has made it nearly impossible for new lithographic technologies to industrialize to the maturity levels needed for high volume, high yield and cost effective manufacturing. The level of investment needed to make these rapid and continual improvements in optical technology, while high, is still small compared to that needed to change to another lithographic technology altogether.

A state of the art reduction stepper lens today, using a Mercury arc source, can image more than 10^9 0.5 μm pixels with absolute image

placement errors of less than 50 nm over an image field diameter of greater than 25 mm. This is suitable for production of the 16 Mb DRAM. Within the next five years we can expect further improvements suitable for 64 Mb DRAM production through exploitation of more aggressive refractive lenses operating at deep-UV wavelengths with laser sources. Before the decade is out, these same precision engineering and manufacturing technology improvements will make it possible to fabricate reflective diffraction limited lenses which will operate in the soft X-ray region printing 0.1 μm circuit patterns over large areas. Supporting examples of these industry trends and tools will be shown.

OPTICALLY BASED ATOMIC FORCE MICROSCOPE THAT ADAPTS TO COMMERCIAL SCANNING TUNNELING MICROSCOPE HEAD

Robert Day, Lonnie A. Theye
Los Alamos National Laboratory
P.O. Box 1663, MS E549
Los Alamos, NM 87545

and
Phillip Russell
North Carolina State University
Precision Engeering Center
Box 7918
Raleigh, NC 27695

BACKGROUND

The Atomic Force Microscope (AFM) was invented in 1986 by G. Binnig, C. F. Quate, and Ch. Gerber [1]. The idea for using atomic forces as a means for producing high resolution images was born out the Scanning Tunneling Microscope (STM) work. The basic design consists of having an atomically sharp tip mounted to the end of a cantilever spring of a known spring constant. By measuring the cantilever's deflection at the tip's location the amount of force at the tip can be determined. By moving the tip across a surface in a raster fashion while monitoring the spring's deflection, a force image of the surface can be made. This force image can be made to relate directly to the surface topography. The magnitude of the forces of interest range from 10^{-11} Newtons to 10^{-3} Newtons. This means that springs with a spring constant of around one Newton per meter must be used in conjunction with deflection detectors that can sense motions of about 10 picometers.

The original deflection sensor used in the AFM was that of electron tunneling [1,2]. Experience with this sensing method revealed that it was very unreliable, however, so other methods were investigated. Some of these methods include using capacitance [3], optical levers [4,5], heterodyne interferometry [6], and fiber optic interferometry [7,8]. It was our desire to use a sensor which could easily fit into a commercially available STM head (namely the Nanoscope [9] head), and which would allow the tip to be scanned instead of having to scan the sample. (All of the commercially available AFM's use an optical sensing scheme that requires the sample to be scanned. Since we were primarily designing this instrument as a means of inspecting the quality of production parts, we felt that a design allowing the tip to be scanned would be more flexible). We determined that the fiber optic interferometer showed the most promise for meeting these criteria.

FIBER OPTIC INTERFEROMETER DESCRIPTION

A schematic of the fiber optic interferometer, as it relates to the AFM, is shown in Figure 1. The fiber optic beam splitter, which consists of two fused single mode fibers with a core diameter of 5 micrometers, comprises the heart of the interferometer. The splitter used was purchased from Gould Inc. [10]. One of the output fibers was inserted into optical coupling gel which effectively eliminated its influence upon the interferometer (not shown in Figure 1). What was left was an interferometer in a Fizeau configuration. In this configuration, the light travels from the helium-neon laser, reflects off the beam splitter, and progresses to the end of the fiber. At the fiber end, four per cent of the light reflects back into the fiber and the other 96 per cent propagates to reflect off of the cantilever. Some of the reflected light from the cantilever renters the fiber and interferes with the light that reflected off of the fiber end. The intensity of the interfering light waves varies as a cosine wave with respect to the optical path difference between the cantilever and the fiber end. Therefore a change in the optical path

distance is the same as changing the phase angle of the intensity profile. This intensity is measured by a photo-optical detector package that was purchased from Optoacoustic Sensors [11].

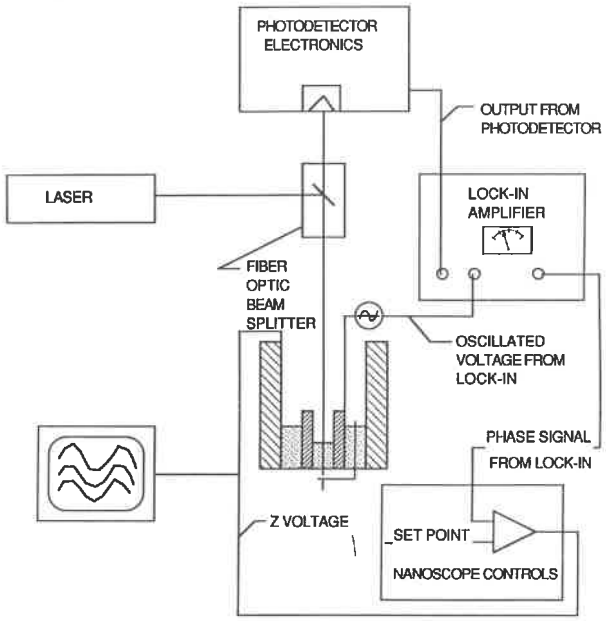

Fig. 1. Schematic of AFM Controls

A phase lock technique, as described by J. Wyant [12], was used to sense very small motions of the cantilever. In the phase lock technique, the phase difference between the two interfering beams is dithered at a high frequency (somewhere between 600 and 20,000Hz) with a small amplitude (10 nm or less). In addition to the high frequency dither a low frequency phase shifter is also required. The expression for the light intensity as a function of time for this arrangement is:

$$I(t) = I_1 + I_2 + 2\sqrt{I_1 I_2}\cos[(\theta + A\sin(\omega t))]$$

where, I_1, I_2 = intensities of the two interfering beams

$A\sin(\omega t)$ = the high frequency phase dither

θ = the phase angle (i.e the distance change) being measured

t = time

Equation 1 can be rewritten:

$$I(t) = I_1 + I_2 + 2\sqrt{(I_1 I_2)}\ \{\cos\theta\,[J_0(A) + f(nw)] - \sin\theta\,[2J_1(A\sin(\omega t) + f(nw)]\}$$

where, f(nw) = higher order harmonics not sensed at the fundamental frequency

J_n = nth order Bessell function

From equation 2 it can be seen that by using the low frequency phase shifter to set θ equal to $n\pi$, then sin θ will equal zero and thus the amplitude of the signal at the fundamental frequency (ω) will be zero. By measuring the phase shift required to make the amplitude at ω go to zero, which can be done by monitoring the distance moved by the low frequency phase shifter, the phase can be determined. In our AFM design the fiber optic is glued into a small tube piezoelectric crystal which is dithered at the high frequency. This assembly is then mounted into the center of the piezoelectric tube scanner on the Nanoscope head. The z-axis motion of the tube scanner performs the low frequency phase shifting. A lock-in amplifier purchased from Princeton Applied Research [13] is used to provide the high frequency dither and measure the intensity change as a function of cantilever motion. Figure 2 shows how the high frequency piezo mounts into the tube scanner and Figure 1 schematicaly shows how all of the hardware just described interfaces to each other to produce an image.

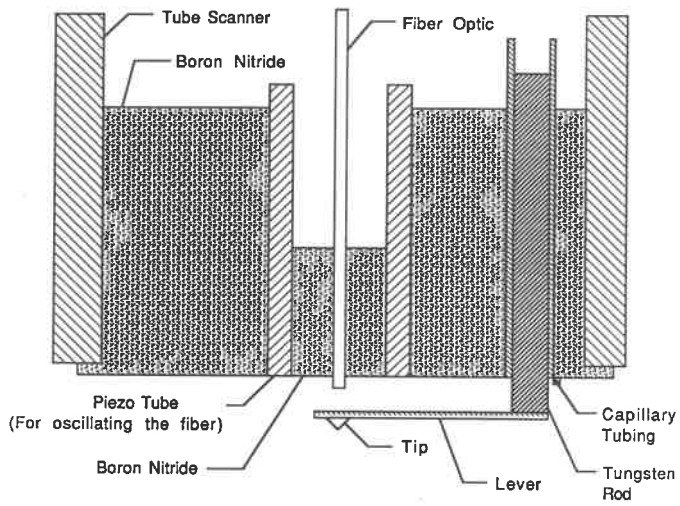

Fig. 2. STM Tube Scanner with Retrofitted AFM Hardware

CURRENTLY ACHIEVED NOISE LEVELS

Table 1 shows the currently noise levels as they relate to distance measured with this instrument.

Table 1 - Currently Achieved Noise Levels

Electronic	0.5 picometer per (square root Hz)
Mechanical	0.3 nanometer (< 0.2 Hz)
	< 0.1 nanometer (> 0.2 Hz).

TIPS FOR USE ON THE AFM

For this AFM, the cantilever/tip assembly is glued to the end of a slightly bent tungsten wire that is about 0.25 mm in diameter. The wire is then inserted into a capillary tube that is mounted to the tube scanner. The Friction caused by the tungsten wire rubbing on the side on the capillary tubing holds the assembly in place. This method of mounting the tip assemblies allows them to be changed fairly easily. Figure 2 is a drawing of the AFM in the region of the tip, which shows the configuration that was just described.

One of the more difficult tasks in building an AFM is that of fabricating the cantilever/tip assembly. The first cantilevers we used were made from aluminum foil that was 4 mm long and 0.5 mm wide and 50 micrometers thick. These had a tip mounted to them that consisted of tungsten wire of 25 micrometers in diameter that was etched to sharp point. This assembly was useful for checking out the instrument and for making load vs. deflection profiles in graphite. It has not been a useful configuration for obtaining images, however. We have recently purchased some commercially available tip assemblies from Park Instruments [14]. We are in the process of making the necessary fixtures to be able to use them on our instrument. These assemblies have the advantages of being relatively inexpensive per assembly, having a high natural frequency, having a low spring constant, having uniform characteristics from assembly to assembly, and being readily available.

CONCLUSIONS

An AFM has been developed that consists of incorporating a fiber optic interferometer and cantilever/tip assembly into a commercially available STM head. This design allows the tip to be scanned over the surface which should make this instrument more flexible than instruments which use designs that require the sample to be scanned. The instrument has sufficiently low noise levels to be able to produce high resolution images on surfaces used for precision engineering applications (e.g. optical quality surfaces). We have used the AFM to perform load /deflection tests in graphite and are changing the tip/cantilever design so that high resolution images can be made.

REFERENCES

[1] G. Binning, C.F. Quate, and Ch. Gerber, Phys Rev. Lett. 12, (1986), Pages 930-933.

[2] O. Marti, B. Drake, S. Gould, P. K. Hansma, "Atomic Force Microscopy and Scanning Tunneling Microscopy with a Combination Atomic Force Microscope/Scanning Tunneling Microscope", J. Vac. Sci. Technol. A 6(3), May/June 1988, Pages 2089-2092.

[3] C. Mathew Mate, Ragnar Erlandsson, Gary M. McClelland, and Shirley Chiang, J. Vac. Sci. Technol. A 6(3), May/June 1988, Pages 575-576.

[4] S. Alexander, L. Hellemans, O. Marti, J. Schneir, V. Elings, P. K. Hansma, "An Atomic-Resolution Atomic-Force Microscope Implemented Using an Optical Lever", J. Appl. Phys. 65(1), 1 January 1989, Pages 164-167.

[5] G. Meyer and N. M. Amer, Appl. Phys. Lett., 53(12), 19 Sep. 1988, Pages 1045-1047.

[6] Y. Martin, C. C. Williams, and H. K. Wichramasinghe, J. Appl. Phys. 61(10), 15 May 1987, Pages 4723-4729.

[7] P. K. Hansma, V. B. Elings, O. Marti, C. E. Bracker, Science Vol. 242, 14 Oct. 1988, Pages 209-242.

[8] A. D. Drake, D. C. Leiner, Rev. Sce. Instrum. Vol. 55 No. 2 Feb 1984, Pages 162-165.

[9] Nanoscope is a commercially available STM produced by Digital Instruments, Inc., 6780 Cortona Drive, Santa Barbara, Ca 93117.

[10] Gould, Fiber Optics, 6730 Baymeadow Drive Suite D, Glen Burnie, MD 21061

[11] Optoacoustic Sensors, 1706 Medfield Rd., Raleigh, NC.

[12] J. C. Wyant, Modern Optical Testing tutorial presented at various APIE conferences throughout the year.

[13] EG&G, Princeton Applied Research, P.O. Box 8007, Gaithersburg, MD 20898-8007.

[14] Park Scientific Instruments, 476 Ellis Street, Mountain View, CA. 94043.

CONFOCAL MICRO-RAMAN PROBE OF RESIDUAL STRESSES AND SUBSURFACE DAMAGE IN GLASS

R. G. Sparks, M. A. Paesler
Department of Physics and the Precision Engineering Center
North Carolina State University
Raleigh, NC

INTRODUCTION

Various applications of the Raman microprobe technique have been reported. Raman spectroscopy has been successfully used for phase and composition identification, the determination of long or short range order (crystallinity or amorphicity), impurity configurations, and superlattice properties.[1] Micro-Raman spectroscopy has also been a valuable technique when used to determine residual stresses in single point diamond turned semiconductors.[2] The use of various excitation wavelengths and the exploitation of their differing penetration depths in absorbing materials has led to the development of computer deconvolution techniques which allow depth profiles of residual stress to be determined for such samples.[3] Since conventional micro-Raman techniques rely on the traditional light microscopes, microscopic depth profiles of stresses, composition, and crystallographic phase have been impossible in transparent or translucent samples due to the large depth of field produced by the optics in such microscopic systems.

Recent developments of confocal optical geometries have allowed the axial resolution of conventional light microscopes to be extended to the submicron range. One of the potentially most useful properties of the confocal optical microscope is its very shallow depth of field. It has been shown that the depth resolution of such a microscope using an objective with numerical aperture of 0.90 and an illumination source of λ=633nm is 0.5μm. The properties of extremely shallow depth of field and high transverse resolution have so far made confocal microscopes very powerful tools for semiconductor metrology, for measuring transparent film thicknesses, and for constructing three dimensional images of integrated circuits.[4] The use of a confocal Raman microscope would allow depth profiles of stress, crystallographic phase, etc. to be obtained in transparent or translucent samples. By incorporating deconvolution techniques similar to those used to generate depth profiles in absorbing materials the effective depth resolution can be extended further into the submicron range. The use of appropriate light wavelengths can also allow the technique to be applied to materials opaque in relatively short wavelength ranges but more transparent at longer wavelengths. Thus the use of longer wavelength light ($\lambda \approx 650$ nm) could allow depth profiles of residual stress to be performed on such semiconductors as silicon and germanium directly.

EXPERIMENT

The experimental apparatus is essentially the same as the general micro-Raman apparatus previously described [2,3], but in order to effectively limit the depth of field of the standard micro-Raman apparatus, several significant changes must be made. The coupling optics whose function is to match the effective numerical apertures of the microscope and the spectrometer are removed. A microscope objective of the same magnification and focal length as the objective used to focus the light onto the sample is introduced into the scattered light beam emerging from the micro-Raman system. The scattered beam is focused by the microscope objective through a 2 μm pinhole which effectively blocks the scattered light emerging from above or below the plane of focus on the sample. The microscope objective must thus be positioned to within ± 0.5 μm of the center of the precision pinhole. Positioning is accomplished with a differential micrometer x y z translation stage with positioning resolution of 0.1 μm. The pinhole need not be located to such exacting tolerances since it merely needs to be coursely positioned in the scattered beam with fine adjustments of the objective to achieve the highest throughput. The sample is positioned using a piezoelectric stack under the focussing objective to accurately and reproducibly move the sample in a vertical plane allowing Raman spectra to be obtained at various distances into the sample. The resulting spectra may then be analyzed for stress induced shifts of the characteristic Raman peaks for each depth probed resulting in much simpler data reduction.

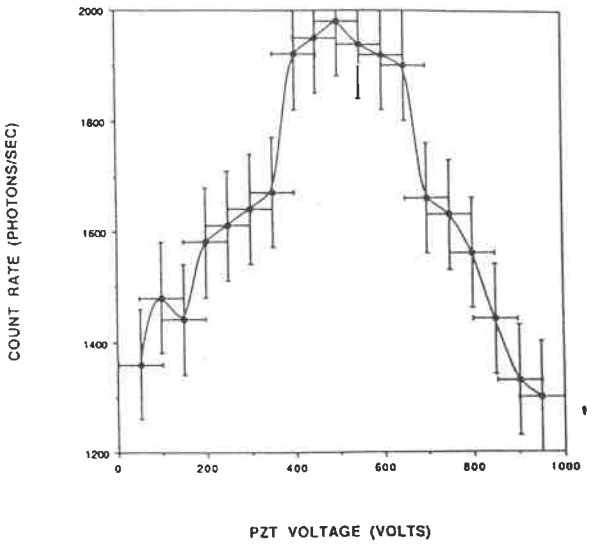

Fig. 1 Count rate versus PZT voltage for 5 micron pinhole in non-scanning confocal Raman microprobe. The maximum count rate occurs at the peak of the implanted chromium concentration demonstrating the validity of the technique.

As a test of the validity of this technique to directly map residual stresses and subsurface defects in transparent media the photoluminescence signal from a sapphire sample ion implanted with chromium atoms has been measured. The magnitude of the photoluminescence signal is directly proportional to the concentration of chromium atoms in the sample. The measured photoluminescence signal follows the Gaussian profile of the chromium concentration as a function of depth as shown in Figure 1. The abscissa is given in terms of the voltage applied to the PZT

stack that is used to move the ruby through the focal plane. We are presently undertaking a precise calibration of the PZT stack to accurately determine depth as a function of applied voltage. Depth profiles of residual stress are currently being mapped in the vicinity of Vicker's hardness indents placed in the ion implanted sample.

Since the characteristic Raman signal from glasses results in quite broad features as shown in Figure 2, stress induced shifts may be difficult to observe. Confocal micro-Brillouin scattering may be needed to directly measure the residual stress states in amorphous materials since the Brillouin peaks are relatively sharp and stress induced shifts of these spectral features are more easily measured. The Raman spectrum is sensitive, however, to the presence of a number of four-fold and three-fold defects which occur in silicate glasses. These defects produce sharp spectral features superimposed on the broad Raman peaks found in silicate glasses. The intensity of these defect peaks is directly proportional to the defect concentration and can thus be used as an indicator of the density of the stress induced lattice mismatch in silicate glasses.

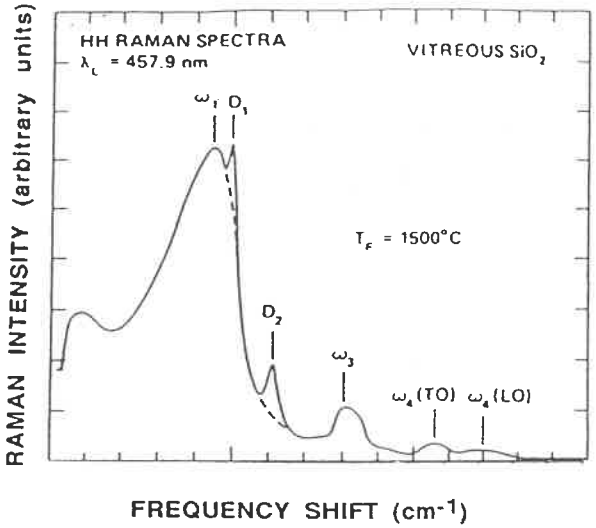

Fig. 2 The Raman spectrum of SiO_2. The broad features labeled ω are the characteristic Raman peaks for the amorphous glass. The sharp lines labeled D_1 and D_2 are due to the presence of four-fold and three-fold planar defects respectively. Changes in sharp defect signatures are generally clearer indicators of damage than shifts in broader Raman features. [5]

We have previously demonstrated that computer deconvolution of micro-Raman spectra can yield valuable axial information in *absorbing* materials.[2,3] We now plan to extend this technique to transparent materials by exploiting the very shallow depth of field in confocal microscopic spectroscopies. The depth response of confocal microscopes has been investigated by several researchers. The primary concern has, to this point, been the quality of images formed using such systems. In our program the main interest is in the amount of light that passes through the apodizing pinhole placed at the intermediate focal plane. Examination of the throughput for various pinhole diameters has led to the concept of deconvolution of spectra as a function of pinhole diameter. The diameter of the pinhole directly effects the depth of field in that the larger the pinhole the greater the depth of field. Thus in a microscope-spectrometer system a large pinhole will sample a larger axial region than a smaller pinhole. Spectra taken with the larger pinhole will show a superposition of spectral information from the entire focal region that passes through the

aperture. Spectra obtained using smaller diameter pinholes would likewise contain information from a much smaller axial region. If several spectra are then taken for various pinhole diameters centered on the same focal plane and lateral region on the sample, the resulting spectra will display superposition broadening analogous to the case of varying light wavelengths in absorbing media. The analogy to the case for absorbing materials is nearly exact. Though the actual function to be fitted is slightly different for the two cases, essentially the same deconvolution technique could further enhance the effective depth of field of the confocal microscopic spectroscopy system allowing accurate and reproducible depth profiles to be obtained.

CONCLUSIONS

The development of a confocal Raman microscope represents an important addition to currently available spectroscopic techniques which can provide a wealth of information not only in transparent glasses and polymers but in a wide range of other materials. Both photoluminesence and Raman spectroscopy can be performed and be used to monitor defect structure, impurity concentration, as well as stress and phase information in non-absorbing materials. The selection of appropriate light wavelengths could also allow this technique to be applied to absorbing materials such as silicon and germanium. The machining of glasses via the techniques of single point diamond turning is currently of interest in a variety of applications, but the physics of the material removal process is not well understood. Confocal micro-Raman spectroscopy can allow depth profiles of defect structures in these materials to be obtained. Such non-destructive evaluations of sub-surface damage can provide critical information about the physics of material removal processes as well as important insights into the effects of process dependent factors (feed rate, spindle speed, rake angle, etc.). A number of microelectronic applications (e.g. Si on sapphire) involve the deposition of opaque materials on transparent (or translucent) substrates. Residual stress information could be obtained at various layers in such substrates using the confocal Raman technique. The validity of the confocal technique has been demonstrated by mapping the concentration of ion implanted chromium atoms in a sapphire matrix. The concentration map also provides a direct check on the depth resolution of the confocal Raman microscope system.

REFERENCES

[1] Nemanich, R. J., Mat. Res. Soc. Symp. Proc., 69, 1986, p.23

[2] Sparks, R. G., Paesler, M. A., Prec. Eng., 10, 1988, p. 191

[3] Sparks, R. G., Enloe, W. S., Paesler, M. A., Microbeam Analysis 1989, p. 149

[4] Xiao, G. S., Corle, T. R., Kino, G. S., Appl. Phys. Lett., 53, 1988, p. 5634

[5] Geissberger, A. E., Galeener, F. L., Phys. Rev. B, 28, 1983, p. 3266

THREE-DIMENSIONAL CONTOURING ON A N/C GRINDER

D. A. Ketelsen, W. C. Kittrell, R.E. Parks
University of Arizona
Tucson, Arizona 85721

Abstract

The Large Optical Generator (LOG) recently completed the generating of six off-axis aspheres. It was decided to use the non-traditional technique of three-axis contouring to solve many of the fabrication and mounting problems. The process and the solutions it provides are discussed, as well as the resultant figure errors and how these compare to the traditional two-axis generating that LOG has done in the past.

Introduction

The LOG is effectively a vertical mill working in a cylindrical coordinate system. Both the vertical and horizontal axes have linear encoders readable to a micron. Designed with the molds of the Sub Millimeter Telescope (SMT) in mind, ie., large panels up to 5 meters off-axis, LOG has an 8 meter capacity with 5 meters of horizontal and 1.5 meters of vertical travel. The work table has a very good 1.8 meter diameter crossed roller bearing providing rotary motion.

Over the years, LOG has met a variety of fabrication challenges. The first major work after installation was the generation of three off-axis parabolic molds for the Sub-Millimeter Telescope[1]. For it, two-axis contouring was utilized (figure 2a), where the optical axis of the part was aligned to the table rotation axis, and the diamond tool swept out the parabolic profile as the part swept past it.

The technique of three-axis generating was developed when Cornell University wanted a 5 meter subreflector for the Arecibo Radio Telescope which had no axis of symmetry, though it did have a plane of symmetry. The solution was to use the table position as the reference, and for a particular horizontal position, the vertical position was oscillated as the part rotated. In this way, as the horizontal was spiraled outward, the non-rotationally symmetric surface was produced. It was realized then that any generic surface could be produced in this manner, even rotationally symmetric parts, but more importantly, it was realized that any part with an axis of symmetry could be mounted and generated with an arbitrary axis lined up on the table axis (figure 2b). This has the potential of greatly simplifying mounting problems for many off-axis parts. In its eventual implementation, the only change in procedure from this early process is that the horizontal axis is the one oscillated, because for parts with reasonable sagitta, oscillating the horizontal transfers less of that axes' backlash into surface error.[1]

How does such a surface appear? Both astigmatism and coma are present to some degree. For most parts reasonably far off-axis and whose diameter is smaller than the radius of the parent asphere, the astigmatism is much larger in magnitude than the coma, and tends to dominate the appearance of the surface[2,3].

Procedure and Error Discussion

The off-axis segment is centered on the LOG table and a transformation of coordinates is done to the LOG coordinate system, whose zero point is now the geometrical center of the segment, which we just aligned to the table rotation axis. The machine actually requires tool center positions, rather than the surface itself, so the surface defined by the tool center is calculated and a spline fit is done to calculate the spiral tool path that is loaded into the machine. The LOG computer is limited to 5500 data entries, and this somewhat limits the machine capabilities for large parts. By careful optimization of the tool and generating geometries, the limitations can be overcome[4].

There are two primary sources of geometry error. The first is radial ripple - caused by tool scalloping modified by the spiral pitch used to generate the surface. One can use a longer radius tool or a finer spiral pitch to reduce this

error. The other error is tangential ripple, where the surface is approximated as the tool moves along the spiral path in a straight line between adjacent data points. This error is reduced by reducing the data spacing along the spiral path.

There are other error sources, the primary ones are due to figure error induced by backlash as the axis changes direction 4 times per rotation. There are also alignment errors and tool radius errors which can usually be reduced in subsequent generator passes, if careful thought is given to the metrology and the error source can be deduced.

The following advantages of three-axis contouring are now summarized:

1) Mounting considerations are greatly simplified.

2) Shorter generating cycle time is realized.

3) Slope change of part is halved - advantages in generating geometry.

4) Smaller machine required - it needs the capacity of part, not distance off-axis.

5) With established software, rapid cycle time between parts and surface types are realized.

To be fair, there are disadvantages to the technique, some of which have been mentioned:

1) Lack of symmetry requires large amounts of memory for tool positions.

2) Backlash errors are transformed to surface error.

3) Aspheric departure must be << total sagitta.

4) Short feedback loop required to minimize phase shift errors.

5) Transformation of coordinates required for measurement and analysis of surface.

The only difficult limitation is that imposed by backlash induced surface error, and that is not a large problem for parts with shallow slopes. The end result is that three-axis contouring is a quite viable alternative to symmetric, two-axis contouring.

NASA 2.5 meter Off-Axis Reflector

The first off-axis surface to be generated was a 2.5 meter reflector for NASA[5]. We first considered using the two-axis contouring method, but immediate problems developed. When the optical axis was aligned to the table rotation axis, not only was the part some distance off the 2 meter diameter table, causing real mounting problems, but the vertical motion required was greater than the 1.5 meter capacity of the machine (figure 2). The three-axis method was really the only method at our disposal.

There was considerable work in preparing the substrate. The reflector, as received, consisted of a lightweight stainless steel structure with urethane machineable foam bonded to it. The foam needed to be machined to the correct off-axis parabolic shape, two layers of fiberglass laid down over it to strengthen the surface, and then a machineable gelcoat[6] (.75 mm final thickness) was used for the final surface. The foam machining with a spherical wheel went very well and measurements showed a surface finish limited by the material. The only problems encountered involved use of a toroidal wheel in final machining of the gelcoat. The model for calculating tool positions are much more complicated than for spherical tools and considerable effort was exerted in debugging that software.

Glass Substrates

Though we had used the three-axis contouring technique previously on composite surfaces (foams and thixotropic gels) and had gotten reasonable results, it was thought that material properties were limiting the surface smoothness and thus the attainable surface error. We were eager to attempt the process with a glass substrate and had the opportunity with a set of 4 off-axis convex parabolic molds for the Jet Propulsion Laboratory, and an off-axis ellipsoid to be used for a polishing experiment for Perkin Elmer. Although three-axis contouring did not offer the only alternative as it did for the NASA reflector, it did simplify the mounting enough that the same mount was used for all the glass substrates with only minor modifications. We chose to keep the Two-axis contouring as an alternative, but with it, a more complicated adjustable tilt and offset mounting would have been required.

The work proceeded with absolutely no problems. The substrates were rough generated to the nearest sphere using a coarse cup wheel. The aspheric was then generated with a 100 grit wheel[7]. When the aspheric cleaned up the surface and metrology showed it to be the correct surface, the same radius 600 grit wheel was substituted for a couple light passes, with metrology verifying that all was well. The final machined surface with the 600 wheel was equivalent to about a 12 micron loose abrasive grind. The shop lights could be seen reflected in the surface. It was intended that polishing of the generated surface could be done without further lapping or grinding. It should be noted that since we used the maximum memory space for all parts, the generating time was the same for all parts. It took about 3 hours for a generating pass, the uncertainty being how aggressively the operator ran the program.

As time went on, we were under increasingly difficult time constraints, but we had also moved well along on the learning curve. The ellipsoid, done third in line, was completed start to finish in 5 working days. The last 1.5 meter off-axis parabolic mold for JPL took 3 days, not counting roughing in the sagitta. The time constraints show up somewhat in the final figure errors attained. However, the larger diameters also contribute to the larger errors. The final results for the NASA and glass substrate parts:

Off-Axis	Diam(M)	Radial Ripple (p-v,microns)	Figure (rms,microns)
parabola	2.5	25	11.2
parabola	1.0	~1	3.65
parabola	1.0	~1	3.67
ellipse	0.6	~1	4.3
parabola	1.5	~1.5	5.4
parabola	1.5	~1.5	6.4

Conclusions

We have demonstrated that the three-axis contouring method of generating is a quite viable generating method. The figure errors obtained are nearly equal to the best results obtained using the two-axis symmetric generating method. The three-axis method also simplifies mounting concerns and has been proven to be very time efficient, particularly when a number of similar parts are done serially.

References

1. Ketelsen, D. A., Kittrell, W. C., Kuhn, W. P., "Three-Axis Contouring with the Large Optical Generator," Proc. SPIE, Vol. 676. 1986.

2. Parks, R. E., "Alignment of Off-Axis Conic Mirrors," Optical Fabrication and Testing Technical Notebook, Optical Society of America, Sept., 1980, Falmouth, MA.

3. Parks, R. E., "The Tradition of Optical Fabrication," Proc. SPIE, Vol. 315, 1983.

4. Parks, R. E., "Parameters for Large Optics Generation," Optical Engineering, Vol. 25, pp 1009-1012, 1986.

5. Sharp, G. R., Wanhainen, J. S., Ketelsen, D. A., "A New Fabrication Method for Precision Antenna Reflectors for Space Flight and Ground Test," Proc. AIAA International Communication Satellite Systems Conference, Los Angeles, CA, March, 1990.

6. Gelcoat of choice was REN 1129 - CIBA-GEIGY 4917 Dawn Ave. East Lansing, MI 48823.

7. Ketelsen, D. A., Parks, R. E., "Spherical Grinding Wheel Use and Fabrication," Proc. Optical Society of America's Optical Fabrication and Testing Workshop, July, 1990 Monterey, CA.

Figure 1. Large Optical Generator

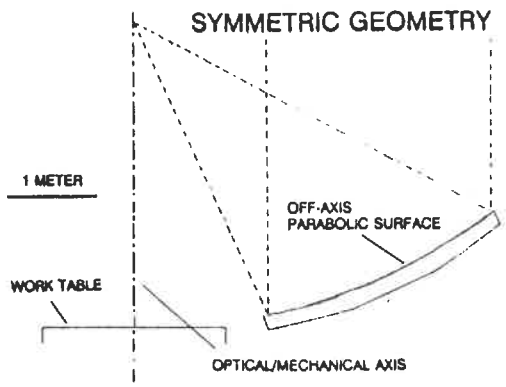

Figure 2a.
2-Axis Contouring Geometry

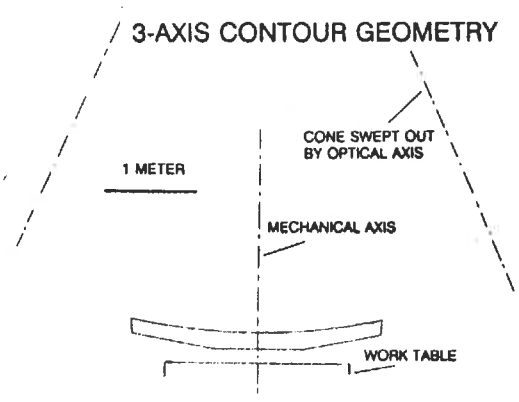

Figure 2b.
3-Axis Contouring Geometry

The Generation of Aspheric Surfaces on Thermal Imaging Materials on a 4-Axis Machining Center

V.C. Venkatesh and C.P. Tan
Center for Manufacturing Research and Technology Utilization
Tennessee Technological University
Cookeville, TN 38501

INTRODUCTION

Traditional methods of generating aspheric surfaces on glass have been time comsuming [1]. A novel technique was developed by Van Ligten and the first author which brought about heavy material removal without affecting the surface finish and profile [2,3]. The authors were able to obtain surfaces which satisfied opthalmic conditions, but not those expected by precision optics. This technique was extended to germanium and silicon using both metal bonded and resinoid bonded wheels. Surface finish, form accuracy, and smoothness were analyzed on a Form Talysurf, while surface integrity was studied on a Scanning Electron Microscope. SEM pictures show material removal by both ductile grinding and by fracture. These results are discussed in this paper.

THE MACHINING METHOD

To remove material quickly and end up with the desired surface, the contact area between the grinding tool and the workpiece should be as large as possible. Since only spheres and toroids permit the condition of full area contact, partial area contact, or line contact will be the best alternative. The use of a machine with a rotating tool suggests that the contact surface must be symmetrically rotational. In general, the shape of the workpiece is not predictable, hence, the condition of the large contact area is put in jeopardy. Thus, the method was chosen based on a long line contact between the tool and the workpiece during the first step of rough grinding. During the subsequent steps of lapping and polishing, the use of a flexible tool allows conformity between the workpiece and the tool, approaching the original condition of a contact area.

Cup-shaped diamond grinding wheels with metallic and resinoid bonding were used. The profile of the grinding edge is circular in this case, but not restricted to this shape, thus, forming a toroid. The important feature is that the grinding surface shape is axially symmetrical. It is now possible to program the toolpath of this tool on the CNC-machine such that it is in line (or arc) contact with the workpiece as it cuts the desired shape on the glass.

To illustrate this, the grinding of a paraboloid will be shown. The cup tool can be thought of as consisting of a collection of circles whose planes are perpendicular to the axis of rotation of the tool. When the paraboloid is intersected by a plane, as shown in Figure 1, the common line is an ellipse. When the task is to cut a concave paraboloid, the tool must fit inside the paraboloid. Hence, the tool must have a diameter smaller than the shortest radius found on the eclipse of intersection of any plane intersecting the paraboloid. In the case of a paraboloid, the shortest radius of curvature on the eclipse of intersection is found when the plane contains the axis of symmetry of the paraboloid.

Any circle at the outer side of the tool can be contained in one of the planes intersecting the paraboloid. The angle that this plane makes with the axis of the parabolid can be adjusted such that the

arc of the circle and that of the ellipse (see Figure 1b) at d, differs in sag height no more than a preset tolerance. This condition will set a certain common arc length over which the difference in sag does not exceed a certain value, say 0.5 micrometers. Now the workpiece can be rotated around line 1 in Figure 1a. After completion of one revolution, the surface left on the glass workpiece will be a zone of the paraboloid, as indicated in Figure 1a. Subsequently, the tool axis can be programmed to take a slightly different position relative to the axis of rotation of the workpiece, as well as relative to the apex *P*, of the paraboloid. The sequence in then repeated to form a neighboring zone of the one indicated in Figure 1a.

The CNC-machine can now be programmed to perform these sequences continuously, until the paraboloid is completed. In this manner, a zone is ground during one revolution. While in cutting with a point tool, in principle one line of the paraboloid is cut. It is, thus, clear that this method of grinding with the nearest arc-contact, can complete the same surface faster than in the case of cutting with a point-tool.

EXPERIMENTAL WORK

Two identical sized diamond grinding wheels were used, one having a resinoid bond (SD240-R100 1369-6mm) and the other a metal bond (D20/30 MIC-L50M-1/4). The thermal imaging materials used were monocrystalline germanium and silicon. Two 5-axis vertical CNC machining centers (Fadal and Deckel) were used. Surface roughness, form accuracy, and smoothness were analyzed on a Form Talysurf, while surface integrity was evaluated on an ISI-SR-50 Scanning Electron Microscope.

Ge and Si blanks were polished after grinding. A special aluminum tool was developed. A felt cloth was glued to the spherical surface of this tool and a polishing paste of one micron alpha alumina was applied to it during polishing. The same set-up was used for polishing on the CNC machine.

RESULTS AND DISCUSSIONS

1. The resinoid bonded wheel was superior for both Ge and Si. It could be redressed and trued, and existing commercial sizes are available. The metal bonded wheel was made to our specifications and had considerable run out (0.279mm) which could not be corrected.
2. Better surface roughness values were obtained with both wheels for Si (Table I).
3. Si, however, was more difficult to polish and a lighter pressure had to be applied to prevent the felt from coming off. Thus, for the same time interval, Ge had a much better surface finish (Table I).
4. Polishing improved the form accuracy with Ge, but not with Si (Table II).
5. Average smoothness improved with both Ge and Si after polishing (Table III).
6. Both ductile and fracture modes of material removal were observed with both Ge and Si (Figures 2 and 3).
7. Better surface roughness, form accuracy, and smoothness can be obtained with a 5-axis CNC jig grinder, and also by dressing the grinding wheel by ductile mode as suggested by Miyashita [4].

REFERENCES

1. Horne, D.F., OPTICAL PRODUCTION TECHNOLOGY, Adam Hilger Ltd, 1984.
2. Van Ligten, R.F. and Venkatesh, V.C., Invention -- machine to make aspheric surfaces, National University of Singapore, patent disclosure, 1986.
3. Van Ligten, R.F. and Venkatesh, V.C., "Diamond Grinding of Aspheric Surfaces on a CNC 4-Axis Machining Center," Annals of the CIRP, Vol. 34, No. 1, 1985, pp. 285-298.
4. Mayashita, M., ULTRAPRECISION IN MANUFACTURING ENGINEERING, Springer Verlag, 1988.

TABLE I
Average Roughness after Grinding (G) and after Polishing (P) in μm.

	Ge	Si
Metal bonded wheel - G	0.722	0.583
Metal bonded wheel - P	0.057	0.123
Resinoid bonded wheel - G	0.706	0.123
Resinoid bonded wheel - P	0.045	0.191

TABLE II
Average Form Accuracy after Grinding (G)
and after Polishing (P) in μm.

	Ge	Si
Metal bonded wheel - G	4.16	6.03
Metal bonded wheel - P	2.867	6.490
Resinoid bonded wheel - G	1.845	1.898
Resinoid bonded wheel - P	1.238	2.433

TABLE III
Average Smoothness after Grinding (G)
and after Polishing (P) in Degrees

	Ge	Si
Metal bonded wheel - G	0.615	0.64
Metal bonded wheel - P	0.18	0.14
Resinoid bonded wheel - G	1.28	1.08
Resinoid bonded wheel - P	0.21	0.39

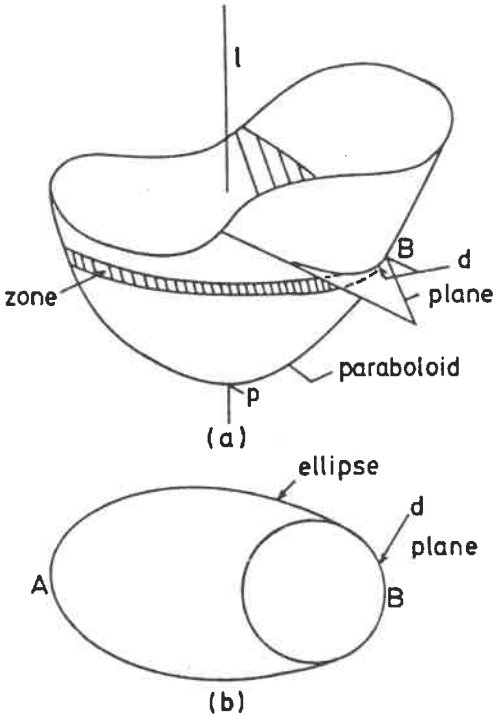

Figure 1
A Plane Intersecting a Paraboloid (a),
in an Ellipse (b)

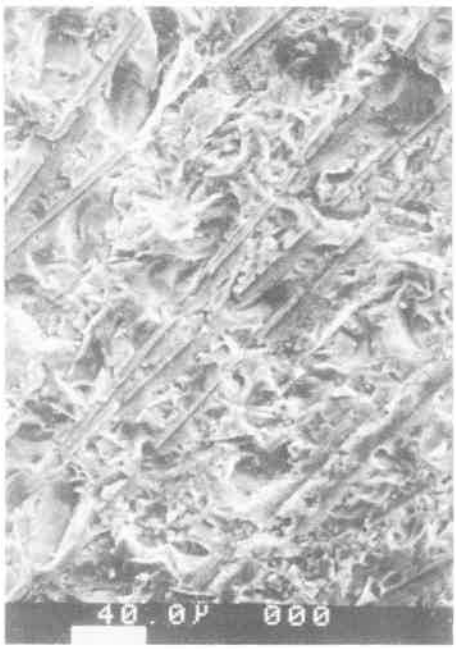

Figure 2
SEM of Germanium Reveals Ductile and
Fracture Regimes after Grinding X 500

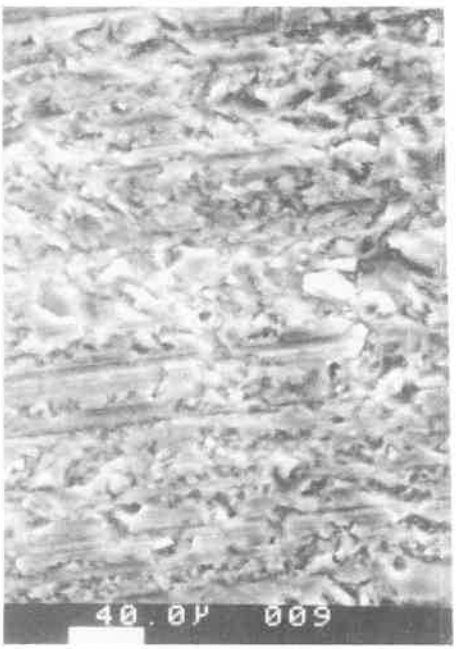

Figure 3
SEM of Silicon Reveals Ductile and
Fracture Regimes after Grinding X 500

Architectures and Algorithms for Computer Control of High Precision Machine Tools

Robert J. Fornaro, Kenneth P. Garrard, Lauren W. Taylor
Precision Engineering Center
North Carolina State University
Raleigh, North Carolina 27695-7918

Introduction. Control of high precision machine tools requires high performance computational capability. A project has been underway in the Precision Engineering Center at NC State University to investigate the relationship between control schemes for advanced machine tools and the computer algorithms and architectures required to implement these schemes on digital processors. In general, control requirements have been found to be computationally intensive relative to control cycle times. Also, control cycle times need to be relatively fast: on the order of a millisecond for hydrostatic slides and tens of microseconds for piezo devices. This translates into a computing requirement that cannot necessarily be economically met by a single processor. An advanced machine tool,when viewed as a system, potentially requires a controller that comprises multiple processing sites. This presents a challenging problem with regard to the details of candidate architectures for such controllers and appropriate mappings of control computations onto these multi-processor systems. This abstract gives a brief description of a multi-processor architecture that is being developed as a test bed for research in advanced machine tool controllers and discusses some of the algorithmic issues related to control computations.

A Multi-Processor Architecture. A Heterogenous Hierarchical Architecture for Real-Time (H^2ART) has been developed. This is a multiprocessor computer system whose architecture is characterized by its ability to incorporate a variety of different processors (heterogenous). These processors are tightly coupled by a hierarchy of busses and memories to improve real-time response and data flow within the system. A PC-AT compatible computer hosts program development for the H^2ART sytem. The system has been prototyped on Multibus I (IEEE 796) form factor boards. There are four board types: Node Controller (Synchronization Processor), Digital Signal Processor (Computation Processor), Digital Input/Output, and Analog Input/Output. The H^2ART architecture is illustrated in Figure 1. Individual board components and their functions are described below.

Node Controller Board. The node controller is based on the Intel 80186 microprocessor and is responsible for communication between Multibus masters (which may be other node controllers or a host computer using a Multibus I interface) and the digital signal processors (DSP). It also can transfer data between the DSP boards which are connected to its local bus. The node controller card has 128K bytes of random-access memory (RAM), 64K of which can be addressed by any Multibus master while the other 64K bytes is private.

Digital Signal Processor Board. The digital signal processor board is based on the Texas Instruments TMS320C25 digital signal processor (DSP). The DSP board contains 64K words of program RAM and 64K words of data RAM all of which is shared with the node controller. The data RAM is divided into two independent 32K word sections so that the node controller may be using one half of the data RAM while the DSP uses the other half. Communications between the

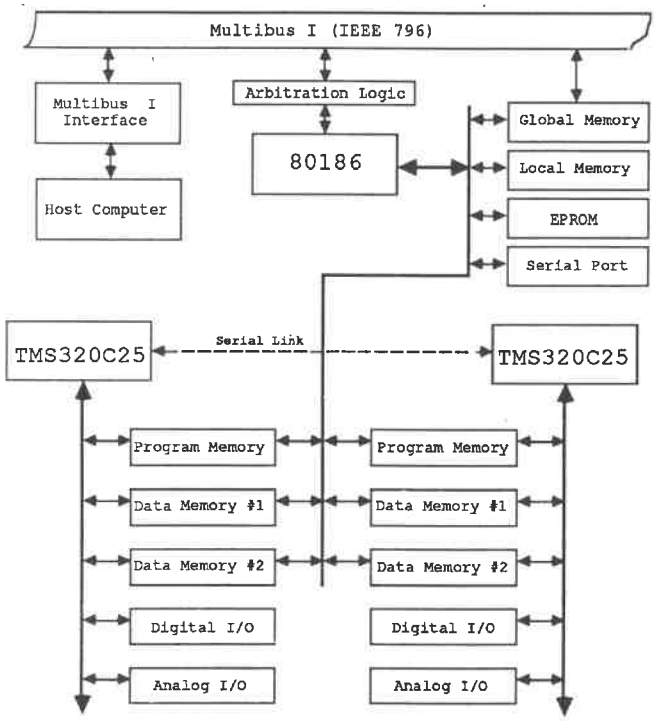

Figure 1: A Typical H²ART Multiprocessor Node

node controller and DSP are handled through a command and status port.

Input/Output Boards. Both digital and analog I/O are provided. The digital I/O board has eight 16-bit ports. Each of these ports may be selected to be either an input or an output port. The analog I/O board has four channels of analog output and three channels of analog input.

Typical H²ART Node. A typical H²ART node consists of a node controller and one or more DSP boards with their associated I/O boards. The node controller loads the DSP's programs, starts the DSP's and handles communication between DSPs and other Multibus I masters. The DSP boards perform high-speed computations and control the I/O boards. Since the DSP's data memory is composed of two separate and independent sections, the node controller can transfer data to and from one half of the data memory while the DSP uses the other half of the data memory for computations and I/O. This feature allows the DSP to execute a program without pausing periodically to receive more data from the node controller (e.g. the continuous transfer of a part program from the node controller to the DSP while maintaining the controller cycle time).

Computational Algorithms.

Three basic computational problems are encounterd in implementing a machine tool controller. First, the part to be machined must be formally defined via some part specification language (e.g. G-codes) or a formal mathematical description. Second, the part specification must be translated into the fundamental components of the machine tool path. For the high-precision machining of complex geometries, the number of components (i.e. blocks) in this tool path may be prohibitively large. This naturally leads to the notion of *on-the-fly* reference signal generation. Lastly, the desired tool path is used as a reference signal for the axes control law calculations. Part specification and reference signal generation processes are discussed in more detail below.

Multi-Step Part Programming. Multi-step part programs are defined by a connected sequence of linear and conic reference surfaces (i.e. program steps or blocks). A continuous stream of reference points is generated *on-the-fly* along the desired surfaces at the specified feedrate. There should be no transitional delay from one program block to the next. Once execution of the part program begins, the controller update cycle must be uninterrupted until the block step has been completed or an error condition occurs. All constraint testing on the coordinates of the commanded moves are performed before program execution begins.

Parametric Reference Surface Generation. All reference surfaces (linear and non-linear) can be generated using a parametric representation of the appropriate mathematical equations. The reference signal generation algorithms for non-linear surfaces utilize parametric forms of the standard conic equations. These parametric forms have three advantages for interpolation algorithms. The specific parametric equations chosen are optimal in that straight lines connecting the generated points will inscribe a polygon of maximal area under the desired curve. Tool correction formulas are conveniently expressed in terms of the parametric variable, which is incremented by a constant on each iteration of the algorithm. This leads to simplification of the tool correction formulas by eliminating the need to directly calculate the value of trigonometric functions. Tool correction has been implemented *on-the-fly* for spherical and parabolic interpolation by assuming a circular tool geometry. The general algorithms necessary for elliptical tools are being developed. The fundamental, unsimplified form of the parametric equations also allows reference signal generation to be performed independently for each axis. A recursive form of the parameterization can be obtained that factors out the trigonometric functions. For the central conics (i.e. circle, ellipse and hyperbola) the familiar parametric equations

$$x_i = a\,\mathcal{F}(\theta_i) \qquad \text{and} \qquad z_i = b\,\mathcal{H}(\theta_i)$$

are used to generate closely spaced points on the desired conic surface. The angle θ_i is measured from the reference conic center in the plane of the tool. Given a constant feedrate, θ_i will change by a constant increment, δ, on each iteration of the control program. By using the appropriate double angle formulas and the recurrence expression $\theta_{i+1} = \theta_i + \delta$, the parametric equations can be simplified to yield

$$x_{i+1} = x_i\,\mathcal{F}(\delta) \pm z_i\,\tfrac{a}{b}\,\mathcal{H}(\delta) \qquad \text{and} \qquad z_{i+1} = x_i\,\tfrac{b}{a}\,\mathcal{H}(\delta) \pm z_i\,\mathcal{F}(\delta)\ .$$

The values of a, b, $\mathcal{F}(\delta)$, and $\mathcal{H}(\delta)$ are constants that are dependent on the conic surface and the programmed feedrate. Their values are computed outside the real-time control loop during part program initialization. For the non-central conic (i.e. parabola) the parametric equations are

$$x_i = 2P\tau \qquad \text{and} \qquad z_i = P\tau^2\ .$$

As with the central conic interpolation equations, simplification is possible using the recurrence expression, $\tau_{i+1} = \tau_i + \delta$. The resulting parametric parabola equations are

$$x_{i+1} = x_i + 2P\delta \qquad \text{and} \qquad z_{i+1} = z_i + x_i\delta + P\delta^2\ .$$

Note that $2P\delta$ and $P\delta^2$ are constants that can be computed outside the real-time loop.

H^2ART Implementation of a DTM/FTS Controller. The unique features of the H^2ART architecture can reduce or eliminate I/O and communication bottlenecks. The very high speed integer processing capability and double buffered memory organization provide a means of controlling each axis with a different processor. Each TMS320C25 processor also has direct I/O

interfaces to the DTM. The direct I/O interface supports digital I/O and analog output within one processor cycle (i.e. 100 ns). Analog input conversion time is 15 μs per word. Continuous control of the X and Z axes is essential. While waiting for commands from the user interface, the H^{2}ART controller maintains the position of each axis. To sustain operation of the controller for large part program instruction sequences, the TMS320C25 double buffered memories are utilized. A control processor operates out of one of its memories while the 80186 node controller is filling the other memory with new commands. The node controller is also be responsible for transmitting status information back to the host. The memory switch takes place within one processor cycle on the TMS320C25. With 32K words in each memory, the switch interval is long enough to absorb the 80186 setup time for memory-to-memory transfers.

The principle problems associated with developing control software for the TMS320C25 environment are the absence of hardware floating-point operations, lack of hardware support for 32-bit integer operations, and the relatively small amount of memory available to each processor. The Texas Instruments C compiler does support 32-bit floating-point operations through software emulation, but does not provide a mechanism for performing 32-bit integer operations. They must be implemented via assembly language calls to user supplied functions. Tests results using the TMS320C25 simulator indicate that linear and circular interpolation algorithms using a floating-point roundoff compensation scheme are too slow to be used for reference signal generation. The fully simplified parametric form of circular interpolation requires 168 μs per axis to generate each reference point due to the emulation of floating-point roundoff calculations. The representation of the reference signal and laser feedback as 16-bit incremental quantities and scaled fixed-point arithmetic are being investigated to further reduce the calculation time.

The integer round-off compensation scheme developed for the parametric linear interpolation algorithm yields more significant speed-up. By eliminating all floating-point operations, the per axis reference point calculation time on the TMS320C25 was reduced by a factor of 25. The basic idea of the new algorithm is to compute the cyclic position increment for each axis as a fraction instead of a floating-point value. By adding the numerator of this fraction into an auxiliary variable on each loop iteration, the accumulated roundoff error is maintained. When the value of this sum is greater than one-half of the denominator of the fraction, an extra count is added to the axis reference point. The denominator must now be subtracted from the sum to reset the roundoff accumulation process. In its final form, this algorithm requires at most four additions (when the roundoff test succeeds) and one test for each axis per iteration. Some timing data for the linear and circular interpolation algorithms is shown in the table below.

Reference Signal Generation (μs)				
Algorithm (single axis)		*TMS320 Simulator C25*	*C30*	*Benchmark 68020*
Linear	(float)	75.19	0.93	19.20
	(integer)	3.05	1.13	2.63
Circular	(trig)	573.14	11.18	61.80
	(no trig)	167.94	2.02	53.99

A H^{2}ART system which uses 32-bit floating-point TMS320C30 DSPs as computational processors is currently being designed. This will preserve the benefits of this architecture and alleviate the computation bottleneck.

MACHINING NON-AXISYMMETRIC OPTICS

Dan E. Luttrell
Senior Development Engineer

Rank Taylor Hobson Inc
P.O. Box 543, Precision Park
Keene, NH 03431

Current single point diamond turning machines have the capability of fabricating complex aspheric optical surfaces. However, these surfaces are limited, by the machine tool, to be surfaces of revolution. With the introduction of two additional axes, spindle position and a high bandwidth axis parallel to the spindle axis, and a high speed control system, the possibility exists to machine surfaces that are non-axisymmetric.

A limited amount of work has been performed by several researchers to machine non-axisymmetric components using both conventional and diamond tools. Douglass[1] made some of the earliest attempts at diamond machining non-axisymmetric surfaces, but encountered problems with the tool actuator and control system that prevented generating optical quality surfaces. Meinel[2] was later able to achieve good results when using a piezoelectric actuator to machine a phase corrector plate. In the realm of conventional machining, Tsao and Tomizuka[3] successfully machined non-circular cylindrical parts.

This paper reports efforts to single point diamond turn non-axisymmetric optical surfaces that are off-axis segments of larger optics. These segments would be used as either off-axis mirrors or as segments to make up a much larger on-axis mirror. An example of the later is the 10 meter Keck Telescope currently under construction[4]. Geometry of these segments will first be described followed by an example to illustrate some of the key implementation details. A description of the experimental machining setup along with cutting results will also be given.

Non-Axisymmetric Geometry

The parent optic considered in this project is a general conic of revolution. This was chosen because a closed form description of the off-axis segment surface is known and can be put into a form that lends itself to real time implementation by a high speed controller. It is important to note that implementation details must be considered at every step in the development of this machining system.

The following equation describes the surface of an off-axis conic segment in cylindrical coordinates,

$$z_3(\rho,\phi) = d_1 + d_2\rho\cos(\phi) \pm \sqrt{d_3 + d_4\rho\cos(\phi) + d_5\rho^2 + d_6\rho^2\cos^2(\phi)} \qquad (1)$$

where z_3 is the segment sagitta, ρ the radius from segment center, ϕ the angular position around the segment and the d_i's are functions of the parent optic and how far the segment is from the parent axis. A detailed development of this equation and a full description of the surface has been given by Gerchman[5].

Presented at the *American Society for Precision Engineering* Annual Conference, Rochester, NY, September 23–28, 1990.

Implementation

Machining the non-axisymmetric segment surface is achieved by coordinating motion of the machine's X and Z axes and the tool servo, defined here as the Z′ axis. As the segment is rotated by the machine spindle, tool servo motion is generated based on measured spindle position. A key to obtaining the proper segment surface is in separating out the Z and Z′ motions so the resulting surface is described by Equation 1. This is done by separating the equation into one part that is ϕ and ρ dependent and another that is only dependent on ρ.

An optimum method to make this separation (in the sense that Z′ motion is minimized) is to precalculate X and Z motions at each value of ρ. By finding the max and min values of $z_3(\phi)$ at each ρ and picking a point half way between them as the reference, a baseline motion for the machine slides can be established. This value at each ρ is then subtracted from $z_3(\rho, \phi)$ to give tool servo motion. By this method the tool servo motion can be described with the following expression,

$$Z'(\rho, \phi) = z_3(\rho, \phi) - \frac{[z_{3\max}(\rho) + z_{3\min}(\rho)]}{2} \tag{2}$$

An example of tool motion based on using this optimal baseline is shown in Figure 1 where tool servo motion is plotted as a function of the angular position ϕ. The solid line is motion at $\rho_{\max}$, dashed line motion at $\frac{3}{4}\rho$, the dash-dot line at $\frac{1}{2}\rho$ and the dotted line at $\frac{1}{4}\rho$. This example is for cutting an off-axis segment of a paraboloid. It should be noted that the motion appears somewhat like a decaying sinusoid, but, as shown by the dotted line, this is not the case toward the center of the segment.

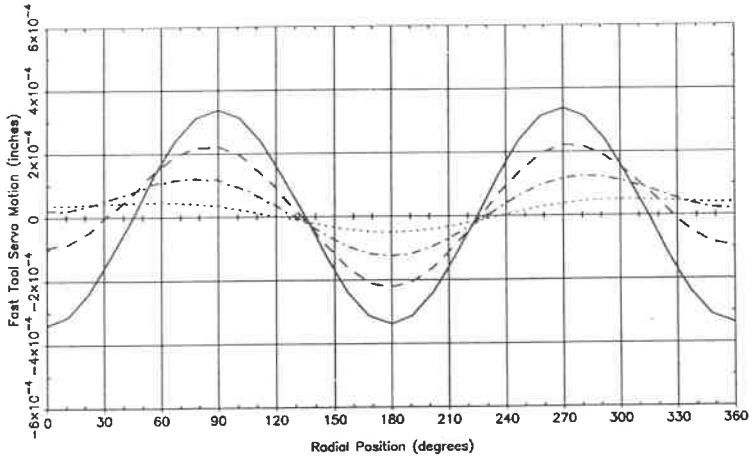

Figure 1: Tool servo motion with optimum baseline subtracted. Solid line is tool motion at $\rho_{\max}$.

Machining Setup

Machining experiments were performed on a Rank Pneumo ASG-2500 using a device known as the Fast Tool Servo (FTS)[6]. This is a short range high bandwidth linear tool motion device based on a piezoelectric actuator. There is an integral capacitance gage used for position feedback to compensate for non-linearities in the actuator. The current device has a range of 20 μm and a bandwidth greater than 1 KHz.

Two other components are needed to make up the complete machining system. First is a High Voltage Amplifier (HVA) that takes a low voltage control signal and amplifies it to a high voltage, high current drive signal for the piezoelectric actuator. Second is the high speed controller that

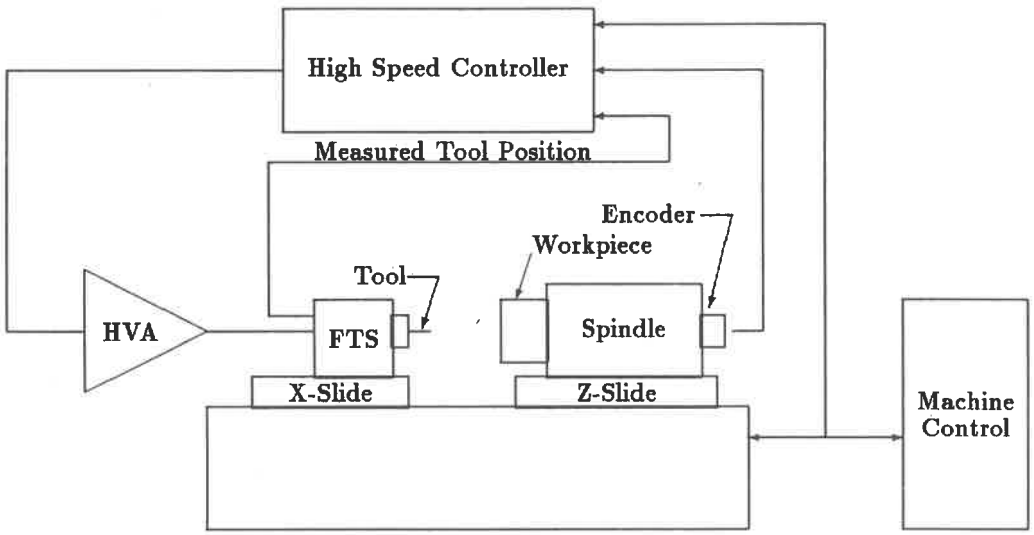

Figure 2: Diagram of experimental setup.

ties all the components together and produces the control signal for the actuator. Figure 2 shows all components of the experimental setup and the interconnections.

Results

A number of different non-axisymmetric surfaces have been fabricated to show the viability of this type of machining and to illustrate some of the possible error sources. For example, a flat surface tilted with respect to the plane perpendicular to the spindle rotation axis was fabricated by generating a decaying, once per revolution sinusoidal signal for the tool servo. An interferogram of this tilted flat with a normal reference flat around its periphery is shown in Figure 3. The inner flat is tilted so that the distance between its lowest and highest point in about 5 μm. The diameter of this tilted surface is 20 mm.

Two surface errors became apparent when machining this tilted surface under less than ideal conditions. Initial attempts at machining were done with no feedback from the capacitance gage and as a result, a non-symmetric surface error appeared. In addition, the X-axis position was not used initially but estimated based on feedrate and X starting position. This produced, as expected, a coma-like surface error – a once per revolution type error. Both of these errors have served to illustrate the importance of a good control system with sufficient inputs.

Summary

Initial experiments machining non-axisymmetric optical surfaces on a diamond turning machine have illustrated the validity of the concept. These experiments have also shown the importance of several key components that make up a system for this kind machining. These components include the high bandwidth tool servo, a high voltage amplifier, a high speed control system with a sufficient number of inputs and efficient software to generate the proper control signal.

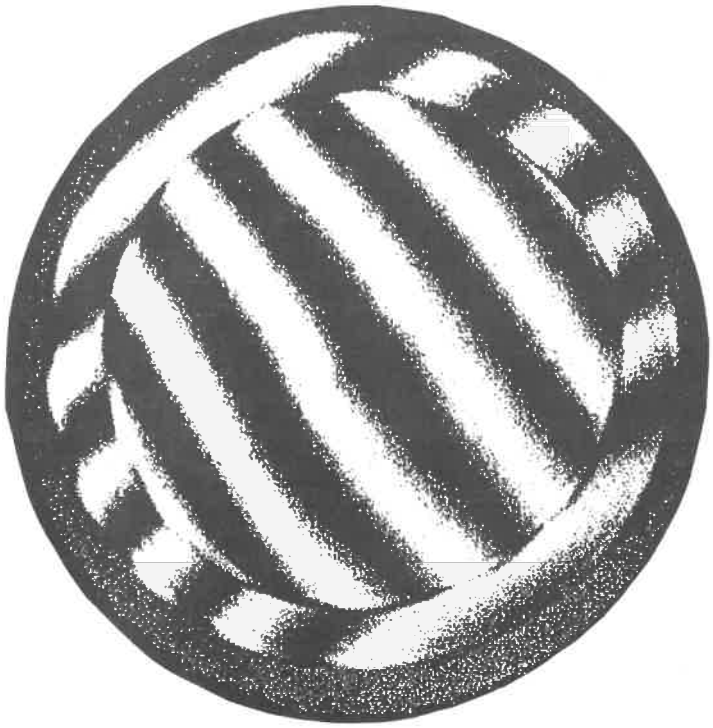

Figure 3: Interferogram of tilted flat surface machined with tool servo at a spindle speed of 480 rpm.

Further work is needed to provide a system with the capability to machine off-axis segments of aconicoid surfaces. Work is currently underway to develop a method that uses Zernike Polynomials to define a more general non-axisymmetric surface and also to develop the control system that uses this description.

References

[1] Douglass, Spivey S., *A Machining System for Turning Nonaxisymmetric Surfaces*, Ph.D. Thesis, University of Tennessee, 1983.

[2] Meinel, A.B., et.al., *Wavefront Correctors By Diamond Turning*, Applied Optics, Vol. 25, 1989.

[3] Tsao, T.C. and M. Tomizuka, *Adaptive and Repetitive Digital Control Algorithms for Noncircular Machining*, Proceedings of American Control Conference, Atlanta, Ga, 1988.

[4] The Keck Telescope is a joint project of the University of California and the California Institute of Technology.

[5] Gerchman, M.C., *A Description Of Off-Axis Conic Surfaces for Non-Axisymmetric Surface Generation*, SPIE Proceedings Vol. 1266, 1990.

[6] Falter, P.J. and T.A. Dow, *A Diamond Turning Apparatus for Fabrication on Non-Rotationally Symmetric Surfaces*, Proceedings of the International Congress for Ultraprecision Technology, Aachen, FRG, 1988.

Sub-Ångstrom Vertical Resolution, 3D Surface Profiling

F. Demarest and R. A. Smythe
Zygo Corporation
Laurel Brook Road, Middlefield, Connecticut 06455

ABSTRACT

A three-dimensional, non-contact laser interference microscope[1] is described which uses computerized phase measurement interferometry to achieve sub-Ångstrom vertical resolution. A new electronics and software platform provides very rapid high accuracy data acquisition and analysis. Averaged data set acquisition is over 100 times faster than previous techniques. Very low noise electronics with 10 bit A/D conversion provides high accuracy and high repeatability. Two cameras are described, a 256 X 256 CID array and a 512 X 512 CID array. Areas profiled with the 256 X 256 CID array range from ≈7mm x 7mm to ≈0.07mm x 0.07mm with a corresponding pixel sampling interval ranging from 28.0μm down to 0.28μm. Areas profiled with the 512 X 512 CID array are approximately the same as the 256 X 256 array with pixel sampling interval ranges of 15.0μm down to 0.15μm.

INTRODUCTION

Non-contract surface profiling is required in many precision engineering applications. Semiconductors, diamond machined components, computer memories, and fiber optics are a few of the areas where non-contact surface profiling is used to improve product performance and monitor the manufacturing process. The surface quality of precision surfaces are improving, this places extra metrology demands on surface profiling instruments. Further with increased performance required in manufacturing, high accuracy, very rapid data processing is required with computer networked instruments facilitating centralized statistical process control (SPC). To meet this growing requirement the Maxim•3D 5700 was developed. The optical head and new software have been described elsewhere.[2,3] The electronics architecture, algorithms and system performance will be described.

ELECTRONICS SYSTEM

The electronics system is designed for growth and performance, figure 1. A complete system consists of a Maxim•3D 5700 interference microscope with instrument electronics, a Hewlett Packard Apollo 9000 Series 300 or Series 400 computer, and a controller board which plugs into the computer. If desired, up to eight Maxim•3D instruments may be connected to a single computer by adding additional controller boards, and the desired instrument selected by software at measurement time.

The controller board, figure 2, includes several functional sections as shown in the block diagram. The Video section is designed for high signal to noise ratio and achieves

---

[1]U.S. and Foreign Patents.

[2]"High resolution phase measuring laser interferometric microscope for engineering surface metrology", J.F. Biegen and R.A. Smythe, SPIE Vol. 897, *Scanning Microscopy Technologies and Applications.*

[3]Article by R.A. Smythe to be published in *Photonics Spectra*, Vol. 24, Issue 8, August, 1990.

this in three ways: The Video ADC converts the analog camera video signal to a 10-bit digital value to achieve lower quantization noise than 8-bit systems. The sampling phase of the Video ADC is set during system calibration for best performance with signals near the Nyquist rate, and the Adder and Data RAM allow up to 62 intensity averages to be accumulated in a 16-bit data word. The software converts the averaged intensity values to phases for further processing. To interface with standard video the Frame Buffer converts the non-interlaced video from the 512 X 512 camera to standard interlaced video compatible with the video monitor and other video accessories. The Frame Buffer is not used for the 256 X 256 camera. To indicate the areas of interest on the video fringe monitor, cursor graphics are digitally inserted into the fringe monitor video. This insures exact registration between the camera image and the graphics.

Phase Measuring Inteferometry requires the modulation of the interference cavity. The PZT Ramp Generator provides the signal to the PZT to phase modulate the cavity. For best measurement accuracy, the amplitude and linearity of the ramp must be correct. For easy correction the ramp is generated by a RAM and a DAC, so the exact shape desired can be created, including linearity correction. Typically the PZT has 5 to 10 degrees of nonlinearity, but when the system is calibrated this is reduced to less than 0.5 degree.

To communicate between the controller board in the computer and the instrument electronics, figure 3, a serial communications bus is used, the Little Data Bus (LDB). A UART (Universal Asynchronous Receiver Transmitter) provides serial communication to the instrument and its accessories. This minimizes cabling requirements, and isolates the controller board design from changes to the instrument or accessory designs. The LDB is a 6-bit bus of Zygo design. An example of a LDB controled function is the laser light level control. The laser light level is controlled by a circular ND filter rotated by a stepping motor. The control may be closed-loop, with the controller sensing the camera video level, or open-loop, with the disc position set through the LDB. The choice of control mode is also made through the LDB.

The host computer uses the UNIX operating system, which offers several advantages. The program environment has virtual memory, which means that the memory available for a program and its data is not limited by physical memory in the system, only by available disk swap space. UNIX is a standard operating environment, suitable for software development as well as running any of hundreds of other application programs. UNIX is a multitasking environment, so that other functions such as printing, plotting, and communications can occur as background processes transparent to the user. UNIX offers excellent networking capability, allowing low cost diskless workstations, transparent access to files on other systems, and remote procedure calls (RPC). The RPC functionality makes it possible to have an instrument connected to one host being operated by a user on a different host.

Speed and accuracy are very important to system performance. To improve accuracy averaging must be performed, yet averaging can greatly slow data acquisition. The capability of doing intensity averaging in hardware on this system greatly increases the speed of making accurate measurements. Conventional phase averaging (for a 256 X 256 camera) requires each measurement to be converted to phase and summed in software, taking 5 to 15 seconds for each averaging loop. Intensity averaging in hardware requires only 180ms for each average loop, plus 5 to 15 seconds to convert the averaged intensity to phase.

During the talk repeatability, accuracy and overall system performance will be discussed.

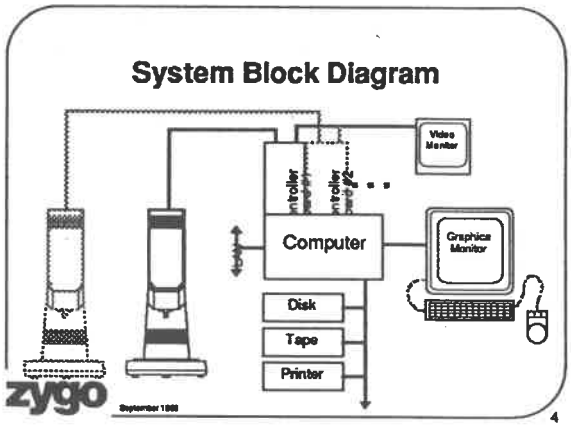

FIGURE 1

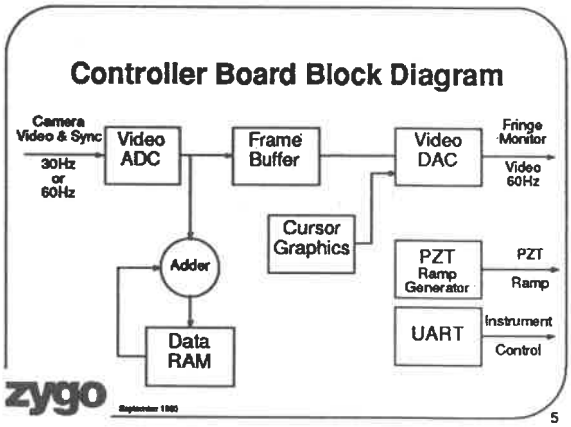

FIGURE 2

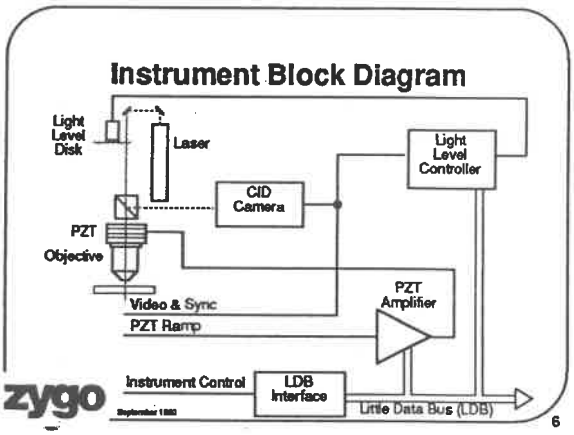

FIGURE 3

MICRO MECHANICAL SYSTEMS:

If you have trouble doing something, get a smaller hammer.

William Trimmer
Bell Laboratories
Holmdel, NJ

In the last several years it has become possible to make motors, gears, valves, and other mechanical devices that will fit inside a human hair. Using electronic fabrication technology, sacrificial and structural layers are deposited on a silicon wafer, and patterned to the desired shapes. Then the sacrificial layers are etched away leaving completely assembled mechanical devices. These micro mechanical systems potentially share with electronics the advantages of batch fabrication, complexity, and low cost. Other micro fabrication techniques such as EDM machining, LIGA, molding, plating, photolithography, etc., are being developed. Precision engineering has many potential applications in building and interfacing to micro mechanical devices, and very rapid micro mechanical controllers may find uses in precision engineering. Other potential applications include angioplasty as an alternative to bypass surgery, micro robots for handling small and fragile parts, micro instruments for scientific investigations, autonomous micro mechanical systems, and micro space craft.

This intriguing, emerging field challenges our preconceptions about mechanical systems. Small systems are inherently fast and consume very little power. As systems become smaller, mass and inertia also become insignificant relative to electrostatics, friction, and presure-related forces like hydraulics. Novel approaches and applications are needed to explore and exploit these micro phenomena. This talk will review recent research in micro mechanics.

DESIGN OF ACTIVE VIBRATION CONTROL SYSTEM

Kazuyoshi Katayama, Yoshinori Takahashi, Nobuyoshi Murai
Technical Research Laboratory, Takenaka Corporation
3-1-8 Mokuzai-Dori Mihara-Town Minamikawachi-Gun Osaka, JAPAN

1. Introduction

A microvibration-free environment is increasingly demanded by super LSI manufacturing processes, other recently introduced industries and the newest technological research facilities. The microvibration-free environment requires a vibration control system with vibration isolation performance which shuts out input base motion, and vibration prevention performance which works against vibration transmitted directly into the equipment.

This paper discusses an active vibration control system equipped with both vibration isolation and vibration prevention controls. A SDOF (single-degree-of-freedom) has been analyzed to clarify the relationship between control effects and control forces in relation to both aspects of the active vibration control system.

2. Active Vibration Control System

Hypothesizing an ideal SDOF active vibration control system which does not take into account the actuator dynamics, this section discusses how to design an active vibration system equipped with vibration isolation and prevention performances. Fig. 1 shows the ideal SDOF vibration control system.

2.1 Vibration Prevention Performance

When harmonic direct disturbance D is added on the system as shown in Fig. 1, the acceleration amplitude of a stationary response of system is given by the following equation:

$$A=[\omega^2/\sqrt{\{(K+K_d)-\omega^2(M+M_d)\}^2+\omega^2(C+C_d)^2}]\times D \quad \cdots\cdots (1)$$

M_d,C_d and K_d : Acceleration, Velocity and Position feedback gain

The acceleration resonance curve at acceleration, velocity and position feedback is shown in Fig. 2. Of these feedbacks, acceleration feedback, capable of reducing amplitude simply in the frequency range higher than the resonance, works effectively to improve the vibration prevention performance of the system. In considering system vibration prevention performance, velocity feedback and

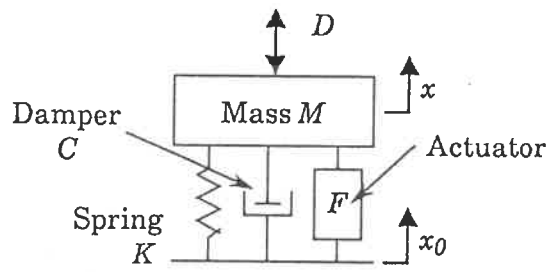

Natural Frequency $f_0=2.0$Hz
Damping constant $h=2.0\%$

Fig.1 Ideal SDOF vibration control system

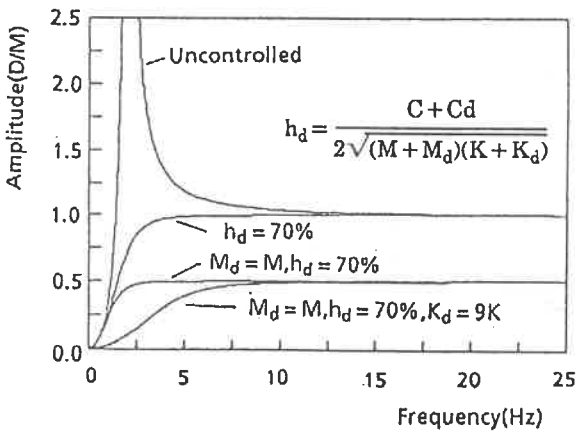

Fig.2 Acceleration resonance curve

acceleration feedback which become $h_d=1/\sqrt{2}(70\%)$ make it possible to design the acceleration amplitude over the entire frequency range of the system receiving direct forces to be below $M/(M+M_d)$ in uncontrolled state.

2.2 Vibration Isolation Performance

In dealing with input vibration from the installation floor, the passive vibration isolation system is constituted by increase/decrease of damper and spring (mechanical damper and spring) laid over the installation floor. The most appropriate design of such a vibration isolation system is described by the optimal regulator which minimizes the performance function taking into account system absolute acceleration ($\ddot{x}$) with the state variable as the response value ($\dot{x}$-$\dot{x}_0$, x-x_0) of the relative coordinate system. It becomes clear from Table 1 and Fig. 3 that a system which achieves vibration isolation by an increase/decrease of mechanical spring and damper aims toward a system constituted by a damper with a damping constant of $h_r=1/\sqrt{2}(70\%)$ for the system reducing the resonance point amplitude and the soft spring which decreases the natural frequency.

Table 1 Optimal regulator design

Weight Factor		Feedback Gain		Pole	
Abs. Acc. α_r	Ctrl. Frc.	Velocity:$\dot{x}$-$\dot{x}_0$ $(C_r^*-C)/C$ $(h_r\%)$	Position:x-x_0 $(K_r^*-K)/K$ (ω_r)	Real	Img
10^0	1	15.11(38.31)	-0.293(10.6)	-4.05	9.76
10^2	1	9.58(67.10)	-0.901(3.96)	-2.66	2.94
10^4	1	2.52(70.36)	-0.990(1.26)	-0.88	0.89
10^6	1	0.12(70.68)	-0.999(0.397)	-0.28	0.28
10^8	1	-0.65(70.71)	-0.999(0.126)	-0.09	0.09

$\omega_r=\sqrt{K^*/M}$, $h_r=C^*/2/\sqrt{MK^*}$

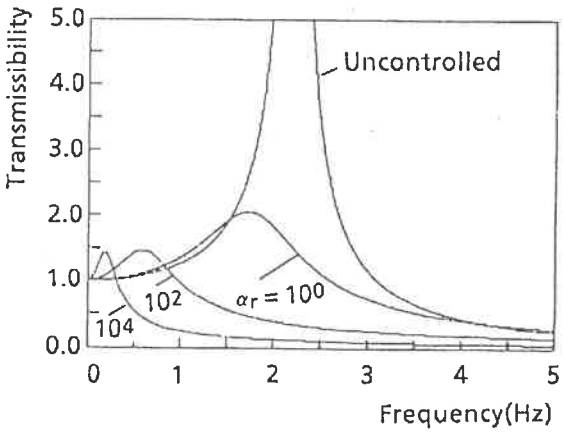

Fig.3 Transfer function (regulator)

System vibration isolation performance can be expressed as a transfer function (X/X_0), a ratio of the structure response to the input base motion. Vibration isolation of the system expressed by the aforementioned regulator is indicated as a transfer function; then a system whose absolute value of the transfer function is less than that of regulator and which feeds back a response value of an absolute coordinate system, not relying on input working toward increasing the mass, damper and spring in order to coexist with the vibration preventive performance, should be considered. When a mechanical spring constant and a damping coefficient obtained from the regulator design are designated as K_r^* and C_r^* respectively, the absolute value of the transfer function of the vibration isolation system is as shown in the following equation:

$$|H_r(\omega)|=[(K_r^{*2}+\omega^2C_r^{*2})/\{(K_r^*+\omega^2M)^2+\omega^2C_r^{*2}\}]^{1/2} \quad \omega\text{:Circular frequency.} \quad \cdots\cdots (2)$$

Furthermore, the absolute value of the transfer function of the system receiving the absolute coordinate system feedback is as follows:

$$|H_a(\omega)|=\{(K^2+\omega^2C^2)/[\{(K+K_a)+\omega^2(M+M_a)\}^2+\omega^2(C+C_a)^2]\}^{1/2}. \quad \cdots\cdots (3)$$

Then we can get the minimum, positive or zero, absolute coordinate system feedback gain M_a, C_a, K_a, as a result of following equation:

$$|H_r(\omega)|\geqq|H_a(\omega)|. \quad \cdots\cdots (4)$$

Thus, when finding the absolute coordinate system feedback gain from Eq. 4, the feedback gains M_a, C_a, K_a, which take into account both the vibration prevention and vibration isolation performance are obtained by giving the following conditions:

$$M_a \geqq M_d \ , \ C_a \geqq C_d \ , \ K_a \geqq K_d. \qquad \cdots\cdots (5).$$

3. Simulation Analysis

Simulation analysis was preformed to confirm the control effect of the absolute coordinate system feedback design described in the forgoing section. In the analysis model, an ordinary passive type vibration isolator is assumed to have the natural frequency of 2Hz and a damping constant of h=2%, as in Fig. 1. In addition, design parameters of vibration isolation performances and requirements for vibration prevention performance are shown in Table 2. Vibration isolation performance produces a transfer function which is less than regulators designed in Cases 1 ~ 3; the vibration prevention performance takes into account Eq. 5 under respective conditions Cases D1 ~ D3 and seeks the design feedback gains M_a, C_a, K_a, which satisfy both of these performances.

In the simulation, response analysis in the time domain was performed using band limited white noise as the base acceleration and direct outside forces in order to study the relationship between the maximum acceleration response value and maximum control force. The average value for 20 waves of white noise generated randomly has been used as the maximum response value.

Maximum acceleration response value and maximum control forces at the input base motion and direct outside forces are indicated in Figs. 4 , 5 and in Figs. 6 , 7, respectively. The vertical axis represents the non-dimensional quantity of maximum acceleration response value and the horizontal axis, the non-dimensional quantity of maximum control force, thus plotting the relationship between the control effects and the control forces. In the diagram, ○ stands for Case D1, △ Case D2, □ Case D3, and as a comparison ● indicates the regulator design value.

Results from the input base motion demonstrate that each design system, Cases D1 ~ D3, generates a greater vibration isolation effect than the regulator, and that Case D1 which dose not take into account the vibration prevention performance exhibits a greater vibration isolation effect at a lower control force than the regulator. Furthermore, in Cases D2 and D3 vibration prevention requirements work effectively on vibration isolation, and these cases show the weaker control force than the regulator with the same level of vibration isolation effect although their control forces are greater than their corresponding regulators.

Results from the input of direct outside forces demonstrate that requirements for vibration prevention performance work effectively. Furthermore, they achieve a greater vibration prevention effect than Case D1 which does not take vibration prevention into account while their control forces tend to be weaker than when the same level of control effects are obtained. Even Case D1 exhibits

Table 2 Design parameters for vibration isolation and prevention performance

Isolation Performance Condition (Regulator)		
Case	Weight Factor	
	Abs. Acc. α_r	Control Force
1	10^2	1
2	10^4	1
3	10^6	1

×

Prevention Performance Condition			
Case	Feedback gain		
	Acc. M_d/M	Vel. h_d	Pos. K_d/K
D1	-	-	-
D2	1.0	70%	0.0
D3	1.0	70%	9.0

a greater vibration prevention effect than the regulator design, showing the added effect of a large damper by absolute velocity feedback.

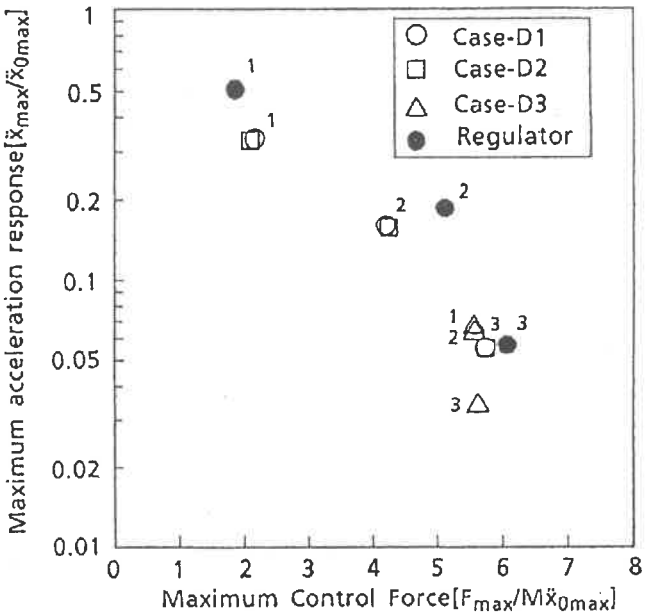

Fig.4 Isolation effect (White noise 0.2~10Hz)

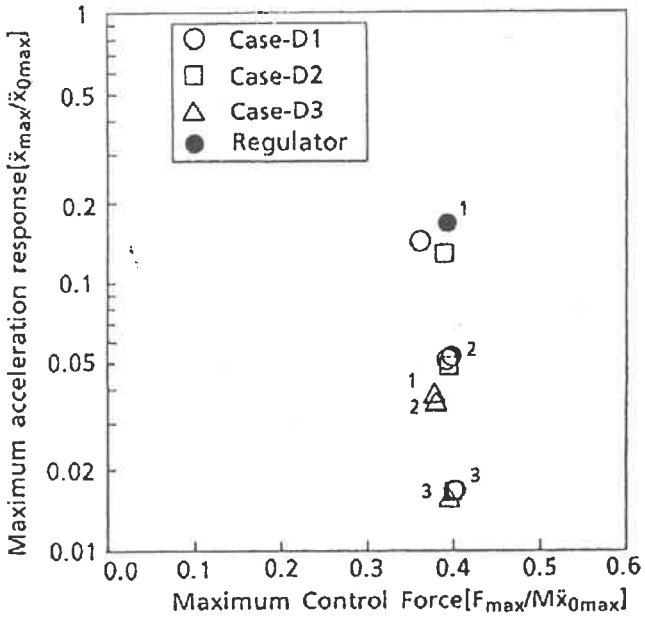

Fig.5 Isolation effect (White noise 1~25Hz)

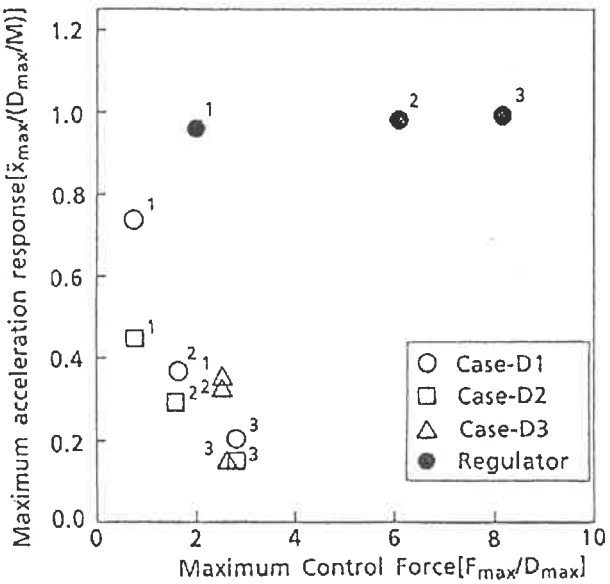

Fig.6 Prevention effect
(White noise 0.2~10Hz)

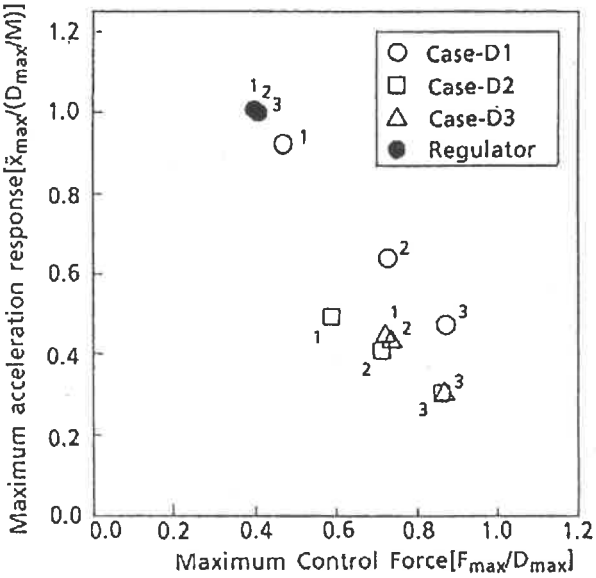

Fig.7 Prevention effect
(White noise 1~25Hz)

5. Conclusion

The active vibration control system can achieve both vibration isolation and vibration prevention performance by feeding back the absolute coordinate response of the system, and the control effect has been confirmed by simulation analysis.

Reference Literature

1) Takahashi et al.: "Study on Active Vibration Control System Using Linear Motor", Journal of Struct. Constr. Engng, AIJ, No. 412, June, 1990

A 0.25μm OPTICAL PROJECTION PRINTER FOR IC LITHOGRAPHY

A. Grenville (*), R.L. Hsieh (*), R. von Bunau (*), D.A. Markle (**), G. Owen (***) and R.F.W Pease (*)

(*) Stanford University, Stanford, CA 94305-4055
(**) Ultratech Stepper, Santa Clara, CA 95054
(***) Hewlett Packard, Palo Alto, CA 94303-0867

I. Introduction

At present, lithography for mass production IC manufacture is carried out at minimum feature sizes of about 0.7 μm or greater, using optical projection printers. These typically work at numerical apertures (NAs) of between 0.40 and 0.54 at a wavelength of 436 nm (G-line) or 365 nm (I-line) and over field sizes ranging from 15 x 15 mm^2 to 20 x 20 mm^2. It is predicted that by the year 2000 the resolution requirement will be 0.25μm, and until recently, it has been assumed that this would necessitate using X-rays as the exposing radiation. However, it is now becoming apparent that this performance can in fact be acieved optically, and a particular way of doing so is by using a "Half-Field Dyson" configuration. A prototype of such a system has been built and is described in this paper.

The resolution of a diffraction limited optical lithography system is approximately $0.7\lambda/A$ where λ is the wavelength of the exposing radiation and A is the numerical aperture. The system described in Section II works at a wavelength of 248 nm, necessitating a numerical aperture of 0.7 in order to achieve 0.25 μm resolution. The resulting depth of focus is given approximately by λ/A^2, which in this case is 0.5 μm. Because of the small depth of focus, accurate focusing is essential, and a possible autofocus scheme is described in Section II.

II. The Optical System

A schematic view of the projection optics of the prototype system is shown in Fig. 1. The lens, mirror and mask are made of fused quartz. The unpatterned surface of the mask is separated from the plano surface of the lens by a thin film of index matching fluid, and the wafer is held lightly in contact with the patterned surface of the mask. The principal ray of the projection optics is drawn as a heavy line: it passes through the mask, which therefore forms part of the optical path. The plano-convex lens and the concave mirror are configured as a Dyson system [1]. To achieve better correction their centers of curvature, which are located approximately at the intersection of the optic axis and the patterned surface of the mask, are separated axially by 40.6μm. The system has unit magnification, is telecentric at both mask and wafer, has a flat field and is almost completely free of geometric and chromatic aberrations. Because of the low chromatic aberration, a mercury arc lamp may be used as the source, radiation with a wavelength of 248±5 nm being selected by an interference filter.

Modified Dyson systems are already widely used in IC lithography, but at much lower NAs (up to 0.42). In this case, the mask and wafer planes are separated by beam folding prisms which are cemented onto the plano-convex lens [2], allowing the mask to be illuminated in

transmission. However, this technique breaks down at high NAs, because the prisms vignette a significant fraction of the field. The Half-Field Dyson configuration overcomes this limitation by using the mask as a reflection object. This is done by coating the concave mirror with a 50% transmitting coating, which allows the illuminating light to pass through it, as indicated by the dashed rays in Fig. 1. The mask is patterned in aluminum, which has a reflection coefficient in excess of 85% at 248 nm.

An indication of size is that that the radius of curvature of the concave mirror is 100 mm. The corresponding size of the object and image fields is 2x4 mm^2. Figure 2 shows patterns exposed in 0.8 μm of Shipley SN248 photoresist at a dose of 7 mJ cm^{-2} using this system: the lines are 0.25 μm wide, on a 0.75 μm pitch. To obtain this performance, the tolerances on figure accuracy and surface roughness of the optical components are severe: in particular, for the mirror, they are better than 1/60 wave measured at 633 nm.

III. An Autofocus Scheme

As was pointed out in Section I, the depth of focus of this system is extremely small. As a result, high precision focusing is essential, and fortunately, the folded beam path of the Dyson system makes this possible. A particular scheme involves patterning two gratings on the mask, these being placed symmetrically outside the object and image fields, as shown in Fig. 1. When the system is in focus, a sharp image of one grating is superimposed on the other one, and a highly modulated signal results if transmitted or reflected light is detected while the mask is scanned in the direction shown in the diagram. As the system is defocused, the modulation decreases, giving an accurate measure of focus. Experimental results obtained in transmision with this "confocal" focusing scheme are shown in Fig.3.

IV. Conclusions

A prototype Half-Field Dyson projection system has been constructed, and initial results indicate that the concept is practicable. For such a system to be useful in IC production, the field of view would have to be substantially increased, and there is good reason to believe that this can be done. A design has been proposed in which the linear dimensions of the optical elements is increased by a factor of about 5, and in which the singlet plano-convex lens is replaced by a doublet: this allows a diffraction limited field sufficient to hold a 256 M-bit DRAM to be achieved. This design also incorporates 0.25 mm air gaps between the mask and the plano-convex lens, and between the mask and the wafer.

Acknowledgements

The authors would like to acknowledge the help given by the Shipley Company, who provided photoresist materials, and by IBM and Signetics (Philips), who provided the masks used in this work. The research was supported by SRC (contract # 88MC500-1) and by IBM (contract # 6324 QSXAB22G).

References

[1] J. Dyson, J. Opt. Soc. Am. **49** (7) 713-716, 1959.

[2] David A. Markle, Semiconductor International, May 1986.

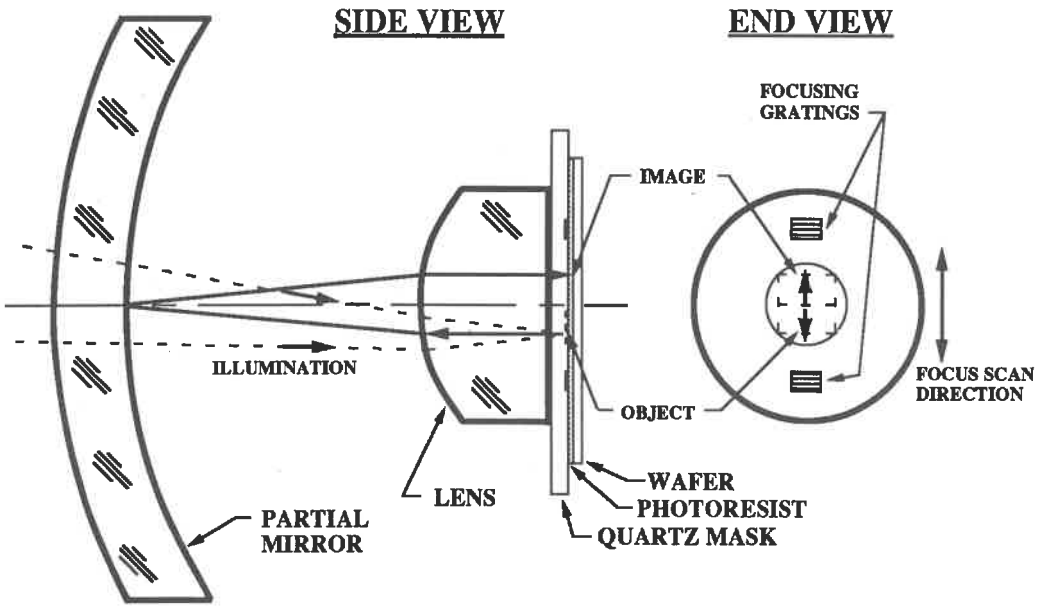

Figure 1: The projection optics of the Half-Field Dyson System

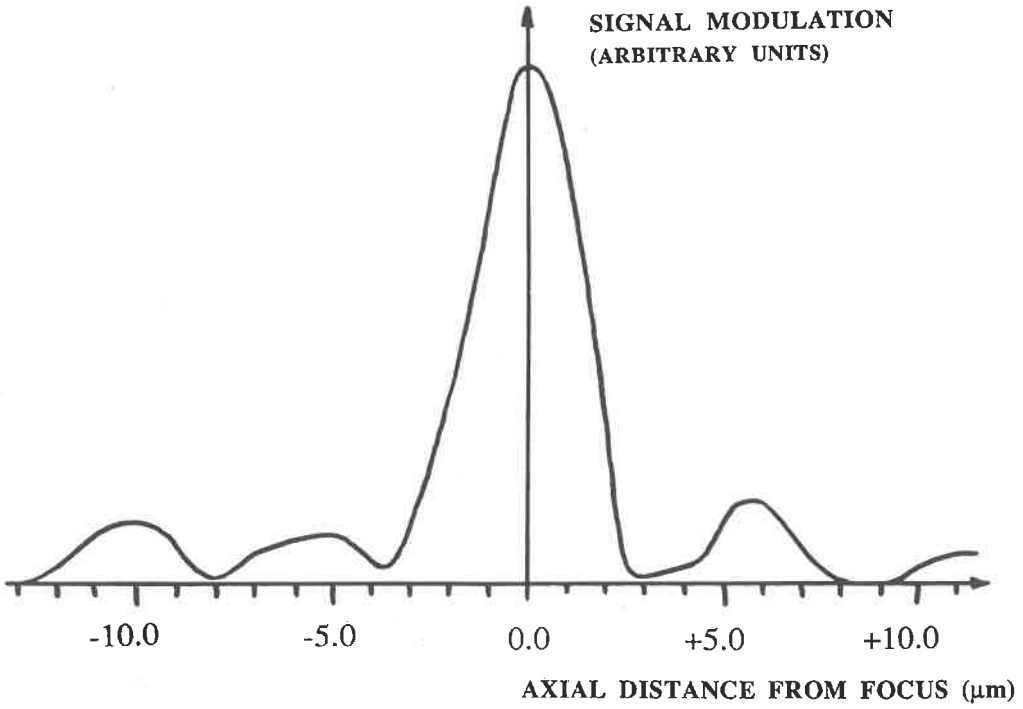

Figure 3: Experimentally measured signal modulation as a function of focus setting

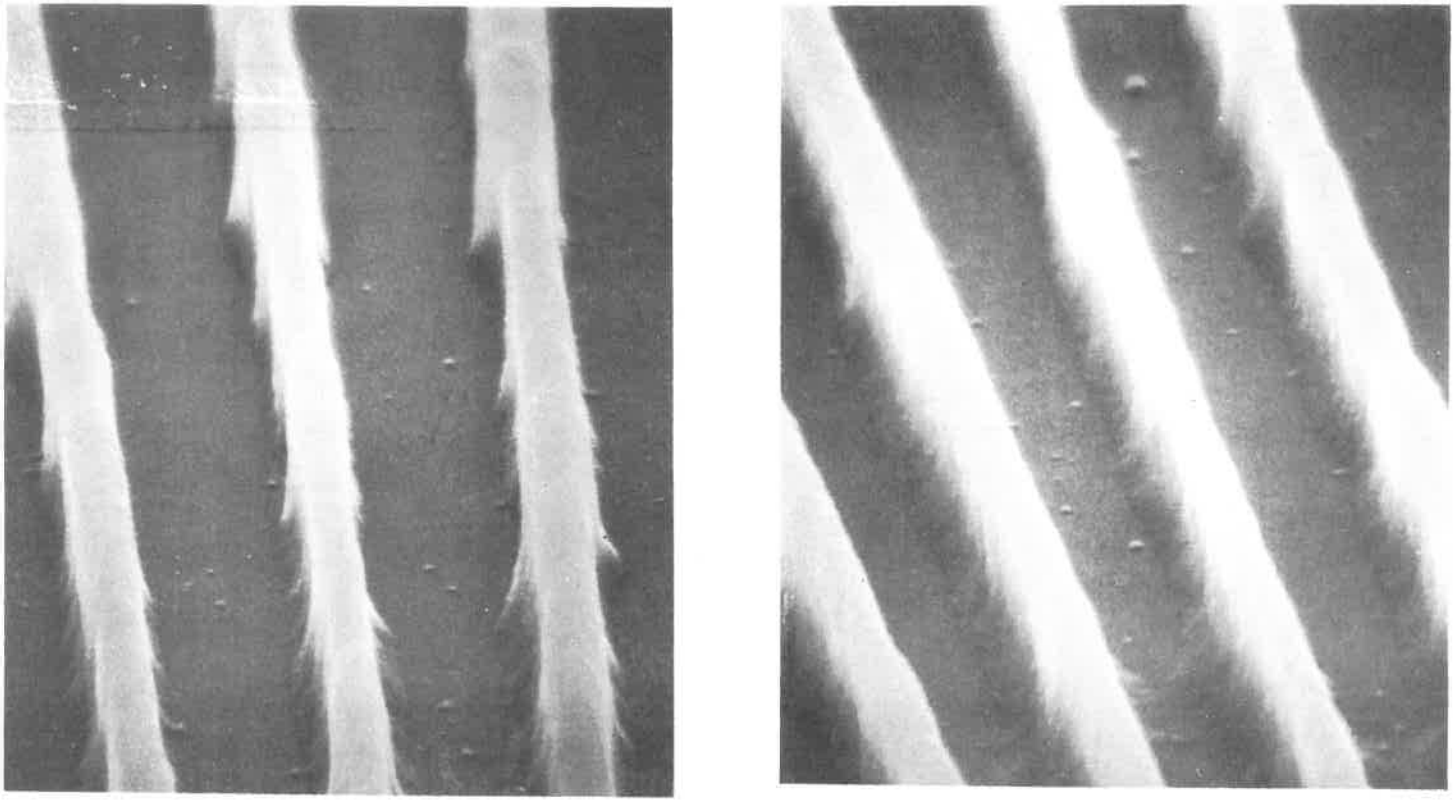

Figure 2 : Two views of 0.25 μm lines on 0.75 μm pitch exposed on the prototype Half-Field Dyson System

THE CHEMISTRY OF GLASS POLISHING

Lee M. Cook

Galileo Electro-Optics Corp.
Sturbridge, Mass.

1. Introduction:

Abrasive wear may be classified as occurring within three distinct regimes. The first is classical grinding, in which large high-energy particles impinge on a solid surface and effect mass removal by fracture. Lower loadings and particle sizes give "ductile" regime grinding, where particle impingement produces stresses near the critical levels for crack propagation, resulting in plastic surface effects but not necessarily crack propagation. Still smaller particles and loadings give rise to surface stresses which are within the elastic limits of the solid. This is the regime in which polishing occurs.

The size of the products of abrasive wear is proportional to the roughness of the worn surface. In the case of polishing, where subnanometer smoothness is routinely achieved, it is clear that removal must occur as small clusters of atoms rather than as discrete particles. Thus polishing must be classified as an essentially chemical process.

The necessary conditions for polishing to proceed at measurable rates are that (a) a suspension of particles having some kinetic energy must be in contact with the solid surface, and (b) that water must be present in the suspension. Therefore, the detailed mechanisms of the polishing process can be understood by examining the behavior of solid surfaces in aqueous solution under the conditions (stresses, pressures, temperatures, and times) which are expected to occur during particle/surface contact. This talk focuses on the aqueous behavior of oxide surfaces, as the aqueous contact surface of most materials of interest to optical fabricators (including glass, polishing compounds, many metals, Si, etc.) is generally accepted to be an oxide layer[1]. An understanding of the polishing chemistry of silicate glasses can provide insight into a more general chemical polishing mechanism.

2. Mechanics of particle/surface interaction

The simplest mechanical model of the particle/surface interaction is a travelling hertzian indenter. The stress distribution expected for such an interaction has been thoroughly discussed in the literature[2,3]. Subsurface stress

intensities are determined by particle size, shape, load, and the elastic properties of the system. For a travelling indenter, a compressive zone is observed at the leading edge of the particle with a corresponding tensile zone extending from the trailing edge. Analysis of particle impact in Elastic Emission Machining (EEM) yielded similar subsurface stress fields whose magnitude and spatial distribution were a function of kinetic energy and incidence angle[3]. For the case of a moving particle, the magnitude of subsurface stress is strongly influenced by the coefficient of friction between particle and glass. Because the scale of interaction is atomic, the coefficient of friction may be determined from the load, the contact area, the extent of atomic bonding, and the bond strengths. This has been reviewed in more detail by Cook[4]. In addition to the subsurface stress fields, it is reasonable to assume that corresponding hydrostatic pressures exist in the liquid medium, together with modestly elevated temperatures.

3. Surface reactions in aqueous solution

Interaction of an oxide surface with water gives rise to surface hydroxyl groups. For the case of silica, the most important oxide glass constituent, this reaction may be simply expressed as

$$\equiv\text{Si-O-Si}\equiv + \text{H}_2\text{O} \rightleftharpoons 2\equiv\text{Si-OH}. \qquad [1]$$

The rate of reaction [1] below the glass surface is believed to be controlled by diffusion of molecular water. As reviewed by Cook[4], molecular water diffusion has been observed to increase exponentially with increasing temperature and tensile stress and decrease exponentially with increasing compression. Molecular water solubility shows the opposite trend. This was explained in terms of the pressure dependence of the equilibrium constant of the water-silica reaction. Thus reaction [1] is expected to proceed forward under compression (glass dissolution) and to reverse under tension (reprecipitation). Calculated water diffusion depths using pressure dependent diffusion coefficients and stress levels predicted from indenter models are consistent with polishing layer depths determined from surface microanalysis.

The surface hydroxyl equilibrium of oxides in solution may be described by

$$\equiv\text{R-OH}_2^{+} \overset{K^1}{\rightleftharpoons} \equiv\text{R-OH} \overset{K^2}{\rightleftharpoons} \equiv\text{R-O}^{-} \qquad [2]$$

where R is a metal cation (e.g. Si^{4+}, Ce^{4+}, etc.). The left species is a Bronsted acid (proton donor) with equilibrium constant K^1 while the right species is a Bronsted base (proton acceptor) with equilibrium constant K^2. When solution $pH \approx pK^1$ the oxide surface shows charge neutrality. This is commonly referred to as the isoelectric pH or IEP. Above or below the IEP oxide surfaces assume increasing

negative or positive charges respectively. For silica, pK^1 is -2, and the IEP is ~2. Thus the silica surface has a significant negative charge except in highly acidic solutions. Measured IEPs for a given oxide may vary over a range of values, influenced by the composition and form of the oxide (crystalline or amorphous), the degree of hydration of the surface, the presence of lattice defects and contaminants, and changes in redox equilibria. Parks[5] used a simple electrostatic model to correlate IEP data for a variety of oxides. An inverse relationship to Z/R_{eff} was found, where Z is the cation charge and R_{eff} is the separation distance between the cation and the adsorbed proton.

The presence of charge at the solid surface requires screening by counterions to preserve charge neutrality, i.e. an electric double layer is formed. Such screening may involve dissolved ions together with the reactions of the solvent. In the case of water, these may be dissociative, as inferred from eq.[2] above or associative, i.e. hydrogen bonding. The high dipole moment of water leads to orientations of the water molecule at the charged surface. This alignment in turn affects molecules further into the solution via hydrogen bonding.

4. Discussion

From the above, it may be concluded that the passage of a particle under load across the glass surface produces a sequence of chemical events which by itself represents the simplest chemical polishing mechanism. First, at the leading edge of the particle hydrostatic pressure and subsurface compressive stresses lead to glass dissolution. Second, at the trailing edge, relief of hydrostatic pressure, together with the presence of subsurface tensile forces act to reprecipitate silica back onto the glass surface, forming the so-called "Beilby Layer". At the same time, molecular water diffuses into the glass surface. This process is repeated as additional particles pass by. Mass removal occurs when the rate of dissolution is greater than the rate of redeposition. However, the above mechanism does not explain differences in polishing rate for different polishing particles.

Cook[4] correlated polishing rate and IEP data for a variety of polishing compounds and silicate glasses. The highest polishing rates were observed for oxides whose IEP was substantially above that of SiO_2 and closest to the solution pH. Relative polishing activity could be estimated from the single R-O bond strength and the difference between the IEP of the polishing compound and the solution pH. This also gave an excellent fit to EEM rate data[6] for Si polished by aqueous suspensions of SiO_2, ZrO_2, and Al_2O_3, indicating a more general applicability.

Conclusions from this were that the difference in surface charge between particle and solid surface determines the extent of contact bonding. This in turn controls the coefficient of friction, the magnitude of subsurface stress, and the extent of glass dissolution. For the case of EEM, where the subsurface stress

fields are solely determined by the particle's kinetic energy, the extent and strength of bonding determines the amount of mass transported away from the solid surface.

In order for bonding to occur between two surfaces, they must be brought into atomically close proximity so that attractive Van der Waals forces overcome the repulsive surface forces of the electric double layer and solvation layers. Two like surfaces (e.g. SiO_2 and SiO_2) exhibit substantial surface repulsion forces, whose magnitude[7] is greater than calculated particle loads during polishing ($\sim 10^{-7}$ N)[4]. These surface forces represent an activation energy barrier which must be overcome for bonding to occur. This can be effected by giving sufficient load or kinetic energy to the polishing particle, or by reducing surface charge density, as the intensity of the repulsive force diminishes with decreasing surface charge. Given that the silica surface is always highly charged in the normal polishing environment, one must consider altering the surface forces of the polishing particle to lower the activation energy for closest approach. At the IEP of the polishing compound, double layer and solvation forces are minimal and bonding should be most efficient. At solution pH < IEP, although the positive surface charge of the particle should yield attractive forces, the interaction should only lead to proton transfer rather than effect a strong ionic bond.

5. Conclusions

Substantial stresses arise from the contact between polishing particles and a solid surface. These stresses lead to a variety of chemical interactions between the aqueous environment and the contacting solid surfaces. The major factors influencing the rate of these reactions and of mass removal are the load and velocity of the abrasive particles, the elastic properties of both solid and abrasive, the rate of dissolution of the solid under the conditions imposed by particle contact, and the surface charge difference between particle and solid. Mechanisms proposed for silicate glass polishing are felt to be a subset of a general polishing mechanism for solid oxides.

References

[1] J. Bolger, A. Michaels, in; Interface Conversion for Polymer Coatings, eds. P. Weiss, G. Cheever (Elsevier, NYC 1968) 3.
[2] B. Lawn, R. Wilshaw, J. Mater. Sci. 10 (1975) 1049.
[3] Y. Mori, N. Ikawa, K. Sugiyama, T. Okuda, K. Yamauchi, J. Japan. Soc. Precision Eng. 51(6) (1985) 1187.
[4] L. Cook, J. Non-Cryst. Solids, 120 (1990) 152.
[5] G. Parks Chem. Rev. 65(1965) 177.
[6] Y. Mori, K. Yamauchi, K. Endo, Precision Eng. 10 (1988) 24.
[7] R. Horn, D. Smith, J. Non-Cryst. Solids, 120 (1990) 72.

AN EXPERIMENTAL PROCEDURE FOR STUDYING DIAMOND TURNING CHIP MECHANICS

Richard L. Rhorer
Los Alamos National Laboratory
Los Alamos, NM

and

Don A. Lucca
Oklahoma State University
Stillwater, OK

EXTENDED ABSTRACT

Diamond turning is the single point machining of optical quality surfaces using single crystal diamond tool bits and very high precision machine tools. The technology of diamond turning is expanding with ongoing research efforts to improve the surface finish produced, the overall accuracy of components, and the adding of new materials to the list of those materials that are currently "diamond turnable." Research into the chip formation during the machining process, or diamond turning chip mechanics, is one of the major areas of interest in efforts to improve the diamond turning process. Research in the mechanics of material removal with single point turning can also contribute to the understanding of more complicated processes such as grinding and polishing.

Diamond turning chip has some similarities to conventional machining; however, the differences are: a) the depth of cut is generally much smaller (in the micrometer range), b) the surface integrity of the final workpiece is often critical, c) the diamond tool has a very high thermal conductivity (which could alter the temperature distribution in the cutting zone compared to conventional machining), and d) the elastic recovery behind the cutting edge becomes important (and therefore the tool edge radius or sharpness also becomes important).

The most straight forward way to study the diamond turning cutting process might be to simply machine surfaces, vary some of the parameters, and evaluate the final product. Indeed, many of us have done just that. The problem arises when trying to understand the fundamental aspects of the process so as to predict what parameter changes will produce a desired result in the final product. To begin to study the process in more detail we have tried to develop a method that will be useful in comparing experimental results to predictive models.

Much of the work in trying to understand the cutting process has been done with two dimensional, or orthogonal, machining models. In order to compare our results more easily with these models we have developed an experimental procedure to produce orthogonal cutting conditions (i.e., two-dimensional tool forces). This method employs a thin disk rotated in the air-bearing spindle of one of our diamond turning lathes. A large radius diamond tool is advanced into the edge of the disk using the x-axis, or cross-slide drive of the computer controlled ultraprecision lathe. The depth of cut is determined by the spindle rotational speed and the in-feed rate programmed into the lathe controller.

We have investigated several methods of obtaining data pertinent to the cutting process. The most important data that we have obtained to date in our experimental program is the tool forces measured by a commercial dynamometer mounted under the tool holder. We are using a three axis piezoelectric type transducer, Kistler Model 9257A. Because it is very difficult to measure DC or steady state forces with a piezoelectric transducer, we have made our specimen disks with notches in the the outer edge. This produces a square wave type signal

from the force transducer. The notched wheel also provides a known distance between notches which is the underformed chip length. An estimation of the cutting ratio, or chip compression factor, can be obtained by comparing the length of an unbroken chip with the original length.

Even though the experimental set-up lends itself to easy access for optical investigation of the cutting process, we have not been successful in obtaining photographic data of the chip formation process. In the range of depths of cuts of interest for diamond turning, the resolution required to actually make measurements of chip thickness or contact length behind the tool is greater than we have been able to obtain.

The advantages observed for this notched disk experimental method are:

1. the geometry allows two dimensional cutting experiments to be done which enables comparison to predictive models,
2. the method allows the cutting forces to be measured with a piezoelectric force transducer because a zero force can be established between cuts,
3. a constant spindle rotational speed and in-feed arte assure a known depth of cut irrespective of any elastic recovery behind the tool,
4. the disk width can be chosen to give absolute cutting forces large enough for measurement.

A series of cutting experiments were performed on OFHC copper. The depth of cut was varied by adjusting the x-axis in-feed rate for a constant spindle RPM. Forces in both the direction of cutting velocity (cutting force) and the direction normal to the cutting velocity (thrust force) were measured.

An example of the cutting force data is shown in Fig. 1. The signal has some noise and therefore is not a perfect square wave; however, a zero base line can be determined and a fit to the upper part of the trace is the average cutting force during the removal of one chip from the top of one of the 'teeth' between the notches. Using the calibration factor provided by the force transducer manufacturer, moving the base line, and smoothing the data, the cutting force appears as shown in Fig. 2.

Using the data obtained for the cutting forces, a plot for the specific cutting energy versus depth of cut can be made. Fig. 3 shows a comparison of the data obtained with the notched disk experiment with that of Moriwaki.[1] Reasonable agreement is observed for both magnitude and trend with depth of cut.

The measurement of cutting forces and hence specific cutting energies is viewed as the first step in understanding the mechanical dissipation of energy in the diamond turning process. A complete understanding of the partitioning of this mechanical energy will provide the basis for further understanding of the process, including the resulting temperatures.

In conclusion, we have developed an orthogonal machining method for studying diamond turning chip mechanics. Cutting forces have been measured and specific cutting energy as a function of depth of cut has been determined. A comparison with published data appears to indicate the method is producing reasonable results.

---

1. Moriwaki, T., "Machinability of Copper in Ultra-Precision Micro Diamond Cutting," Annals of the CIRP, Vol. 38/1/1989.

ACKNOWLEDGEMENTS

There are many who have helped with this ongoing work at Los Alamos, and we would like to give special acknowledgement to: Jon Sollid (Sollid Optics, Inc) for leading our efforts to use optical techniques; Norm Elliott (Los Alamos, group MST-7) for SEM examination of tools and chips; Chris Evans (National Institute of Standards and Technology) for tool characterization and advise on the experiments; Phil Hannah (Los Alamos consultant) for advise on experimental methods; and Felix Garcia, Jake Bartos, Aaron Lopez, and other technicians at Los Alamos for their work setting up, running experiments, and data acquisition. Y. W. Seo from Oklahoma State University has assisted the project with data reduction and model development.

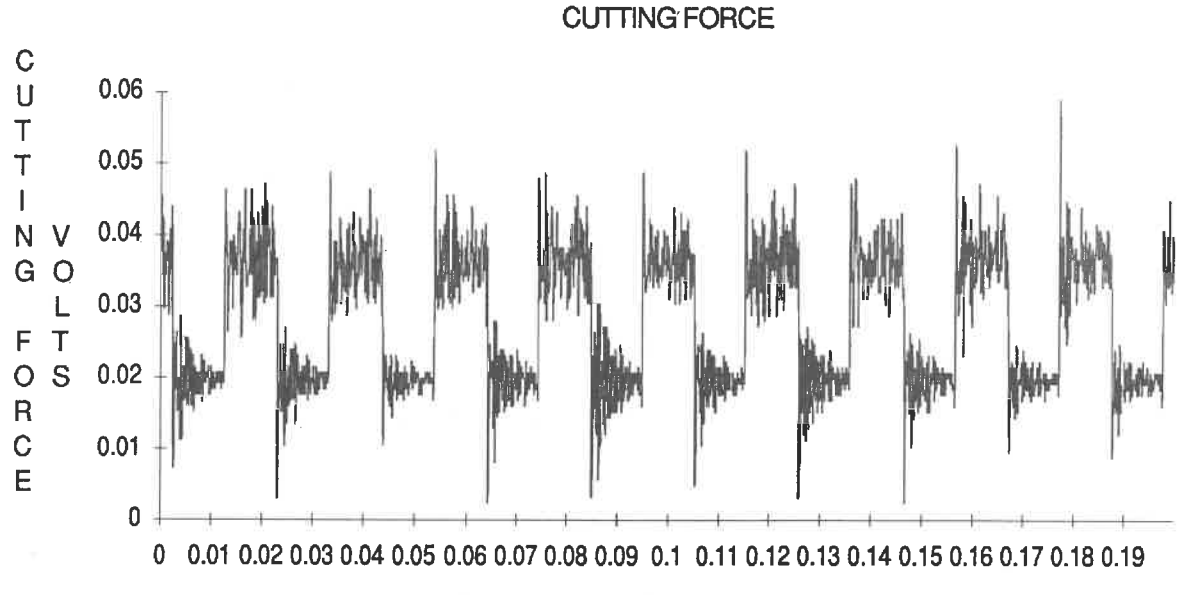

Fig. 1 Example of Signal From Force Transducer

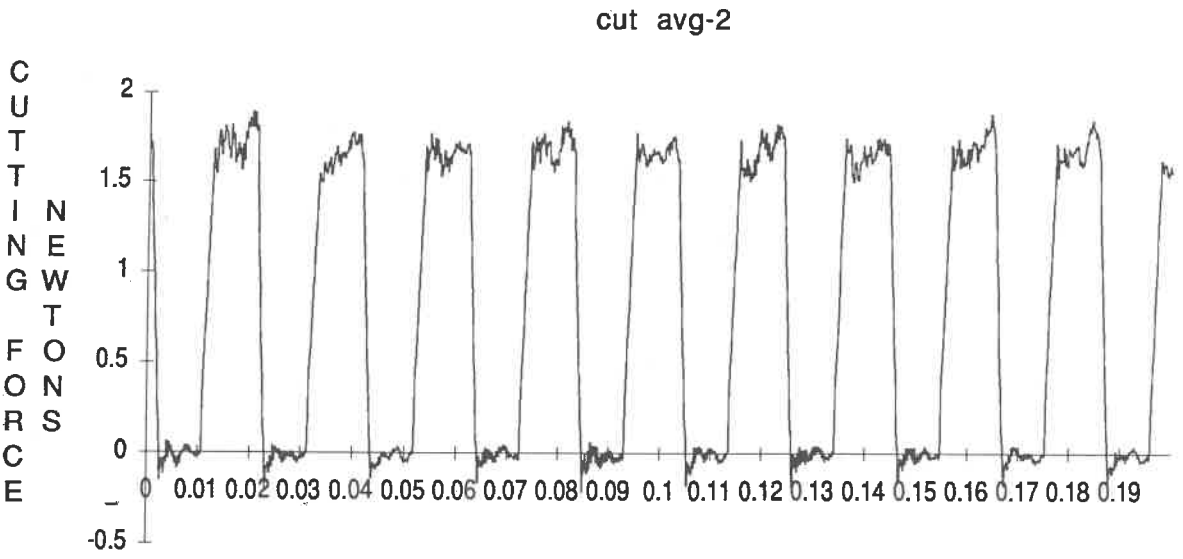

Fig. 2 Example of Cutting Force Data

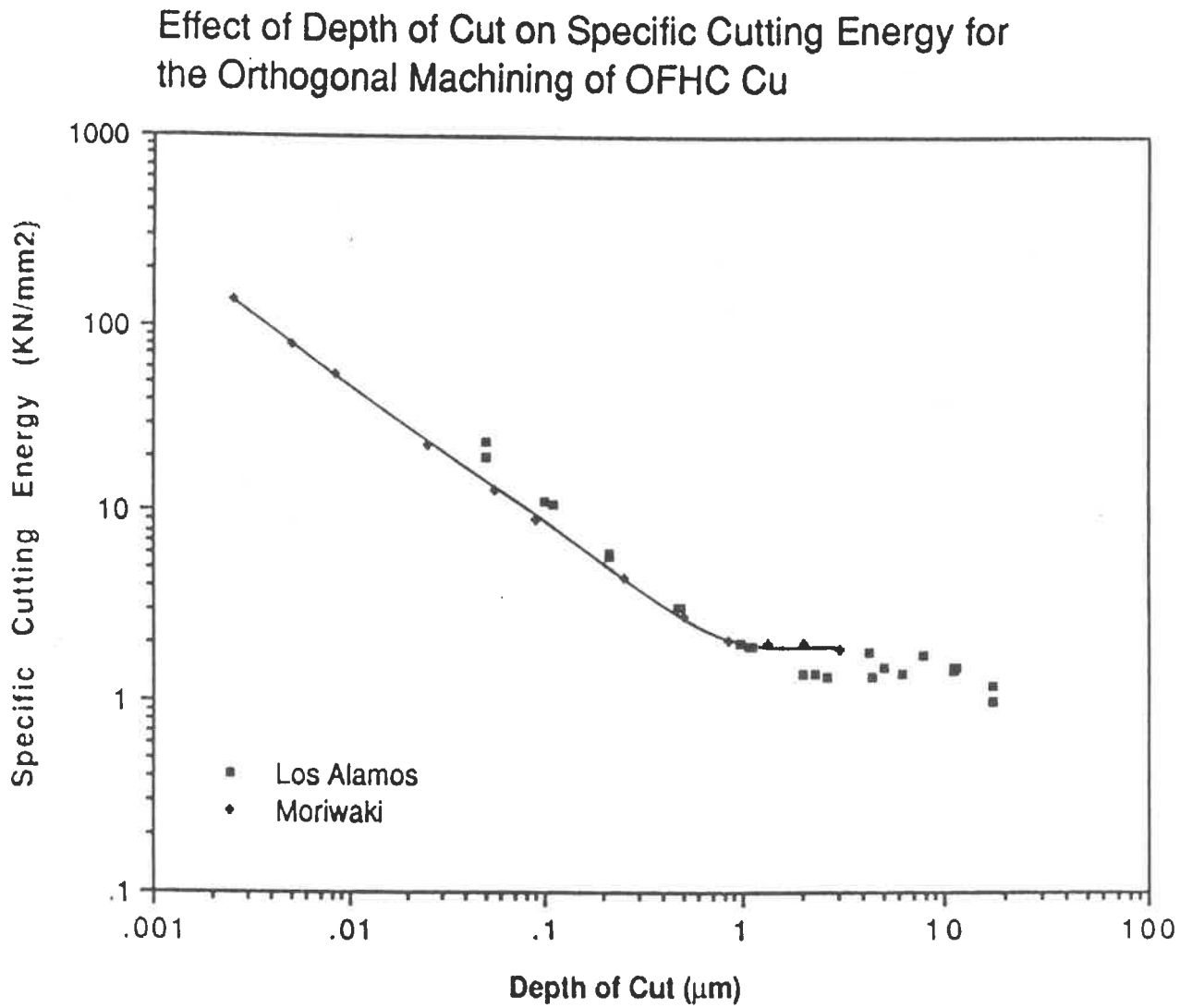

Fig. 3. Comparison of Los Alamos Cutting Force Data

SURFACE STUDIES of DIAMOND MACHINED POLYMERS

Jeffrey W. Carr and Claudius Feger
T. J. Watson Research Center
IBM Research
PO Box 218
Yorktown Heights, New York 10598
phone (914) 945-2504
fax (914) 945-2141

Machining of polymeric materials has become increasingly important in the field of precision engineering. Often, injection molding, extrusion or compression molding of plastic components does not have the accuracy and precision required for applications in optics and electronics. Techniques used in single point diamond turning posses the required accuracy for the control of product shape; however, the dominating factor in product quality is often the response of the material to the machining process. We have attempted to relate the surface roughness of polymeric materials machined with a single point diamond tool to the chemical and physical properties of that material and to the operating conditions of the cutting process.

A previous study, using a series of thermoplastic polymers with different glass transition temperatures (Tg), found that the Tg of a polymer effected the surface morphology. The temperature of the cutting zone could be controlled by varying the speed of the tool bit. In order to produce a smooth surface, the cutting speed had to be increased to compensate for the increase in the Tg of the workpiece (1). Although the glass transition temperature is an important characteristic of a given polymer, material properties depend on other factors as well.

In particular, there is a strong dependance of the mechanical and flow processes on the molecular weight and molecular weight distribution of a particular polymer. The influence of the molecular weight on mechanical properties like tensile strength tends to plateau at values greater than 20,000. However, the molecular weight dependance of the melt viscosity (u) is given by the equation:

$$u = kM^{3.4}$$

where k is a constant and M is the weight average molecular weight. There is clearly a strong dependance of the melt viscosity on the molecular weight. The involvement of polymer melts in the process of single point diamond machining had not been suggested prior to these experiments; however, we have seen a possible link between melt viscosity and the deformation processes as they are encountered under certain conditions of cutting velocity and configuration of the diamond tool.

To investigate the effect of melt viscosity and molecular weight on the surface roughness of diamond machined polymers,

polymethyl methacrylate (PMMA) with molecular weights ranging from 22,000 to 2.3 X 10^6 and molecular weight distributions of smaller than 1.1 were machined under varying conditions of tool geometry, spindle speed and depth of cut. The quality of the cut was determined by measuring surface roughness with either stylus profilometery or angle resolved scattering spectrometry. In addition, the effect of the machining process on the molecular weight distribution of the PMMA removed during cutting and on the surface of the bulk material that remained on the workpiece was determined by gel permeation chromatography. Highly magnified images of PMMA and other polymeric materials have been obtained using scanning tunneling microscopy and atomic force microscopy. The images show the range of surface topography that can be obtained within the operating conditions of the machine tool.

A number of previous investigators have shown that PMMA can be machined with a single point diamond tool to produce remarkably smooth surfaces. With a Tg of slightly over 100 °C, it is not surprising that PMMA exhibits ductile regime material removal over a wide variety of machining conditions. In contrast, Vespel, a thermoset plastic available from DuPont, has been observed to cut in the brittle fracture regime under all conditions available with our present equipment. As in the case of PMMA, a number of experiments were performed to determine the surface roughness of Vespel under a variety of operating conditions. Unlike PMMA, the surface roughness was first seen to decrease with an increase in cutting speed and then to increase with a cutting speed past a tool velocity of 32 meters/sec. (figure 1). The relaxation rate and flow properties of the Vespel appears to play a role in determining the final surface roughness of the material. However, in contrast to PMMA, the temperature of the cutting region is thought to be below the glass transition temperature (Tg is difficult to measure in Vespel but is somewhere around 350 °C; Tm, the melt temperature, is calculated to be 592 °C and measured to be 587 °C).

Our observations can be understood by considering the viscoelastic response of the materials under investigation. In the cutting region, material is separated by the tool edge, leaving the finished surface behind and throwing the chip away from the workpiece. In the case of polymers if the deformation rate is sufficiently slow the molecular chains will untangle and flow past the diamond edge without the breaking of chemical bonds. If the relaxation rates are high enough, plastic flow and tension of the surface material will result in a smoother veneer. One mechanism to increase the flow or relaxation rate of a polymer is to increase the temperature of the system. This can be accomplished by external heating of the workpiece, increasing friction through the use of a diamond tool with a rounded nose or increasing the cutting speed. In our experiment, we have attributed the initial decrease in surface roughness of Vespel with the increase in cutting speed to a rise in frictionally generated heat and the corresponding increase in the flow of the polymer.

If the cutting speed is increased past a certain point, the polymer will be unable to respond to the deformation by flowing around the tool edge. Instead, the material will undergo brittle fracture and a crack will form, propagating in the direction of the force vector. The magnitude and direction of this force vector is determined by operating parameters such as tool geometry and depth of cut (2). Generally, the direction of the vector is not exactly parallel to the cutting plane. When a crack propagates below the plane of the finished surface a pit will form when the chip is removed. A crack directed upwards will leave material above the cutting plane. Depending on the compressibility of the polymer, the quality of the diamond edge and the direction of the cutting force, the material remaining above the surface plane will either be further removed or compressed as the diamond edge moves past. If the material sees further cutting the crack process will be repeated until the excess is small enough to be compressed below the diamond edge. After the diamond is past, the compressed material will rebound, moving above the cutting plane and increasing the roughness of the surface. In the case of Vespel, the rebound rate is relatively slow and can take up to two minutes.

If machining conditions such as tool angle and depth of cut are optimized to send the crack in front of the tool and along the cutting plane we would still expect a surface inferior to that obtained under conditions that raise the temperature of the cutting zone above the Tg of the workpiece. Without a melt, flow of the material without the applied force of cutting would be limited and surface tension could not act to pull the polymer flat. In addition, the chaotic nature of crack propagation would limit the ability of the operator to direct the fracture along the cutting plane. The slight wandering of the crack above and below the cutting plane would lead to rougher surfaces.

We have determined that the surface quality of polymers with high glass transition temperatures is controlled by two mechanisms that work against one another in this experiment:

i) The effect of temperature on the flow characteristics of the polymer -an increase in tool velocity results in an increase in frictional heating. The temperature shift increases the mobility and flow of the polymeric chains leading to a faster response of the polymer to the intrusion of the diamond edge. The greater the flow, the smoother the surface.

ii) Brittle fracture occurs when the rate of deformation of the polymer exceeds the rate at which the material can deform - the same increase in tool speed causes an increasing amount of brittle fracture leading to rougher surfaces. The greater the extent of the cracking, the rougher the surface.

The ultimate quality of a surface that experiences brittle fracture is determined by the relative contribution of these two separate factors. Alternatively, for polymers cut at or above the Tg, we would expect cracking to be minimal or nonexistent. In addition, the flow of a molten surface and the surface tension of the melt may erase some of the

microstructure imposed by imperfections on the tool edge. Assuming the polymer had time to respond before cooling, the result would be a surface smoother than expected.

1) E. L. Smith and R. O. Scattergood, "Diamond Turning of Amorphous Polymers", presented at the 3rd Annual Precision Engineering Conference of the American Society for Precision Engineering, Oct. 24-27, 1988, Atlanta, Georgia.

2) A. Kobayashi and K. Saito, "On the Cutting Mechanism of High Polymers", Journal of Polymer Science, 58, 1377-1396 (1962)

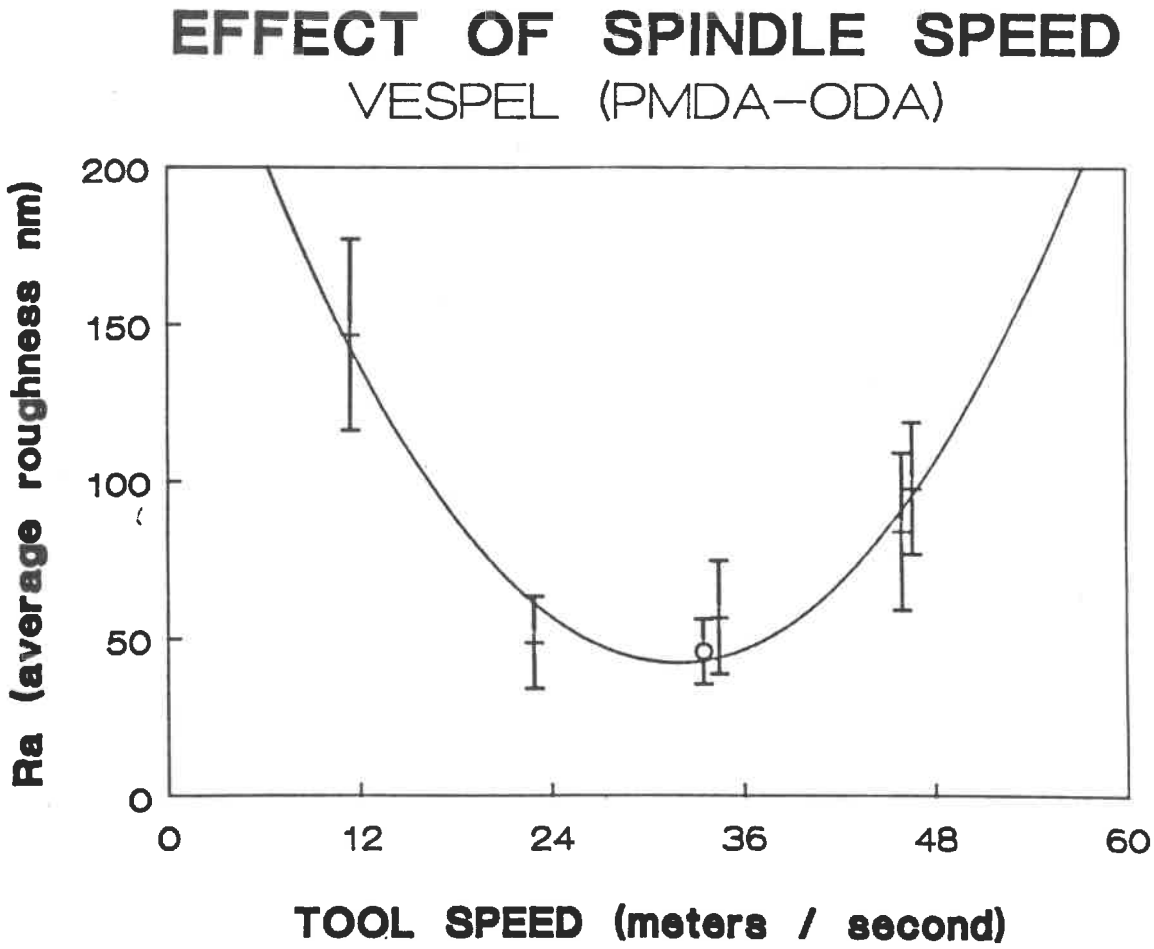

Figure 1

DIAMOND TURNING OF NON-SYMMETRIC LASER OPTICS*

M. Weck, M. Pyra
Fraunhofer-Institut für Produktionstechnologie
IPT, Aachen, Germany

The increase of applications of CO_2-Lasers in production, e.g. cutting, hardening, welding and surface treatment, requires laser machines of high efficiency and high performance capabilities. Especially the laser-beam guiding and shaping elements have a great influence on the process results (Fig.1).

The high demands of modern laser machining can be satisfied by the application of specially shaped laser optics. State of the art are rotational symmetric copper-mirrors, which can be manufactured with diamond turning techniques. Requirements are to produce non-rotational-symmetric optics, e.g. with waves of some μm on the surface. The use of these mirrors in laser resonators will lead to higher laser powers and higher efficiencies. Further on these optics can be used as beam forming optics to influence the power distribution of the laser beam. These mirrors can be turned by dynamical variation of the cutting depth while the spindle is rotating.

For this project a special group of researchers is established at the Fraunhofer-Institutes for Production Technology and Laser Technology. The common task of this group is to find new methods for developing, manufacturing and the applications of non-rotational-symmetric optics (Fig.2).

Based on models of an optimized beam guide in laser-resonators different kinds of surface structures are calculated and defined (project part 1).

Surface topographies with e.g. variable radius of curvature in their main axis demands special mechanical components and control systems of ultraprecision machines. This represents the mean task of project part 3.
On the other hand technological studies of microcutting with variable cutting depth must be conducted to realize the high demands on surface quality and surface roughness (project part 2).
Content of project part 4 is the quality assurance. Therefore test methods for the quantitative analysis of shape deviations has to be developed and applied. The results of the surface testing should be used for further improvements of the workpiece quality.
At last the manufactured optics are implemented in laser-resonators or beam guiding systems for practical tests.

*This project is sponsored by the Deutsche Forschungsgemeinschaft (DFG)

The mechanical conception to produce non-rotational-symmetric optics provides a fast tool servo system. This system, shown in Fig.3, based on a monolithic parallel spring mechanism. With this device the tool position can be varied in a range of 20 μm and is directly be measured with an integral capacitance gage. The dynamic feed motion is realized by using a low voltage piezo stack. For this task a new low voltage piezo amplifier has been designed and tested. Main problem of low voltage piezo translators in comparison to high voltage systems is the heat generation caused by the much higher currents. To minimize the thermal deformations of the tool holder, the monolithic structure is made of invar and a cooling of the piezo stack is provided.

Fig.4 shows the complete structure of the control system. Within three phases the conception should be developed and realized. In the first phase the ultraprecision machine has to be extended by the fast tool servo system. In the next phase the connection of the fast tool servo system with the NC-axis of the machine will be realized. Therefore it is necessary to get information about the actual position of the x-slide, the z-slide and the relativ position of the spindle. These signals are transfered to a digital processor and correlated with the feed motion of the tool. In the third phase the software has to be developed to generate the data for the control system. The surface topography has to be calculated by considering the surface correction data, which have been determined by practical surface analysis (project part 4). To reduce dynamic effects of the machine, its compliance will be meassured and will be taken into account for the generation of tool path signals.

References:

- Patterson S.R. Magrale E.B. — Design and testing of a fast tool servo for diamond turning, Precision Engineering July 1985 Vol 7 No. 3

- Patterson S.R. Saito T.T. — Diamond turning wavefront correctors, SPIE San Diego, California, 1986

- Weck M. Modemann K. — Checking surface modulation on metal optics by analysing ultraprecision machines, SPIE conference Den Hag, April 1987

- Weck M. Hartel R. — Test and measuring methods to analyse undulating effects on micromachined optical surfaces generated by vibration on precision machinery, SPIE conference Orlando, 1986

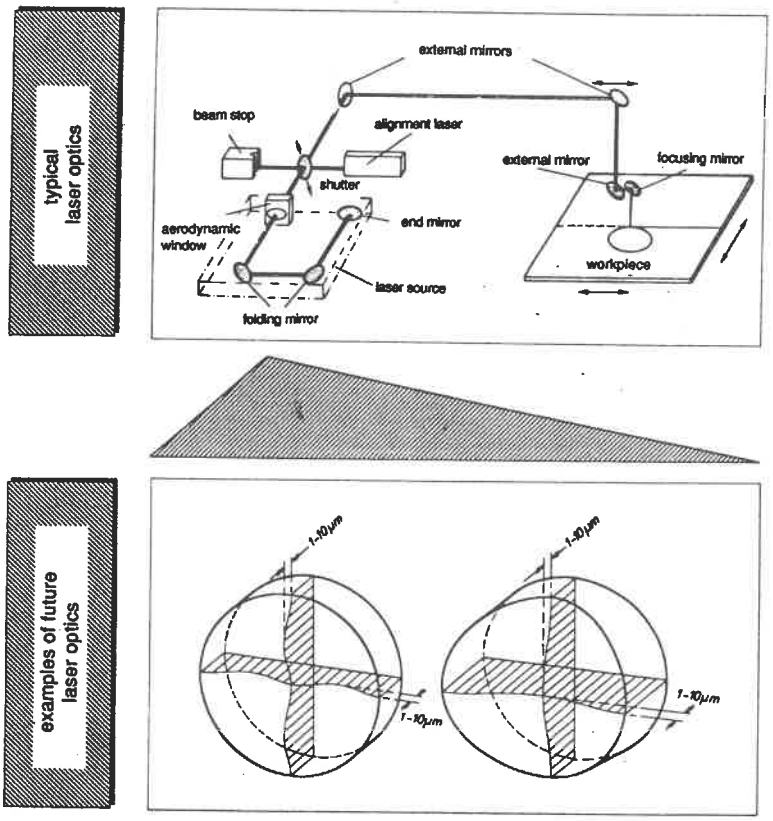

Figure 1: Optics for CO_2-laser applications

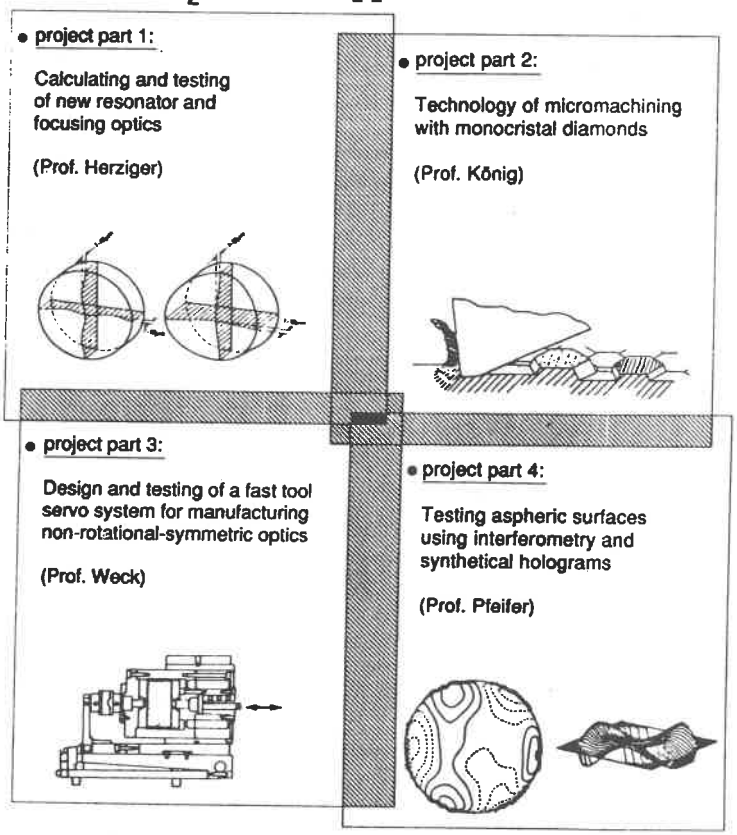
• project part 1:
Calculating and testing of new resonator and focusing optics
(Prof. Herziger)
• project part 2:
Technology of micromachining with monocristal diamonds
(Prof. Kõnig)
• project part 3:
Design and testing of a fast tool servo system for manufacturing non-rotational-symmetric optics
(Prof. Weck)
• project part 4:
Testing aspheric surfaces using interferometry and synthetical holograms
(Prof. Pfeifer)

Figure 2: Project: Non-rotational-symmetric laser optics

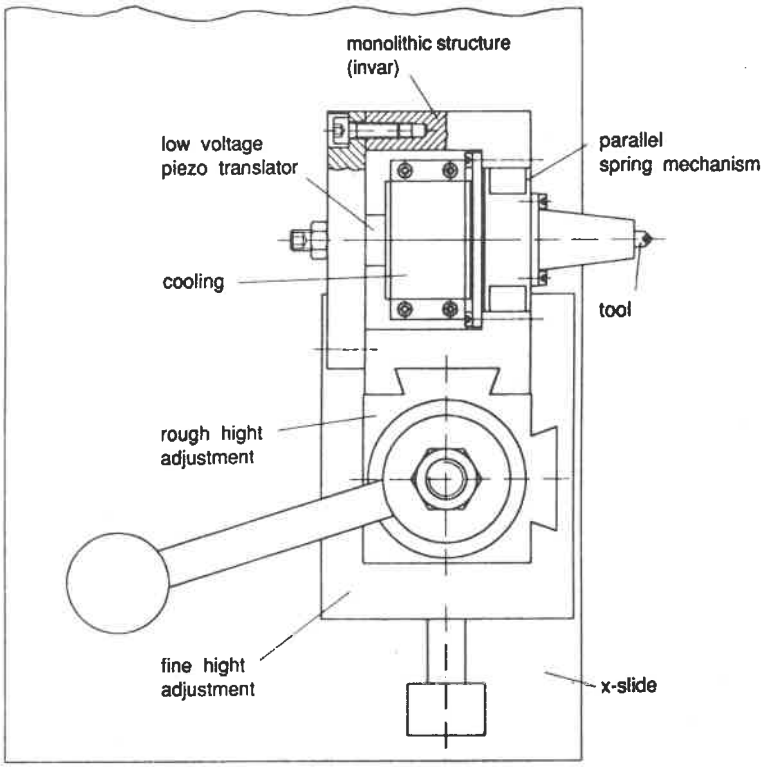

Figure 3: Design of the fast tool servo

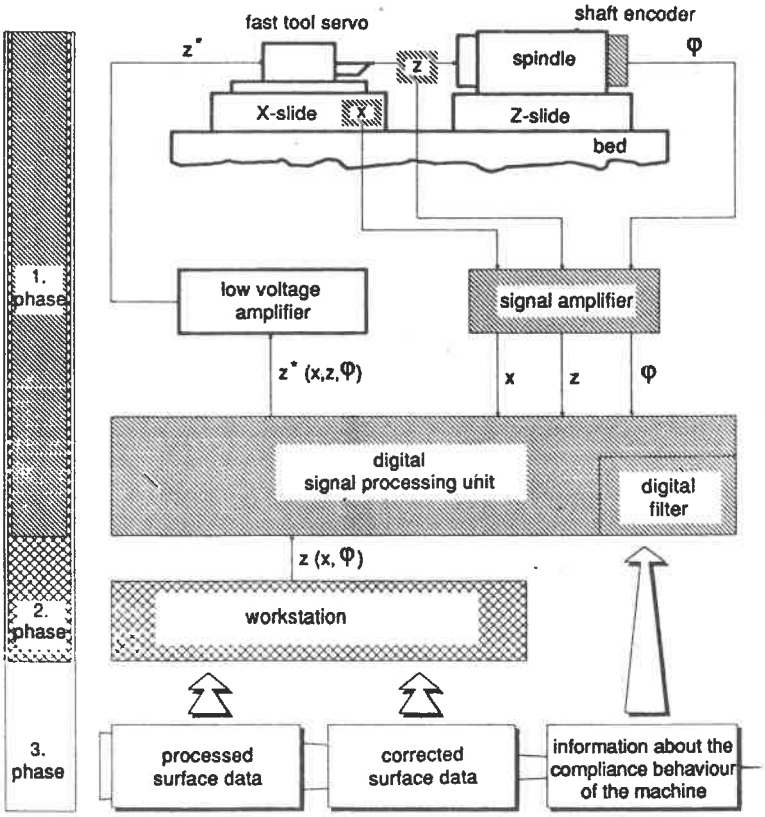

Figure 4: Complete structure of the control system

STEP HEIGHT MEASUREMENTS WITH A PHASE-SHIFTING INTERFERENCE MICROSCOPE

A.W. Hartman and T.V. Vorburger
National Institute of Standards and Technology
Gaithersburg, MD 20899

The accuracy of surface roughness and step height measurements often relies on the use of calibrated step height standards. Analysis and measurement results are presented for the height measurement of one-sided and two-sided steps, using a commercial phase-shifting interference microscope. The results for five precision step standards are compared with results obtained by a calibrated mechanical stylus instrument and by multiple-beam interferometry.

At NIST standard steps are characterized using all three techniques. At present, the obtained step height uncertainty ranges from 1 nm for 30 nm steps to 7 nm for 3000 nm steps. Improvements in accuracy are sought in a continuing program of characterizing the instrumentation. Also, different algorithms for expressing the height of single and double sided steps are examined in order to accommodate imperfections in the shape of standard steps.

Two-dimensional phase-mapping interference microscopy is useful for the characterization of steps at NIST. Utilizing an image sensor containing typically 250 × 250 detector elements, one can in principle take the equivalent of 250 stylus traces simultaneously. When these are combined into a single step height value, the fluctuations from the averaging process are considerably less than 1 nanometer. This is of great help when characterizing instrument sensitivity to small changes in operating conditions and instrument performance, such as: focusing, object surface tilt, changes in phase angle increment (with phase-shifting interference microscopes), non-linearity instrument response, and others.

In Fig. 1 is given a comparison of step height measurements obtained with three indicated techniques. The found differences are well within the error bars of each. Figure 2 shows the variations in height along one side of a two-sided 29 nm step measured with a phase-shifting interference microscope. Fortunately, those along the other side were in essentially the opposite direction, giving a variation in the two-sided step height of only 2 nm peak-to-peak. In Fig. 3 is indicated how defocusing can introduce small changes in measured step heights.

Among the examined step height algorithms, the one that fits a straight line through the step itself and a second order curve through the step base plane has proven very useful with steps, especially those that have appreciable imperfections in shape.

COMPARISON OF PRECISION STEP HEIGHT MEASUREMENTS
All results are expressed in nm.

Stylus	Multiple Beam Interferometry	Interferometric Microscope	Largest Differences
3035	3042	3037	7 (0.2%)
1017	1015	1016	2 (0.2%)
303	305	303	2 (0.7%)
91.4	92.0	90.7	1.3 (1.4%)
29.1	29.4	29.6	0.5 (1.7%)

Figure 1

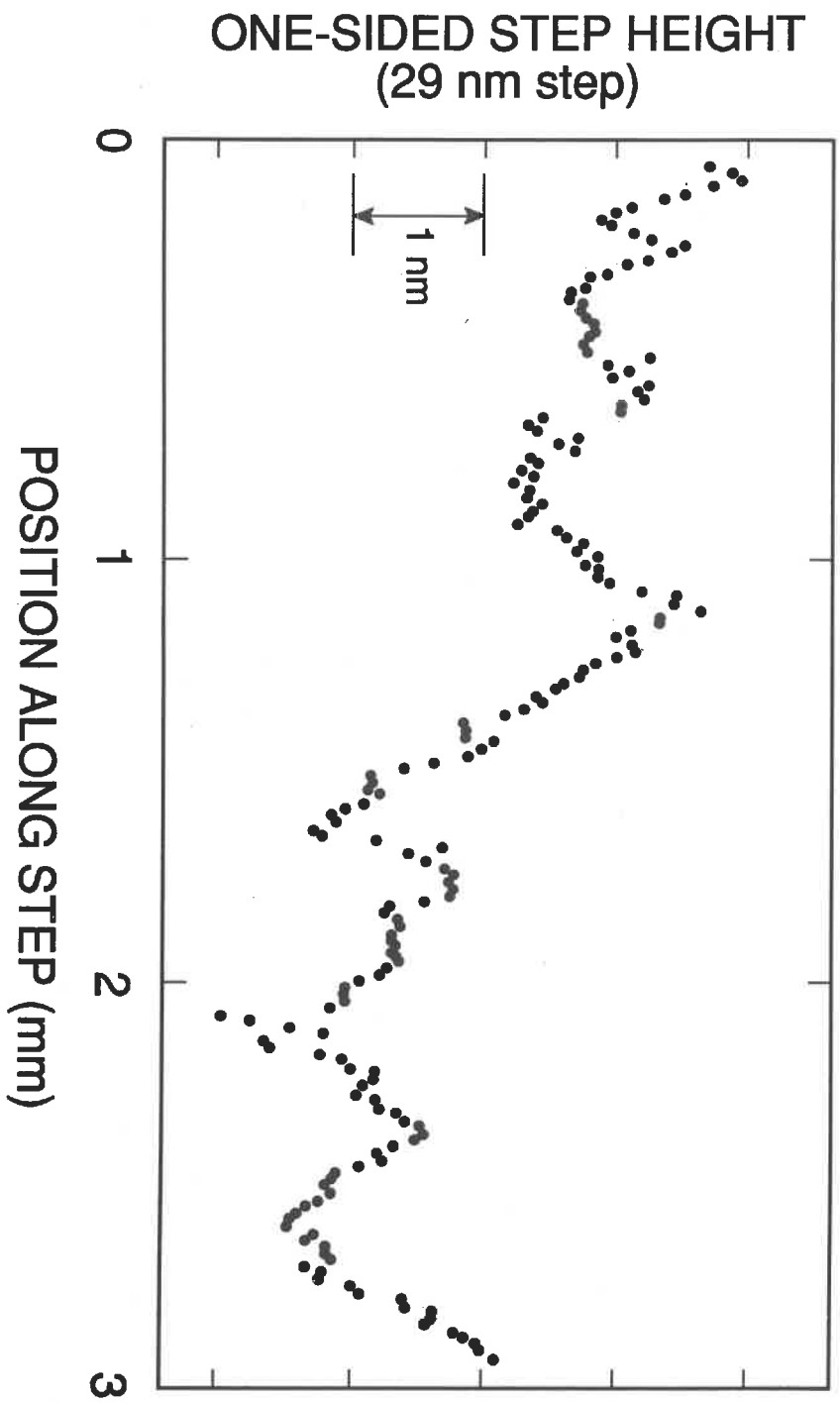
ONE-SIDED STEP HEIGHT
(29 nm step)
1 nm
0
1
2
3
POSITION ALONG STEP (mm)

Figure 2

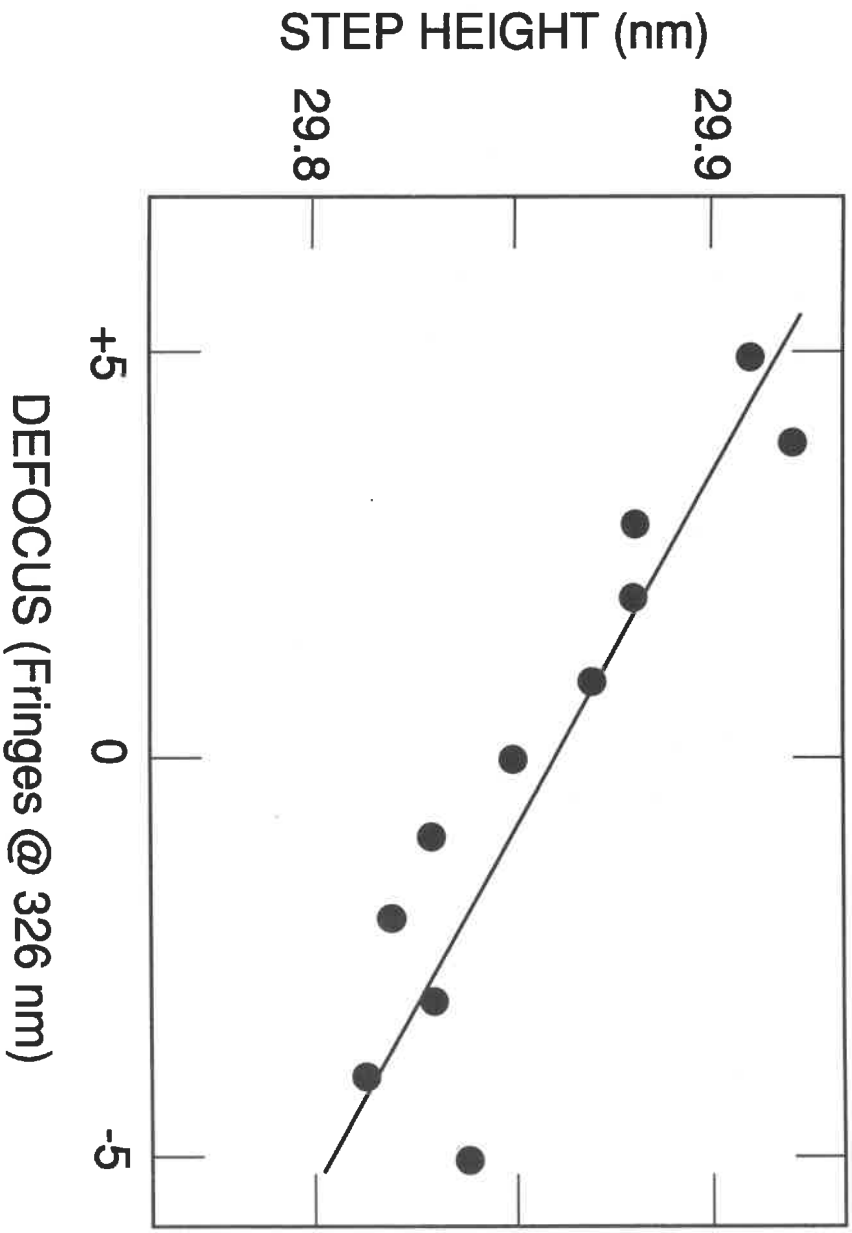

Figure 3

REVOLUTION IN X-RAY OPTICS

N. M. Ceglio
Advanced X-ray Optics Program
Lawrence Livermore National Laboratory
Livermore, CA

In the past half decade or so there has been a technological revolution in our ability to generate, manipulate, focus and detect x-rays. The emergence of x-ray lasers and synchrotron insertion devices has increased the brightness of laboratory x-ray sources 8 to 12 orders of magnitude over what was available in the late 1960's. In addition, the past few years have been witness to significant advances in the development of normal incidence x-ray mirrors and beam splitters, diffraction limited x-ray lenses, and CCD x-ray detector arrays. Utilizing these new capabilities, we are taking the first steps toward the development of sophisticated x-ray optical systems including soft x-ray interferometers, high intensity x-ray lasers, and projection optics for x-ray lithography. Details of these developments will be discussed, with special emphasis placed on the challenges and opportunities in Soft X-ray Projection Lithography.

MECHANICS OF MATERIAL REMOVAL IN DIAMOND TURNING

S. Blackley and R. O. Scattergood
Precision Engineering Center
North Carolina State University
Raleigh, NC 27695-7918

Because of their low toughness, brittle materials like ceramics and glasses are very difficult to machine or grind without introducing surface fracture damage. However, production of optical surfaces using machine tools has the advantage that a complex form can be deterministically generated, for example, an aspherical surface. Consequently, considerable interest exists in developing "ductile regime" single-point diamond turning and diamond grinding technologies for brittle materials. The work reported here is aimed at gaining a better understanding of the mechanisms that underlie these processes. The development and verification of models for single-point diamond turning in a ductile regime are addressed.

Fracture under conditions where the loads applied are localized in spatial extent is of particular interest for machining of brittle materials. A large literature exists for indentation fracture produced by a sharp indenter on a brittle substrate. When the indentation plastic zone reaches a critical size, median/radial and lateral cracks are generated [1]. Fracture initiation plays a central role for ductile-regime machining. A critical penetration depth d_c for fracture initiation can be derived from indentation fracture mechanics analysis as [2]

$$d_c = \beta \left[\frac{K_c}{H}\right]^2 \left[\frac{E}{H}\right] \quad \ldots (1)$$

where K_c is fracture toughness, H is hardness and E is elastic modulus. β is a factor that will depend upon geometry and process conditions, for example, tool rake angle and coolant.

Given that a critical depth d_c separates the transition between plastic shear flow and fracture in single-point diamond turning, a key aspect of model development involves the role played by tool geometry and chip cross section. A round nose diamond tool moves through the workpiece as shown in Fig. 1. The shaded area along the uncut shoulder in front of the tool is the [uncut] chip cross section. Fig. 2 shows a projection of the tool perpendicular to the cutting direction. The effective cutting depth varies from zero at tool center to maximum at the top of the uncut shoulder.

Using the critical-depth concept, fracture damage will initiate at the effective cutting depth d_c in Fig. 2. This damage propagates to an average depth y_c as shown. If the damage does not replicate below the cut-surface plane, ductile-regime machining conditions are achieved. Cross-feed f is a key machining parameter because it determines the position of d_c along the tool nose. Larger values of f move d_c closer to the tool center line. It is important to note that when ductile-regime conditions are achieved, material removal still occurs by fracture. Damage generated in the uncut shoulder at cutting depths greater than d_c in Fig. 2 is removed by successive tool passes.

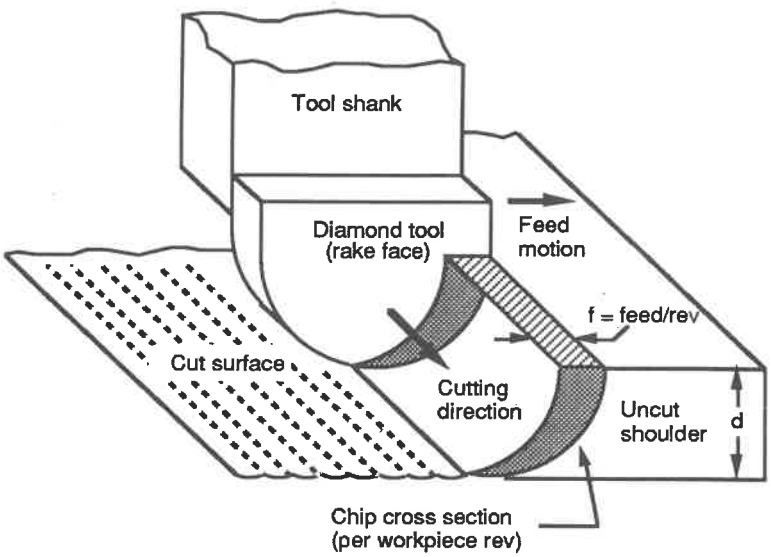

Figure 1 Geometry for single-point diamond turning.

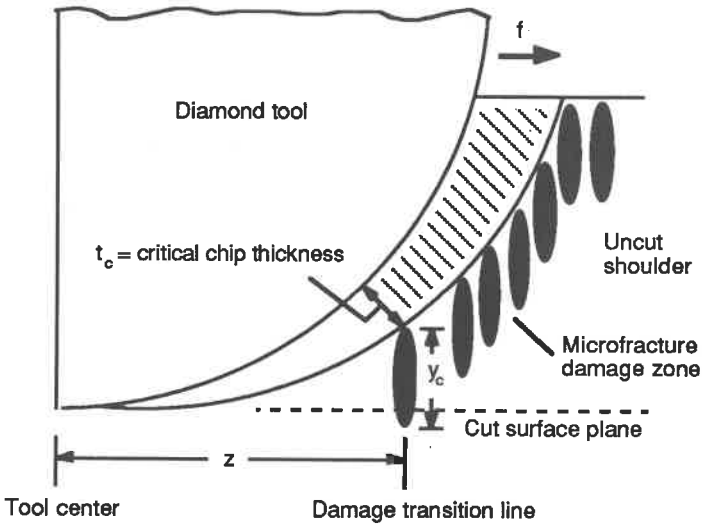

Figure 2 Plane normal to the cutting direction in Fig. 1 ($t_c \equiv d_c$ in the figure).

The model proposed in Fig. 2 has been verified by interrupted cutting tests [4-5]. Using a PZT servo, the tool is rapidly withdrawn from the workpiece during a test cut. The distance z in Fig. 2 from the tool center to the damage transition line can then be measured experimentally. From a careful analysis of the tool geometry and damage parameters, one can derive the relation [5]

$$\frac{z^2 - f^2}{R^2} = \frac{d_c^2}{f^2} - 2\left[\frac{d_c + y_c}{R}\right] \quad \ldots (2)$$

where R is the tool nose radius and the other parameters are defined as shown in Fig. 2. By conducting a series of experiments at different cross-feeds f, results of the kind shown in Fig. 3 are obtained. This is a plot of eq. (2) using coordinate variables that predict a straight line. As can be seen, a linear correlation results. Furthermore, the slope and intercept of the line allow the damage parameters d_c and y_c to be determined experimentally. For the data shown in Fig. 3 at a tool rake angle of -30°, d_c = 127 nm and y_c = 1280 nm.

The interrupted cutting test results provide an experimental verification of the model concept embodied in Figs. 1 and 2. Such tests permit the damage parameters d_c and y_c to be determined, and to be correlated with machining conditions. The former parameter relates to crack initiation while the latter relates to crack propagation. As is evident from Fig. 2, both of these parameters are important in determining the limits for ductile-regime machining. They can be related to a maximum limiting feed rate for ductile regime conditions [5].

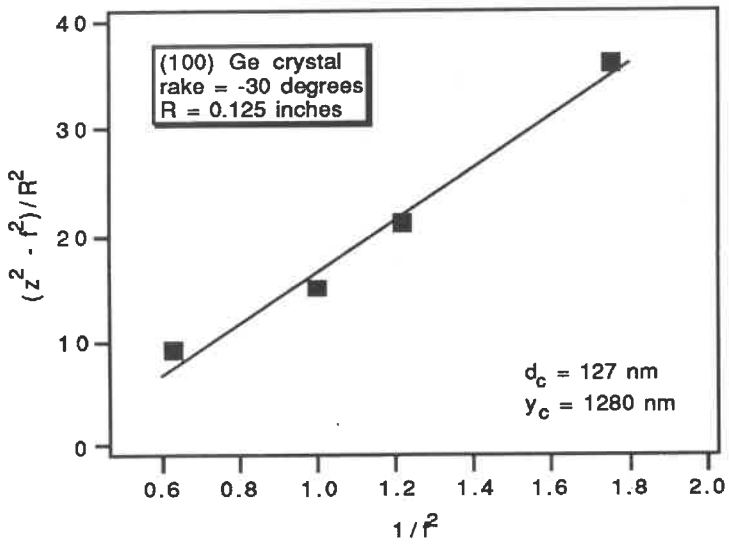

Figure 3 Data for (100) germanium crystals [5] plotted according to eq. (2).

Eq. (2) is a phenomenological relation derived from geometric considerations. Further analysis is needed to develop a mechanistic model based on elastic-plastic deformation and fracture mechanics. Fig. 4 presents the basis of such a model using the stress field from a line force on a half space to represent the tool forces. The plastic yield zone is determined using the von-Mises criterion. This plane-strain stress solution is taken to represent an orthogonal cross section at any effective cutting depth t_{eff} along the tool nose (Fig. 2). When t_{eff} reaches a critical value d_c, the maximum stress intensity factor for the elastic-plastic field K_{max} equals fracture toughness K_c and the (necessary) condition for crack initiation obtains. d_c and y_c follow from this criteria.

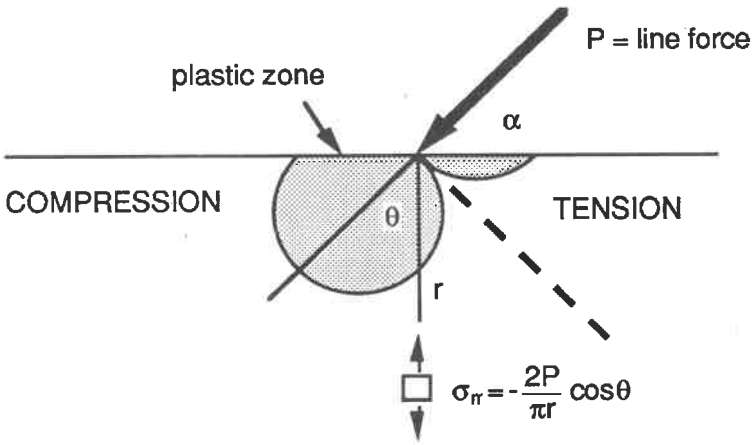

Figure 4 Elastic-plastic solution for line force contact. Plastic zones are shaded.

Predicted values of d_c and y_c obtained from the analysis (FP Model) are shown in Figs. 5 and 6, along with experimental data from interrupted cutting tests. The two arbitrary parameters in the model are $[K_c/H]^2$ and the tool rakeface friction coefficient μ. For (100) germanium crystals, the best fit to the model predictions gives $[K_c/H]^2 = 5.6$ nm and $\mu = 0.47$, which are quite reasonable values. The former agrees well with values of $[K_c/H]^2 \cong 4$ to 7 nm obtained from published material data. The predicted values of crack depth y_c at the initiation step are always too small, and it appears that subcritical crack growth in the unloading (residual) stress field must be taken into account. This was done in Fig. 6 by assuming that crack length y_c scales with the plastic zone depth, which determines the wavelength of the residual stresses driving subcritical crack growth.

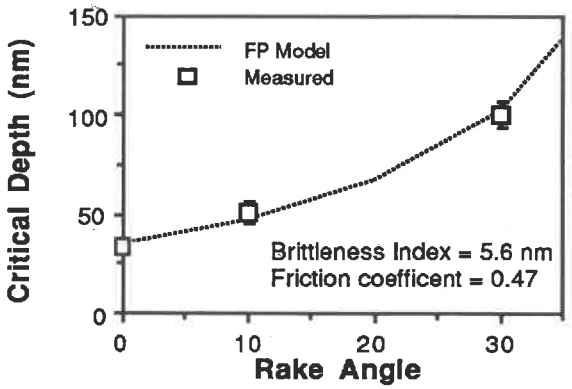

Figure 5 Predicted (line) and measured (points) d_c values for (100) Ge *vs* rake angle.

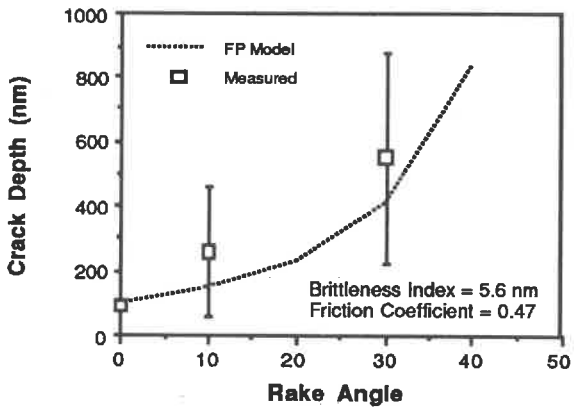

Figure 6 Predicted (line) and measured (points) y_c values for (100) Ge *vs* rake angle.

1. B. R. Lawn and T. R. Wishaw, *Indentation Fracture: Principles and Applications*, J. Mater. Sci., 10, [6],1049 (1975).
2. D. B. Marshal and B. R, Lawn, *Indentation of Brittle Materials*, ASTM-STP 889, 26 (1984).
3. T. G. Bifano, T. A. Dow and R. O. Scattergood, *Ductile-Regime Grinding of Brittle Materials: Experimental Results and the Development of a Model*, Proc. SPIE, 966, 108 (1988).
4. P. N. Blake and R. O. Scattergood, *Ductile-Regime Machining of Silicon and Germanium*, J. Am. Ceram. Soc., in press (1990)
5. S. Blackley and R. O. Scattergood, *Ductile Regime Machining Model for Diamond Turning of Brittle Materials*, submitted to Prec. Engr. (1990).

APPLICATION OF HYDROSTATIC BEARINGS IN SPINDLE SYSTEMS FOR HIGH PRECISION MACHINING

M. Weck, U. Böttger
Fraunhofer-Institut für Produktionstechnologie
IPT, Aachen, Germany

For the production of high precision copper laser-mirrors ultraprecision machines are used. Beneath the accuracy and sharpness of the diamond tool the workpiece spindle has dominant influence on the quality of the produced workpieces.

Most of the commercially available and also of the research-diamond turning machines aerostatic spindles are applied. The main disadvantages of air bearings are the low load capacity and the poor damping. By using hydrostatic oil bearings most reqirements of high precision machining, e. g. high accuracy of axis of rotation, high stiffness and load capacity and high damping, could be met.

The main problem of hydrostatic oil bearings is the thermal drift caused by power losses due to the friction. To analyse the influences on the thermal behaviour and to develop solutions to reduce the thermal drift a hydrostatic research spindle has been designed and built up, figure 1.

The spindle bearings are inserted into a steel collet which has been casted into the polymer concrete headstock. The heat of the bearings can be removed by a water-cooling-pipe, which is wound around the collet. For the examination of the spindle properties capacitance gauges are used to measure displacements of the spindle nose. Temperature distributions in and outside the housing can be measured with attached temperature sensors.

According to the research plan shown in figure 2 the influences of different rotor materials, several oil supply systems and different cooling systems of the hydrostatic oil and the spindle housing will be determined. Goal of the investigations is to stabilize the thermal drift of the spindle nose to less than 0.1 μm in all three directions.

In figure 3 an illustration of the cooling system for the spindle housing is shown. The heat generated by the friction of the bearing will be removed from the housing by the inner cooling circuit which has a constant flow rate of water. In the heat exchanger the energy is transferred to the outer circuit which is cooled by the tank of chilled water. The temperature of the inner circuit is controlled by the flow rate of the outer circuit. Figure 4 illustrates the improvements which can be achieved by optimizing the system. The curves shown in figure 4 have been determined by an immideate increase of the spindle speed from 60 rpm up to 1200 rpm. The steel spindle without temperature control shows a displacement in axial direction of approximately 4.5 μm.

In contrast to these results the optimized system with temperature control and another spindle material has a thermally induced displacement of only 0.25 μm. Comparing the stabilization-times of the two analyzed spindles a reduction from 30 minutes of the steel spindle to approximately 10 minutes has been achieved.

References:

- Weck, M. Werkzeugmaschinen Band 2, Konstruktion und Berechnung, 2. Auflage 1980, VDI Verlag
- Roblee, J. W. Precision Temperature Control for Optics Manufacturing, 2nd International Symposium on Optical and Electro-Optical Applied Science and Engineering, Cannes, 1985
- McClure, E. R. Manufacturing Accuracy Through the Control of Thermal Effects, D. Eng. Thesis, LLNL 1969

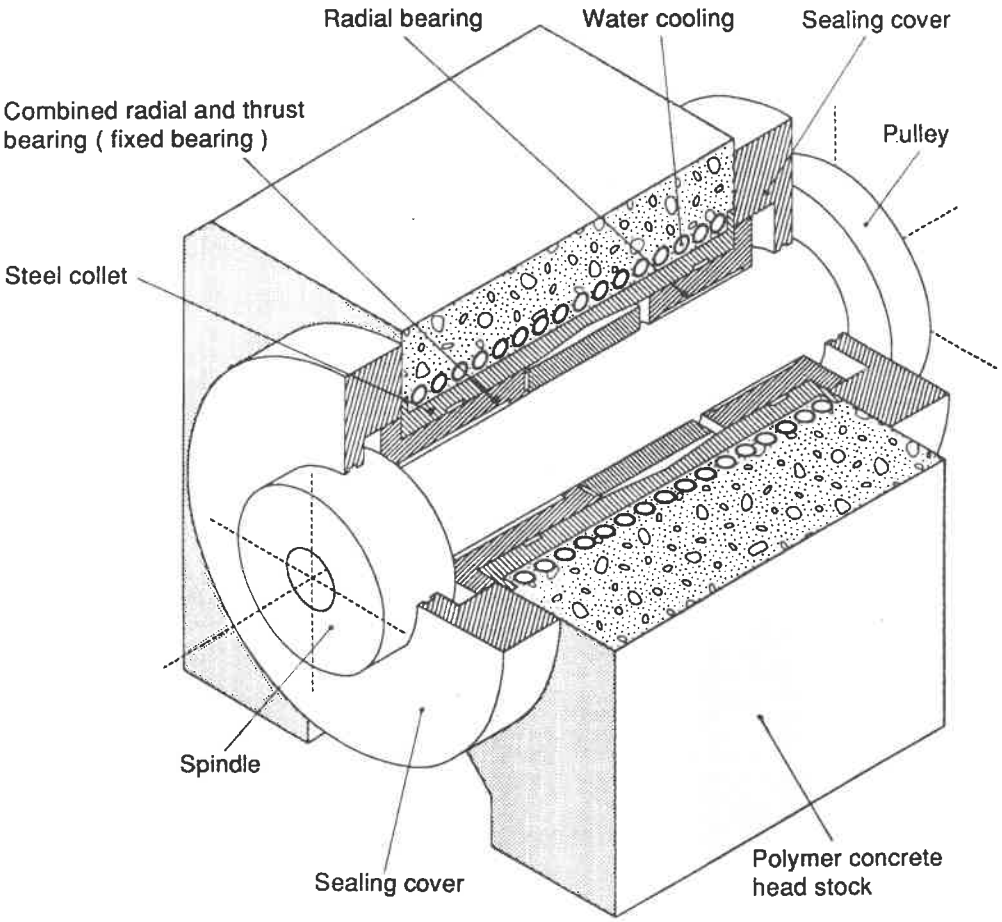

Fig. 1 : Hydrostatic research spindle

Object of investigation	Varying parameters
• Rotor materials	- Steel - Invar - Ceramics (Silicon nitride) - Carbon fiber reinforced plastics
• Temperatur control of - hydrostatic oil - spindle housing	- T = const. - T = f(n,∂x,∂y,∂z)
• Hydrostatic bearings	- Gap resistor (Zollern) - Orifice resistor

Fig. 2 : Research plan

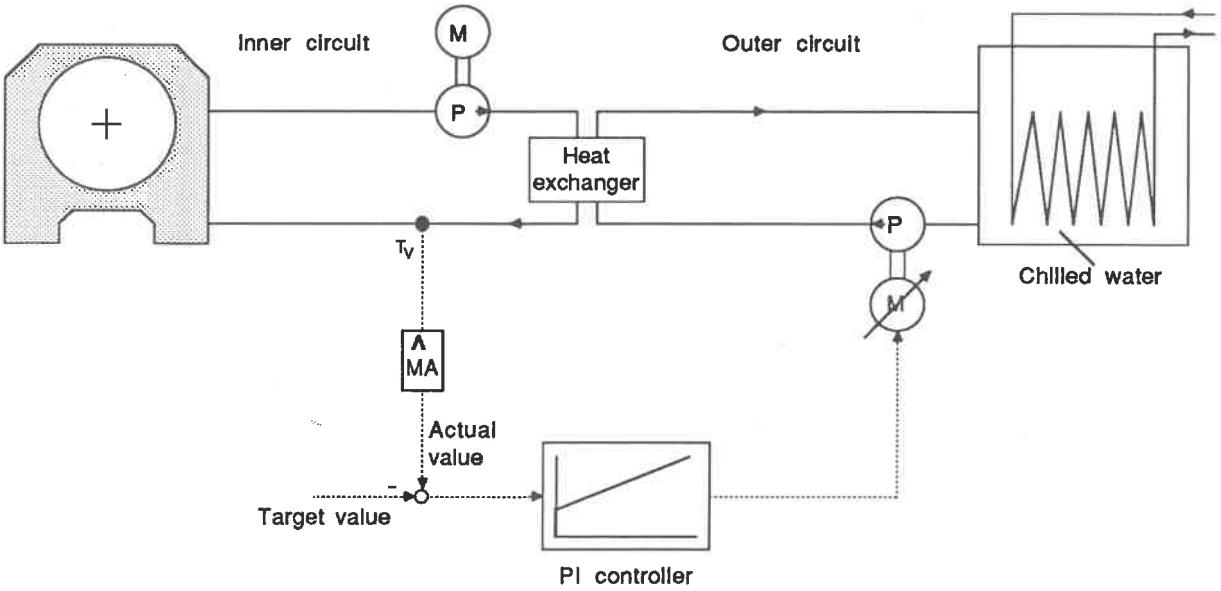

Fig. 3 : Cooling system for the spindle housing

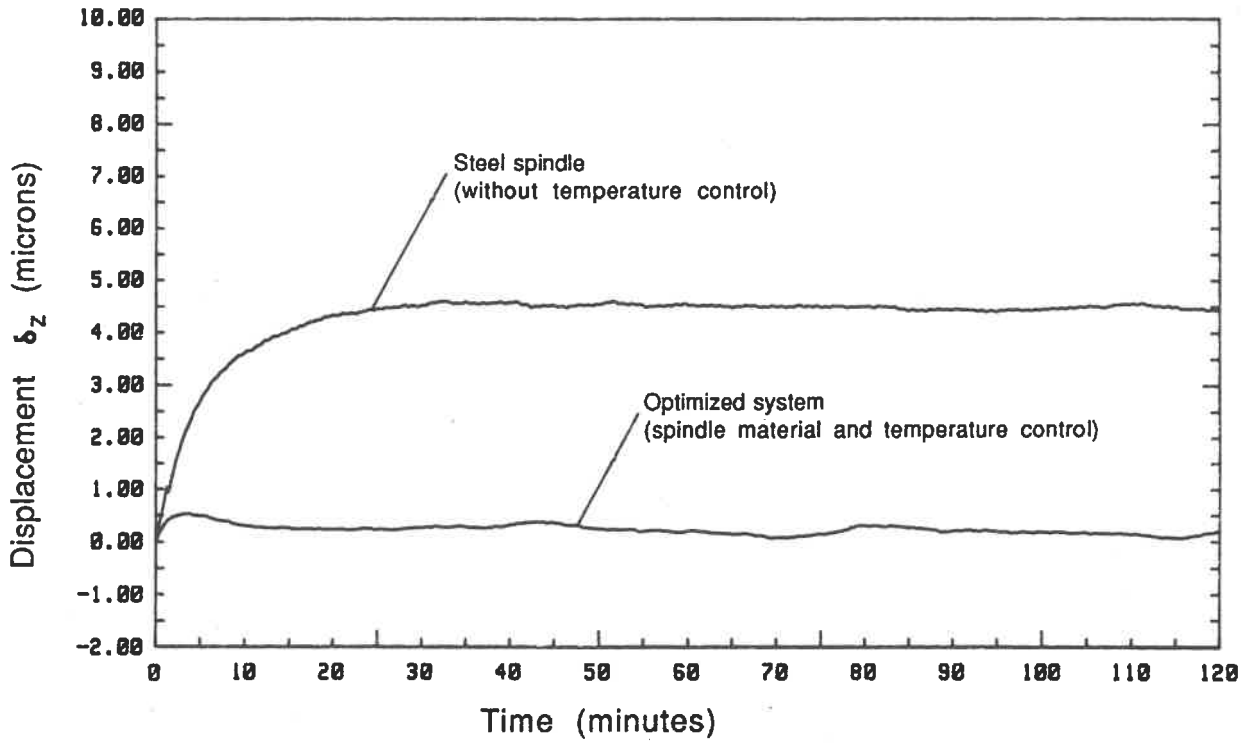

Fig. 4 : Thermal displacement of a hydrostatic spindle

A MOLECULAR DYNAMICS MODEL OF THE ORTHOGONAL CUTTING PROCESS*

James F. Belak and Irving F. Stowers
University of California
Lawrence Livermore National Laboratory
Livermore, CA 94550

Introduction

Material removal, as found in the cutting and grinding processes, is important in many areas of fabrication technology. Examples include high-speed machining by single point turning, surface milling and drilling. An idealized model that contains the essential physics of these processes is the two-dimensional orthogonal cutting geometry (see Figure 1). Following the work of Shaw[1], we also attempt to obtain a fundamental understanding of the commonly observed phenomena in the chip forming process: the atomistic mechanisms of plastic deformation within the primary shear zone and the observed shear angle (ϕ); the resultant energy flow from the tool doing work; the stress, strain and material flow fields; the morphology of the chip (smooth, segmented, crystalline or amorphous); the role of different depths of cut (t), rake angles (α), and clearance angles (θ); and the role of the tool tip radius, roughness (friction), and wear.

The molecular dynamics computer simulation method is an ideal tool for the study of the atomistic mechanisms of these deformation processes. We have performed simulations for a model of copper at room temperature using 10^3-10^6 atoms, depths of cut in the range 1-50 nm, and cutting speeds of 1-2500 meters per second (m/s). These simulations are strictly two dimensional (plane strain). Here, we focus on the chip forming process, the atomistic mechanisms of plastic deformation, the flow of energy into the chip and workpiece, and the material flow and stress fields for the orthogonal geometry ($\alpha = 0$), sharp tools, and shallow depths of cut ($t \approx 5$ nm). We will also show a computer animation movie of our simulation that we have found useful in understanding the results.

Atomistic Computer Simulations

The molecular dynamics computer simulation method is very simple in principle. Given a configuration of atoms, we first evaluate the force on each atom due to its interactions with its neighboring atoms. We then integrate the equation of motion for all the atoms to obtain new positions and velocities. The process is then repeated. The art is in the proper application of realistic inter-atomic forces, boundary conditions and external constraints (e.g. a thermostat). The interested reader may find the elementary introduction given by Gould and Tobochnik[2] useful.

In Figure 1, we show the typical orthogonal cutting geometry in two dimensions. All of the motion is confined to two dimensions (plane strain). The calculations are performed within the reference frame of the tool. The material flow rate (cutting speed) is induced by forcing all of the atoms within a two lattice spacing (a_o) skin of the outer boundary (solid circles) to move to the right at the material velocity (v_m). When the material has moved

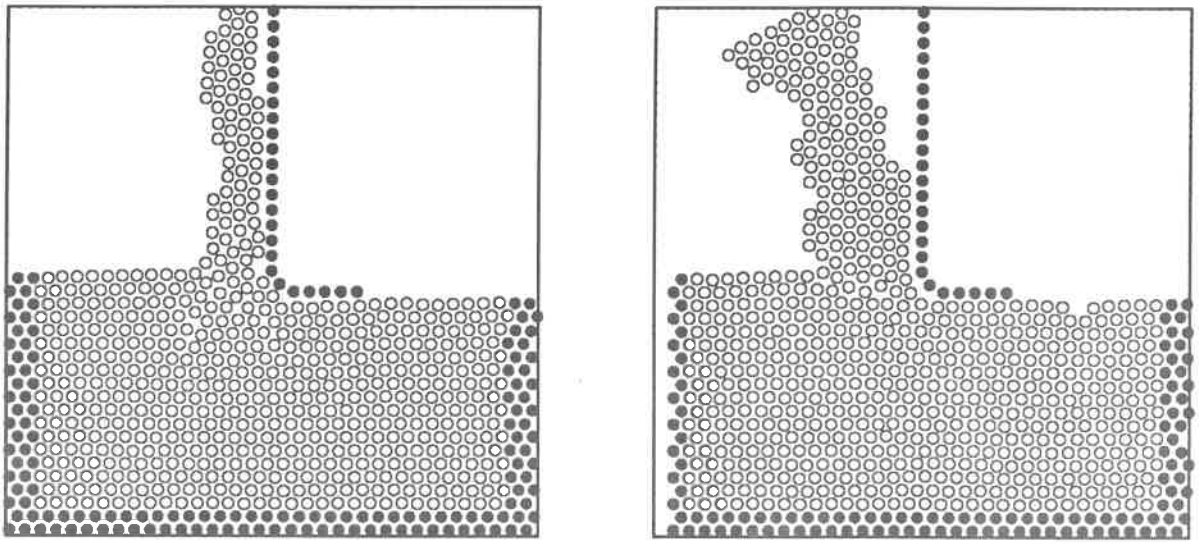

(a) (b)

Figure 1: Two frames from our molecular dynamics computer simulation of the orthogonal cutting of copper in two dimensions at one fourth the melting temperature. Both frames contain about 1000 atoms, a depth of cut of two layers and a tool tip diameter equal to two atomic diameters. (a) A cutting speed of 2500 m/s. (b) A cutting speed of 500 m/s.

one lattice spacing, a new layer is inserted from the left, producing a *steady state flow.* The tool atoms remain fixed and the remaining atoms (open circles) are free and are coupled to a thermostat at one fourth the melting temperature. Atoms, that leave the outer boundary, are thrown away.

To model a workpiece material resembling copper, we use an embedded-atom interatomic force model. Details may be found in our recent study of surface indentation in two dimensions[3]. The workpiece material atoms interact with the cutting tool atoms through a shifted and truncated Lennard-Jones force model[4] that is always repulsive.

Results

As is clear from Figure 1 and 2, we have demonstrated a successful atomistic model of the chip forming process. Our chips look like those formed in the actual machining of metals. Here, we briefly outline some of our important results. The chip is formed by an intense shearing process. The primary shear plane is at 30° in the workpiece crystal (not one of the easy slip planes). The chip re-crystalizes at 90° with respect to the workpiece. The chip hugs the tool face for fast cutting speeds and tends to fall away for slower cutting speeds. There is a stagnation region at the tool tip and we observe the formation of a build up edge. Slip dislocations are continually initiated from the tool tip. They propagate into the workpiece material, bounce from the lower rigid boundary and leave steps in the surface in front of the tool. Larger depths of cut are harder to shear uniformly. We observe regions

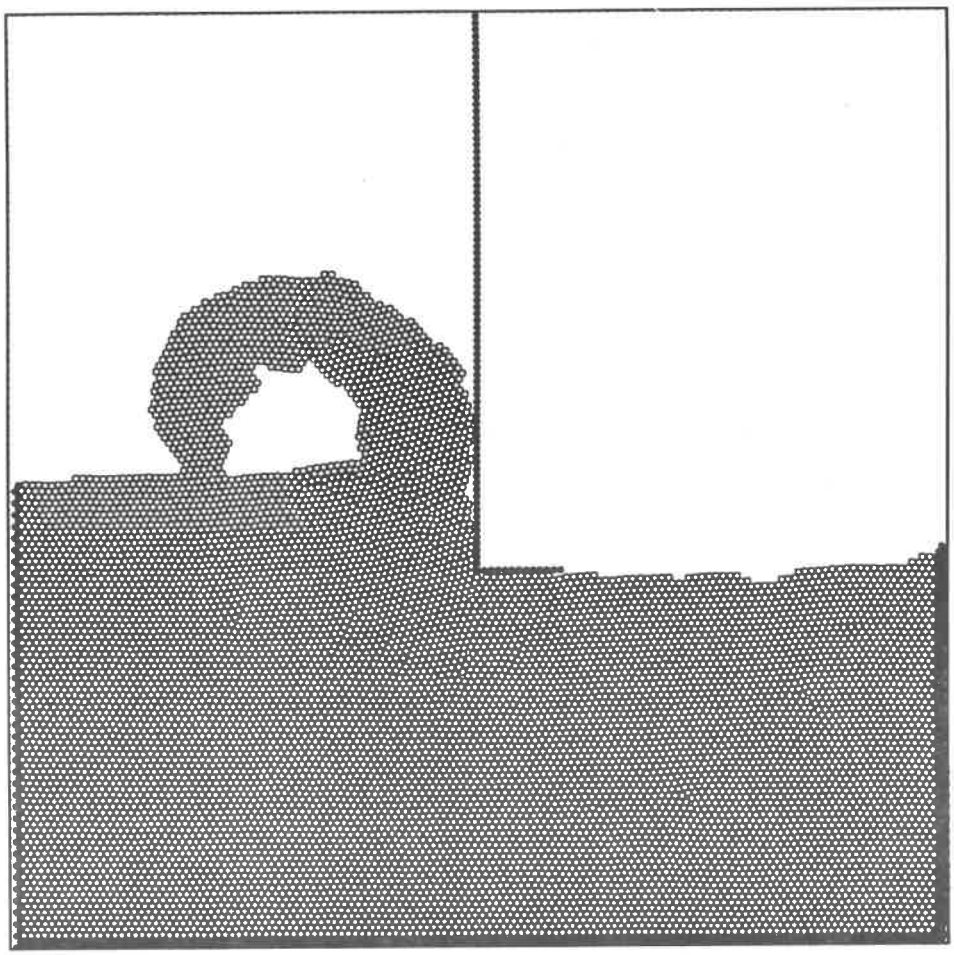

Figure 2: A molecular dynamics simulation of the orthogonal cutting of copper in two dimensions at one fourth the melting temperature. The frame contains about 10,000 atoms, a depth of cut of 5 nm at a cutting speed of 500 m/s.

within the chip of undeformed material reminiscent of the segmented chip formed in ultra-high-speed machining[5]. Our calculated specific work ($u = F_x/t$) is consistent with the relation $u \propto t^{-0.2}$[1]. We are currently generating data to test this relation. The deviatoric stress field (Figure 3) clearly displays the intense shear plane.

We are currently analyzing our results in order to understand the nature of energy flow, material flow, and plastic deformation. We will present a computer animation movie of these fields and the atomistic motion that gives rise to plastic deformation.

Acknowledgments

* Work performed at the Lawrence Livermore National Laboratory under the auspices of the Department of Energy pursuant to University of California–Lawrence Livermore National Laboratory Contract W-7405-Eng-48. We gratefully acknowledge the generous support of the Massively Parallel Computing Initiative at the Lawrence Livermore National Laboratory, without whose support these calculations would not have been possible. It is

combine the individual error components to predict the resultant error at the cutting tool. Figures 2 and 3 show sample data from these characterization measurements.

Correction of the tool path based on the prediction of the geometric and thermal errors has previously been achieved by modifying the hardware and/or software of the machine-tool CNC controller. But, this type of modification requires specific knowledge of the existing controller. This has been the major obstacle to implement real-time error compensation of machine tools by the user community. To resolve this problem, we developed a generic "black box" called the Real-Time Error Corrector (RTEC) [4]. The RTEC is inserted between the encoder-type position feedback devices and the machine-tool controller as shown in Figure 4. It is capable of modifying the tool path without any knowledge about the machine-tool controller's design. The RTEC consists of an 8-bit microcomputer chip and a quadrature decoder/counter chip as shown in Figure 5. The position feedback signals generated by the encoder are fed to the decoder chip, that translates this information into servo counts and sends them to the microcomputer. The microcomputer then converts the servo counts into axis position and sends this to a PC-type computer. The amount of correction required is sent by the PC back to the RTEC. RTEC in turn generates new feedback pulses adding or subtracting from the encoder pulses and sends them to the machine controller. For positive axis movements, if there are additional pulses, the machine stops earlier than the programmed nominal position. If pulses are subtracted, the machine moves further than the target position. The current version of RTEC can modify tool path up to 30 in/min slide traverse rates with a resolution four-times coarser than the controller resolution.

Process-Intermittent Control Layer

The purpose of the process-intermittent control layer is to obtain information about the workpiece before it is taken off the machine tool using various on-machine measuring techniques and to correct for the errors on the part caused by the process-related error sources, such as cutting forces and tool wear. The correction is performed by changing tool-dimension offsets and/or automatically generating modified NC code for the finishing cut. On-machine dimensional and shape measurements are performed using touch-trigger probes. In order to gather enough information about the shape of the part feature, a comprehensive on-machine probing cycle should be performed. To minimize the measurement time, probing should be carried out as fast as possible. We use the RTEC to facilitate fast probing. The probe trigger signal is interfaced to the RTEC to generate an interrupt in the microcomputer. When a probe trip occurs, the RTEC latches onto the axes positions within a microsecond, resulting in useable probing rates up to 100 in/min [4]. Probing data is analyzed by the PC to determine the corrective action for the finish cut. Independent analysis by the PC gives the opportunity to implement powerful CMM-type algorithms in the part measurements.

Surface quality of the part is also checked during the process-intermittent control cycle. Using an on-machine ultrasonic sensor, the surface finish is measured and compared with the desired value. The cutting parameters for the finish cut are adjusted based on this measurement. Since surface quality is also a function of tool condition, tool wear is detected as a result of this measurement.

Post-Process Control Layer

The purpose of the post-process control layer is to verify the metal cutting process by inspecting the features of each part and correlating the errors of these features back to machine-tool errors and the process parameters. Once the correlations are established, the previous two control

layers will be tuned by modifying the parameters in the geometric and thermal error models or in the corrections applied to the finishing cut, thus achieving a geometric adaptive control system for the machining process. A CMM and a quality monitoring PC execute this control layer. The CMM transfers all feature related measurement information to the quality monitor through a data base. The quality monitor then carries out the analysis to determine if the process needs any modification or tuning. Currently, we are in the process of automating the CMM inspection process under the Dimensional Measuring Interface Specification (DMIS) strategy. The implementation of the quality monitor will start next year.

Conclusions

A multi-layered control architecture for a small-batch automated manufacturing environments is being implemented at NIST. Based on deterministic manufacturing principles, this adaptive machining strategy is believed to be a feasible approach to maximizing the accuracy capabilities of existing and future manufacturing systems.

References

1. R.J. Hocken, et al., "Three Dimensional Metrology", Annals of CIRP, vol. 26, 1977.
2. Dimensional Metrology Group of NBS, Annual Progress Report for Bureau of Engraving and Printing, 1979.
3. M.A. Donmez, et al., "A General Methodology for Machine Tool Accuracy Enhancement by Error Compensation", Precision Engineering, vol. 8, no. 4, 1986.
4. Progress Report of the Quality in Automation Project for FY89, T.V. Vorburger, and B. Scace, eds., National Institute of Standards and Technology (US), NISTIR 4322, 1990.

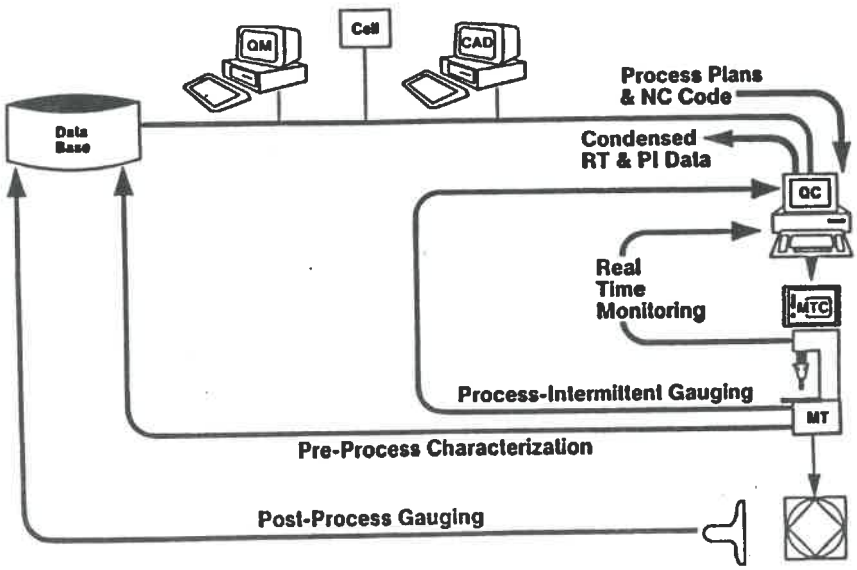

Figure 1. Overall QIA Control Architecture

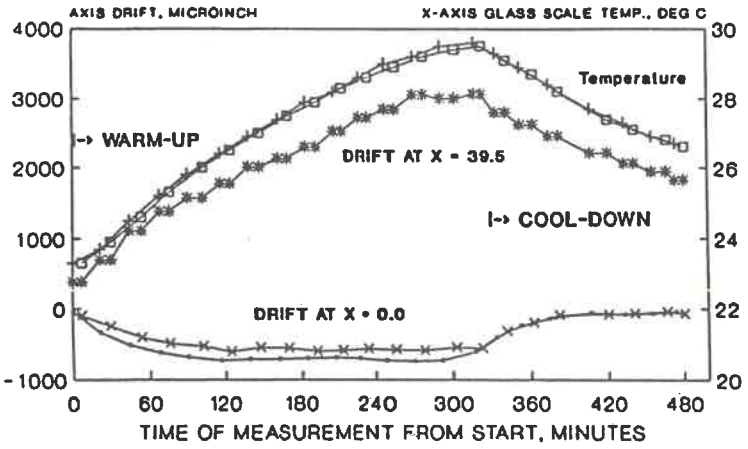

Figure 2 - Changes in linear displacement error as a function of glass scale temperature

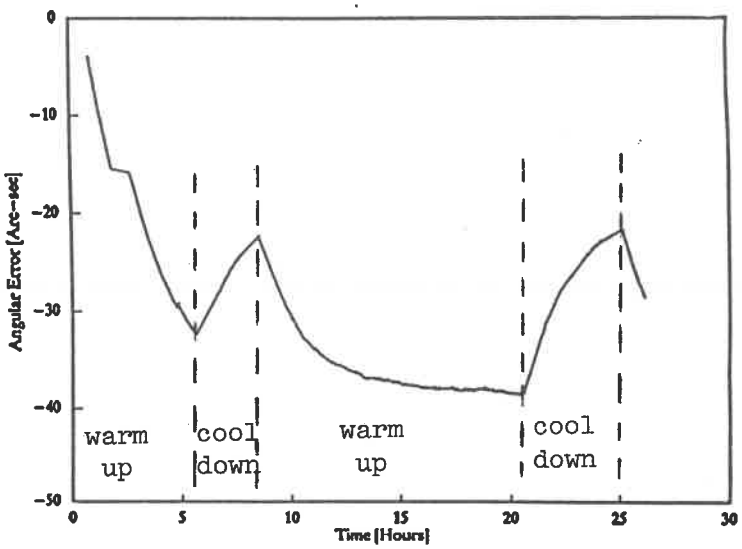

Figure 3 - Yaw error drift during intermittent warm up period

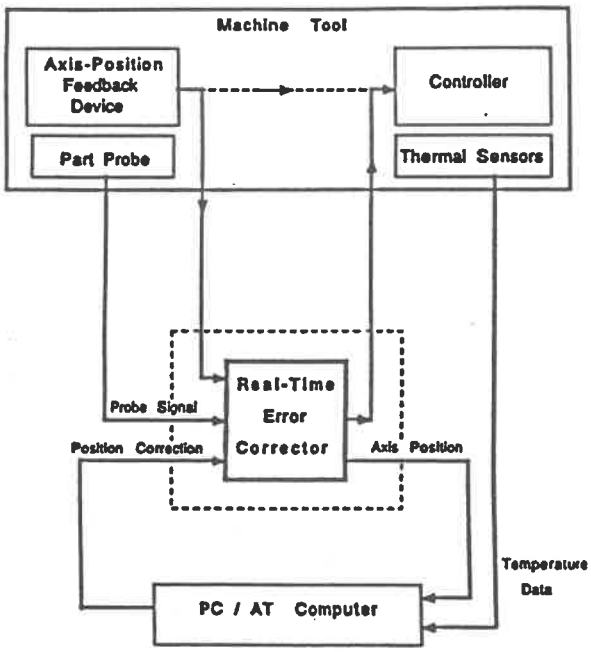

Figure 4 - Real-Time system overview

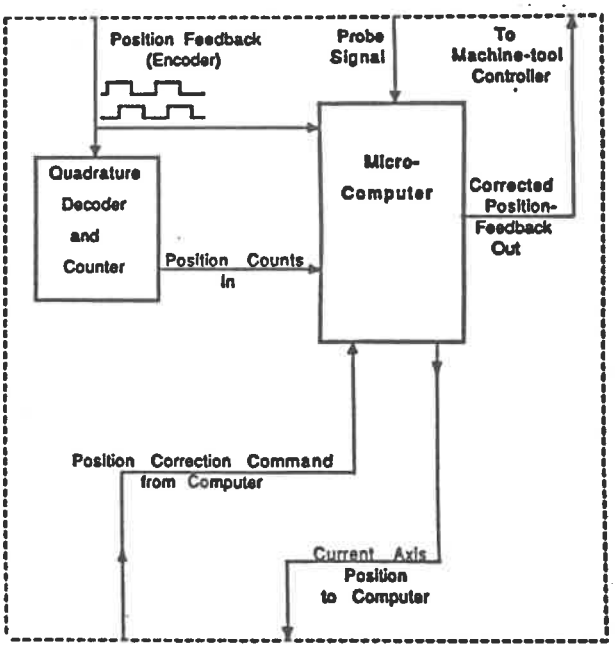

Figure 5 - Real-Time error corrector

SOME RECENT DEVELOPMENTS IN THE ANALYSIS AND INTERPRETATION OF SURFACE TOPOGRAPHY

Dr Paul J. Scott
Rank Taylor Hobson Ltd
2 New Star Road
Leicester
UK

Introduction

The monitoring of surface characteristics is widely considered to have two main areas of application: to ensure control of the manufacturing process and to ensure control of the functional performance of the surface. To maximize control it is important that useful information contained in the measured surface data is fully extracted. The analytical tools used to characterize the measured data are critical if this objective is to be achieved. Traditional approaches to the characterization of measured data are examined here, together with some recent ideas for more powerful analytical tools.

Generation of Surfaces

A simulation study of a lathe has been carried out [Reference 1] to consider what information could be contained in the surface topography. It was not the intention of this study to develop detailed models of a lathe but to simulate generic features of the surface creation process. In this study the surface creation process was treated as a dissipative dynamic system.

The investigation of dynamic systems is currently undergoing rapid development with new concepts and techniques supplementing more traditional analytical methods. A brief outline of some of these new techniques is given in Reference [1]. The long term behaviour of a dissipative dynamic system can be described in terms of the attractors of the system. The use of attractors greatly simplifies the task of assessing the dynamic behaviour of a lathe and the mutual dependencies contained in the surface topography.

Using linear models to simulate a lathe, the long term behaviour of the tool tip with respect to the surface produced periodic and quasiperiodic motion. The introduction of some very simple non-linearities into the models, such as a nonlinear spring rate, the tool leaving the cutting surface etc., also produced periodic and quasiperiodic motion as well as chaotic motion.

The tool tip describes a helical path around the workpiece being turned. While the tool remains in contact with the workpiece it will leave a signature of its motion along the helical path. A profile taken parallel to the axis of the workpiece will intersect the helical path every revolution. The profile will thus consist of a series of turning marks. The shape of the turning marks describe the

shape of the tool tip. The height of the individual turning marks describe a series of stroboscopic points that are related to the dynamic motion of the tool tip. In terms of dynamic systems theory these stroboscopic points are called a Poincare section.

In the analysis of dynamic systems, Poincare sections are often used as part of the investigation into the attractors of such systems. If a sufficient number of points are available in a Poincare section, many of the properties of an attractor can be deduced. Hence, if a profile contains a sufficient number of Poincare points, information about the attractor, and hence the dynamic motion of the tool tip, can be extracted.

The Analysis of Profiles

Analytical tools, such as the periodogram (power spectrum) and the profile height density curve, are traditionally used to characterize profiles. Most profile parameters defined in National and International Standards can be derived from the periodogram and the profile height density curve. It has been found that when the tool tip displays chaotic motion, not all of the mutual dependencies in the profile can be detected by these traditional tools.

The failure of traditional analytical tools to detect certain mutual dependencies in a profile can be demonstrated by considering an artificially constructed profile. Here the profile height density curve is Gaussian and the autocorrelation function is zero at nonzero lags. From this evidence it would appear that this profile is Gaussian white noise.

This particular profile was constructed from a symmetrical nonlinear deterministic relationship between the heights of adjacent profile points. No randomness was used in the construction of this profile. Hence the profile is certainly not Gaussian white noise. Adjacent points have zero correlation due to the symmetry of this relationship. This is also true of all other nonzero lags. The autocorrelation function (or alternatively the periodogram) can detect only the linear part of the mutual dependencies (ie. the linear correlation), it can not detect the non-linear dependencies, such as those contained in the example.

It is assumed that the surface creation process can be adequately described by a suitable attractor and that a signature of this attractor will be left in the topography of the surface. A profile from such a surface will contain a Poincare section from which many of the properties of the attractor can be deduced. Here the Poincare section is used in addition to traditional tools to characterize profiles.

Recent mathematical advances have lead to state space methods being regularly used in the investigation of dynamic systems. The state space is a useful concept for investigating the attractors of a dynamical system. It is an abstract space whose co-ordinates are the

degrees of freedom of the system's motion. Attractors and Poincare sections are reconstructed in the state space.

The first stage in the reconstruction of the Poincare section is to extract the Poincare points from the profile. In the case of a turned surface this can be achieved either by filtering out the turning marks or by the method of motif combination. The latter method is a very simple pattern recognition scheme that identifies the main features (motifs) from a profile [Reference 2]. Here the individual turning marks would be identified as the motifs.

To reconstruct the state space it is necessary to obtain independent quantities from the Poincare points to act as co-ordinates in the state space. It has been suggested in Reference [3] that for a time series, X(T) say, the time series with a number of fixed delays (i.e. X(T), X(T-S), X(T-2S),...,X(T-NS)) could be used as suitable co-ordinates. Methods to choose a suitable dimension N for the state space plus other refinements to this technique of reconstructing the state space are to be found in References [3]-[7].

Unfortunately, in practice a measured profile will only contain a relatively small amount of Poincare points, typically only a few hundred. With this number of points available only the full topological structure of the very simplest attractors, such as periodic and quasiperiodic attractors can be reconstructed, though many properties of the more complicated attractors can still be deduced. Fortunately simple attractors are the most common found in practice. From the study conducted so far, for lathes non-simple attractors only seem to occur when there are problems with the surface creation process.

Practical Profiles

Finally some measured profile data are used to illustrate the use of state space methods.

The first example is a turned surface that exhibits quasiperiodic waviness. Quasiperiodic motion is typical of a dynamic system that contains two weakly coupled oscillators whose frequencies have no common period. Here this could be the tool tip vibrating in different directions. The attractor of such a system resembles the surface of a doughnut or torus. The motion's orbit winds round the torus with one oscillator governing how fast the orbit circles the short direction, and the other oscillator governing the motion in the longer direction. By projecting the reconstructed attractor onto a suitable torus it is possible to deduce deviations from true quasiperiodic motion.

Observation of the resulting projection reveals that the resulting motion is indeed quasiperiodic but with occasional jumps around the shorter direction of the torus. Since this particular surface was hand turned these jumps may correspond to small pauses in the feed rate of the tool. This needs to be investigated further.

The final example is also a turned surface with waviness that exhibits a non-simple attractor. Using techniques described in Reference [7] it is possible to determine the dimension of the reconstructed attractor. This had a value of 3.3 $\pm$ 0.2, thus the attractor has a fractal structure corresponding to a chaotic attractor. Hence the tool tip's motion was chaotic. An examination of the periodogram of the measured profile reveals very high subharmonics of the feed wavelength. This is characteristic of a worn or damaged tool tip, further evidence that there was a problem with the surface creation process in this example.

Conclusions

State space methods appear to provide useful additional techniques, complementing more traditional tools, in the analysis of surface topography. It has been demonstrated that useful information about the dynamics of the machining process can be extracted from a measured surface.

The theory of dynamic systems is currently undergoing rapid progress. Further improved techniques from this field may also be of beneficial use in surface metrology and machine dynamics.

REFERENCES

[1] Scott, P.J.;
"Nonlinear dynamic systems in surface metrology", Surface Topography, 2 (1989), pp345-366.

[2] Scott, P.J.;
"The mathematics of motif techniques and their use for functional simulation", To appear.

[3] Packard, N.H., et al;
"Geometry from a time series", 1980, Phys. Rev. Lett., **45**, pp712-716.

[4] Fraser, A.M., and Swinney, H.L.;
"Using mutual information to find independent coordinates for strange attractors", 1986, Phys. Rev., **33A**, pp1134-1140.

[5] Broomhead, D.S. and King, G.P.;
"On the qualitative analysis of experimental dynamic systems", 1986, Physica, **20D**, pp217-249.

[6] Broomhead, D.S., et al;
"Topological dimension and local coordinates from time series data", 1987, J. Phys. A: Math. Gen. **20**, pp563-569.

[7] Eckmann, J.-P., and Ruelle, D.;
"Ergodic theory of chaos and strange attractors", 1985, Rev. Mod. Phys., **57**, pp617-656.

ERROR MODELING AND CORRECTION OF A LASER TRACKER

John Patten, John Grant, Paul Tullar, and Robert Hocken
University of North Carolina at Charlotte
College of Engineering
Charlotte, NC 28223

Abstract

Since their invention in the early 1980s, laser tracking systems have rapidly evolved and are now commercially available from several suppliers. These systems are of two distinct types which we call single-beam and multiple-beam systems. A single-beam laser tracker is a metrological device which uses a laser beam to track a cooperative target, such as a retroreflector, in three dimensions. The displacement of the target is measured using laser interferometry (usually heterodyne) and the angle to the target measured with sensitive angular encoders. A single-beam tracker thereby provides a spherical coordinate system in many ways analogous to that provided by a theodolite or total station. The second type of laser tracker uses three or more laser beams again servoed to track a cooperative target with the displacement of the target being measured by interferometry. Since at least three displacements are measured, no angular measurement is required in order to compute the target position. Since laser interferometers only measure displacement, both of these systems contain an unknown, the initial distance to the target, which must be obtained by calibration or other subsidiary measurements.

At the University of North Carolina at Charlotte, we have been studying an early prototype single-beam laser tracking system produced by a small company. The goal of our effort was to extend the range of the tracker, increase tracking speed, and to develop a complete error model for correcting the device for systematic errors. In our modeling we have addressed environmental effects, system mechanics (such as scale errors, squareness errors ("height of standards"), collimation, servo system performance), and algorithms for measurement control and alignment. Wherever possible we have attempted to use self-calibrating reversal techniques to provide internal consistency checks.

Description of the System

The basic single-beam laser tracking system has been described elsewhere [Lau, 1986; Ma, 1989]. A schematic of the tracker we tested is shown in Fig. 1. The tracking mirror can be rotated in two angles, the azimuth and the elevation, and changes in the radius (distance to the target) as well as these two angles are measured. The system is computer-controlled and has been modified to improve the system performance and enhance its utility.

Error Model

In our examination of the laser tracker we analyzed the following errors.

1. Squareness - orthogonality error ("height of standards"). The squareness error is the error caused by the non-orthogonality of the two angular axes.
2. Distance measuring error. This is the error in distance measurement caused by errors in calibrating the starting distance to the active target.

Since interferometers measure displacement to extremely high accuracy, this initial calibration is the prime contributor to the distance measuring error.

3. Beam alignment ("collimation error"). The beam alignment error refers to the error caused by small positional misalignments of the beam center with the center of the tracking mirror.

4. Tilt error. This is the error which results from misalignment of the laser beam with the azimuth axis of the tracker head.

5. Beam profile induced error. The error caused by changes in the centrus of the optical beam. This error is further explained in the text below.

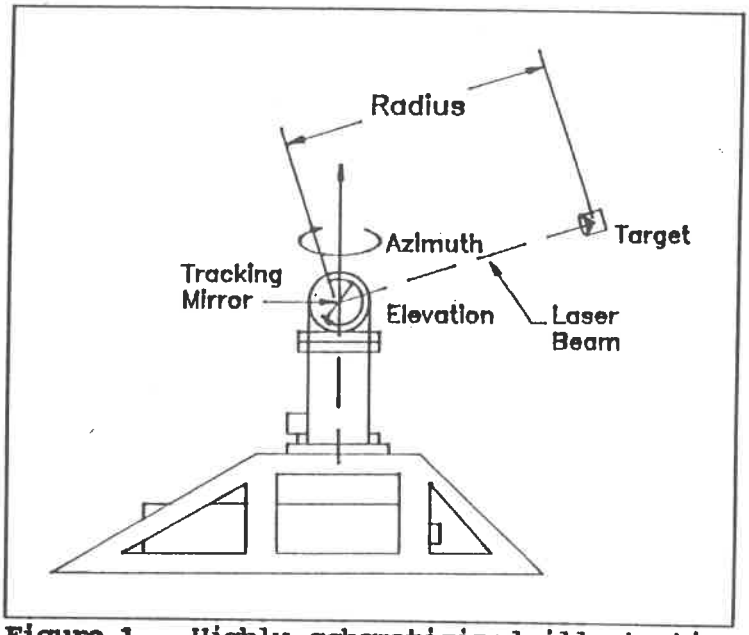

Figure 1. Highly schematicized illustration of the laser tracker. The dashed line is the laser beam and the target is a high-accuracy retroreflector.

6. Refractive index effects, including beam bending. These errors are of two types: the first is simply the change in wavelength of the laser due to changing atmospheric conditions; and the second, which is dominant in this type of tracker, is the actual bending of the beam due to refractive index gradients.

7. Mirror offset error. This error is caused by the surface of the tracking mirror being offset from the elevation axis.

8. Thermal expansion induced errors. These are errors caused by expansion and contraction of the laser tracker mounting frame which, because of the interferometer design used in this particular tracker, is in the interferometer-measuring path.

9. Servo/encoder errors. Two types of errors occur in the servo/encoder system: the first is simply due to the servo's inability to precisely center the beam due to finite gains; and the second is caused by errors in the angle encoders.

10. Deadpath error. This is the traditional deadpath error which exists in all interferometer systems and is readily compensated for with proper measurement of atmospheric temperature and pressure.

In addition to the above, the basic resolution of the laser interferometer, its electronics, optical non-linearities, and thermal drift were considered. In this system these errors are small and can be minimized through proper warm-up and operation [Steinmetz, 1990].

Of the errors described above, three were identified as being the major contributors to the overall error budget. These are squareness errors, beam profile errors, and beam bending errors. The squareness error has been discussed in the literature [Lau, 1986]. We devised a simple test to map this error as a function of the elevation (vertical) axis position. Squareness is tested by placing a retroreflector on a vertical track, locking the laser tracker on the

retroreflector, and reversing the head 200 gons[1] in the horizontal axis and an appropriate amount in the vertical axis to relocate the tracking mirror so that the laser beam can re-lock on the target. The values of the azimuth angle at lock are noted for each orientation of the tracker head. (This procedure is directly analogous to the surveyor's "face left/face right".) This process is repeated at several positions of the retroreflector along the vertical track in order to exercise the elevation axis over one-half (approximately 30 gons) of its complete range of travel. If there is a squareness error, the angular difference between the forward and reversed positions will differ from 200 gons, and this difference will increase as the elevation angle deviates (increases or decreases) from its value at the level plane.

Beam Profile

The beam profile error has been partially addressed in the literature [Puttock, 1978]. For the laser tracker the wavefront profile is particularly important, as X-Y lateral effect photodiodes are used to provide the error signals for the servo loops. Any change in the beam profile due to atmospheric or other effects is sensed as a positional change of the retroreflector. To test the beam through various atmospheric conditions, the beam path length was varied through twice the working range of the instrument. A commercial CCD camera was used to provide a two-dimensional intensity map. These data were analyzed to compute the centroid of the beam intensity profile which is assumed to be the "center" of the beam as detected by the lateral effect photodiode.

Beam Bending

The beam bending error was analyzed based upon the work of Estler [Estler, 1986; Estler, 1990] and Roberson [Roberson, 1990]. The refractive index of the atmosphere is considered to be a function of both temperature and pressure. As the refractive index changes with elevation, the tracking beam bends proportionally to the refractive index gradient. The apparent position of the retroreflector is thus different than the true position. This is illustrated schematically in Fig. 2. Since the refractive index is proportional to the density, and the density of air is proportional to temperature and pressure, there is always a bending effect simply due to altitude changes. In most laboratories or plants there is also commonly a vertical temperature gradient which exacerbates this effect. The error term is a non-linear function of the distance to the target, the temperature gradient, and the pressure gradient. The largest effect is due to the temperature gradient. For example, with an elevation angle of 33 gons and a temperature gradient of 6.5 degrees Centigrade per kilometer, the error at 100 meters is 170 micrometers. As a worst-case assumption, we computed the error at 10 meters with a gradient of 10 degrees Centigrade per meter. This leads to an error of 2000 micrometers. For a more normal "shop" environment with a gradient of 2 degrees centigrade per meter, the error at 5 meters is 30 micrometers.

---

[1]The gon is the metric unit of angle used commonly by surveyors. There are 400 gons in a circle.

Conclusions

Although single-beam laser trackers provide extremely high resolution, it is clear from our studies that extreme care must be taken in removing the systematic errors. Many of these errors can be calibrated and removed from the system; however, a dominant error, beam bending, will have to be compensated for in real time with accurate measurement of the temperature gradients present in the measurement volume. This will be difficult for large measurement volumes. For multiple-beam trackers, this effect is a cosine error and is thus very much smaller. Since multiple-beam trackers require a large stabilized measurement platform, they are, however, not so readily portable as is the single-beam tracker. Thus, for some applications single-beam trackers may be preferred.

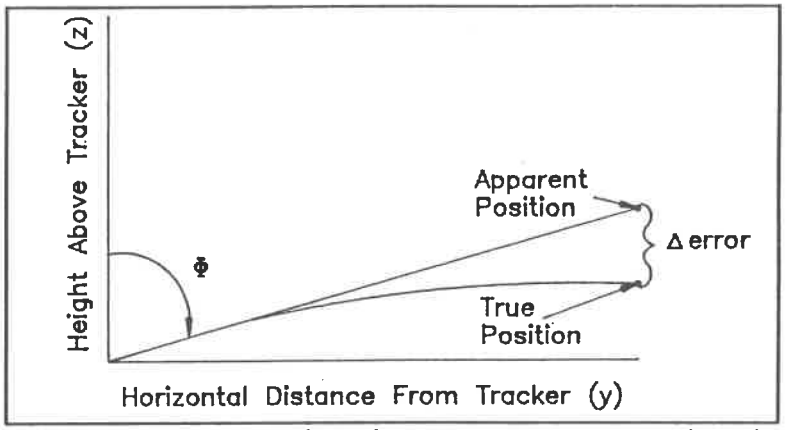

Figure 2. Schematic diagram of beam bending in an atmosphere with a refractive index gradient.

Acknowledgments

This work was supported in part by a grant from the National Institute of Standards and Technology.

References

Brown, L., Merry, J., and Wells, D., "Coordinate Measurement with a Tracking Laser Interferometer", Lasers and Applications, Oct. 1986, pp. 69-71.

Estler, T., NIST, private communication, 1990.

Estler, T., Borchardt, B., Fronczek, C., and Veale, R., "Rail Straightness Metrology at the David W. Taylor Model Basin", NBSIR-86-3443, Oct. 1986.

Lau, K., Hocken, R. J., and Haight, W. C., "Automatic Laser Tracking Interferometer System for Robot Metrology", Precision Engineering, Vol. 8, No. 1, Jan. 1986.

Ma, Q., Lau, K., and Tan, P., "Use of An Advanced Laser Tracking System For Large Dimensional Measurements", Huntsville, GA, June 1989, U.S. Army TMDE Symposium.

Puttock, M. J., "Large-Scale Metrology", CIRP Annals, Manufacturing Technology, Vol. 27, 1978, p. 351-355.

Steinmetz, C. R., "Sub Micron Position Measurement and Control on Precision Machine Tools with Laser Interferometry", Precision Engineering, Vol. 12, No. 1, Jan. 1990.

Roberson, J. A., and Crowe, C. T., Engineering Fluid Mechanics, 4th edition, Houghton Mifflin, Boston, MA, 1990, pp. 39-42.

DIAMOND TURNING OF NON-ROTATIONALLY SYMMETRIC SURFACES

Thomas A.Dow
Precision Engineering Center
North Carolina State University
Peter J. Falter
Westinghouse Defense and Electronic Systems

1 Introduction

A laboratory-scale diamond turning machine capable of fabricating non-rotationally symmetric optical surfaces in metallic materials has been described in [1]. That paper discussed the design of the piezoelectric-driven Fast Tool Servo (FTS), workpiece-based metrology, and high-speed digital control of the servo. The objective of the current paper is to discuss the results of recent fabrication experiments and the potential for non-rotationally symmetric optics [2].

2 Mechanical/Electronic Systems

Parallel Axis Ultraprecision Lathe PAUL is shown in Figure 1. It consists of a pair of 100 *mm* air bearings with vertical axes mounted on a rigid, horizontal steel base. One bearing supports the workpiece and is driven by an integral dc motor. The second bearing holds the cutting arm with the Fast Tool Servo. A dc motor-driven lead screw is used to push the cutting arm across the surface of the workpiece in a shallow arc. A coarse adjustment of the depth of cut can be made using a differential screw which holds the FTS to the cutting arm and fine adjustment is made with the piezoelectric actuator.

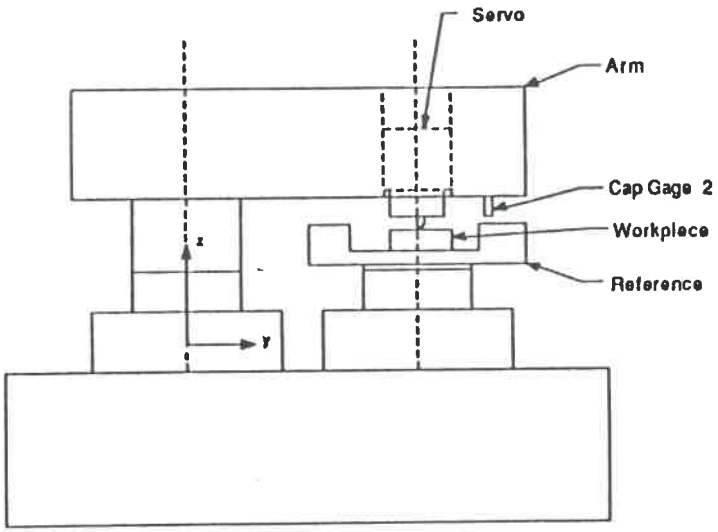

Figure 1. PAUL with FTS for fabrication of non-rotationally symmetric optical surfaces

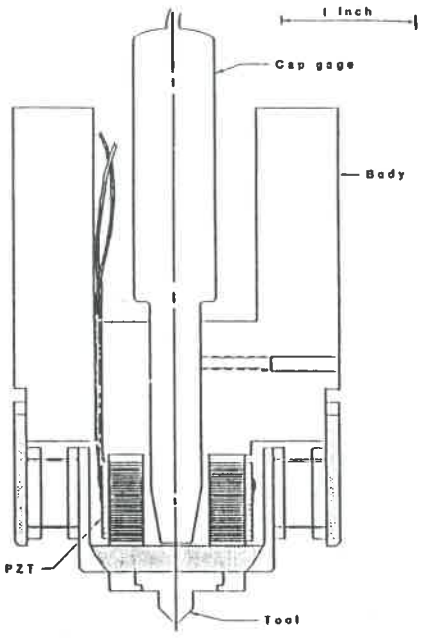

Figure 2. Details of Fast Tool Servo

the square of spindle speed, spindle growth can become significant in high-speed applications. For diamond turning, spindle growth can cause significant errors in parts machined before the spindle has "warmed up". Experiments were made using the PAUL/FTS apparatus with and without closed-loop feedback for spindle compensation. In each case, the errors due to spindle thermal effects were reduced by 85% to less than 0.1 μm.

Following Error Following error is the error in position of the tool compared to the reference signal. An example of the following error for a 2.5 μm 40 Hz sine wave is shown in Figure 3. The large sine wave is the reference waveform and the smaller signal is the difference between this reference and the output to the piezoelectric actuator, ie. the following error. This error is the maximum when the reference signal has its maximum velocity which is to be expected for the PI control scheme. The maximum following error for this condition is only ± 30 nm or about 2% of the input.

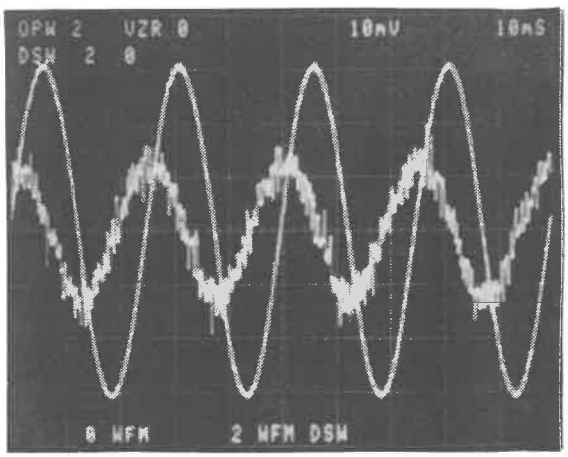

Figure 3. Following error (60 nm) of tool compared to reference sine wave (2.5 μm PP)

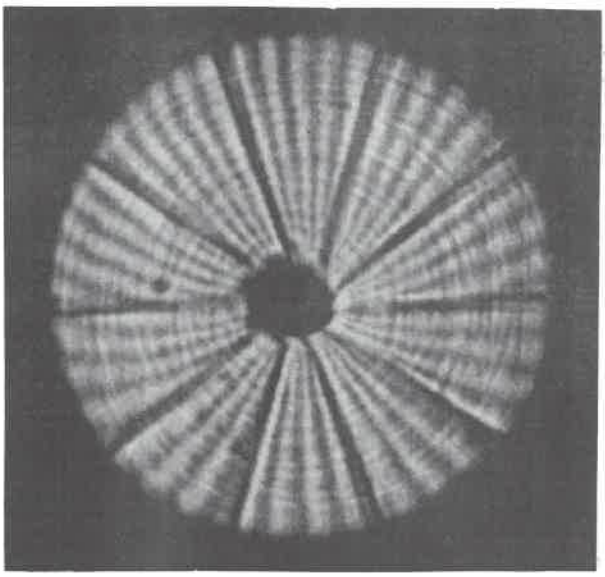

Figure 4. Interferogram of ramp surface with 2.5 μm PP amplitude

Surface Features Several surfaces were machined with non-rotationally symmetric features in the form of sine waves and triangle waves. To fabricate these surfaces a reference shape was input to the controller and feedback from the metrology system was used to correct errors in the shape. Typical of these surfaces is an OFHC copper ring with eight 2.5 μm peak-to-valley ramps waves per revolution. The interferogram of this surface is shown in Figure 4. It was machined at 200 rpm and the corresponding sinusoidal frequency was 26.5 Hz. Inspection of the surface with a modified roundness profiler showed a PP height of 2.5 μm but no measurement of distortion of the profile could be made.

Figure 5 shows a profilometer trace of several waves of a 2.5 μm ramp machined on an OFHC surface with 40 waves per revolution. The cutting speed was 100 rpm so that the fundamental frequency for the sawtooth pattern was 67 Hz. From the trace, the repeatability of the peaks is evident and the PP height of the surface is 0.2 μm. The rounding of the waveform and the resulting reduction in the height occurred as a result of the low gain used in the controller during

Fast Tool Servo The details of the FTS are illustrated in Figure 2. The heart of the servo is a hollow piezoelectric actuator (25 mm OD and 18 mm long) with a range of 20 μm. This element is preloaded by a set of round, plate-like flexures which are integral with the cutting tool mount. The moving mass, including the tool and its mount, is approximately 140 gm. The natural frequency of the FTS is on the order of 10 KHz.

Metrology System The metrology system consists of a pair of capacitance gages and a moving reference surface. The first gage is integral with the FTS and is used to measure the motion of the tool relative to the cutting arm. The second gage is mounted on the cutting arm and measures the relative position of this arm and a reference surface attached to the workpiece. The diamond-turned reference surface is shown in Figure 1. The controller computes the instantaneous depth of cut from these two gage outputs.

Amplifier A high-power amplifier was designed and built to drive the FTS. This unit was designed to produce voltage and current sufficient to move the piezoelectric element to its full extension at quasistatic conditions and about one-fourth of its full extension (5 μm) at 1 KHz. The resulting amplifier design consists of a push section of 14 power transistors in series which supply current to the piezoelectric element and a similiar pull section which drains current from the actuator. Even though the amplifier was capable of continuous operation, the piezoelectric element could not be run at a constant high frequecy because of internal heat generated by the losses in the crystal. A cooling system could be developed to overcome this problem.

3 Control System

System Model The proper selection of a control structure and operating parameters requires an understanding of the process to be controlled. The major mechanical components have been described above. The ancillary components include the servo drive electronics, metrology equipment, and filters. The geometry of the apparatus will determine the relationship between the motion of the capacitance gage in the FTS and the gage on the reference surface.

Computer Hardware The high-speed control calculations for the FTS were performed on a digital signal processor (TI TMS320C25). This chip has a 100 ns cycle time and an instruction set optimized for the computations required to implement filters, controllers, and other real-time applications. It is part of a commercial data acquisition board which includes two channels of A/D, two channels of D/A, and PC Bus interface electronics.

4 Experimental Results

The results of the fabrication experiments using the PAUL/FTS are discussed for two modes of operation: 1) Quasistatic correction for spindle growth errors, and 2) dynamic operation for the fabrication of non-rotationally symmetric optical surfaces.

Spindle Growth Correction Spindle growth is a form of thermal distortion found in hydrostatic, aerostatic, and mechanical bearing spindles. Since the amount of heat generated varies with

this test. The shape of the surface was identical to the motion of the tool as measured by the FTS capacitance gage before the tool was fed into the workpiece. This indicates that the cutting forces have little, if any, effect on the form accuracy of the surface.

Disturbance Rejection Disturbance rejection is a measure of the control system's ability to compensate for noise, unmodeled dynamics, and other disturbances. The unmodeled hysteresis of the piezoelectric actuator, for example, has been successfully overcome through the use of the feedback capacitance gage. Structural vibrations are another important error source in precision machining. Such disturbances may be generated by machine elements or the cutting process or may be transmitted through the floor or the air. To study the disturbance rejection capability of the PAUL/FTS, an electromagnetic shaker was attached to the base of the machine stand and was used to produce vertical disturbances at 40, 90 and 140 Hz - below, above, and at the primary mode of vibration of the the cutting arm (90 Hz). Cutting experiments were preformed on a brass workpiece with the controller on and off and the PP roughness of the surfaces produced were measured. These experiments illustrate the enormous benefit from this control system as the magnitude of the disturbances were reduced by over 75% , e.g. from 380 nm to 63 nm at the 40 Hz disturbance frequency.

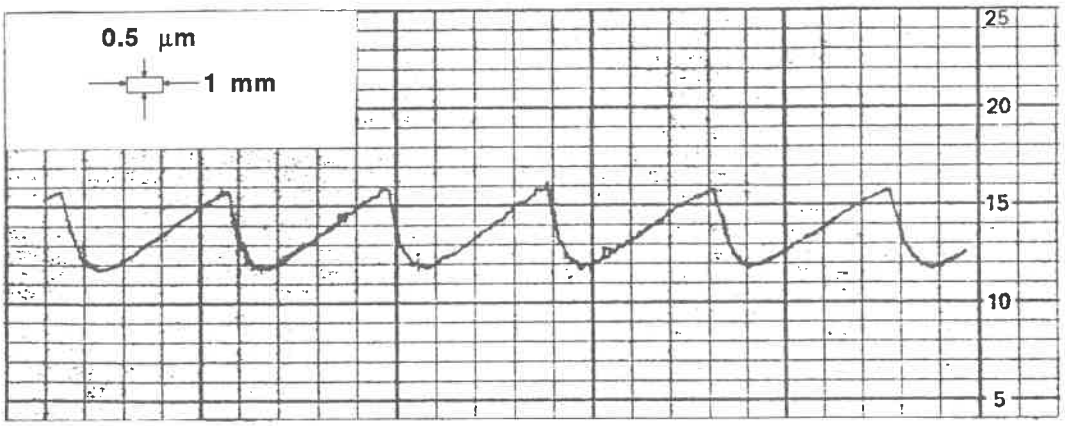

Figure 5. Profilometer trace of a ramp surface with PP amplitude of 2.5 μm and 40 waves per revolution.

References

[1] P.J. Falter and T.A. Dow, "A Diamond Turning Apparatus for Fabrication of Non-Rotationally Symmetric Surfaces", *Proceedings of the International Congress for Ultraprecision Technology*, M. Weck, ed., Aachen, W Germany, May 1988, Springer Verlag, pp 187-201.

[2] P.J. Falter, "Diamond Turning of Nonrotationally Symmetric Surfaces", *PhD Dissertation*, North Carolina State University, 1990.

PRECISION ENGINEERING IN MASS DATA STORAGE DEVICES

Professor D. B. Bogy
Director, Computer Mechanics Laboratory
Department of Mechanical Engineering
University of California, Berkeley, CA

The mass storage systems of magnetic and optical disk drives require precision engineering in their quest for ever increasing areal densities of stored information. For magnetic disk drives the head/disk spacing must be reduced to the 100 nm range. This places severe restrictions on surface roughness and asperity control of the media disks as well as the design and performance of the air bearing sliders that carry the read/write transducer.

In this talk laser based measurement techniques will be described that are used for this purpose. Also, evaluation of media surfaces by use of scanning tunnelling microscopy will be shown. Finally, some issues related to mechanical stability of tracking systems will be mentioned.

Dynamics Analysis and Control of a Precision Slide with Coulomb Friction and Stiction

by

Paul I. Ro, Roy S. Colby , Peter I. Hubbel

Precision Engineering Center
North Carolina State University

Abstract

A study of the effect of Coulomb friction and stiction on the servo performance of a computer-controlled precision slide system is presented. First, it is observed that the dynamics of the slide system change significantly from a nominal linear approximation as the commanded input signal decreases. This phenomenon can be attributed mainly to the presence of the nonlinear friction, plus other residual effects due to a higher noise-to-signal ratio for a smaller input signal, the digitization of the servo error, etc. Secondly, a limit cycle behavior is observed for certain combinations of gains under PI velocity control. The analysis using a Sinusoidal Input Describing Function (SIDF) shows that the limit cycle behavior depends on the natural frequency of the slide plus the gains associated with PI control. A nonlinear feedforward compensation term based on an *a priori* model of the nonlinear friction is added to the current command to eliminate the limit cycle. Although a reduction in the friction effect is apparent using the feedforward term, the method is sensitive to deviation of the actual friction value from that of the model.

The Coulomb friction and stiction nonlinearities present in all mechanical systems poses a difficult control problem. It affects the transient and the steady-state behaviors as well as the system stability. For the x and z slide systems of the DTM, the steady-state error and possible limit cycle behavior resulting from the nonlinearities can have a detrimental effect on the overall surface quality of machined parts. Moreover, diamond-cut surface contours often require very fine motion increments, which requires the ability of the x and z slide systems to respond to a very small control input. However, as the magnitude of this input error signal decreases, the degree to which the nonlinear friction dominates the system behavior increases. Historically, its effect had been largely neglected due to the limitations of the linear control schemes conventionally used for controlling mechanical slide systems. To achieve higher accuracy, design approaches that resulted incorporate linear motors, air bearings and hydrostatic bearings have been used to reduce the effect of the nonlinearities.

Further improvement in the performance of mechanical slide systems with Coulomb friction and stiction nonlinearities can be achieved by means of control. Various existing control schemes have been developed and implemented. Won [1] studied the effect of Coulomb friction in a DC-motor driven robotic joint. To achieve zero steady-state error a LQR (Linear Qaudratic Regulator) based optimal control scheme was applied, and a satisfactory result has been obtained. The scheme utilized the full-state feedback approach with various combinations of weighting on the state feedback. Another novel approach to 'null' any nonzero steady-state error due to the nonlinear friction has been developed by Yang [2]. In this approach, an adaptive control scheme is used to generate a series of pulses of differing widths to overcome the stiction effect. The width of the pulse is obtained using both the MRAC (Model Reference Adaptive Control) approach and the STR (Self-Tuning Regulator) approach, and the stability proof in each case has been shown.

Both Won and Yang have also investigated a possible limit cycle behavior using a SIDF (Sinusoidal Input Describing Function) approach first introduced by Tou [3]. It is shown that in the presence of integral action, the system with the nonlinear friction can exhibit a limit cycle. Another adaptive approach has been developed by Canudas [4]. In this work, the effect of Coulomb friction without stiction on the velocity servo performance of a typical DC-motor was investigated.

Townsend [5] studied the effect of the nonlinear friction on force control with integral feedback. The work showed that stiction can cause the applied force to enter a limit cycle, and Coulomb friction can extend the system stability bounds but may lead to an input dependent stability. Hollars [6] attempted to feed forward a joint torque to compensate for Coulomb friction in a compliant tendon-driven manipulator joint with some success. However,the stiction effect could not be attenuated, and the stability was input dependent.

In this paper, the effect of the nonlinear friction on the precision slide is analyzed and demonstrated through experiments. For a small input signal, a ball-screw driven prototype precision slide system undergoes a significant change in dynamics, and the change is illustrated both in the time and the frequency domains. Also, certain combination of PI gains resulted in a limit cycle behavior. The effect of adding a feedforward term to cancel this nonlinear friction effect is demonstrated.

A prototype precision linear testbed is built for an experiemental purpose. It comprises an air bearing slide driven by a precision ball-screw. The slide is coupled to the ballscrew by a custom-designed non-influencing coupling to isolate the slide from the off-axis motions induced by the ball-screw. A servo-controlled dc motor drives the ball-screw, and appropriate feedback control loops regulate position and velocity of the slide. The motor is powered by a linear power amplifier rated at 15 V, 20 A. This amplifier has ample capacity to drive the slide at any desired speed and load. The amplifier is operated in conjunction with an analog current regulator circuit which adjusts the amplifier voltage to maintain a commanded value of motor current.

Slide position is measured by a laser interferometer with a resolution of 15 nanometers (nm) per count and a range of approximately 4 meters. Motor tachometer feedback is also available for an inner velocity loop in the servo control. An IBM-PC compatible computer equipped with an analog and digital interface card is used to control the slide. The interface card has multiplexed A/D channels with 16-bit A/D converters, and two 16-bit D/A output channels. Sixteen bits of digital I/O are also available.

The electromechanical dynamics of the linear testbed are modeled as a fourth order system, in which the input is the command from the computer to the analog current regulator, and the output is the linear position of the slide. The current regulator is a PI circuit whose bandwidth is sufficiently high that the electrical dynamics may be neglected in the model. The control input to the system is therefore the current, or equivalently the torque, to the dc servo motor, and the dynamics to be modeled are strictly mechanical.

The ability to respond to a very small input signal and generate a fine motion is an essential ingredient for any precision slide system. However, the performance of all mechanical slide systems is hampered by the existence of Coulomb friction and stiction which are characterized by a sharp discontinuity at zero velocity. So, as the servo error signal approaches zero, the dynamics of the slide system are dominated by these nonlinearities. Another effect of the signal approaching zero is that the noise-to-signal ratio increases, and the system becomes much more erratic as it tries to respond to amplified sensor noise and other external noise. For digitally controlled slide systems, performance is further degraded by the additional nonlinear approximation introduced by digitization.

A series of tests was performed on the slide system described above to characterize its small motion dynamics. The first test was done just on the motor drive system with the slide and the ball-screw disconnected. A command velocity signal was generated under velocity servo with PI control, and the tachometer output was observed. Two different

command signal sizes were used; one for a relatively nominal feedrate and another for much slower case. The first case shows a typical output profile for a nominal signal size. However, for certain combinations of PI gains, when the signal size is reduced by a factor of 10 in the second case, the output profile demonstrates a distinctly nonlinear behavior. We observed for the latter case that even though there is a significant drop in the average velocity of the motor as expected, the amplitude of variation has increased by a factor of 5, and it exhibits a very low frequency limit cycle envelope, which did not appear when the signal size was larger. The envelope frequency is much too low (0.16 Hz) to be associated with any mechanical resonance. In fact, we observed the envelope of the same frequency with the slide and the ball-screw connected. It can be argued that the digitization error with the sampling frequency of 1 kHz can hardly contribute to such a low frequency envelope. The only possible source for the limit cycle may be the nonlinear friction.

The second test performed on the motor-amplifier system involved obtaining the open-loop Bode plots for different random signal input magnitudes. To perform this test, a 3.0 inch cantilever arm was extended from the center of the motor shaft, and the position at the end of the arm was monitored using a high resolution capacitance gage. For the first case, the system was excited with a random signal input with the amplitude limited to 30.5 mV. The resulting magnitude and the phase of capacitance gage output were compared with those of the reference random signal and plotted versus frequency. From the magnitude plot, the natural frequency of the motor amplifier system is observed at around 50 Hz with a relatively large damping characteristic. The same test was repeated for the second case with the only difference being that the random signal amplitude was limited to 3.05 mV, or one tenth of the first case. The resulting Bode plot shows that the natural frequency of the system increased to about 100 Hz with much lighter damping characteristic.

The increase in the natural frequency suggests that the dynamics are characterized by a nonlinear spring with a higher initial slope (stiffer spring constant). So, as the control signal approaches zero, the stiffness of the motor system goes up which results in a higher natural frequency. Combined with the lessening damping coefficient, the test results suggest that the dynamics of the system for the second case is largely characterized by the elastic deformation of the shaft bearings. In this regard, the increase in stiffness is the stiffness associated with the bearing deformation, and the decrease in damping is explained by the fact that there is no sliding between metal surfaces. This kind of phenomenon was observed by other researchers [7] as well.

The third set of tests were performed on the entire slide system (with slide and the ball-screw connected) to demonstrate the tradeoff that exists between the need for an integral action for the maximum accuracy and the servo stiffness and a possible limit cycle. According to a describing function analysis using the analytical model for Coulomb friction and stiction obtained by Tou [3], a stable limit cycle would occur at a relatively low frequency, and this prediction is verified through experimental results. At given PI gains with the velocity loop closed, the entire system exhibited a 0.5 Hz limit cycle. Also, the analysis shows that the motor-amplifier system alone (with the slide and the ball-screw disconnected) would not exhibit a limit cycle. This is also verified through the experiment as no limit cycle is observed at the same PI gains when the ball-screw and the slide are disconnected. A quick intuitive explanation for such behavior would be that by disconnecting the ball-screw the overall Coulomb friction and stiction level has been significantly decreased so as not to cause a limit cycle. However, a careful describing function analysis using a 4th order system model shows that the addition of the extra mass and the stiffness associated with the ball-screw and the slide mass plays the essential role. According to the analysis, the lower the natural frequency associated with the ball-screw and slide mass system, the more likely a limit cycle would occur.

Finally, a simple nonlinear feedforward term is added to the current command to test its ability to minimize the nonlinear friction effect. The feedforward term is a computer model of the nonlinear friction based on empirical data. Originally, the tachometer output was used as the input to the feedforward term. But, the noise inherent in the signal resulted in a severe chattering behavior. Use of velocity command as a triggering signal, instead, shows much improvement, and it reduced the limit cycle amplitude by an order of manitude. This simple feedforward scheme, however, proved to be very sensitive to deviation of the actual friction from the model. A more robust nonlinear compensation scheme is forthcoming.

References

[1] S.C. Won, D.J. Lim, and D.H. Chyung, "D-C Motor Driven Robotic Manipulator Control", Proc. of 24th Conf. on Decision and Control,Dec. 1985.

[2] S. Yang and M. Tomizuka, "Adaptive Pulse Width Control for Precise Positioning Under the Influence of Stiction and Coulomb Friction", ASME Jour. of Dynamic Systems, Measurement, and Control, Vol. 110,Sept. 1988

[3] J. Tou and P.M. Schultheiss, "Static and Sliding Friction inFeedback Systems", Journal of Applied Physics, Vol. 24, No. 9, Sept. 1953

[4] C. Canudas, K.J. Astrom, and K. Braun, "Adaptive Friction Compensation in DC Motor Drives", Proc. of 25th Conf. on Decision andControl, Dec. 1986

[5] W.T. Townsend and J.K. Salisbury, Jr., "The Effect of Coulomb Friction and Stiction on Force Control", Proc. of 26th Conf. on Decisionand Control, Dec. 1987

[6] M.G. Hollars and R.H. Cannon, "Initial Experiments on the End-Point Control of a Two-Link Manipulator with Flexible Tendons", ASME WAM,Miami Beach, Fla, Nov., 1985

[7] S. Futami, A. Furutani, and S Yoshida, "Nanometer Positioning and its Micro-dynamics", Nanotechnology, July, 1990.

Computer-Controlled Off-Axis Optical Fabrication

Timothy J. Wilson
Eastman Kodak Company, Federal Systems Division
Advanced Technology Products
Special Optics Fabrication
Rochester, New York 14650-0803

Abstract

Eastman Kodak Company has developed a new family of optical processing equipment to process large, highly accurate off-axis aspheric optics that meet the requirements for surveillance, tracking, communication and strategic defense programs. These systems include an abrasive water jet machining system, the Off-Axis Aspheric Grinding Machine (OAGM), tthe Computer Controlled Small Tool Polisher (CCSTP) and the Ion Figuring System (IFS). An abrasive water jet machining head mounted to a positioning robot plays an integral role in specialized mirror blank design and construction. The OAGM, the CCSTP and the IFS are computer controlled systems that can be used for generating, grinding, polishing and final figuring of these specialized optical components.

These systems address the specialized requirements for processing off-axis aspheres. Ongoing research efforts have developed the fundamental algorithms to transform the coordinate system of a parent optic into a coordinate system that is relative to a given off-axis segment mounted in an optical processing system. We are currently developing and testing a unified modular software package that can utilize these algorithms and apply them to removal function path generation in each of these new large optic processing systems. The traditional approach to the development of the required control software, i.e., separate programs unique to each process, is costly and creates a sizeable maintenance problem. A unified approach is being implemented which takes into account common elements of these processes.

In principle, the effects of these errors on optical performance can be expressed equally well in terms of their power spectrum, S(f), or their auto-covariance function, C(t). In practice, however, it is essential to perform analysis and modelling in the frequency rather than the lag domain to account for the bandwidth and transfer-function effects present in real measurements. This is especially important for surfaces with inverse-power-law spectra, for which the apparent correlation function can take on "reasonable" but totally spurious forms because of the convolutional effects of the measurement bandpass.

The high-frequency limit of profile measurements is generally determined by the Nyquist frequency of sampling interval, and the low-frequency limit by the length of the measurement trace on the surface. The latter enters through the data-detrending procedures introduced in the data analysis to eliminate artifacts of the measurement process and the anticipated focussing properties of the mirror. These effects are generally unimportant for surfaces with short correlation lengths, but are important for power-law surfaces which would otherwise exhibit "divergent" low-frequency behavior.

4. Scattering. In order to relate the measured/modeled surface statistics to mirror performance we propose -- a la Ockham -- to use the simplest scattering formalism which captures the essential physics of the present application. As a first cut we consider Beckmann-Spizzichino diffraction theory [1], which leads to a particularly simple expression for the measured reflected-plus-scattered intensity in the image plane.

This is in the form of a one-dimensional Fourier transform of the product of five factors in lag space, each representing a different physical aspect of the system: The source size, the mirror illumination/aperture, the detector slit width, and the surface "figure" and "finish" errors [2].

5. Testing and Specification. The five-factor formula predicts the combined reflected and scattered (coherent and incoherent) intensities in terms of the measured surface statistics and system parameters. As such, it provides a framework for both testing -- i.e. predicting performance from laboratory measurements -- and specification -- i.e. stating mirror requirements in terms of functional performance.

The two simplest specifications are given in terms of the allowable scattered intensity at points outside the specular core, and the allowable reduction of the on-axis image intensity relative to its perfect-surface value -- the so-called Strehl factor. In the smooth-surface limit the scattered intensity is simply proportional to the surface power spectrum, S(f). The interpretation of the Strehl factor in terms of surface statistics is more interesting:

For surfaces with correlation lengths much less than the effective transverse coherence length on the surface, the Strehl factor is the square magnitude of the characteristic function of the surface height distribution.

A Gaussian height distribution then leads to the familiar Gaussian or Debye-Waller form of the Strehl factor, which depends only on the intrinsic root-mean-square (rms) surface roughness. Other height distributions lead to non-Gaussian dependences on this quantity.

Surfaces with long correlation lengths lead to Strehl factors which depend on system as well as surface parameters, and which may be non-Gaussian even for a Gaussian height distribution. In the smooth-surface limit the factor depends on a high-pass integral of the surface spectrum which can, if desired, be expressed in terms of the rms height of the "finish" error and the rms slope of the "figure" error.

The analysis of the long-correlation-length case must also include the fact that when these mirrors are used, each member of the ensemble is tilted to conform to a desired specular direction, and may also be translated along the optic axis to optimize its focussing properties. These operations are the exact analogues of the detrending operations in the analysis of profile measurements mentioned above.

Additional specifications can be given in terms of the shape of the image core, such as measures of its width and the "encircled energy".

6. Comment. Our discussion of these problems has been given with reference to synchrotron-radiation mirrors, although they also have direct application in x-ray astronomy, the development of multilayer interference coatings for normal-incidence x-ray optics, and the use of x-ray scattering as a tool for the study of surface and interface structures. The general issues of metrology, estimation and scattering have universal application.

7. References.

[1] P. Beckmann and A. Spizzichino, The Scattering of Electromagnetic Waves from Rough Surfaces, MacMillan, New York NY (1963), reissued by Artech House Books, Norwood MA (1987).

[2] E. L. Church and P. Z. Takacs, "Prediction of mirror performance from laboratory measurements", Proc. SPIE 1160 323-336 (1989). Expanded version accepted for publication in Optical Engineering (1990).

Analytical photon scanning tunneling microscopy

*#M.A. Paesler, *#P.J. Moyer and *C.E. Johnson
*Physics Department and the #Precision Engineering Center
North Carolina State University, Raleigh, NC 27695-8202

R.C. Reddick, R.J. Warmack, and T.L. Ferrell
Health and Safety Research Division, Oak Ridge National Laboratory,
Oak Ridge, TN 37831
Department of Physics and Astronomy, University of Tennessee,
Knoxville, TN 37919

The photon scanning tunneling microscope (PSTM) has been operated in spectroscopic mode to both image the topography and analyze stress features on a micro-indented, chromium-implanted sapphire surface. Light originating primarily from the evanescent field generated by an internally reflected beam, with some contribution from scattering by roughness features and radiation from fluorescence and luminescence, was coupled into the probe tip. The topographic resolution observed (~50 nm) is appreciably finer than the diffraction limit. Stresses of 3 kbar around micro-indents were measured by monitoring shifts in the photoluminescence peaks. A discussion of the spectroscopic resolution obtainable with this "analytical PSTM" and applications are presented.

The scanning tunneling microscope senses the exponentially decaying electron tunneling probability above the surface of a conductor. A similar type of microscope called a photon scanning tunneling microscope, or PSTM, has recently been developed.[1,2] With the PSTM, one senses the exponentially decaying evanescent field above a dielectric in which total internal reflection is made to occur. The probe tip of this optical scanning microscope is a sharpenned optical fiber.[1,2] The resolution of the PSTM has been shown to be as small as $\lambda/20$ laterally and $\lambda/100$ vertically where λ is the wavelength of the radiation which is suffering total internal reflection within the dielectric. In addition to topographical surface data, spectroscopic information can also be obtained from the internally reflected beam.[1]

In the region above the surface of the sample where the evanescent field is sensed in a PSTM, there may also be radiation which contains information about this surface. For example, if a Raman or a photoluminescence event takes place, then this signal can also couple into and propagate through the fiber whose end constitutes the PSTM probe tip.[3] In an analytical PSTM, provision must be made to measure two signals: i) the signal resulting from detection of the evanescent field, the intensity dependence of which gives the topographic image of the surface, and ii) the signal resulting from the Raman or photoluminescence event, the spectral dependence of which yields information about the nature of the surface. In the following, results demonstrating the successful construction and operation of an analytical PSTM are presented. The spatial resolution of the

spectroscopically analyzed signal in this PSTM is briefly discussed, and a number of possible applications of this novel microscope are mentioned.

To demonstrate the operation of the analytical PSTM, a cylindrical rod of sapphire was cut in a plane along its axis so as to have two parallel flat faces. The end of the cylinder was cut along a plane with normal tilted 45° with respect to the cylinder's axis. All faces of the sapphire were polished with a series of diamond grits, the final size being 250 nm. The longest face of the sample was then implanted with Cr^{3+} ions so as to achieve a profile of ruby (Cr^{3+} doped sapphire) with peak dopant concentration approximately 44 nm beneath the sample surface and a profile width on the order of 25 nm. The sample was annealed to relieve any implantation-induced damage. To create surface features that might be used to determine the lateral resolution of the analytical PSTM, an array of micro-indents was then placed in the implanted surface of the sample. Each indent creates a stress field that decreases with radial distance from the indent. In ruby, a photoluminescence doublet occurs at 692.7 and 694.2 nm and shifts linearly to lower energy with increased hydrostatic pressure - i.e. compressive stress - by 0.0365 nm/kbar. This luminescence doublet provides the spectroscopic signal measured. The sapphire was put on the sample stage of an existing PSTM[1] which uses as a sensing probe an optical fiber chemically etched to a tip radius on the order of 100 nm. Using the 442 nm line of a He-Cd laser, light was made to suffer total internal reflection at the polished and implanted surface in the region of the indent array.

A beam-splitting **Y** is put in the sensing fiber of the PSTM so as to allow the light sensed by the tip to proceed down two identical channels. One of these channels is returned to the z-axis (vertical) control of the PSTM while light emerging from the fiber comprising the second channel of the **Y** is dispersed in a monochromator (dispersion of 2.5 nm/mm and resolution 0.5 nm) and detected with a cooled photomultiplier. The output of the photomultiplier was plotted versus wavelength to obtain photoluminescence spectra.

The PSTM image of a region of the sample surface near a micro-indent is shown in figure 1. This grey-scale contour map represents a region 10 μm x 10 μm, and features a micro-indent (lower left) which extends to a depth of 250 nm below the average plane of the sample surface. Features on the polished sample surface (upper right) appear to be several tens of nanometers across, thus indicating topographical imaging resolution to be less than 100 nm. Three photoluminescence spectra were taken at positions marked by the numbers 1, 2, and 3 in figure 1. Spectrum 3 represents a ruby photoluminescence doublet which is indicative of a relatively low stress region. The distance from the center of the indent is approximately 8.6 μm. As the probe tip approaches the micro-indent in taking spectra 2 and 1, the rather large compressive stresses known to exist in the region around the micro-indent manifest themselves in a shifted and broadened photoluminescence spectrum. The spectra taken at positions 1 and 3 are shown in figure 2. The shift of the peaks to lower energy indicates increased compressive stress closer to the indent. Perhaps more important than the shift in

the peak position is the significant broadening toward compressive stress that occurs as the probe is moved closer to the indent (i.e. for spectrum 1.)

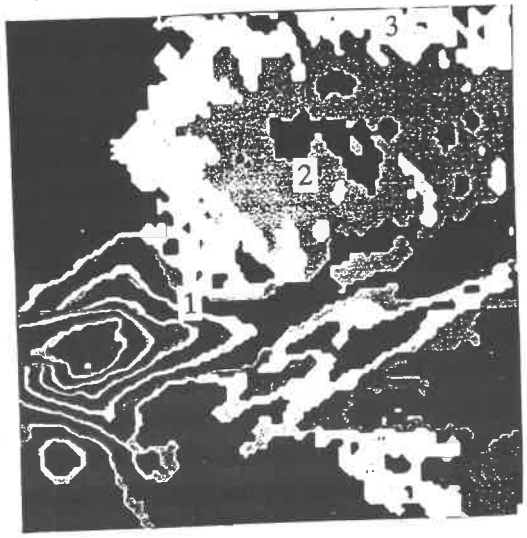

Figure 1. *Grey-scale contour map of the surface of the indented sapphire sample taken with the photon scanning tunneling microscope, or PSTM. This micrograph represents a region on the sample surface 10 μm x 10 μm. Each grey scale cycle represent a 50 nm height change. The indent extends to a depth of 250 nm below the sapphire surface plane. The wavelength of the radiation which was used to make this microgram was 442 nm, and resolution of surface features is ~ 50 nm.*

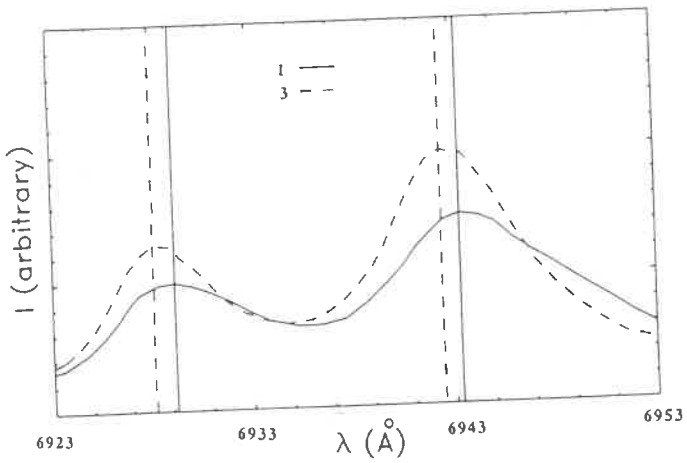

Figure 2. *Ruby photoluminescence spectra taken with the analytical PSTM, at positions 1 and 3 as shown in figure 1. The spectrum taken on the surface plane (spectrum 3) indicates a region of low stress with relatively unshifted and unbroadened luminescence lines. Nearer the indent, the spectra shift slightly and broaden significantly indicating increased compressive stress in the region of the indent.*

For these samples the lateral resolution of the PSTM is clearly finer than the diffraction limit, but it is difficult to accurately determine the resolution of the analytical PSTM. It is straightforward, however, to show that the lateral resolution of the analytical PSTM is significantly finer than that obtainable in conventional microscopic spectrometers. Using the 40x, 0.6 numerical aperture microscope objective on one such instrument,[4] a spot size on the order of 1 μm is obtainable. Conventional photoluminescence spectra taken with this instrument at positions 1, 2 and 3 on the sample shown in figure 1 result in linewidths considerably larger than those obtained in the analytical PSTM. Care was taken to duplicate the instrument resolution of the spectrometer used in the analytical PSTM experiment so that the measured linewidth was determined solely by the collection optics. A plot of the linewidth of the two lines of the ruby photoluminescence doublet for the analytical PSTM and for the conventional micro-Raman spectrometer appears as figure 3. These data must be viewed in

light of the fact that the stress is known to be monotonically increasing as one approaches the micro-indent. As seen in figure 3, the widths of the spectra at any given position are measurably greater for the conventional microscope, thus the analytical PSTM samples an appreciably narrower region than the microscope in the micro-Raman spectrometer. Although these data do not confirm that the resolution of the analytical PSTM is finer than the diffraction limit, they clearly demonstrate that resolution is considerably better than that provided by the 1 μm spot obtainable in the micro-Raman spectrometer.

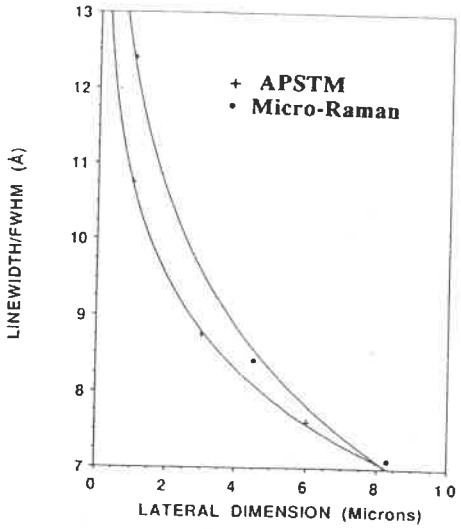

Figure 3 *The linewidth of the photoluminescence spectra taken at positions 1, 2 and 3 shown in figure 2 for the analytical PSTM (solid dots) and for a conventional micro-Raman spectrometer (open dots). The conventional microscope on the micro-Raman spectrometer was focused to a 1 μm probe spot. The decreased linewidth of the analytical PSTM spectra taken at the same positions on the sample indicates considerable improvement in spatial resolution for the analytical PSTM over the conventional microscope.*

The wealth of information available using conventional optical spectroscopic techniques has long proven useful in precision engineering applications. However, as nano-fabrication techniques become more available, the fundamental diffraction limit of these techniques places severe limitations on the applicability of these techniques to precision engineering problems. The demonstration of the spectroscopic capabilities of the PSTM presented in this paper suggests that studies of structures smaller than the wavelength of the radiation used in the investigation may be meaningfully studied. As the capabilities of the PSTM become realized, it can be expected that important precision engineering problems will be investigated with this important new tool.

REFERENCES

1. R.C. Reddick, R.J. Warmack, and T.L. Ferrell, Phys. Rev. B **39**, 767 (1989).
2. D. Courjon, K. Sarayeddine, and M. Spajer, Opt. Comm. **71**, 23 (1989).
3. P.J. Moyer, C.L. Jahncke, M.A. Paesler, R.C. Reddick, and R.J. Warmack, Phys. Lett. A **145**, 343 (1990).
4. The micro-Raman spectrometer used was the Spex Industries *Micramate* which is discussed in, for example, R.J. Thibeau, C.W. Goldfarb, and A.Z. Heidersbach, J. Electrochem. Soc. **127**, 37 (1980).
5. D.P. Tsai, H.E. Jackson, R.C. Reddick, S.H. Sharp, and R.J. Warmack, Appl. Phys. Lett. **56**, 1515 (1990).
6. G. Binning and H. Rohrer, Physica **127 B**, 37 (1984).
7. H.K. Wickramasinghe, Scientific American **261**, 98 (1989).
8. Robert Pool, Science **247**, 634 (1990).

COMPARISON OF OPTICAL AND MECHANICAL MEASUREMENTS OF SURFACE FINISH

Thomas R. Lettieri, Aaron B. Kiely, Lin-xiang Cao, and
Theodore V. Vorburger
National Institute of Standards and Technology
Gaithersburg, MD

Introduction

Surface finish plays an important role in many precision-engineered systems, and historically such measurements have been made using a mechanical stylus instrument [1]. Today, however, light scattering and other optical techniques are increasingly finding application in the measurement of surface finish [1,2], so it is important to know how well both types of measurement agree. The primary motivations for the growing use of optical techniques are that such methods are noncontact, nondestructive, area-averaging, and potentially very rapid and accurate. The noncontact aspect is important, for example, when the surface to be measured is easily damaged.

In surface-finish studies which compare optical techniques to mechanical techniques, the parameter of interest is often the root-mean-square (rms) surface roughness, R_q [3]. In contrast, the emphasis in the present work is on a different parameter, namely the rms surface slope, Δ_q [3]. The angular spread of light scattered from a rough machined surface, Γ, has been shown theoretically to be linearly related to Δ_q [4]. The experiments reported here were undertaken primarily to test this theoretical relationship between Γ and Δ_q for three types of machined surfaces having 1-D roughness (i.e., surfaces with lay): sinusoidal, hand-lapped, and ground. A secondary objective of the work was to study the sensitivity of the optical measurements to variations in the incidence angle and the angular resolution (this was done for the sinusoidal and hand-lapped specimens only). Each of the specimens was measured with both a diamond-stylus instrument and one optical probe, either the NIST Detector Array for Laser Light Angular Scattering (DALLAS) instrument (for the sinusoidal and hand-lapped surfaces) or a Rodenstock RM 400 [5] optical surface-roughness probe (for the ground surfaces).

Sinusoidal and Hand-lapped Surfaces

Fifteen 1-D roughness specimens were studied using a range of incidence angles and angular resolutions in the DALLAS apparatus. Three of the specimens were made of brass, another three were made of nickel, and the remaining nine were made of stainless steel. The brass and nickel specimens had diamond-turned surfaces with sinusoidal amplitude profiles, and the stainless steel specimens had hand-lapped, random-roughness surfaces with a well-defined lay. The R_q's for these specimens ranged from $\approx$0.07 to $\approx$3.3 μm.

Mechanical Stylus Measurements A commercial stylus instrument was used to measure Δ_q for all fifteen roughness specimens, with Δ_q defined as [1,3]

$$\Delta_q = \sqrt{[(1/N)\textstyle\sum_j [(z_{i+1} - z_i)/\tau_o]^2]} \qquad (1)$$

where N is the number of points in the stylus trace, τ_o is the sampling interval, and z_i is the i^{th} value of the trace height.

DALLAS Optical Measurements The DALLAS light-scattering instrument is described in detail elsewhere [6]. Briefly, a helium-neon laser beam is incident onto the rough surface, and the scattered light is collected by a semi-circular yoke of lenses/detectors spaced at 2° intervals (the yoke rotates about the X axis). The light-scattering patterns are collected by a desk-top computer as a series of photodiode voltages as a function of angle

Two different experiments were conducted using DALLAS. In the first experiment, the sensitivity of the scattering patterns to changes in the incidence angle, θ_i, was studied. To this end, θ_i was set to +30°, 0°, and -30° while the DALLAS detector yoke was tipped at a small angle, ϕ_s = -2°, with respect to the vertical (Z) axis. Only the brass and nickel sinusoida samples were measured in this experiment, with the lay of the specimens oriented along the Y axis (i.e., perpendicular to the rotation axis of the yoke). The result of this experiment was that all three patterns were almo identical in shape over a wide angular range surrounding the central peak. quantify the shapes of these patterns, a second moment of the intensity abo the specular beam can be defined as

$$\Gamma = \sqrt{[\Sigma_j [(\theta_j - \theta_s)]^2 I_j / I_{tot}]}$$

where $I_{tot} = \Sigma_j I_j$, θ_s is the weighted mean scattering angle = $\Sigma_j I_j \theta_j / I_{tot}$, and I_j is the scattered light intensity collected by the lens at angle θ_j. The summation in Eq. 2 ranges from j=1 to 87, since the total number of sampling points (lenses/detectors) along the DALLAS yoke is 87.

A second DALLAS experiment was done to determine the influence of angul resolution on the measurement of Γ. The same nickel and brass sinusoidal specimens were again used, but this time the surface lay was oriented paral to the yoke (i.e., along the X axis). With the incidence angle set to θ_i = 14°, the DALLAS yoke was rotated by means of a stepping motor in 1° increme over the range -86° ≤ ϕ_s ≤ +86°; in this manner, 173 angular distributions were measured with 1° angular resolution. The same procedure was repeated t with ϕ_s incremented in steps of 2°, 4°, and 8° to provide 87, 44, and 23 angular distributions, respectively. A similar experiment, for 2° steps onl was conducted with the nine hand-lapped stainless steel specimens. [Note: The second moment measured with 1° angular sampling is denoted Γ_1, and likewise for Γ_2, Γ_4, and Γ_8.]

Data Analysis For a given sinusoidal or hand-lapped roughness specimen, Γ_1 and Γ_2 were so close in value that an angular resolution (i.e., sampling interval) of only 2° should be adequate for most light-scattering measurements of rms surface slope. By comparison, both Γ_4 and Γ_8 were different enough from these Γ values to indicate that angular resolutions of 4° and 8° would be too coarse. This conclusion is consistent with the angul resolution of the Rodenstock RM 400 optical surface-roughness probe used on the ground roughness specimens (see below).

A linear equation was found to relate the mechanically measured rms surface slopes, Δ_q, to the optically measured Γ_1 and Γ_2 values. A "univ linear regression, obtained by combining the six sinusoidal data points wi the nine hand-lapped data points, resulted in a linear regression of the for

$$\Delta_q = 0.464\Gamma - 0.0068$$

is measured in radians. All 15 data points, together with the
e linear fit, are shown in Fig. 1. The linear relationship in Eq.
and the rms surface slope (Δ_q) is in agreement with the
predictions of Rakels [4] and Brodmann, et al. [4].

Ground Surfaces

Fifteen 1-D rough surfaces were also measured using the
lus instrument, but this time a commercial optical roughness
to get a measure of the light-scattering pattern. These
either ground steel surfaces or electro-plated nickel replicas
ces, with R_q's ranging from about 0.14 to 0.94 μm.

s **Measurements** Stylus measurements of Δ_q were made using a
h roughness specimen was measured at 0.1 μm, 0.2 μm, and
ing.

Measurements For the ground surfaces, a commercial
enstock RM 400) was used to measure a parameter related to
c instrument has been described in detail elsewhere [7]. In
ssion from an LED is focussed onto the rough surface at
ncidence, and the angular spread of the scattered
linear diode detector array gives a parameter called S_N:

$$S_N = \sum_j (\theta_j - \bar{\theta}_j)^2 (I_j / I_o) \qquad (4)$$

tion constant, θ_j is the j^{th} scattering angle, $\bar{\theta}_j$ is the
I_j is the j^{th} scattering intensity, and $I_o = \sum_j I_j$. The
o 20 (i.e., there are 20 photodiodes in the Rodenstock
S_N is equivalent to r^2, except that S_N is measured over
of ±15° in the Rodenstock instrument (compared to ±86°

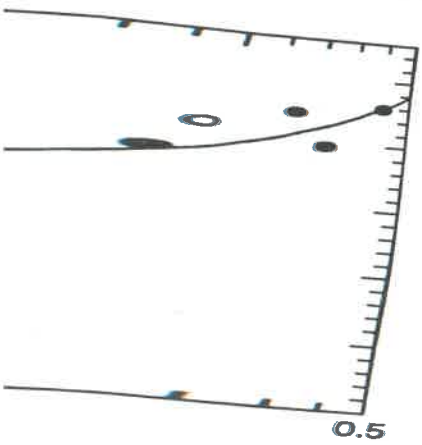

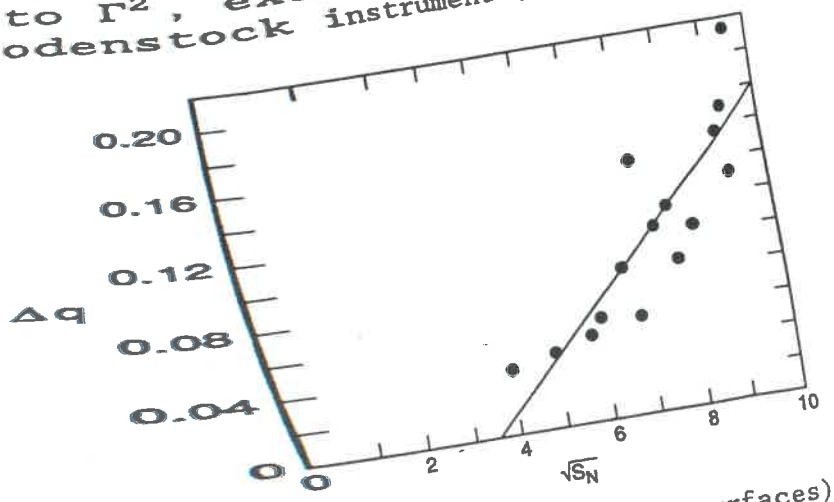

Fig. 2 Δ_q vs. $\sqrt{S_N}$ (ground surfaces)

The measurements on ground surfaces are plotted
g. 8. is a least-square linear fit to the data
near regression is:

$$\Delta_q = 0.0125 \sqrt{S_N} - 0.0125 \qquad (5)$$

Note that this line does not pass through the origin; this is due to the instrumental broadening in the Rodenstock optical probe. Because of this broadening, the minimum value of S_N for a perfectly smooth surface is 5, rather than 0. As a result, the line in Fig. 2 should pass through ($\sqrt{5}$,0). However, because of experimental uncertainty, the least-square fit passes instead through (3.5,0). In addition, the Rodenstock instrument has an upper limit on S_N of 99.9, which also affects the linearity of the instrument for large values of Δ_q.

Conclusion

For machined rough surfaces with lay, there was a definite relationship between the mechanical stylus values for Δ_q and the optical parameters which characterized the angular width of the light-scattering patterns (either Γ or S_N). In the case of the sinusoidal and hand-lapped specimens, there was a clear linearity between Δ_q and Γ, independent of the sample material (nickel, brass, or stainless steel). For the ground surfaces, however, the linear fit between the stylus and the optical measurements was not as good. One conclusion to be reached from these results is that Γ and S_N are both valid measures of rms surface slope, at least for the types of machined rough surfaces studied here. In addition, the DALLAS measurements indicated that measurements of Γ are surprisingly independent of both the incidence angle (up to ±30° and possibly more) and the angular resolution (up to 2°). The significance of the former result is that a measurement of rms surface slope is not appreciably affected by choice of the incidence angle. This is important for on-line measurements of surface finish because it implies less stringent optical alignment requirements without significantly sacrificing measurement precision.

References

[1] See for example: J. M. Bennett and L. Mattsson, Introduction to Surface Roughness and Scattering (OSA, Washington, DC, 1989).

[2] T. V. Vorburger and E. C. Teague, "Optical Techniques for On-Line Measurement of Surface Topography," **Prec. Engr. 3**, 61 (1981).

[3] ASME/ANSI B46.1-1985, Surface Texture (American Society of Mechanical Engineers, New York, 1985).

[4] J. H. Rakels, "Recognized Surface Finish Parameters Obtained from Diffraction Patterns of Rough Surfaces," in Surface Measurement and Characterization, SPIE vol. 1009, 119 (1988); R. Brodmann, M. Allgauer, "Comparison of Light Scattering from Rough Surfaces with Optical and Mechanical Profilometry," **SPIE 1009** 111-118 (1988).

[5] Certain commercial instruments are identified in this extended abstract in order to adequately specify the experimental procedure. Such identification does not imply recommendation or endorsement by the National Institute of Standards and Technology, nor does it imply that the equipment identified is necessarily the best available for the purpose.

[6] T. V. Vorburger, E. C. Teague, F. E. Scire, M. J. McLay, and D. E. Gilsinn, "Surface Roughness Studies with DALLAS - Detector Array for Laser Light Angular Scattering," **J. Res. NBS 89**, 3 (1984).

[7] R. Brodmann, D. Gerstorfer, and G. Thurn, "Optical Roughness Measuring Instrument for Fine-Machined Surfaces," **Opt. Engr. 24**, 408 (1985).

ULTRA PRECISION STYLUS PROFILOMETRY FOR LARGE OPTICAL COMPONENTS

P.B. Leadbeater, W.J. Wills-Moren, P.A. McKeown
Cranfield Precision Engineering Ltd.
Cranfield Institute of Technology
Cranfield, Bedford, MK43 OAL, UK

Whilst interferometric testing has always been an integral part of the fabrication of high precision large optical components stylus profilometry can provide an additional method of determining the figure accuracy. This method has the advantages of speed, ruggedness, adaptability and may be carried out at various stages in the manufacturing process, e.g. before interferometry is possible, in-situ on the machine etc.

The paper describes a number of examples of instruments and important design principles are covered together with some of the problems which can be experienced. Both stand-alone systems and those which operate in-situ to the machining process are discussed.

For the purposes of the paper a profilometer is an instrument which causes a stylus to be translated within an appropriate coordinate frame of reference in such a manner that the stylus is maintained in contact with the workpiece enabling its coordinates to be recorded.

Design features incorporated in a profilometer system are typically the probe, measuring system, reference system and instrument structure.

For the examples covered an air bearing probe has been included in a variety of forms fitted with a retroreflector, plain mirror, an LVDT or even a combination of these depending on the application. A typical example of such a probe suitable for horizontal use is shown in Fig. 1.

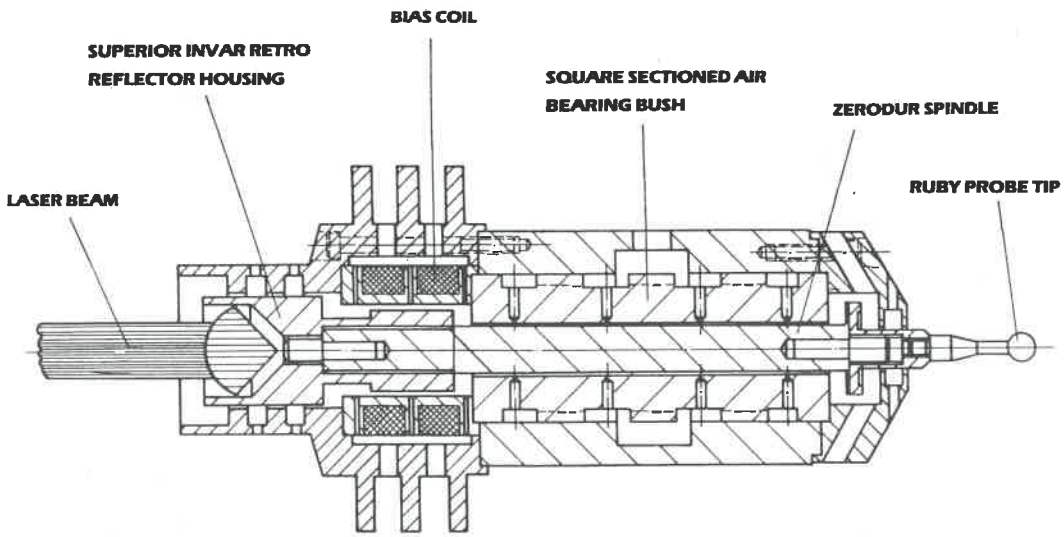

Fig. 1

It is important that the mass of the moving parts should be as low as possible and this is particularly necessary for applications where the axis of the probe is vertical as a carefully designed counter balancing system must be added to achieve contact forces down to 50 mg.

When the sag of the optic is small the measurement can usually be accommodated within the probe stroke. For larger deviations however a probe with an additional LVDT may be employed (Fig. 2d), which is operated in a null seeking mode causing a precision carriage on which the probe is mounted to be servo positioned such that the probe is kept nominally at the centre of its travel. Typical probe systems are shown diagrammatically in Fig. 2a, b, c and d.

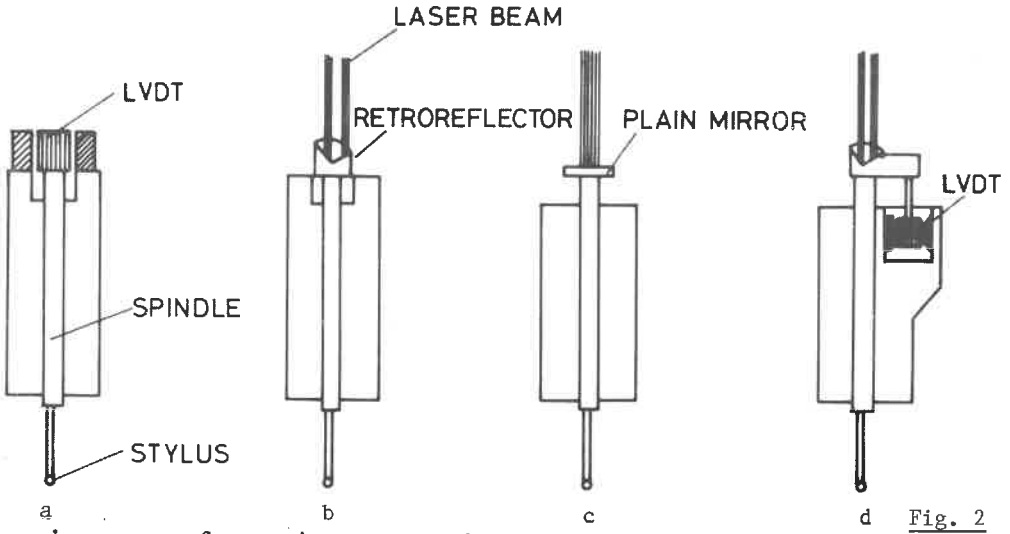

Fig. 2

The measuring system for equipment required to achieve the highest order of accuracy is generally based on a laser transducer system, in many cases incorporating a wavelength tracker. The system will then monitor and adjust for variations in the environment whilst components are undergoing inspection. This is of particular importance where the cycle time for determining a complete surface profile is lengthy. Compliance wherever possible with the Abbe Principle should be achieved in the design. An error budget to determine the effect of all contributory factors should be produced at the design stage.

In order that the measuring system may achieve its maximum potential a reliable coordinate reference system is required. This could take several forms depending on the parameters the instrument is designed to determine. Diameters for example require a calibrated Zerodur or invar diameter reference gauge from which to base the starting point for measurement. A profile reference may well take the form of a reflective Zerodur straight edge whilst more complex equipment would include two or even three reflective straight edges to form a metrology frame as a basis of measurement as it is unlikely that direct use of guideways will lead to the accuracy required.

Important factors in the design of the support structure for any reference are that it is supported kinematically in a manner which will minimise deflection, any deflections are always constant, i.e. there is no change in attitude of the reference, the reference and its support structure sees no variation in loading and that whenever possible the reference is calibrated in the attitude in which it will be finally mounted. Should it not be possible to calibrate as above, predicted variations may be added to the calibration results and the result used as the data for the reference surface. An example of this type of support is shown diagrammatically in Fig. 3 where three straight edges are related together to form a metrology frame.

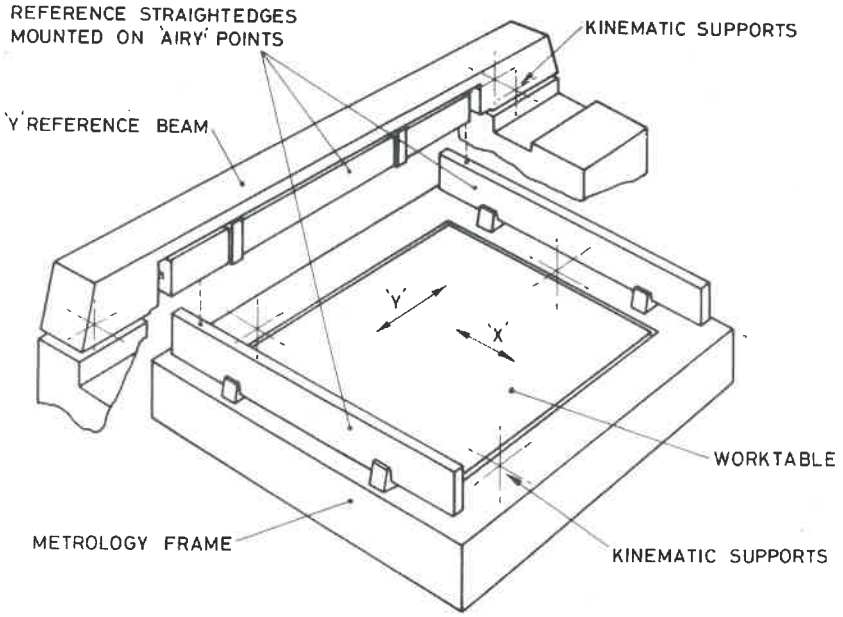

Fig. 3

One profilometer system designed and supplied by Cranfield Precision Engineering Ltd. may be seen schematically in Fig. 4. This equipment has 1 metre 'X' capacity and may be linked to a high precision linear air bearing motion in the 'Y' direction or a 1 metre air bearing rotary table and in operation performs linear traces across the optic.

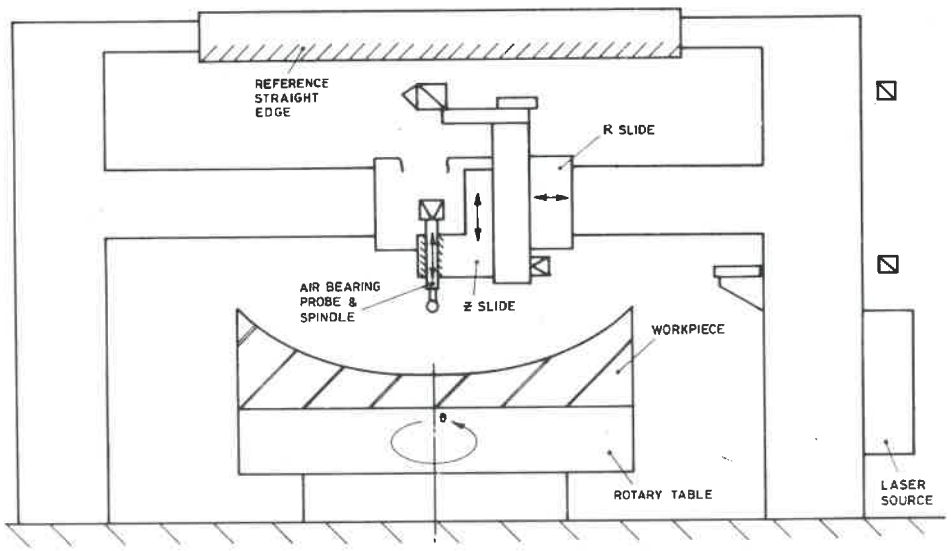

SCHEMATIC OF R Z θ PROFILOMETER

Fig. 4

Another system supplied to Hughes, Danbury Optical Systems Inc. is shown in Fig. 5 and will be used to perform high precision metrology on the inner surfaces of the optics being fabricated in Zerodur for the AXAF telescope. The instrument is predicted to be able to determine the absolute inner diameter measurements, including all alignment and environmental effects to better than $\pm$ 2.5 μm and circularity to $\pm$ 0.02 μm RMS after averaging.

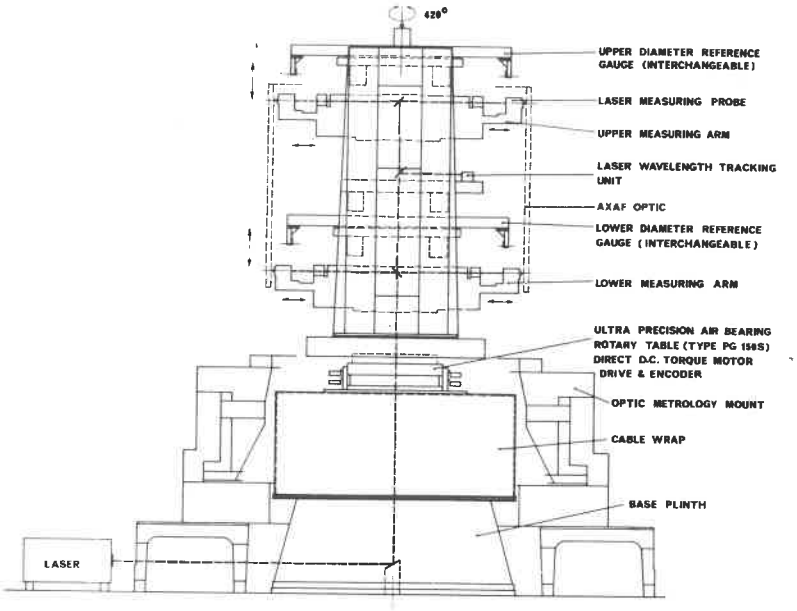

CIRCULARITY & INTERNAL DIAMETER INSTRUMENT

Fig. 5

A further example is the in-situ metrology system for a Large Off Axis Grinding Machine, 2.5 m x 2.5 m x 0.61 m capacity. This machine installed at Eastman Kodak Company, Rochester, N.Y., incorporates all the previously described design considerations and additionally uses error compensation extensively in order to map the surface of optical components whilst in production on the machine. Fig. 6 shows diagrammatically the laser transducer design for monitoring all machine movements.

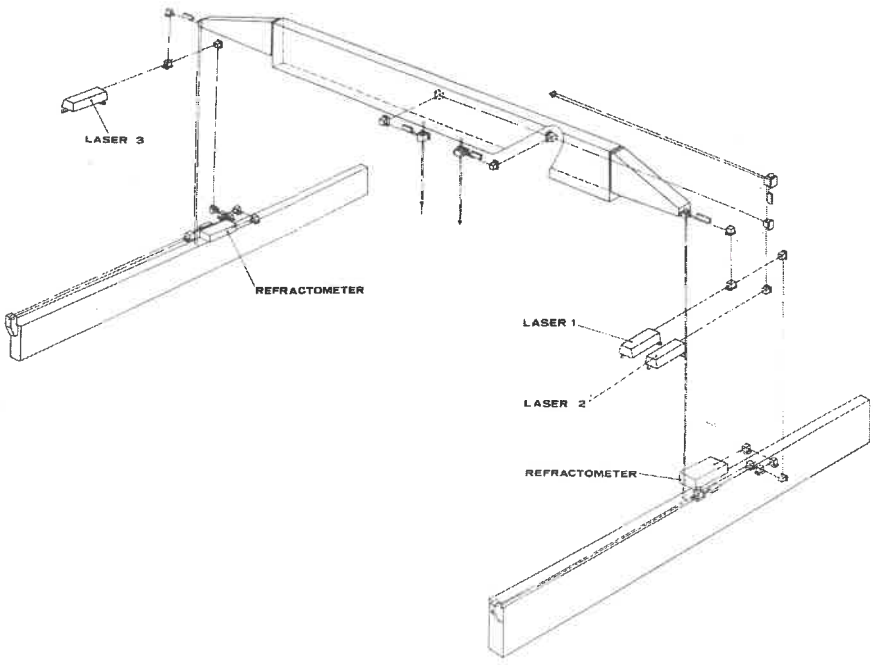

Fig. 6

The examples given and discussed in detail in the paper clearly show that reliable profilometry of large optical surfaces may be readily achieved using contact stylus techniques providing the correct design procedures for the equipment are followed.

OVERVIEW OF THE ADVANCED X-RAY ASTROPHYSICS FACILITY (AXAF)

Dr. Leon Van Speybroeck
Smithsonian Astrophysical Observatory
Cambridge, MA

The AXAF project has been underway for over a decade. It is now scheduled for shuttle launch in 1997. The purpose of AXAF is to conduct detailed measurements in the astrophysically important energy range 0.1 - 10 keV. To collect these high energy X-ray photons a 12 element nested Zerodur mirror with a maximum diameter of 1.2 meters and inner grazing incidence angle of 0.5 degrees or less is required. The resolution must be 0.5 arc seconds or better.

TRW has been given the system responsibility. Hughes Danbury Optical Systems will build the 12 mirror elements. Eastman Kodak will assemble and align the mirrors in a special structure. The mirror will then be tested in a long evacuated X-ray test facility at Huntsville.

The tolerances that are necessary to achieve the 0.5 arc sec resolution constitute a major challenge to the precision engineering community. For example, the differences in circularity over the 36-inch length of each element (delta, delta R) must be less than 5 microinches RMS. The tolerance on longitudinal sag is one microinch. Surface finish requirements are on the order of 5 Angstroms RMS. These tolerances must be accomplished on 1.2 meter diameter conical elements with wall thicknesses of less than an inch.

SCANNING TUNNELING MICROSCOPY BIT-MAKING FOR USE IN HIGH DENSITY MEMORY CHIP APPLICATIONS

Jimmie A. Miller and Robert J. Hocken
Mechanical Engineering and Engineering Science
University of North Carolina at Charlotte
Charlotte, NC 28223

With the demand to increase the memory density on computer chips, new techniques must be developed to overcome the limitations of present technology. We used a scanning tunneling microscope (STM) to modify the surface of highly oriented pyrolytic graphite (HOPG), producing 2-3 nm hole-hill combinations which readily lend themselves to be used as write-once memory bits.

STMs operate by moving an atomically sharp conducting tip close enough to a conducting sample to allow a tunneling current to flow (about one nanometer sample tip separation). An applied potential between the tip and sample produces a current which is monitored for feedback height control of the tip. The current between tip and sample is on the order of nanoamps. With low feedback gain the tip keeps a constant height position and the changing current is recorded. With a high feedback gain the tip tracks a constant current position above the sample and the height is monitored. The tip is swept in a raster fashion to produce a two dimensional height or current topograph of the surface. We operated our STM in the constant height mode of operation.

Holes were maufactured by superimposing a voltage pulse on an existing sample bias. The parameters of the voltage pulse and STM were varied creating damaged regions in the HOPG varying in size. Fig. 1 illustrates the range of possibilities for hole sizes. Images of an HOPG surface with holes 150 nm, 20 nm, 1 nm in size, and one image showing one atom displaced suggest that modification of surfaces can be achieved down to atomic dimensions.

The size of the manufactured holes were dependent on initial bias, initial current, pulse amplitude, pulse frequency, and pulse shape. Varying the initial bias while keeping the pulse amplitude, period and shape constant showed that there were bias regions where there was no surface damage with some biases producing damaged areas up to 150 nm in diameter. Varying the scanning current from 0.5 nA to 8 nA changed the size of the damaged region from 20-30 nm to 60-80 nm. Varying the pulse shape (square, triangular, sinusoidal) and duration (0.1 - 10 microseconds) had an effect

on surface modification. The square pulses produced surface modification at pulse times from 0.1 to 1000 microseconds with similar results at all pulse times below 10 microseconds. The triangular and sinusoidal pulses required pulse times greater than 10 microseconds to have an affect on the surface. Varying the pulse amplitude showed that there was a threshold of at least 2.5 volts for surface modification to occur. Varying the amplitude from 2.75 - 8.0 volts produced damaged regions from 20 - 200 nm.

A single pulse would often create more than one hole. The STM image shown in Fig. 2(a) reveals two holes manufactured by the same voltage pulse. The STM image in Fig. 2(b) shows the same effect on a smaller scale. A 0.05 microsecond -3.50 volt square pulse superimposed on a -0.7 volt sample tip potential produced the 1 nm hole and hill combination and also a 'v' shaped crystallographic appearing defect on the surface of the HOPG [Fig. 2(b)]. In general the most repeatable results were obtained with a 1 microsecond triangular pulse superimposed on a -1.4 volt bias. By repeated pulsing of the voltage we were able to manufacture a 40 nm 'L' shaped structure (10 nm line thickness) out of 2-3 nm hole-hill combinations produced by the pulses. The amplitude of the pulse had to be increased during the modification to continue the hole-hill making process. An STM image of the 'L' shaped structure is shown in Fig. 3.

The ability to make hole-hill combinations within 5 nm of other hill-holes demonstrates the possibility of creating a high density write once read many memory. With 5 nm hole-hill structures acting as memory bits, one could place one gigabyte of information on a one square millimeter surface.

Future research will be geared toward using surfaces other than graphite, manufacturing an STM on a chip, using microelectronics compatible structures and materials, and highly accurate tracking and positioning of the STM tip.

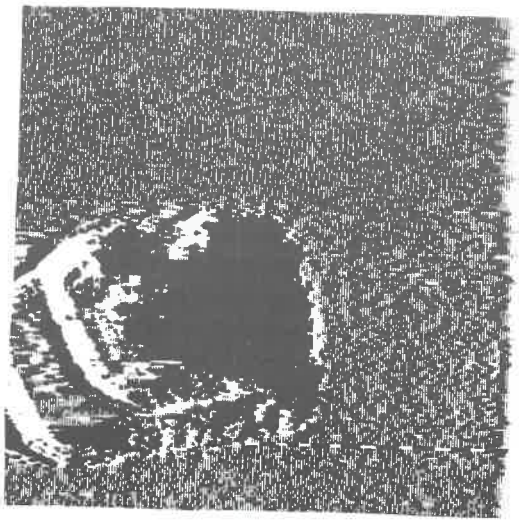

(a)

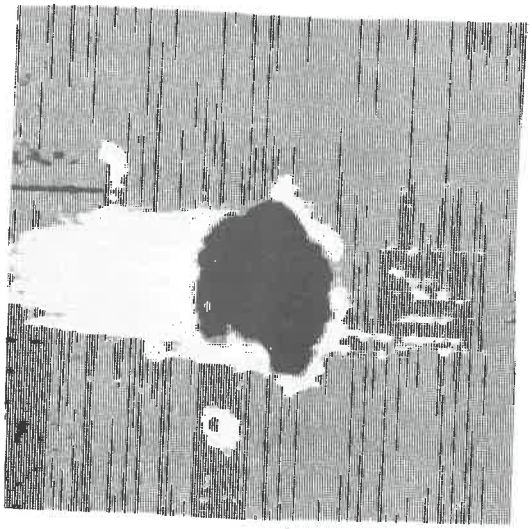

(b)

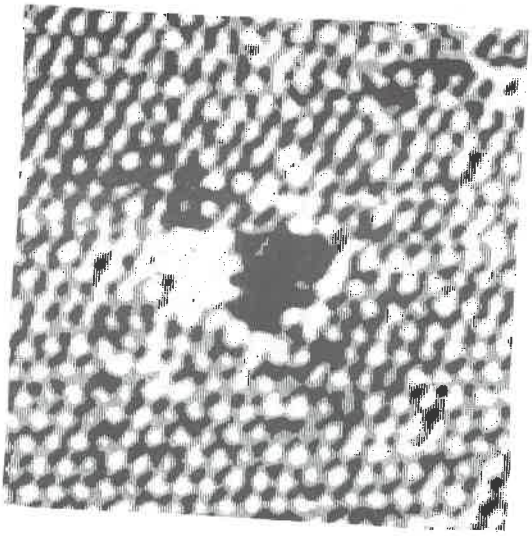

(c)

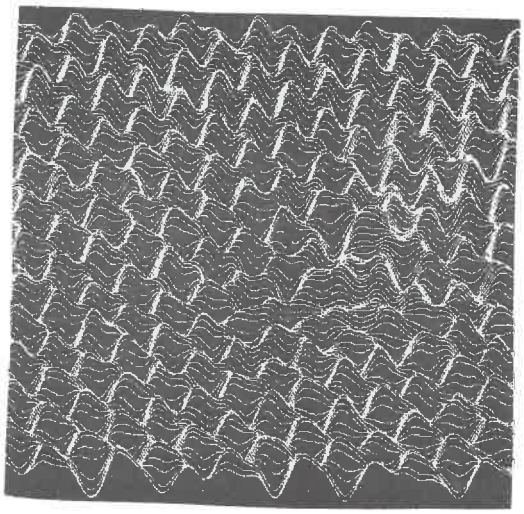

(d)

FIG. 1. Scanning tunneling microscopy images of holes created by electrical pulses. In (a), a 300×300-nm image reveals a 150 nm hole. In (b), an 80×80-nm scan reveals a 20 nm hole. In (c), a 5×5-nm scan reveals a 1 nm hole. In (d), a sideview lineplot of a 3×3-nm scan reveals an atom that has been displaced.

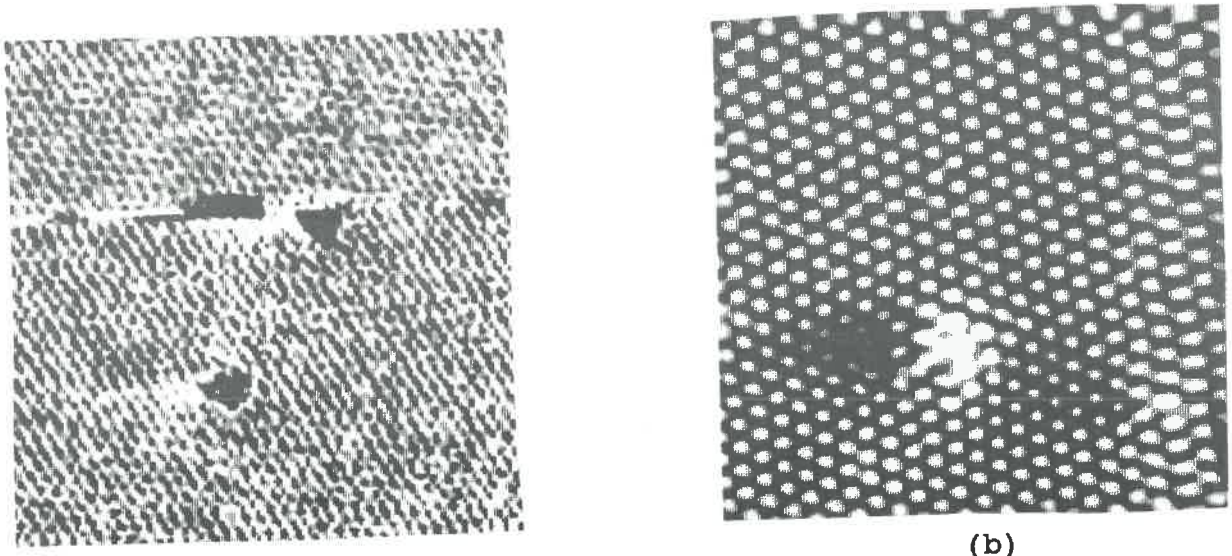

(a) (b)

FIG. 2. STM images demonstrating multiple hole creation. Dark areas are holes. In (a), an angle view image of a 15×15-nm scan reveals a pair of 2 nm holes manufactured by the same voltage pulse. In (b), a 5×5-nm scan reveals a 1 nm hole with a hill beside it, and an atomic scale defect 2 nm away from it. The hill-hole pair and the defect were created with the same voltage pulse.

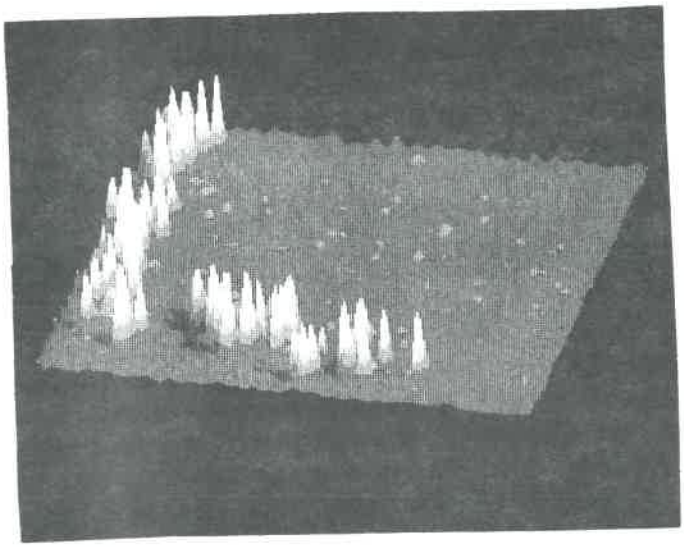

FIG. 3. A 60×60-nm STM scan reveals a 40 nm 'L' shaped structure. The structure was manufactured by multiple voltage pulses. The STM tip was moved after each pulse to achieve the structure. The hills (light areas) are about 7 Å high.

Cutting and Surface Planing of Diamond Film by YAG Laser

Shinichi Tezuka, Naoto Ohtake and Masanori Yoshikawa
Tokyo Institute of Technology
2-12-1, O-okayama, Meguro-ku, Tokyo 152, Japan

1. Introduction

Diamond films have been synthesized by CVD method, and growth rate gained 0.9mm thickness per hour. Application of diamond films to cutting tool, heat sink, electronic device, and so on are anticipated, so it is necessary to process the diamond films precisely. By conventional machining method, however, it is very difficult to process diamond films because of its hardness, thinness, large thermal conductivity, high optical transparency, large surface roughness, and low electric conductivity.

In this report, we have applied YAG laser for the processing of such unique material. First, we synthesized two kinds of diamond films by arc discharge plasma jet CVD, and investigated the phenomena of diamond films irradiated by YAG laser. Secondly, we carried out cutting and surface planing of diamond films by laser. Thirdly, the application of laser processed diamond film to a cutting tool was examined.

2. Experimental

Two type diamond films used in the experiment were synthesized by arc discharge plasma jet CVD method(1). Diamond deposition conditions are listed in **Table 1.** The diamond films synthesized at methane concentration of 12% consist of globular diamond particles. As a result of Raman spectrum analysis and X-ray diffraction, these diamond films include large amount of amorphous carbon. SEM observation of the diamond film is shown in **Fig.1(a).** On the other hand, the diamond films synthesized at methane concentration 4% have automorphic face and as a result of the same analysis led us that these diamond films have good crystallinity without amorphous carbon. SEM observation of the diamond film is shown in **Fig.1(b).**

Laser irradiation conditions are listed in **Table 2.** The properties of the YAG laser used in experiment are maximum 12W in average power at CW beam and maximum 23kW in peak power by the pulse beam using Q switch. After the laser beam was oscillated at TEMoo mode, the beam is focused by convex lens, the laser beam is irradiated on to the diamond surface. The diamond film is fixed on X-Y stage and can be traversed. As the diamond films are put in the chamber, irradiation atmosphere and gas pressure can be controlled.

3. Results and Discussions

3.1 Laser Cutting and Etching

Since a diamond is the metastable material in room temperature, and atmospheric pressure, the diamond is oxidized at 660°C in O_2 gas, and is transformed into graphite at 1660°C in inert gas. Heated graphite and amorphous carbon are oxidized more easily in comparison to diamonds. Thus, when the diamond films, which include amorphous carbon and defects, are

irradiated under the low energy density beam, the amorphous carbon portions and defect portions are preferentially oxidized and etched.

Figure 2 shows the diamonds etched by laser. Diamond film surface synthesized at methane concentration of 12% turned the globular particles into pyramidal diamonds, which is shown in **Fig.2(a)**. **Figure 2(b)** shows the diamond film surface synthesized at methane concentration of 4% after etched. The grain boundaries and defect portions are etched by laser irradiation. Continuing the laser irradiation, exposed diamond particles were also oxidized and vaporized but cutting groove or drilling holes could not formed.

On the other hand, by the laser irradiation under the high energy density, a groove or hole is formed, and cutting can be conducted. **Figure 3** shows the cross section of a diamond film cut by YAG laser. No cracks are visible, it is recognized that clear cross section is obtained. When diamond films were cut in air or inert gas, it is observed that graphite was deposited around the groove. According to the irradiation experiment under various O_2 gas pressure, the graphite deposition was not observed under the condition of more than 700 torr of O_2 gas pressure. Moreover, the higher peak power applies, the larger aspect ratio of cutting groove obtains. As for the laser cutting at 1kHz pulse repetition of Q switch, the groove width is constantly about 30 μm not depending on the average power, however, the groove depth become larger by increasing the average power or laser scanning times. We obtained the same results about cutting of a natural diamond grit(2).

3.2 Surface Planing

When diamond films are processed by vertical incident laser beam, the cutting cross section inclines to 7-15° for the vertical line. By controlling the incident angle of the laser beam, optional inclined face can be gained. So by irradiating the laser beam parallel to diamond surface, it is possible to plane the diamond surface. The procedure of surface planing is as follows: first, the laser beam parallel to diamond films surface is focused at the point of 10 μm thickness from the top of the diamond film surface, and diamond film is traversed; secondly, the focus point is moved forward, and diamond film is traversed; thirdly, above process is repeated until whole surface is planed, and the focus point of laser beam is removed at the point of 30 μm thickness from the top of the new surface; lastly, these procedure is repeated. **Figure 4** shows the diamond film which is planed by the YAG laser. The roughness of the diamond film planed by laser is 3 μm Rmax.

3.3 Application of Diamond Films

Figure 5 shows the diamond chip cut and planed by laser. It took 7 minutes to process 3 mm^W x 2 mm^L x 0.4 mm^t size. **Figure 6** shows the diamond cutting tool. The flank face is the planing surface and the rake face is the cutting cross section. We have carried out turning experiment of aluminum alloy with this tool. The result indicate that this tool can be used as a cutting tool.

References

1. N.Ohtake and M.Yoshikawa,"Diamond Film Preparation by Arc Discharge Plasma Jet Chemical Vapor Deposition in the Methane Atmosphere", J. Electrochemical Soc., **137**,2(1990), pp.717-722.
2. S.Tezuka,H.Tokura and M.Yoshikawa,"Cutting of Diamond Grit with YAG Laser", Proc. 1st.Int.Conf. on New Diamond Sci.& Technol.,Tokyo,Japan(1988).,

Table 1 Diamond deposition conditions

Gas flow rate	
H_2	1.5 SLM
CH_4	0.06, 0.18 SLM
Ar	7.5 SLM
CH_4/H_2	4 %, 12 %
Substrate	Molybdenum
Substrate temp.	1000°C

Table 2 Laser processing conditions

YAG laser system	
Mode	TEMoo
Average power	0-12 W
Pulse repetition	1-99 kHz
Focus length	50 mm
Traverse velocity	0-10 mm/s
Atmospheres	Ar, Air, O_2 Vacuum

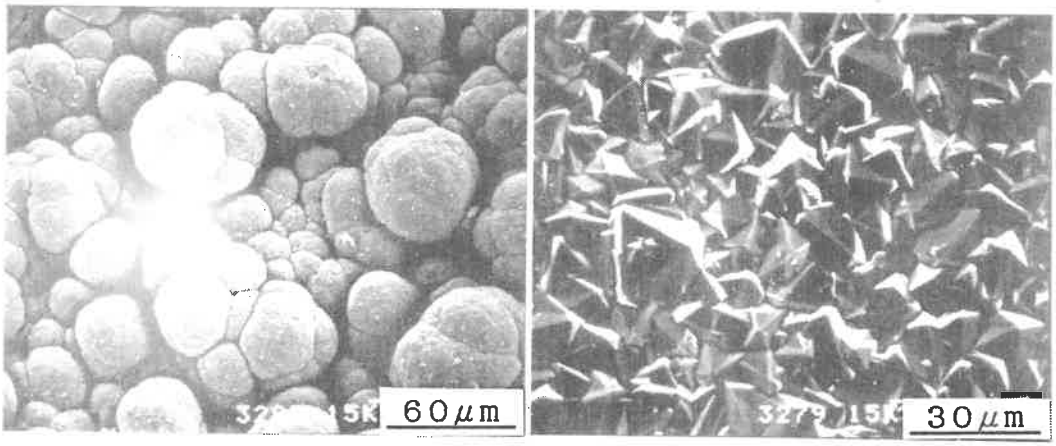

(a) (b)

Fig.1 SEM photographs of diamond films deposited at methane concentration of 12%(a), 4%(b)

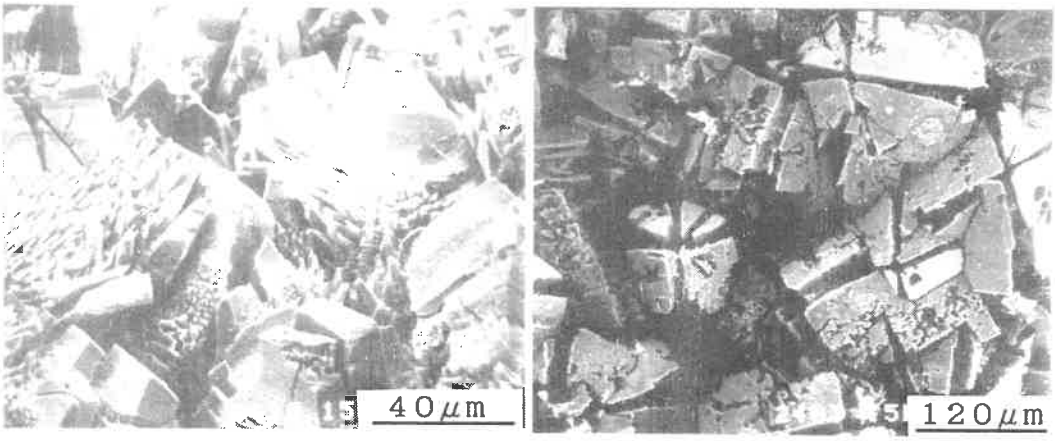

(a)
Average power 4W
Pulse repetition 70kHz
Irradiation time 10sec
Atmospheric gas O_2

(b)
Average power 3W
Pulse repetition 30kHz
Irradiation time 10sec
Atmospheric gas O_2

Fig.2 SEM photographs of diamond films after laser irradiation

economies of scale, improvements in fabrication technology, and discussions with several finishing vendors on what we can expect in the future.

The important initial step is to determine baseline costs for comparing with all other estimates; these are determined from vendor estimates. Outside of production scale-ups and facilitization issues, these estimates employ only proven, existing technology. Moreover, our cost analysis must also scale to the costs for building the present Nova system since some of these technologies were used on that system.

The following is a list of optical finishing technologies under consideration. The list is not all-inclusive in that incremental changes in baseline technologies are also being considered. Improvements in handling procedures and metrology may also demonstrate significant cost leverage, but are not included here.

Fixed-abrasive fine diamond grinding: use of a fixed-abrasive wheel for the final grinding step

Micro-grinding: fixed-abrasive grinding in which subsurface damage is greatly reduced, but where the removal mechanism remains in the fracture mode

Ductile grinding: fixed-abrasive grinding with minimal subsurface damage and a non-fracture removal mechanism

High-speed double-sided polishing: double-sided polishing with significantly higher speeds and pressures than in pitch polishing; involves use of synthetic lap materials

Double-sided grinding: the double-sided version(s) of fixed-abrasive grinding, e.g. pellet grinding

Plasma-assisted chemical etching (PACE): glass surfaces figuring by traversing a well-defined footprint of a reactive chemical plasma over a surface to remove a prescribed contour of material

Ion beam figuring (IBF): surface figuring by traversing a well-defined beam of ions (non-reactive) over the surface to sputter away a prescribed contour of material.

Estimates are made for the R&D costs necessary to bring these new methods into production status in a 2-4 year period. In general, higher risk development programs reflect higher R&D costs.

From the alternate and baseline finishing techniques, we assemble modified fabrication processes that begin with a rough blank and produce a finished optic. These processes might becombinations of several new techniques, or they might involve a single substitution in the baseline process.

It is typically straightforward to estimate machine time and handling time for each step in the process. However, it is necessary to determine the conversion from machine time to manhours, which ultimately affects the cost of the optic. Although detailed cost estimates for each process can be done (at great expense) that incorporate the division of labor, number of shifts, supervision, etc., these details can mask the cost leverage issues associated with each technology.

An alternative approach to the detailed analysis is to assign a labor cost multiplier to the machine time associated with each operation. This multiplication factor is estimated from the anticipated number of people required for an operation, overhead rates, supervision, etc. Although this has more uncertainty in terms of absolute cost than a detailed estimate, the relative costs among different processes should be sufficiently informative to make cost leverage comparisons. Furthermore, changes in the assumptions about labor rates or operator skill levels are accommodated by simple changes in the multiplication factor.

The total recurring cost per part is determined by summing the process and handling costs. The lot cost is obtained by multiplying by the number of parts.

Facilitization costs are estimated for each process based on process throughput, existing industry capabilities, the number years in the production cycle, floorspace availability, etc.

The overall program cost is then determined by summing the lot cost, the R&D costs, and the facilitization cost (if necessary). Each process is ranked according to its total cost and then compared to the baseline. Those processes with the greatest cost leverage have the lowest cost.

Perhaps the largest source of uncertainty in this analysis is the assessment of risk. For example, if a given technique has been demonstrated on fused silica, but has failed on laser phosphate glass, then the risk associated with using this technique on amplifier disks is high; this would be evidenced by a high R&D cost, even if the recurring cost is potentially low.

From our preliminary analysis, we believe that significant cost leverage can be obtained by: 1) reducing the subsurface damage generated during the final grinding step; 2) employing high-speed polishing techniques; 3) improving the convergence rates during the final figuring operation (which minimizes the number of metrology cycles); and 4) minimizing handling time such as for part washing.

Table 1. Principal optics for the 18 beam, 2 MJ ICF laser.

Optic	Material	Size (cm)	Quantity
Amplifier disks	Nd: phosphate glass	30 x 60	3200
Lens segments	fused silica	30 x 30	1600
Mirrors	BK7; pyrex	35 x 30	1900
Windows, wedges	fused silica	30 x 30	1300
Polarizers	fused silica	60 x 30	320
Crystals	KDP; KD*P	32 x 32	1000

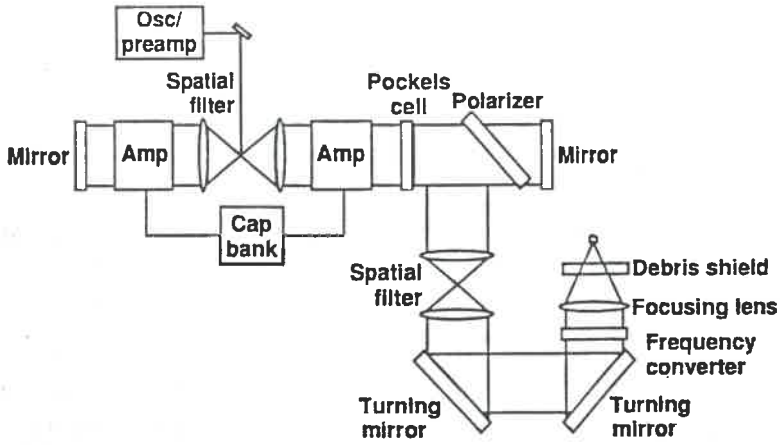

Figure 1. Schematic arrangement of components for one beamline of proposed ICF solid state laser.

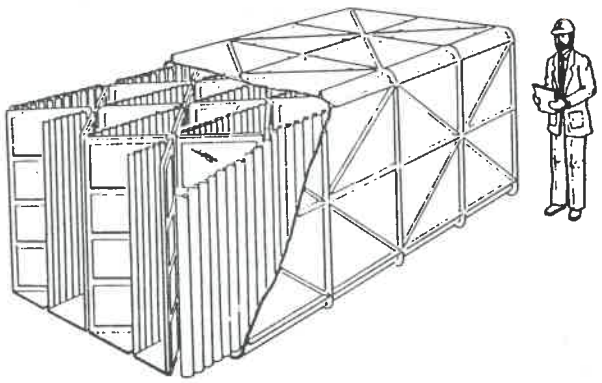

Figure 2. Multi-segment amplifier consisting of 4x4x11 plates of Nd:glass pumped by five banks of flashlamps.

A NANOMETER DIGITAL INTERFEROMETRIC CONTROL FOR A STOP START GRATING RULING ENGINE

Robert Wiley, Semyon Zheleznyak, Jeffrey Olson, Erwin Loewen, and John Hoose

Milton Roy Company, Analytical Products Division
820 Linden Avenue, Rochester, NEw York 14625

The University of Chicago ruling engine was designed by Albert Michelson and was constructed at the University of Chicago near the turn of the century (1910 - 1925). In 1947 the engine was obtained by Bausch and Lomb Inc. and rebuilt by Robert Wiley. For many years it has been successfully ruling gratings by purely mechanical means.

A precisely shaped diamond tool reciprocates continuously in a fixed plane above the grating carriage. The grating carriage is moved in a direction orthogonal to the direction of the diamond motion in discrete amounts determined by the mechanical gearing of the engine.

During the ruling stroke, the grating carriage remains motionless while the diamond is lowered so that it comes into contact with the grating blank as it passes over it, forming a triangular groove by burnishing in a thin metal layer. During the indexing (return) stroke, the diamond is raised and the grating carriage is advanced a fixed amount. The carriage must remain perfectly still during the ruling stroke.

The primary objective of the digital interferometric control system is to overcome the minor mechanical limitations on the engines ability to position precisely the grating carriage, better than can be achieved with the original correction cam. It was decided to keep the start-stop mode of operation, because it leads to low mechanical noise, given the unusual ability to remain stationary to one nanometer after the indexing. Positioning errors fall into three general categories: periodic errors , errors of run, and random errors.

Periodic errors, caused by cyclic imperfections in the engine's gear train, lead screw, and drive mechanism, cause "Rowland Ghosts" if the period is on the order of a few millimeters, or "Lyman Ghosts" if the error repeats every few grooves.

Errors of run are those errors that occur slowly over the entire ruling causing an inconsistency in the groove spacing which ultimately results in distortion of the diffracted wavefront. For example, a change of temperature during the ruling, left uncorrected, would produce an error of run due to lead screw expansion or contraction.

Random errors from any part of the translation mechanism give rise to inter-order scatter.

In order to retain the start-stop mode of operation, a digital interferometric servo control system is employed to measure precisely the grating carriage position during the ruling stroke, and correct for residual errors during the indexing stroke. As a result, the error on the last groove is corrected in indexing on the current groove. The implications of this will be discussed.

The Michelson engine servo control system consists of three primary elements:

1. Interferometer system
2. Control system
3. Mechanical system

The interferometer system's primary function is to measure precisely the incremental displacement of the grating blank, and transmit measurement data to the control system. The control system processes the measurement data, determines the correction, and sends the correction to the mechanical system. The mechanical system physically corrects the position of the grating blank. The interferometer system forms the feedback element in the servo system. The ZYGO Axiom 2/20 system consists of a dual frequency HeNe laser, linear interferometer, wavelength compensator (refractometer), and controller.

We show results of measurements made on gratings ruled with and without the interferometric control. We compare the level of "ghosts", inter-order stray light and diffracted wavefront quality. We also discuss some of the more subtle considerations involving 'resolution' and 'accuracy' of interferometric control systems which can lead to substandard performance.

It is an interesting characteristic of the ruling process that errors in the nanometer domain can be quite readily detected with simple optical tests.

MILTON ROY CHICAGO RULING ENGINE
SERVO CONTROL SYSTEM
CORRECTION CALCULATION

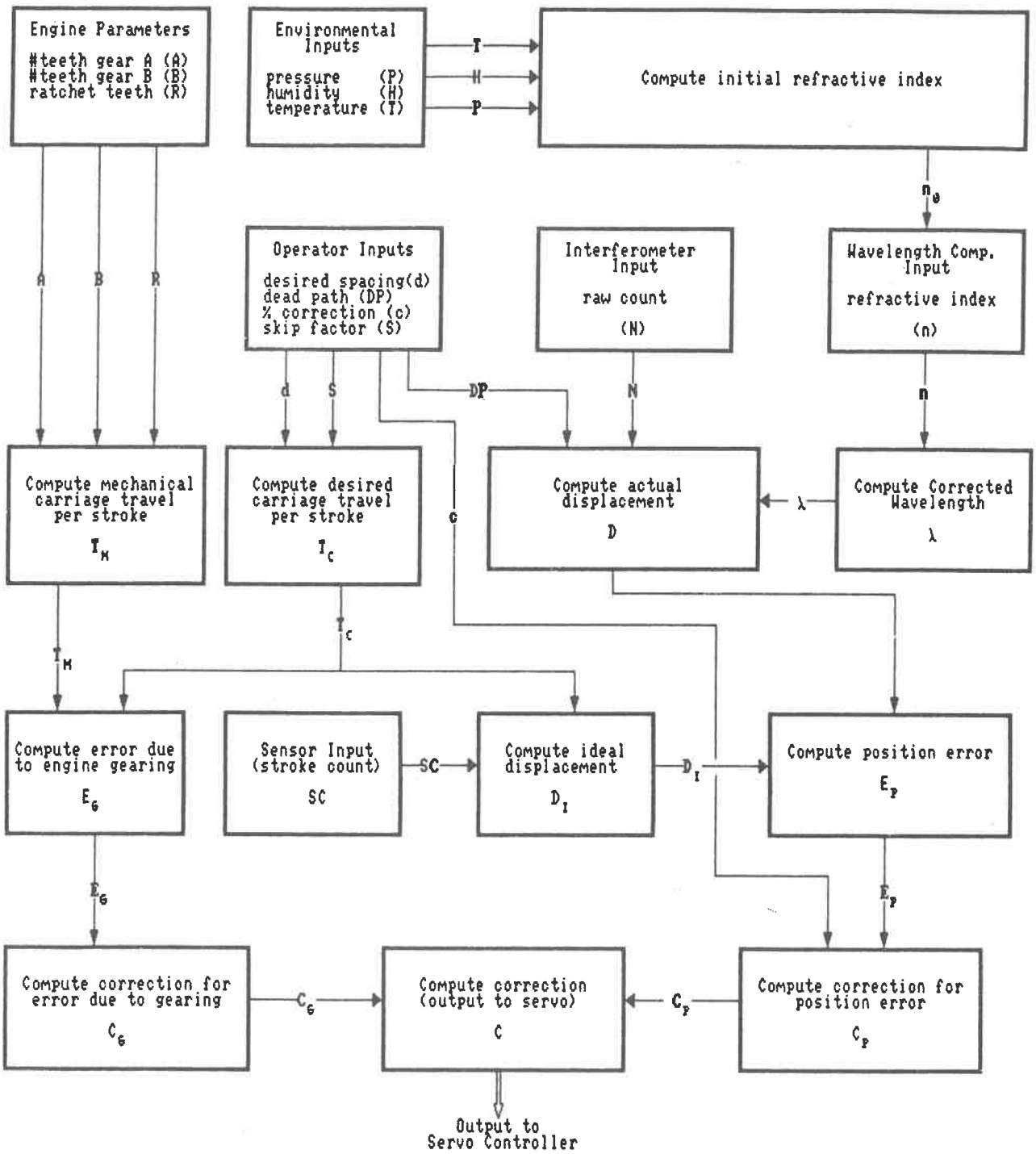

J. Olson
06-25-90

MILTON ROY CHICAGO RULING ENGINE
SERVO CONTROL SYSTEM
FUNCTIONAL BLOCK DIAGRAM

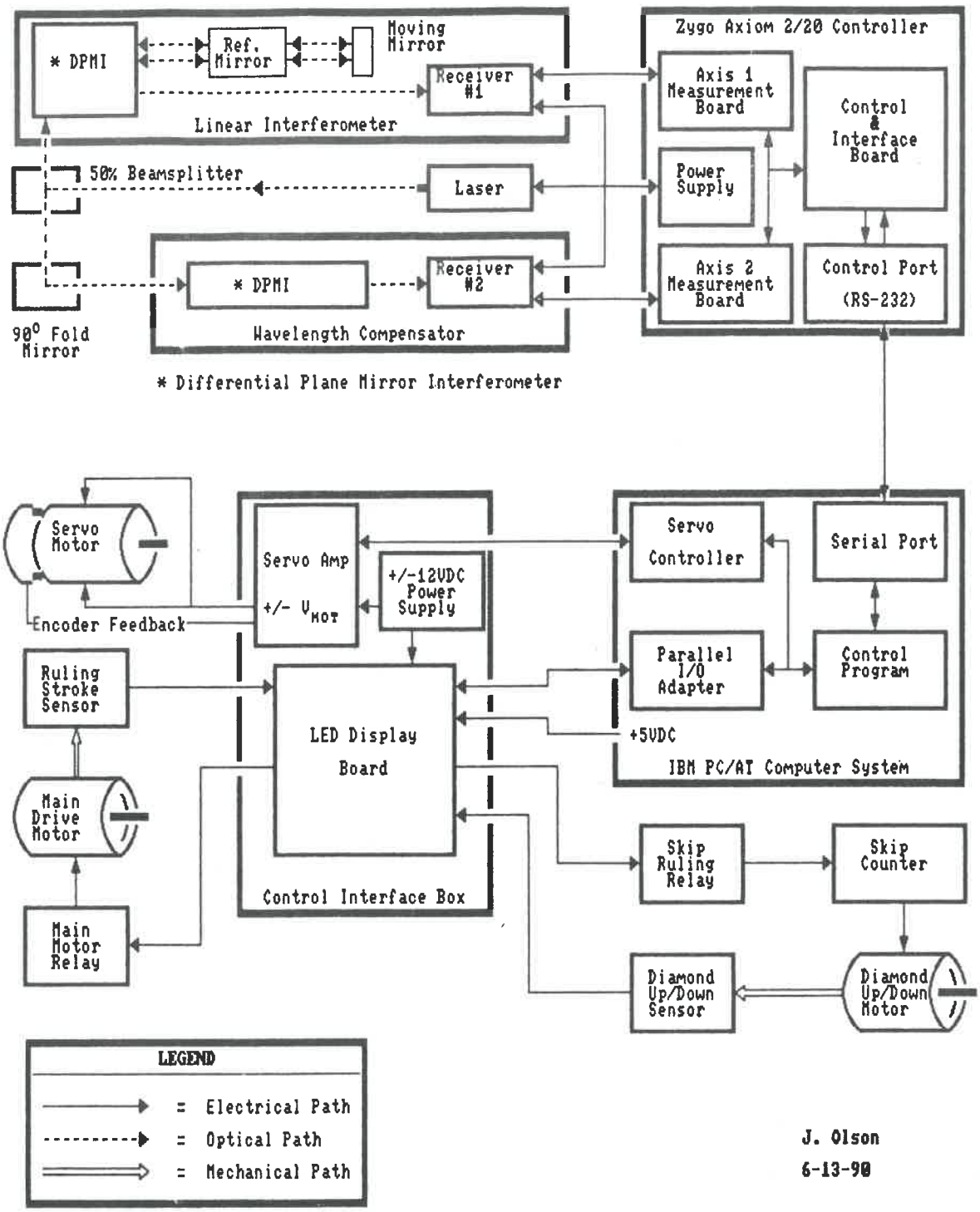

J. Olson
6-13-90

Extension of the 1-D Critical Depth of Cut Model for Brittle Materials to 3-D Contour Grinding

Steven C. Fawcett
Thomas A. Dow

Precision Engineering Center
North Carolina State University
Raleigh, NC 27695

The majority of precision refractive optical components are fabricated from brittle glasses. The fabrication usually involves grinding the desired contour of the component followed by polishing to remove the undesirable surface features. These surface features are remnants of the brittle fractures that occur in the grinding operation. Previous studies at the Precision Engineering Center have demonstrated the feasibility of achieving ductile material removal (**Ductile Mode Grinding**) on samples of brittle materials. Experimental measurements and analytical models have demonstrated the relationship between the depth of cut and the damage to the surface [1]. The extrapolation of such one dimensional critical depth information to three dimensions is being developed through computer simulations of the grinding process and the resulting chip geometry.

MODEL DEVELOPMENT

To accurately determine the geometry of the chip resulting from a contour grinding operation, a graphical model was developed [2]. This model predicts the surface finish, calculates the theoretical roughness, and the final chip geometry for a grinding operation. The model is based on Euclidean geometry at the intersection of the surfaces of two solid objects. By assuming that the wheel has particular "*high spots*", the grinding process can be modeled as a fly cutting operation that only removes material a specified number of times for each revolution of the grinding wheel. This geometric model was programmed to calculate the remaining surface topography as the wheel progresses across the part. The result is a series of Z coordinates in the X-Y plane which can then be plotted as an isometric or top-down view of the surface.

A typical surface resulting from the model is shown in Figure 1(a). This surface is characterized by features along the cutting direction (at the infeed rate) and a series of peaks at an angle to the cutting direction. This phase angle is a result of the relative speed of the grinding wheel and the workpiece as the wheel moves across the face of the part. Similar peaks have been observed in ground SiC surfaces when measured with a Zygo Maxim 3-D interferometric microscope as shown in Figure 1(b). The experimental surface roughness (P-V

= 127 nm) is larger than the roughness (P-V = 70 nm) predicted by the model. However, these features are predicted from geometric calculations and do not take into account features occurring due to brittle fractures.

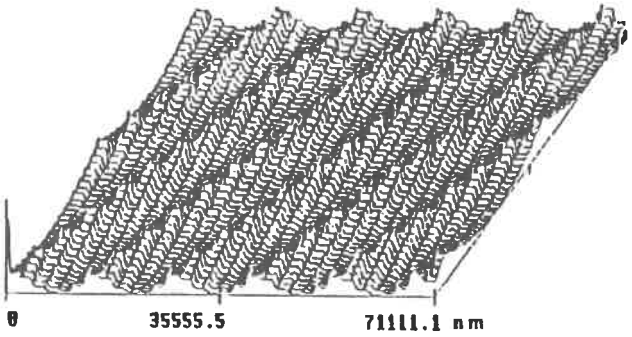

(a)

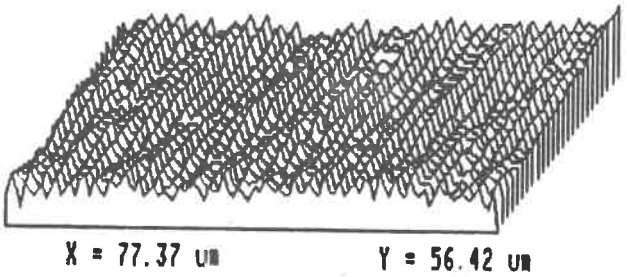

(b)

Figure 1: Theoretical (a) and actual (b) surface profiles of a ground part.

Surface Finish

The surface finish resulting from a specific grinding operation was calculated using the geometric model [2]. For this example a single parameter was varied while the remaining parameters were held constant. In Figure 2 the predicted roughness is compared to the actual roughness achieved in contour grinding of HIP SiC. This plot shows the predicted roughness assuming one cutting point per revolution of the grinding wheel (Theor.1), two cutting points (Theor. 2), an infinite number of cutting points (Theor. SPDT) and the measured values. The actual values for this specific case appear to correspond with the assumption of 2 cutting points. Since the surface finish results from several factors (machine vibrations, brittle fracture sites, geometric relationships, etc.), the assumption of two cutting points is only valid for this particular experiment. An assumption of more cutting points would be a better approximation of the theoretical surface finish which would actually be larger as a result of the other influences to give the measured surface finish.

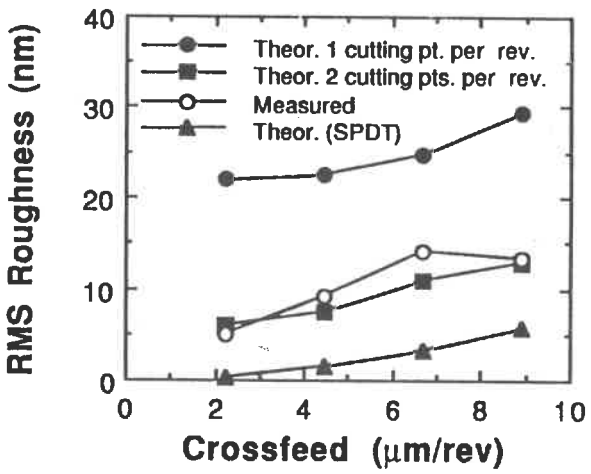

Figure 2: Theoretical and actual surface roughness versus crossfeed rate.

Chip Geometry

An analytical model for diamond turning of brittle materials pointed out the importance of the chip geometry on the ductile/brittle material removal transition [1]. A critical chip thickness was defined for this geometry below which no fracture damage was observed on the final machined surface. Experimental verification of this model using single crystal Si and Ge indicated that in the ductile regime of machining, some of the material was still being removed by fracture; however, damage free surfaces could be produced if the damage did not propagate through to the finished surface.

To extend this understanding to the contour grinding process, a complete picture of the relationship between the operating conditions and the geometry of the resulting chips must be available. A graphical model of the chip geometry has been developed which calculates the topography of the chip from the shape of the surface after successive grinding wheel revolutions [2]. Figure 3 shows two views of a surface as the wheel progresses through one revolution. Figure 3(a) is the surface at a specific time and Figure 3(b) is the same surface after one grinding wheel revolution. The difference between the two surfaces gives an approximation of the three dimensional geometry of the chip. This difference is plotted in Figure 4. Because of the limitations of the graphics routine, the output had to be normalized to a flat plane and plotted simply as height variations. This geometry will be combined with the fracture mechanics analysis to define the structure of the surface resulting from a combination of grinding wheel, material, and operating conditions. This analysis is not currently complete however, and some empirical observations will be made concerning this relationship.

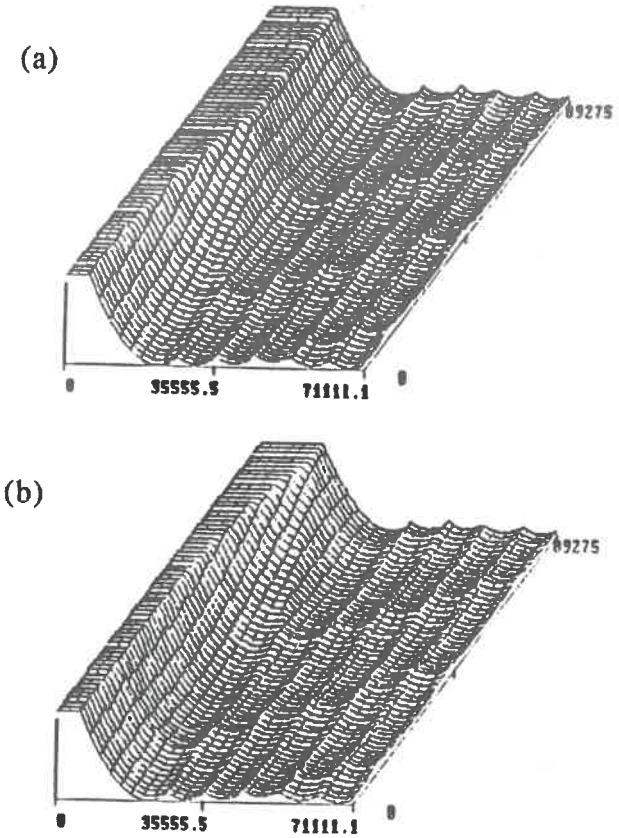

Figure 3: Theoretical surface profiles detailing successive wheel revolutions.

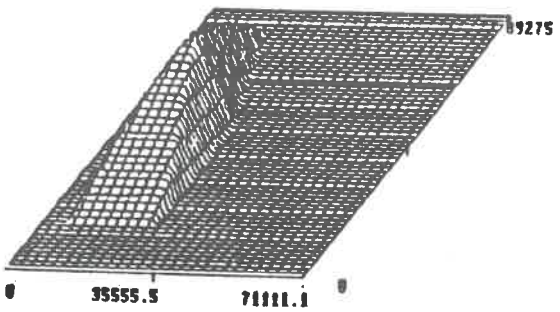

Figure 4: Theoretical chip geometry.

The geometric model can be used to evaluate the contribution of the geometry of the wheel and the operating conditions on the surface finish. Damage to the surface in the form of fractures will probably occur at the location of the maximum chip thickness and these cracks will penetrate some distance into the material. If this penetration is less than the thickness of the material removed on the next pass of the wheel, a damage free surface will result. In lieu of a complete analytical model, it seems reasonable to assume that the damage on the final surface would be proportional to the maximum chip thickness. The proportionality factor is not known at this time but an empirical value can be extracted from the experiments. As an example, the model was used to calculate the expected chip thickness for different crossfeed rates. Data obtained from the 1-D plunge grinding of HIP SiC was then used to estimate the percent fracture corresponding to these chip thickness values. Identical samples were ground on the 3-D contour grinding machine at the different crossfeed rates and the amount of fracturing was measured. Figure 5 shows the amount of fracturing predicted from the 1-D plunge grinding in conjunction with the simulated chip geometry and the actual fracturing that occurred as a function of the crossfeed rate. The trends developed in these simulations can be used to optimize a particular grinding situation to achieve the desired chip size for minimum surface fracture. These calculations could give be repeated for any specific set of grinding parameters and give insight into the ductile grinding process.

References

1. Blake, P.N. and R.O. Scattergood, "Ductile-Regime Machining of Germanium and Silicon", *Journal of the American Ceramic Society*", 73, [4], pp 949-957, 1990.

2. Fawcett, S.C. and T.A. Dow, "Computer Simulations of Precision Ground Surfaces", *Science of Optical Finishing Conf. Proc.*, Monterey, CA, June 10-12, 1990.

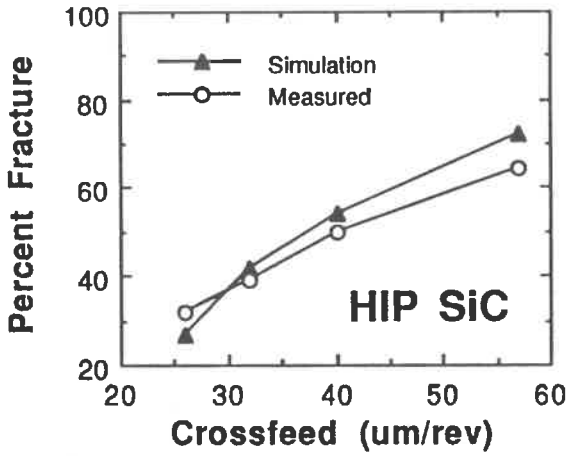

Figure 5: Plot of the simulated and actual areal percent fracture versus crossfeed rate for HIP SiC.

Implementation of an Open Loop Control Technique for High Speed Micropositioning in a Single Point Diamond Turning Process

H. Ozisik, R.F. Keltie
North Carolina State University
Precision Engineering Center
Raleigh, NC 27695-7918

An investigation is undertaken to minimize residual vibrations associated with high speed, low amplitude machining processes. A numerically computed input signal allows the system to follow a desired output trajectory once an accurate dynamic model of the system is developed. Specific application of this method is focused on controlling tool motion while cutting micron depth surface features into a flat, rotating workpiece during a single point diamond turning process. The synthesized input signal, applied open loop, is used to eliminate transient surface features which are created by uncontrolled motion of the tool when it is plunged into the workpiece surface during the cutting process. Controlled and uncontrolled cuts are shown to demonstrate a significant improvement in resulting surface features.

In the present study a tool is positioned to cut precision features into a rotating workpiece during a single point diamond turning process. The need to control the tool during the entry and exit of the cut (depth of 0.30 microns) was noted while producing rotationally asymmetric surfaces using a diamond turning machine . When the diamond tipped tool is plunged into or extracted out of a rotating workpiece by means of an uncontrolled step in voltage to a piezoelectric actuator (servo), the resulting workpiece is marred by transient surface features induced by free oscillations of the tool while in dynamic contact with the workpiece as seen in Figure 1.

Reducing the unwanted tool motion requires coupling an estimated 50 microseconds control time with a complex control law. In this case a closed loop cannot be utilized to supply real time control needed to minimize residual vibration because of the feedback loop. Since the actual path of the tool determines the contour of the cut, the present investigation focuses on developing an appropriate input signal, based on modeled system dynamics, to produce a specified output motion of the tool. This type of an approach not only minimizes residual vibration at the end of the control point but also emulates the tracking ability of a closed loop system by following a specified trajectory.

In this investigation the method is implemented for a complex system associated with diamond turning which involves the control of three modes of vibration (8 kHz, 10 kHz and 20 kHz) in a 50 microsecond period of time while maintaining a specified contour.

The general problem which is being addressed involves the reduction of residual vibration during a low amplitude, high speed positioning process. Specific application is to a single point diamond turning process. Open loop low pass filtering of the input signal to the servo had been suggested to eliminate the oscillations but this type of an approach, despite being a simple solution, would result in a slower actuator response time because of the loss of the higher frequency contents of the signal. The trade off in this case would be the reduction in residual vibration but with the loss of sharp surface features resulting from the decreased actuation time. One open loop method implemented for micropositioning on the order of a structure's natural period involves a novel two step approach for controlling residual vibration . This method has shown to be effective in controlling ringing but is applicable for only one mode of vibration. Other open loop control methods minimize positioning response time by some form of optimization of an input signal and/or reduction of residual vibration at the termination point. Bang-bang control is an example of obtaining very fast response times while reducing residual vibration at the positioning termination point depending on the applied constraints during the control interval. This method is effective if no concern is given to the dynamic behavior of the structure during the control interval. With this type of method the input signal can excite different modes of vibration during the course of positioning. Severe directional changes of the input signal encountered in this method can be very demanding on electrical requirements such as current draw. The result of such a solution in the present problem would eliminate transient surface damage but would not necessarily guarantee a smooth contour. Other investigations have focused on reducing the effect of dominant modes of vibration present in the system by attenuating the frequency spectrum at those particular locations , but again the path of the tool has not been addressed. The type of control needed for this problem is a scheme possessing the tracking ability of a closed loop system but which can yet be implemented in an open loop fashion.

In order for this type of scheme to be effective physical parameters of the dynamic system such as resonant frequencies and associated modal damping are experimentally determined These parameters are then incorporated into a mathematical model representing the physical system. The output signal is specified and input the control signal is numerically

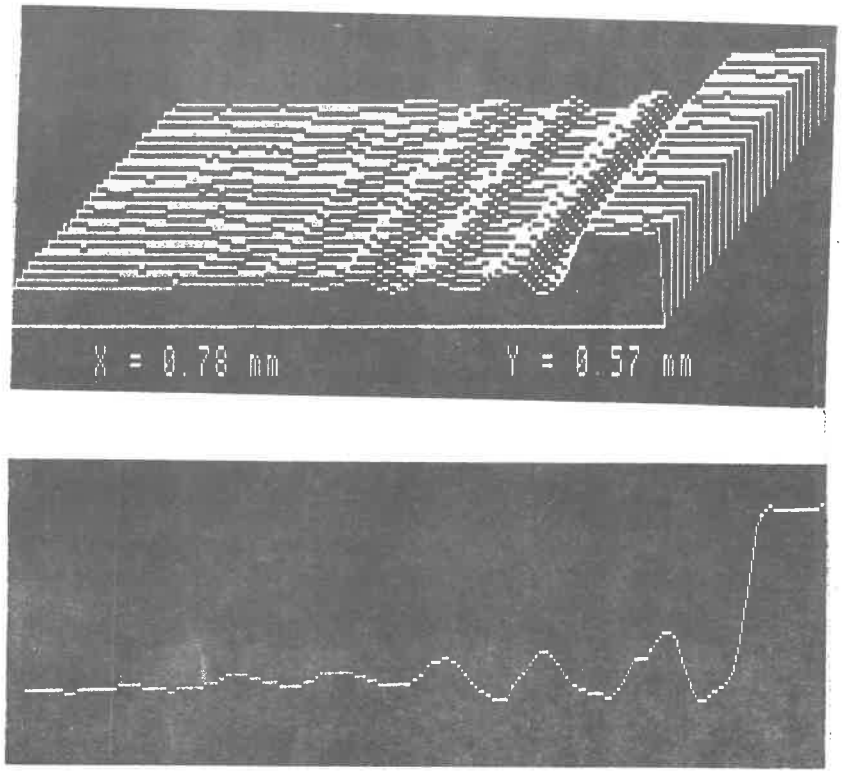

Figure 1 *Uncontrolled cut into a brass workpiece at 200 rpm taken using a 3D laser interfometer profilometer.*

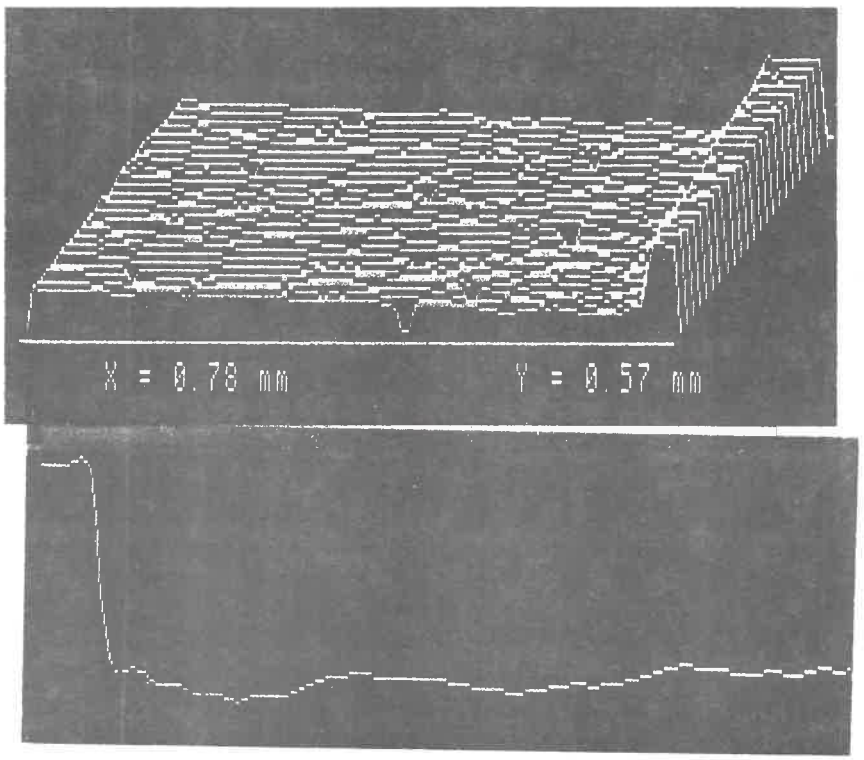

Figure 2 *Resulting surfce from a controlled cut in to brass at 200 rpm.*

generated. Since there is no provision to feed back any error in positioning, it is the accuracy of the model which dictates the performance of the control effort.

Results indicate that an accurate model for application to the cutting process can be completely described by the dynamics of the servo in a noncutting situation. This would of course imply that the dynamic forces created by the cutting process are not significant compared to the inertial forces generated by the servo. This is indeed the case if one compares normal tool force measurements with required inertial forces. Therefore, any transient surface features in the workpiece after the tool is plunged into or retracted out of the workpiece is therefore a direct result of the uncontrolled response of the servo.

Once the control signal is numerically generated, it is downloaded to a high speed D/A board (capable of 40 Mz DAC speed) housed in an IBM-XT. The control signal is then amplified and output to the servo at the appropriate time using information from a rotary optical encoded which monitors spindle speed. A capcitance probe mounted inside the servo mechanism is used to detect axial motion of the tool curing the cutting operation. The actuating servo mechanism is an annular piezoelectric stack which behaves electrically as a 0.3 microfarad cpacative load. The amplifier was custom designed and built to provide 50 volts and an withstand a peak current draw of 3 amps. Nominal current draw during the cutting processis estimated to be around 1 amp. The 3 dB point was set at around 2 MHz as not to low pass the digitally generated signal. A typical result of a controlled cut is seen in Figure 2. This is again brass cut at 200 rpm. Results do not varry with spindle speed or change in workpiece material (copper or aluminium).

References

H. Ozisik and R.F. Keltie, "Development and Implementation of a High Speed Open Loop Control Technique for Micropositioning of Mechanical Structures", Journal of Precision Engineering, Vol. 11, No. 4, October 1989, p. 225

Furukawa and N. Nobuyuki, "Effect of Material Properties on Ultra Precise Cutting Process", Annals of the CIRP, Vol. 37/1, p.113, 1988

P.H. Meckl and W.P. Seering, "Minimizing Residual Vibration for Point-to-Point Motion", Journal of Vibration, Acoustics, Stress, and Reliability in Design, Vol.107, October 1985, p.378

P.J. Falter and T.A. Dow, "A Diamond Turning Apparatus for Fabrication on Non-Rotationally Symmetric Surface", Ultraprecision in Manuafacturing Engineering, May 1988, p.187 Y.

Design of Centerless Grinding Machine for Ductile Mode Grinding of Brittle Materials

J.Yoshioka*, M.Miyashita**, A.Kanai*, M.Daito***, F.Hashimoto****

* NUTR KK, ** Ashikaga Institute of Technology

*** Nissin Machine KK, **** The Timken Research

ABSTRACT

The field of ductile mode grinding of brittle materials using grinding wheels of which grain size is larger than the ductile-brittle transition d_c value is defined as nanogrinding technology. This is the second generation of ultraprecision machining technology for brittle materials.

In the present paper, new design concepts applied to a centerless grinding machine, aiming at developing ultraprecision and high stiffness machine tools for nanogrinding are introduced. Effects of application of these concepts on the motion characteristics such as motion accuracies, feed resolution and stiffness are shown by the experimental results.

The applied major design concepts are :

1. geometrical arrangement satisfying the Abbe's principle as for the guideway, linear actuator and position feedback sensor,
2. introduction of the concept of functional surface in the kinematic principles by application of the composite guideway bearings,
3. introduction of the high stiffness and high resolution hydraulic linear actuator based on the principles of force control, and

4. introduction of the hydrostatically supported ultraprecision diamond wheel on stationary spindle resulting high stiffness and precise remountability.

The major test results of the carriage on the slideway plane bearings with nonlinear frictional characteristics are:

1. feed resolution 2 nm/step
2. static stiffness in feed direction 10 N/nm
   dynamic stiffness in ζ (estimated) approx. 0.20
3. backlush less than the feed resolution
4. high repeatability less than the feed resolution

These results show break-through of the stiffness limitation of the ultraprecision machine tools based on the conventional design concepts of no backlush and no friction for high repeatability.

Poster Paper Index

The Poster Session at the ASPE Annual Meeting is designed to provide an alternative to the standard lecture format of presentation. Papers that the Organizing Committee felt lent themselves to significant verbal interaction, were concise but important discoveries, or were strongly visual or tactile subjects have been scheduled for the Poster Session. The posters will have a prominent location at the Meeting site and will be hung for the entire meeting. A period from 2:00-4:00 on Wednesday afternoon has been set aside for the authors to be present to discuss their work.

Session Chair: Thomas Bifano, Boston University

- ***Measuring the Spatial Frequency Response of an Optical Surface Profiler***
  Joseph Bietry and R. Anthony Auriemma (Chapman Instruments) ..... page 147
- ***Coordinate Measuring Machine Sampling Techniques and Algorithms***
  Gregory Caskey, K. Chen, Y. Hari, D. Palanivelu, R. Wilson, J. Yang, and R. Hocken (UNC-Charlotte) .. page 151
- ***The Cutting of Polygon Mirror with first Korean Diamond Flycutting M/C***
  H.Z. Choi, H.S. Yu, J.U. Jeon, H.D. Jeong, and N.B. Yim (Korean Institute of Science & Technology) .... page 155
- ***Spatial Resolution Limits of an Optical Profiler***
  Katherine Creath (WYKO Corp.) ..... page 159
- ***Reducing Sub-Surface Damage in the Grinding of Glass***
  Doug DePiero and Thomas Bifano (Boston Univ.) ..... page 162
- ***Surface/Tool Relationships in Diamond Turned Copper***
  Joseph Drescher and Thomas A. Dow (NC State Univ.) ..... page 166
- ***Hysteresis in Piezoelectric Actuators: Implications for Precision Servo Design***
  J. Duduch and Anthony E. Gee (Cranfield Institute of Technology) ..... page 170
- ***Nanometer Positioning Using Micro-dynamics of Rolling Guide***
  Shigeru Futami, Akihiro Furutani, and Shoichiro Yoshida (Research Development Corp. of Japan) ..... page 174
- ***Circumferential and Inner Diameter Metrology of Advanced X-Ray Aetrophysical Facility (AXAF) Optics***
  Thomas Gordon (Hughes Danbury Optical Systems) ..... page 178
- ***Ultra Precision Aspherical Lens Processing Machine***
  Keishi Kubo , H. Nagano, S. Kubota, S. Yochida, M. Takahashi, K. Matsumura, S. Ueda (Matsushita Electric Industrial Co.) ..... page 182
- ***A Portable Non-Recirculating Temperature Enclosure***
  Dan Luttrell (Rank Taylor Hobson Inc.) ..... page 186
- ***Absolute Laser Refractometer***
  Hans-Peter Meiser, D. Frolich, and H. Meiser (Spindler & Hoyer) ..... page 189
- ***Fast Tool Servo Implementation For Diamond Turning***
  Michele Miller and Thomas A. Dow (NC State Univ.) ..... page 192

- ***Micro Grinding at an Ultra-High Speed Region***
  Shouro Mochida, M. Takahashi, and S. Ueda (Matsushita Electric Industrial Co.) ..... *page 196*
- ***Application Of A Novel Two Step Digital Control Algorithm For Precision Actuation***
  Hakan Ozisik, Thomas G. Bifano, and Thomas A. Dow (NCSU) ..... *page 200*
- ***Precision Engineering Aspects of the PATS Project***
  Richard Rhorer (Los Alamos Nat'l Lab), Wayne Hobson, and Jeff Jarosz (Moore Special Tool Co.) ..... *page 204*
- ***Evaluation of Silicon Wafer Polishing Pads***
  Yamato Samitsu (Nippon Steel Corp.), Nobuo Yasunaga, Takahumi Yoshida, Takashi Ohmoto, and Sadamu Horie (NSCE Electron Corp.) ..... *page 208*
- ***Chip Formation in Single Point Diamond Turning***
  M.C. Shaw (AZ State Univ.), H.G. Shafer and M. Adler (Corning) ..... *page 212*
- ***Use of Lasers in Nanomaterial Synthesis***
  Peter Strutt (Univ. of Connecticut) ..... *page 216*
- ***Study on the Polishing of Diamond by Metallic Plate***
  Hitoshi Tokura, Masanori Yoshikawa, and Cheng-feng Yang (Tokyo Institute of Technology) ..... *page 220*
- ***Measurement and Compensation of Guideway Errors by a Laser Doppler Displacement Meter***
  Charles Wang (Optodyne, Inc.) ..... *page 224*
- ***Stiffness Characteristics of Externally Pressurized Gas Bearings***
  Junming Wang, P.H.J. Schellekens, and A.C.H. van der Wolf (Eidenhover Univ. of Technology) ..... *page 228*
- ***Dynamic Simulations as a Design Tool for Precision Machine Tool Installations***
  Scott A. Woodard and Gerald Hegarty (Fabreeka International, Inc.) ..... *page 232*
- ***Newly Developed Electron-beam Lithography System for Fabricating High Accuracy Concentric Circle Patterns with Large Diameter***
  Yuji Yamazaki, K. Nakamura, T. Sasaoka, M. Mitsui, H. Murao, T. Maeda, H. Goto, S. Ogata, and T. Yamashita (Omron Corp.) ..... *page 236*

Measuring the Spatial Frequency Response of an Optical Surface Profiler

by

R. Anthony Auriemma and Joseph Bietry

Chapman Instruments
50 Saginaw Drive
Rochester, New York 14623
716-461-1950

INTRODUCTION

Quantitative measurements of surface features is a concern in many areas of precision manufacturing. Contact and non-contact profile scans are routinely made to measure various roughness characteristics of surfaces. It is important to be aware of the inherent characteristics of the test instrument in order to properly interpret the measured data. A standard engineering method for characterizing instruments is to measure their frequency response function. This function shows the degree to which the distribution of surface spatial frequencies will be modified by the instrument. This paper will describe experimental measurements made on a differential interference optical surface profiler to determine its spatial frequency response function.

DIFFERENTIAL SCANNING INTERFEROMETRY

The basic concept of the profiler discussed in this paper is based on the principles of differential interference microscopy[1,2]. The instrument quantifies the technique commonly used qualitatively in Nomarski microscopy[3].

The optical path of the existing microprofiling instrument is shown in Figure 1. An expanded and collimated beam from a helium-neon laser passes through a non-polarizing beamsplitter into a compact translating interferometer head. The beam is turned 90 degrees where it then enters a Wollaston prism and microscope objective. The Wollaston prism splits the beam into two orthogonally polarized beams with a 90.2 microradian angular shear. The objective focusses the two polarized beams into two separate focal spots on the test surface. The beams reflect from the sample back through the objective and angularly recombine in the Wollaston prism. The return beam is then reflected by the non-polarizing beamsplitter and enters a polarizing beamsplitter cube which decomposes the beam into its two orthogonal linear components which strike detectors 1 and 2.

The two focussed spots on the test surface overlap but do not interfere since they are orthogonally polarized. The reflected beams have a relative phase shift which can be

related to the surface slope at the location of the two overlapping beams through a calibration procedure[4,5]. Surface profile is then derived by numerical integration of the slope data using distance data derived from a precision encoder mounted on the translating interferometer head.

ANALYSIS TECHNIQUES

Several techniques are commonly used to measure the frequency response function, $H(\omega)$, of a system being characterized[6]. The first, a direct method, systematically applies sinusoidal stimuli to the system at a series of test frequencies and measures the response of the system. The ratio of the input amplitude to the response then provides the frequency response function. A second, indirect method is frequently used to characterize electrical circuits. With this method the stimulus to the system is a very narrow pulse, and the appropriately scaled response of the system is the "impulse response function," h(x). A well known result from linear system theory derives the frequency response function of the system as the Fourier Transform of the impulse response function:

$$H(\omega) = \mathcal{F}[h\ x)]$$

Unfortunately, neither of these techniques can be applied to surface profiling instruments because there are not adequate sinusoidal or pulse surface standards in the height range (10-200 Ångstrom) of interest for this measurement. A third, indirect method exists which does have an adequate reference stimulus surface. This method applies a "step" stimulus function, which can be obtained approximately by using a step height sample, to the system under test. Here the properly scaled response of the system is known as the "step response function," s(x). Because the system is linear, the impulse response function can be obtained from the step response function by differentiation:

$$h(x) = \frac{d}{dt}\ [s(x)]$$

The frequency response is then calculated from the first equation above. Furthermore, since the profile data for instrument is obtained by integrating the slope data, the derivative of the profile data <u>is</u> the slope data. Thus the slope data provides the impulse response function directly, when the stimulus to the system is a step.

METHODS

The stimulus to the instrument was a roughness standard manufactured by a silicon etching process to produce a repeated pattern of steps with a pitch of 60 micrometers and a calibrated step height of 176 Ångstroms[7]. This step size was less than 3% of the wavelength of the laser light source of the system, and well below the 12.5% ($\lambda/8$) limit of the instrument. Measurements made for 10X and 20X objectives demonstrated that the

measured impulse response functions had dropped to less than 0.5% of their respective peak values at a spatial separation of +/- 10um, well within the +/-30um step width of the standard. Slope samples were taken at 0.2um intervals. The impulse response curve was obtained by averaging 36 step stimuli. These were obtained by temporally aligning the digitized slope data using a computer program. The program first located sequentially the peak value of the slope data for each step, and then centered the response around the corresponding spatial point when calculating the average. The average was calculated for +/- 15 um around the peak value, to provide the impulse response function. No additional spatial filtering was applied to the data. The impulse response function curves were normalized by dividing by the peak value. The frequency response function was then computed by an FFT method. The frequency response curves were normalized by dividing by the value at zero frequency.

RESULTS

The impulse response functions for the system with 10X and 20X objectives are shown in Figure 2. The curves are seen to be symmetrical and "Gaussian" in shape. Comparison with a computed Gaussian curve showed close agreement with the measured data until the amplitude of the computed curve was below 2% of its peak value. The frequency response functions for the system with 10X and 20X objectives are shown as Linear plots in Figure 3 and as Log-Log plots in Figure 4. These curves show that the instrument system is "flat" in the passband range of spatial frequencies below 0.1 cycle/um and then roll off smoothly to below 1% transmission. The curves are again Gaussian in shape, as would be expected. The 10X curve drops to 1/2 of its peak value at a spatial frequency of 0.18 cycles/um and the 20X curve does so at 0.36 cycles/um.

CONCLUSIONS

A method has been developed for measuring the frequency response function of an optical differential interference surface profiler. It should be noted that the results from this method do require that the step height sample have very "square" steps, i.e. no rounding at the edges, and a true 90 degree edge from top to bottom. A deviation from these conditions will make the frequency response function appear to roll off more rapidly than it actually does. However, if the shape of the step is known in detail, it is possible to make corrections to the data through the process of numerical deconvolution.

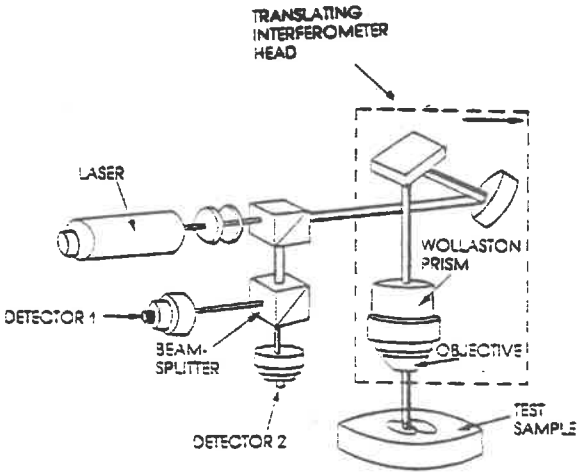

Figure 1

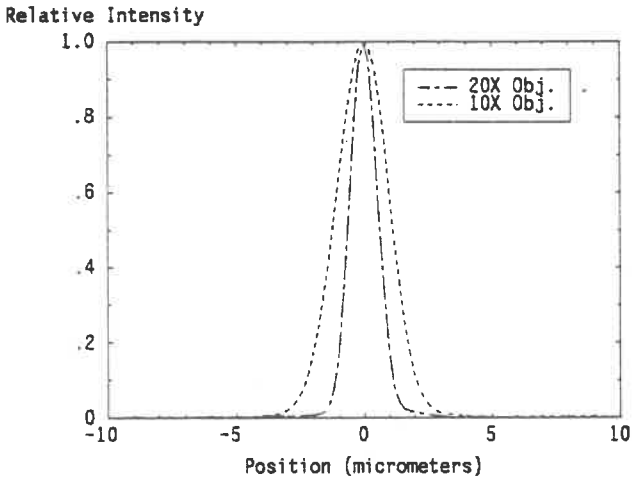

Figure 2

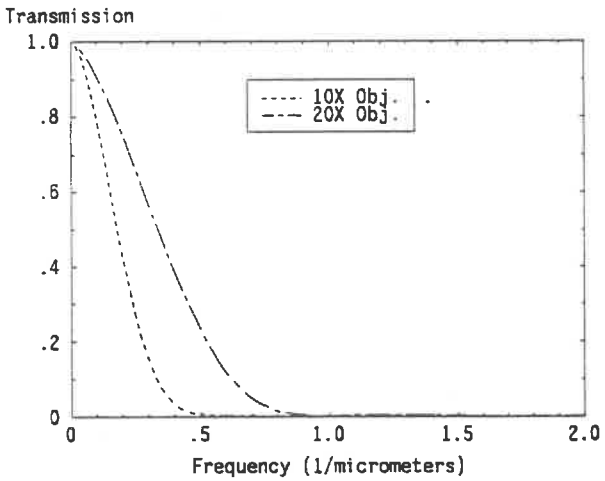

Figure 3

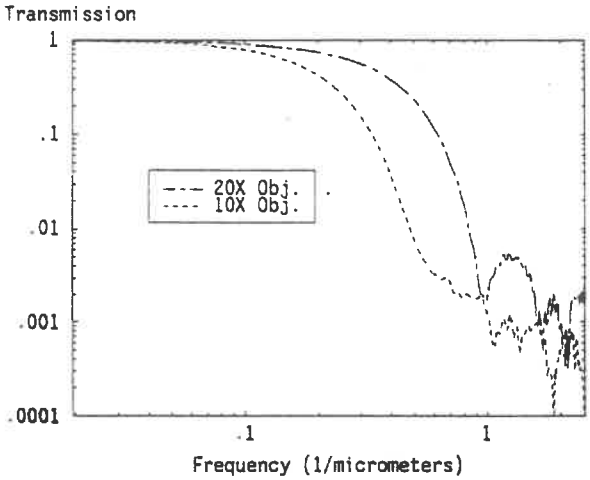

Figure 4

1. J. M. Eastman, J. M. Zavislan, SPIE Proc. 429, 569(1984)

2. J. M Zavislan, J. M. Eastman, SPIE Proc. 525, 169(1985)

3. T. C. Bristow, D. Lindquist, SPIE Proc. 816(1987)

4. D. L. Lessor, et. al., J. Opt. Soc. Am. 69, 357(1979)

5. J. S. Hartman, et. al., Appl. Opt. 20, 2665(1981)

6. D. K. Cheng, Analysis of Linear Systems Addison-Wesley Publishing Co, 1959, p224.

7. VLSI Standards Inc. Model RAS-0090A. Chrome coated silicon dioxide on silicon dioxide.

COORDINATE MEASURING MACHINE SAMPLING TECHNIQUES AND ALGORITHMS

G. Caskey, K. Chen, Y. Hari, D. Palanivelu,
R. Wilson, J. Yang, and R. Hocken
University of North Carolina at Charlotte
College of Engineering
Charlotte, NC 28223

Abstract

In the past decade the computer-controlled coordinate measuring machine has become the inspection instrument of choice for the dimensional measurement of mechanical parts. The reasons are numerous. Most importantly, the coordinate measuring machine allows the acquisition of detailed dimensional data on most part surfaces and readily gives the relationship between the various part features. Coordinate measuring machines are easily reprogrammed for changes in product or simply changes in product design. Finally, since the coordinate measuring machine can acquire detailed dimensional data readily, the results of a coordinate measuring machine inspection can be used to assess trends in the manufacturing process and feedback data to correct the process before a part, or a feature on a part, drifts out of tolerance.

Coordinate measuring machines and the data acquired by them have some drawbacks. Since a coordinate measuring machine acquires data on a point-by-point basis, the results obtained from an inspection need to be analyzed to create a geometric model of the feature or features being measured. This analysis is handled by algorithms whose results are strongly dependent upon many factors, including the sampling method chosen for data acquisition, the noise in the data, systematic deviations of the measured surface from ideal, and algorithm correctness and robustness. Therefore, though it may appear to the user that data of high accuracy are obtained, the results reported after analysis may contain large errors. To compound this problem, the current methodology for dimensioning and tolerancing is based around technologies that were developed in an environment where coordinate data were not readily accessible. In particular, the tolerancing methods contain implicitly the assumption(s) that the part is to be checked using either surface-plate technology or some type of gaging system. Gaging systems are cumbersome, inflexible, "non-diagnostic" and expensive (some say nearly obsolete) but do have the advantage that, when a part fits a mating gage, one is assured to a high degree of confidence that it will also fit the designated mating part that the gage "replicates". Algorithms that attempt to emulate the "gaging" function have been developed, but they have problems in robustness, convergence, and run-time and are not routinely supplied with CMMs. Algorithms in common use on many CMMs give results that may not conform to the tolerancing system in the presence of systematic error [Pond, 1988].

At UNC Charlotte we have been systematically examining the interaction between the sampling strategy, the machine errors, the part errors, and the algorithms used to reduce the sample data to geometric features ("substitute geometry"). In order to do this, we have developed a library of least-squares and minimax algorithms (for lines, planes, circles, spheres, cylinders, and cones), built an error model of our coordinate measuring machine, and tested our algorithms against both real and computer-generated data to determine their range of applicability. Here, due to space limitations, we only report some of the results of our experiments on a single feature, the three-dimensional (3D) line.

Data Generator

The data generator used to test the 3D line algorithm was relatively simple. An ideal line was first created. Systematic error in the form of sinusoidal functions with selectable spacial frequency, amplitude, and phase were then added to the "perfect" line. Finally random errors of different magnitudes (drawn from a uniform distribution) were added to the generated data set. The line was then rotated to an arbitrary angle in 3D space. Sampling was done at regular intervals (which included the end points). Parameters used for our initial tests are given in Table 1.

Table 1
Test of 3D Line Software Algorithms

Parameter	Value(s)
Line Length	1000 mm
Sample Pattern	Equidistant
Sample Size(s)	5, 25, 50
Sinusoidal Form Error	
Amplitude	0.01, 0.005, 0.002 mm
Cycles (Number)	1, 2, 3
Phase	0
Random Error (3 Sigma)	0.01, 0.005, 0.002 mm
Rotations	
About X	30 Degrees
About Y	45 Degrees
About Z	35 Degrees

Algorithm and Algorithm Correctness for the 3D Line

For the testing described in this paper we used the algorithm recommended by Forbes [Forbes, 1989]. This algorithm was implemented in Quick BASIC and tested initially against the PTB data sets [Porta, 1986]. As part of this effort we also had to determine what the correct solution should be. We decided that the correct answer should be the answer obtained for infinite sampling density on the line with systematic error and no random error. (This definition was evolved after considerable internal discussion and consultation with the B89.1.12 Software Committee.[1]) In the case of a 3D line, this solution may be obtained analytically. This is not the case for the other features mentioned above.

The presence of the "true" answer is particularly important in our case where we added sinusoidal error of low frequency onto the original line as, depending upon the phase, frequency, and amplitude of the sinusoid, the correct least-squares solution may have a slope differing from that of the original "perfect" line.

[1]ASME, B89.1.12 Committee has the charter to develop Standards for the performance of Coordinate Measuring Machines.

Results and Displays

We show the results of these fits using a representation developed at UNC Charlotte in consultation with the B89.1.12 Software Committee and Ted Hopp of NIST [Hopp, 1990]. It is designed to display the data in a physically meaningful fashion. The line segments are parameterized in terms of their direction cosines and the mean value of the line coordinates [BSI, 1989]. The first plot (Fig. 1a) shows the angular difference between the direction of the fit line segment and the direction of the true line segment. The data are generated by "DO LOOPS" nested in the order given in Table 1. The three sections on the graph represent the results of fits with the same cycle of systematic error at different sampling densities. The second plot (Fig. 1b) shows the distance perpendicular to the true line segment between the mean point of the true line segment and the closest point on the fit line segment. Again, this parameter was chosen to be physically meaningful, that is, a measure of the coincidence of the two lines at this point in space. Notice the wide divergence and oscillation even for relatively small form error when the sample size is small. We expect that this problem will be compounded when more complicated substitute geometries are investigated.

Conclusions

Results of these computer experiments are somewhat discouraging in the sense that they display considerable sensitivity to the sample size and to the form error. Since most coordinate measuring machines are equipped with switching-type probes, it is usually desired to take very few points. It appears, however, that if measurements of high-accuracy are required, a larger number of points will have to be sampled than is customary. Furthermore, more elaborate sampling strategies may be required. It should be noted that the errors added in these tests are not unusual and could have been errors induced by systematic errors in the measuring machine, rather than any form error on the part. For example, on many measuring machines a sinusoidal straightness of a few micrometers is perfectly possible.

Acknowledgements

The authors would like to thank J. Raja and the members of the ASME B89.1.12 software subcommittee for their helpful suggestions and input. This work was supported by the National Science Foundation.

References

BSI, "Assessment of Position, Size, and Departure from Nominal Force of Geometric Features", British Standards Institution, BS 7172, 1989.

Forbes, B. A., "Least-Squares Best-Fit Geometric Elements", National Physical Laboratory Report DITC 140/89, 1989, National Physical Laboratory, U.K.

Hopp, T., NIST, private communication, 1990.

Pond, J. B., "Answers to CMM Problems Sought After GIDEP 'ALERT'", Metal Working News, Dec. 1988, p. 23.

Porta, C., and Waeldele, F., "Field Testing of Three Coordinate Measuring Machine Evaluation Algorithms", Physicalish Technische Bundesanstalt, Germany, March 1986.

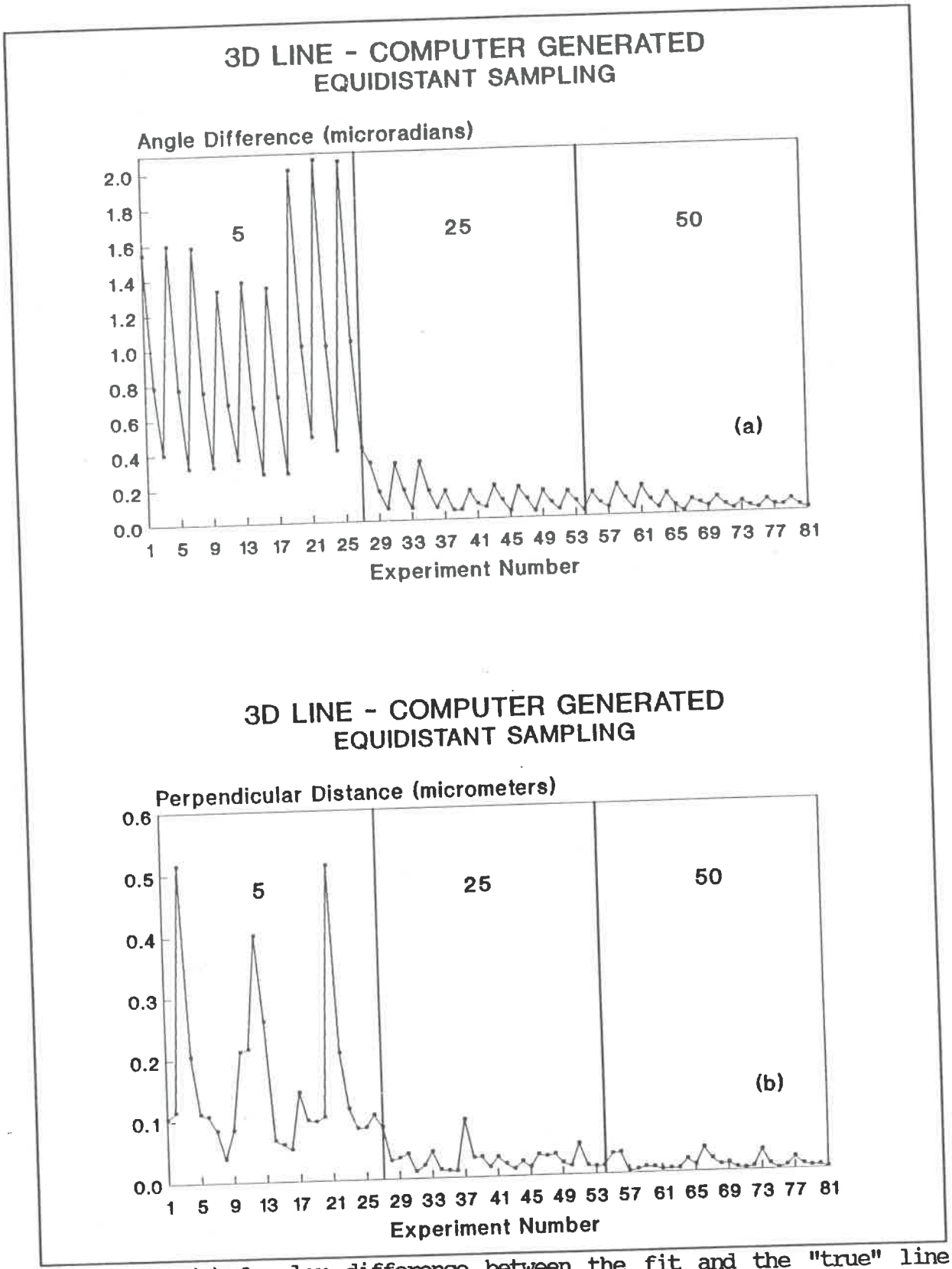

Figure 1. (a) Angular difference between the fit and the "true" line segments. (b) Perpendicular distance between the fit and "true" lines.

The Cutting of Polygon Mirror with First Korean Diamond Flycutting M/c

* ** *** *** ***
Dr.-ing H.S.Yu, Dr.-ing H.Z.Choi, J.U.Jeon, H.D.Jeong, N.B.Yim

Headquarters of Research & Development
Korea Academy of Industrial Technology
Guro Danji P.O.Box 27, Seoul, Korea
(Tel) -02-8601-316
(Fax) -02-8601-344

The demand of precisely machined parts is rapidely increasing in advanced countries. For the ultra high precision machining, we need not only the machine design technology or component technology but also the measuring and machining technologies.

From this point of view, we have made the First Diamond Flycutting Machine through the aid of Ministry in Korea andwill develop the machine for manufacturing of the spherical or nonspherical surfaces.

This paper presents the introduction of the prototype diamond flycutting m/c for manufacturing polygon mirrors. Finally we give test results in various conditions.

1. Diamond Flycutting M/C (fig 1)

- Machine total accuracy is 1 μm and decreasing by continuous study.
- Aerostatic spindle with high accuracy of rotation and rigidity.

a. Accuracy of rotation : radial : 0.1 μm
axial : 0.1 μm

b. Rigidity : radial : 3 kgf/mm^2
axial : 6 kgf/mm^2

-Aerostatic work-table with high accuracy and rigidity driven by friction driver.

a. Accuracy : linearity : 0.1 μm/100 mm
pitch, yaw, roll : 1 arcsec/100 mm

b. Rigidity : 16 kgf/mm^2

2. Surface Measurement by Phase-Measuring Interferometry.(fig 2)

- A measuring principle for the fine surfaces has been established by adopting the phase measuring principles.
- A prototype measuring system has been built by optical and electronic units.
- An Algorithm has been developed which can analyze the measured signals.

3. Test results in various cutting conditions.

- Aluminum Alloy (Mg 5 %) with high purity is very important for getting a good mirror surface.
- Geometry of Diamond tool is senstive to mirror surface. Large relief angle (α) and Negative rake angle (r) of the Diamond tool are effective to mirror surface (but, $1° \leq \alpha \leq 10°$, $-5° \leq r \leq 5°$).
- Cutting oil should have high viscosity, high thermal conductivity for better surface.
- Suitable choice of cutting speed and feed rate is also important in order to get mirror surface. Cutting speed of about 2000 rpm and feed rate of 10 mm/min are suitable for making a mirror surface.

Polygon mirrors machined by First Korean Flycutting M/C are in fig 3.

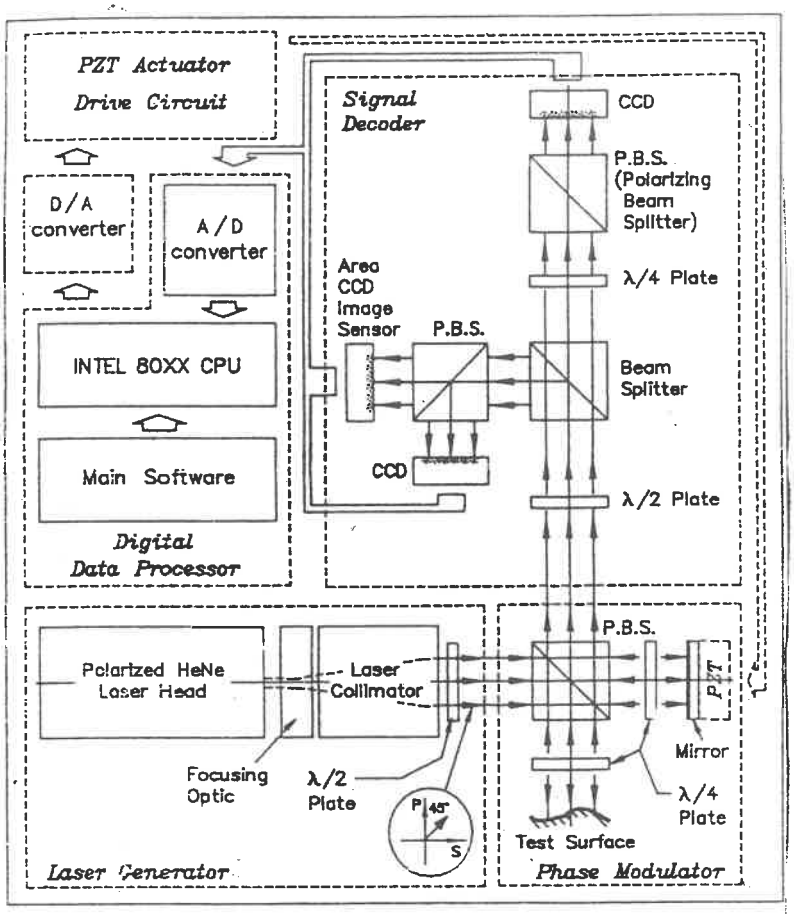

Fig2. Schematic diagram of Instantaneous Phase Measuring Interferometry

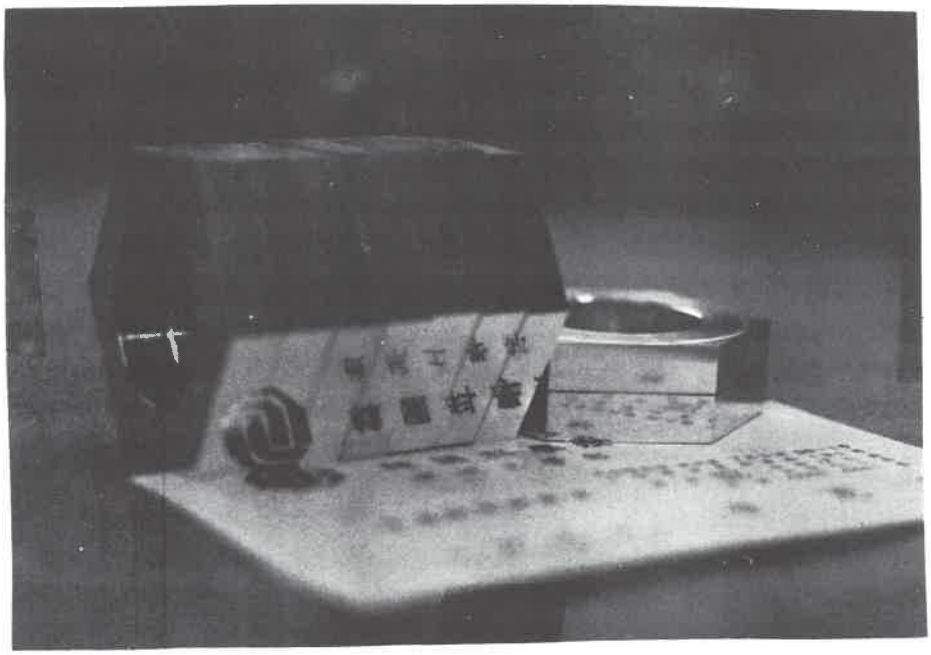

Fig3. Polygon mirror machined by First Korean Flycutting M/C

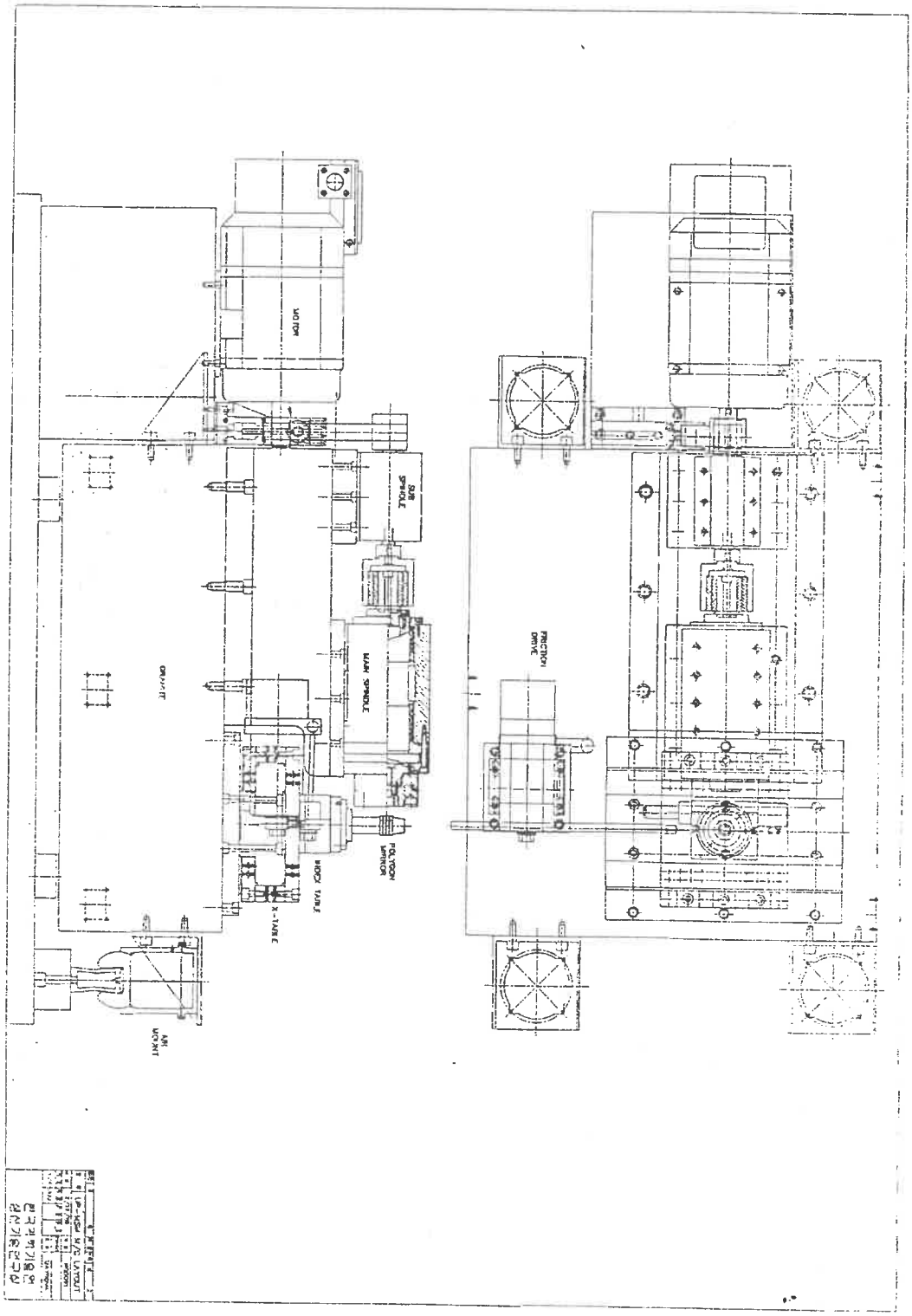

Figl. Assembly diagram of First Korean Flycutting M/C

Spatial Resolution Limits of an Optical Profiler

Katherine Creath
WYKO Corporation
2650 East Elvira Road, Tucson, Arizona 85706
and
Optical Sciences Center
University of Arizona, Tucson, Arizona 85721

Abstract

Interferometric optical profilers have a spatial resolution which is either limited by the detector array sample spacing and element size or by the optical resolution of the system. To test the working spatial resolution of an optical profiler, a sinsusoidal grating with 300 lines/mm was measured using an optical profiler at 10×, 20×, 40×, and 200× with detector arrays having element-to-element spacings of 6.8 μm, and 40 μm. The highest magnification gave the greatest and most accurate depth for the grating for all of the detectors. At 40×, as long as there were more than about 8 sample points per cycle as there were with the two smaller detector spacings, the grating depth can be measured quite accurately. With fewer points, the peak-to-valley height measurement of the grating is too low even though the optical resolution of the system is sufficient enough to resolve the grating. The results of this work show that for accurate representation of surface heights containing high frequency structures oversampling is desirable.

Summary

The spatial resolution of an interferometric optical profiler depends upon both the optical resolution of the system and the characteristics of the detector array used to sample the image. The limiting resolution will be the larger of the optical and detector resolution. One means of defining optical resolution is the Sparrow criterion which states that the image of two points is just resolved when they are separated by $r = \lambda/(2\,(NA))$, where NA is the numerical aperture of the microscope objective and λ is the illumination wavelength.

The detector resolution depends upon the element-to-element spacing and the size of each detector element. Due to the sampling theorem, there must be two detector elements for each optical resolution element in order to see a surface feature of the size given by the optical resolution element. Figure 1 shows plots of twice the sampling interval for the two detectors versus magnification of several commercially available microscope objectives along with the optical resolution at each magnification. The sampling interval is found by dividing the element-to-element spacing of each detector by the magnification of the objective. In order to sufficiently sample the image, the line indicating twice the sampling interval should lie below the dots in order for the system to be limited by the optics. From

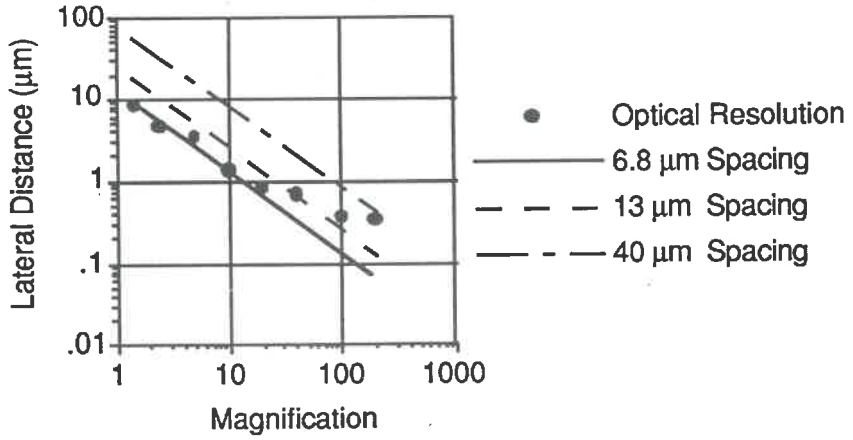

Figure 1. Twice the sampling interval and optical resolution versus magnification for different detector arrays.

Fig. 1, the 40 µm detector spacing undersamples for all the magnifications except 200×. With the 6.8 µm detector spacing, the image will be sufficiently sampled at all magnifications, and will be oversampled for 20× and above. This means that if the object surface contains features with spatial frequencies near the optical resolution, the detector which provides sufficient sampling is necessary in order to reconstruct the surface profile.

The size of each detector element also affects the ability to accurately reconstruct the object's surface profile. Because the detector elements have finite width, the image is averaged over the size of the detector element. To understand the effect of detector element size, consider a single spatial frequency from the object of frequency incident upon the detector array. Assuming that the optical system images this spatial frequency perfectly, the effect of a single detector element is to average the signal over its area. Therefore, it is necessary to consider the detector sampling interval as well as the detector element size to be able to accurately measure high spatial frequency surface features. Ideally, an array of point detectors should be used; however, in practice, such arrays are not commercially available.

In order to study the effects of the detector array on measurements using an interferometric optical profiler, a sinusoidal grating with an amplitude of ±21.2 nm and a spatial frequency of 300 lines/mm (period = 3.3 µm) is measured using different magnifications and two different detector arrays. For this experiment, a Mirau interferometer with a magnifications of 40× as well as a Linnik interferometer with a magnification of 200× were used to measure the grating.

Both of the cameras used have close to a unity fill factor. The largest element-to-element spacing is the 256 × 256 element array with elements separated by 40 µm. The other detector array has 1320 × 1035 active pixels which spaced 6.8 µm in both directions.

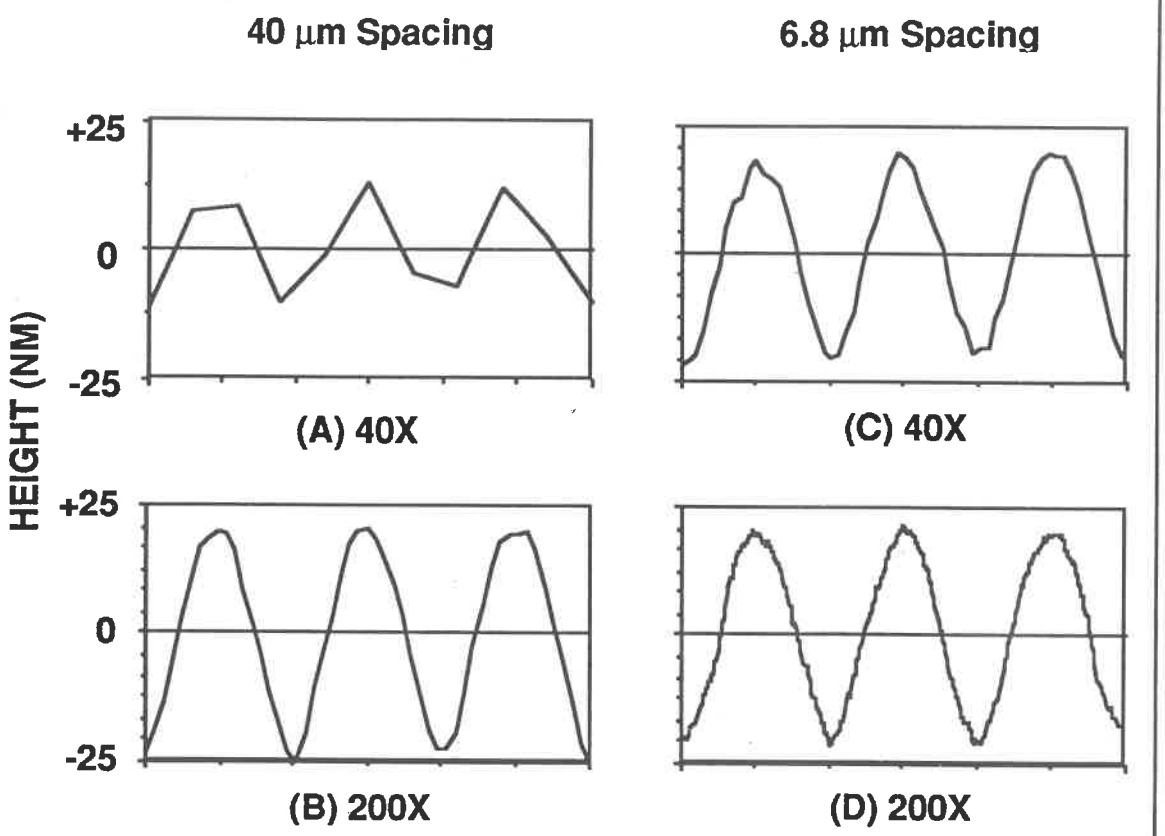

Figure 2. Measurements of 300 line/mm grating using detector arrays with 40 μm and 6.8 μm detector element spacings. (10 μm scan lengths)

The results of measuring the grating with the different magnifications are shown in Fig. 2. This figure shows a 10 μm scan on a height scale of ±25 nm. Note that at 40×, the 40 μm spacing measures a much lower amplitude than the 6.8 μm spacing. This is due to the fact that there are only 3 detector points per period of the grating, and the optical resolution is less than the detector sampling interval. For the 6.8 μm spacing there are 19 detector points per period of the grating at 40× with 4 pixels per optical resolution element, and the amplitude of the grating is approximately ±21 nm. At 200×, both detectors measure amplitudes which are close to the actual value. The low resolution camera samples the image at slightly less than 2 pixels per resolution element and the high resolution camera samples the image 10 times for each optical resolution element. The higher spatial sampling interval enables the measurement of object features with a high resolution using a lower magnification objective. Thus, it is advantageous to oversample the image and have at least 5 pixels per optical resolution element to accurately determine surface feature heights.

REDUCING SUB-SURFACE DAMAGE IN THE GRINDING OF GLASS

Douglas DePiero and Thomas Bifano
Aerospace and Mechanical Engineering
Boston University
Boston, MA 02215
(617) 353-5619

Evaluation of a Large Optics Grinding Machine

In the production of large glass optics, typically the optical blank is first ground to achieve the desired contour, then it is polished to remove subsurface fracture induced by the grinding process. This abstract describes an effort to evaluate the performance of a large optics grinding machine and to measure the subsurface damage resulting from the grinding process. The grinding machine that was analyzed is a three-axis CNC grinder with a working volume of 3 x 3 x 0.6 meters. Currently, this machine is used to coarse-grind aspheric optics, which are subsequently polished using a computer controlled, iterative polishing process to attain an optical quality surface. It is important to know how "fine" the glass grinding operation can be made on this machine. Because grinding is faster and less expensive than polishing, it is worthwhile to push the grinding process to the limits of the grinding machine's precision before polishing.

Three aspects of the machine's dynamics were measured: vibration in the direction normal to the grinding contact, spindle growth as a function of time, and the response of the machine to large and small step commands in each of the three linear axes of motion. Figure 1 is a graph of the vertical vibration of the spindle housing as a function of the spindle rotational speed. The vibration reaches a peak amplitude of 25 micrometers at a spindle rotational speed of about 3000 RPM. For precision grinding, it is clear that this spindle should be operated below 1500 RPM, where the vibration amplitude drops to a value below 1 micrometer. The spindle growth for this grinding apparatus followed a first-order model, with a steady state growth of 50 micrometers and a time constant of 33 minutes, based on a spindle speed of 4400 RPM. Therefore, it takes approximately 2.25 hours for the spindle to settle within 2% of its steady state position. Measurement of the machine's step response permitted two conclusions. First, the computer controller requires an operator-generated, fixed dwell time between commands to avoid an attenuated motion response.

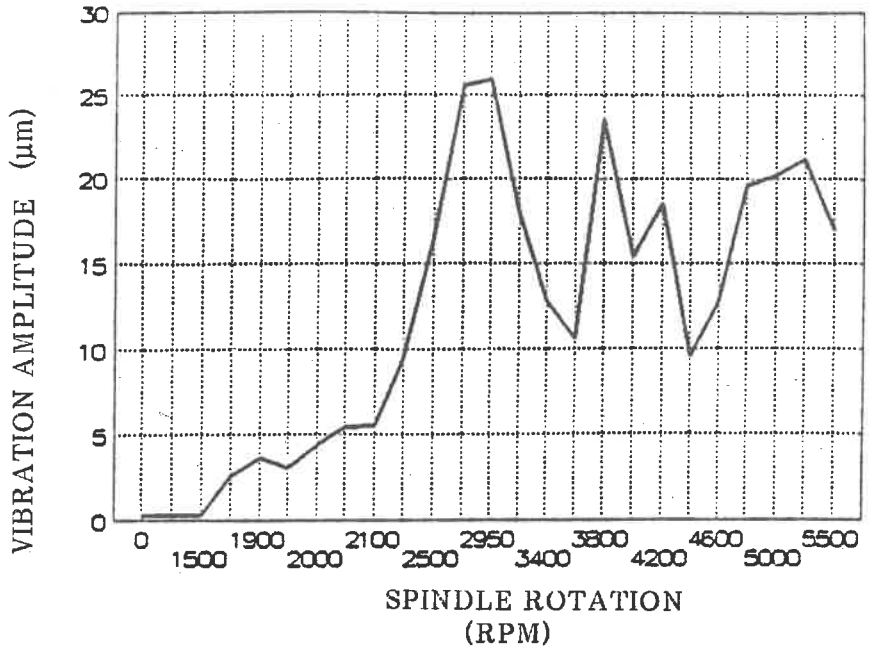

Figure 1: Vertical vibration of the grinding spindle housing as a function of spindle rotational speed.

Second, there are systematic backlash errors in two of the three axes. The third axis exhibits no backlash, but has a systematic inaccuracy in its step size.

Measurement of Subsurface Damage

Replication is a widely used, locally destructive technique for measuring the depth of the damage layer induced in large glass optics by grinding processes. Because the replica is small, it can be examined using an optical microscope. Typically, the peaks and valleys on the replica are alternatively brought into focus on an optical interference microscope, permitting measurement of the damage depth with a resolution on the order of one micrometer. Two potential sources of concern with this technique are its reliability and its precision. Reliability is an issue because it is unclear whether the replica is a faithful reproduction of the glass surface. The precision of the technique is currently limited by the resolution of the optical microscope. Nevertheless there is potential for extending replication analyses to damage depths in the 1-5 micrometer range by using scanning electron microscopy (SEM).

In the replication process, the machined surface is first etched with a 40% hydrofluoric acid solution for 30-120 seconds to open the subsurface cracks. The replicating solution, a mixture of cellulose acetate and acetone, is applied to the etched surface and covered by a sheet of cellulose acetate. After drying

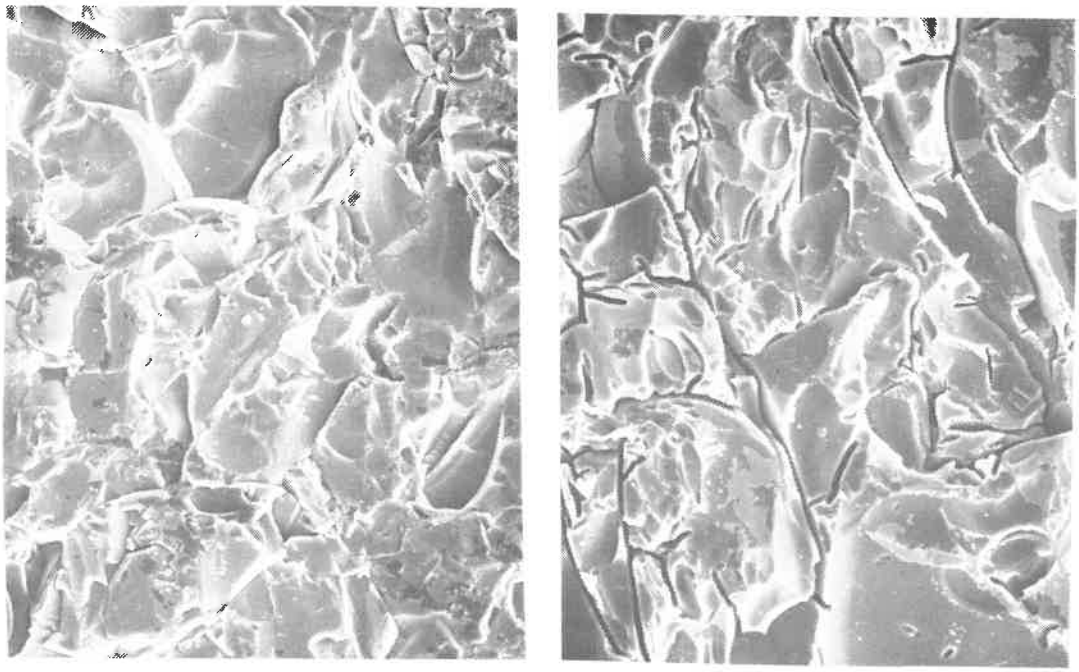

Figure 2: SEM Photographs of ground BK-7 surfaces (1200x). Left: Unetched. Right: Etched

for 15 minutes, the hardened replica is peeled off. Two replicas of a given area are made. The first replica removes glass debris and foreign particles from the surface of the glass. The second replica is used for microscopic analysis of the damage layer.

For this study, samples of BK-7 optical glass were ground on the large CNC grinder described above. All samples were ground with a 220 grit diamond wheel, at a feed rate of 2.5 mm per minute and a depth of cut of 0.1 mm. After grinding, half of the sample surface was etched in a 40% hydrofluoric acid solution for 2 minutes. SEM photographs of the etched and unetched surfaces are shown in Figure 2.

To evaluate qualitatively the effectiveness of the replication process, the etched glass surface was compared to a replica of the same surface using an SEM. Both surfaces were first sputter coated with 200 angstroms of gold and palladium. As illustrated in Figure 3, the etched glass surface contains residual patches of hardened replicating solution. These residual markings served as an efficient way to match areas on the glass with corresponding impressions on the replica. An area of the etched glass is matched with its replica in Figure 3. It can be seen that the glass and replica are nearly perfect mirror images of one another.

From the evidence of residual replicating fluid on the glass surface, it seems reasonable to suspect that some of the replicating fluid is also left in the cracks, resulting in a less than perfect replica. However, the thickness of

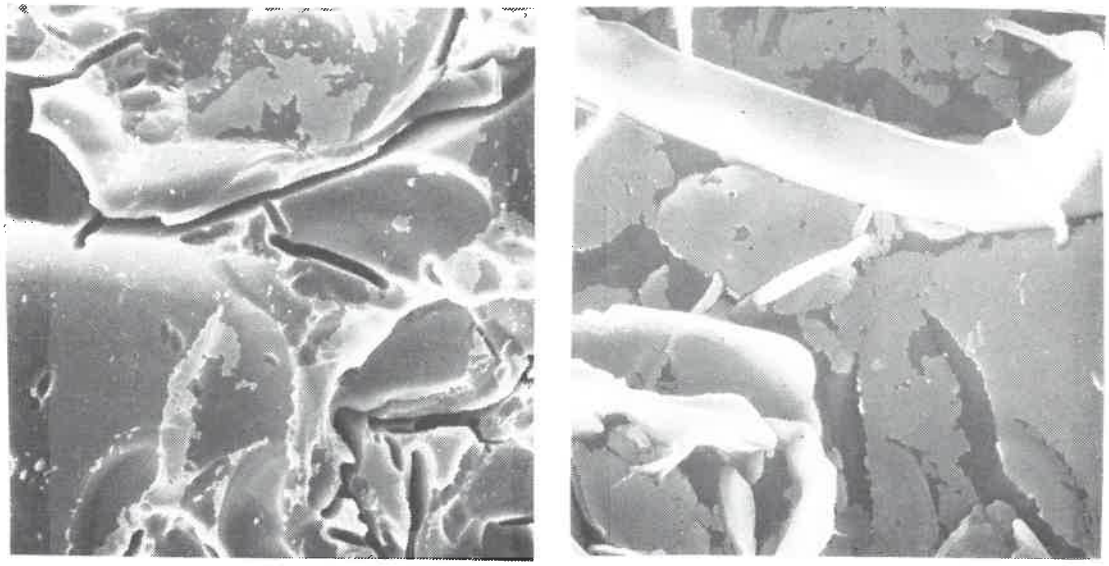

Figure 3: Left: Ground, etched BK-7 surface. Right: Replica of the same surface. Cracks in the glass are seen as peaks in the replica (2400x).

the residual replicating fluid is small in proportion to the crack size, so the dimensions of the replica are not significantly affected. A more important effect is probably due to the fact that many of the large cracks do not propagate in a direction normal to the surface. Whether the replicating solution can enter these meandering cracks and be withdrawn intact is still uncertain. From these initial photographs, however, it appears that the replication process creates a reasonably accurate impression of the surface. Also, it is clear from these SEM photographs that the resolution of the SEM permits evaluation of glass surfaces and replicas well beyond the capabilities of optical microscopy. For fine grinding of large glass optics, with damage levels in the 1-5 micrometer range, replication and SEM analysis may be well suited as techniques for damage depth measurement.

Acknowledgements

This work was sponsored by the Strategic Defense Initiative Organization, Producibility and Logistics Directorate, and funded through the Optics MODIL, Oak Ridge National Laboratory, as part of the Faculty Off-Site Research Program, and was performed in collaboration with Litton-ITEK Optical Systems.

Surface / Tool Relationships in Diamond Turned Copper

J.D. Drescher, T.A. Dow
Precision Engineering Center
North Carolina State University, Raleigh, NC

Introduction

A major goal of research in Diamond Turning (DT) is an understanding of the process which can lead to improved quality of the finished product. This understanding is also necessary to determine the achievable limits of the DT process and what the limiting factors are. Although DT has been an accepted manufacturing process for over 25 years, basic research in this area is still needed. As limits in machine design and closed loop process control are approached, the mechanics of tool-workpiece interaction become even more important.

One basic need in developing a model for DT is the ability to measure tool forces. A model which can accurately describe how the force components change with the cutting conditions, material properties, and tool parameters is essential for achieving the best possible part quality. This paper deals with measured components of force in an orthogonal, plane strain cutting process. It relates the steady-state, average force components to depth of cut and undeformed chip cross-sectional area. These forces are also affected by the condition of the tool edge as it wears. Changes in a DT surface caused by degradation of the tool edge condition are also documented [1]. The edge of the diamond tool is therefore the key parameter for connecting measured tool force to the surface quality of the finished optical component.

Experimental Procedure

Several tools were used in the cutting experiments. They all had approximately 60° included angle with 0° rake and very small nose radius as the top view in Figure 1 indicates. The overall edge length of the tools, L, varied from 0.584 to 1.651mm.

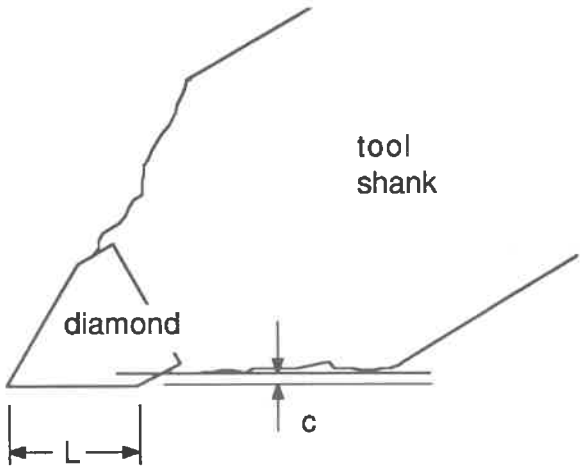

Figure 1: Schematic description of the "dead-sharp" tools

Orthogonal, plane strain cutting was achieved using a Pneumo ASG 2500 DTM which is a 2-axis machine. The cutting edge of each diamond was aligned perpendicular to the spindle axis to within one arc-minute. A 200mm diameter copper workpiece was fed into the tool along the spindle axis while the tool remained stationary. For each new cut the tool was withdrawn and incremented toward the center of the spindle by the de-

sired width of cut. This width, l, varied from 127 to 1016μm. The distance which the tool advanced into the workpiece per spindle revolution was 0.16 to 2.54μm. The ratio of uncut thickness to chip width therefore varied from $\frac{1}{6000}$ to $\frac{1}{50}$.

Figure 2 is force output of a single cutting test which involved all four infeeds at a constant edge length (chip width). The top portion of Figure 2 is a plot of force in the cutting direction (i.e. y-direction as defined in Figure 3). The bottom half of Figure 2 is the z-direction force which is perpendicular to the y-direction. The magnitude of the y-direction force is approximately three times that of the z-direction force in this case.

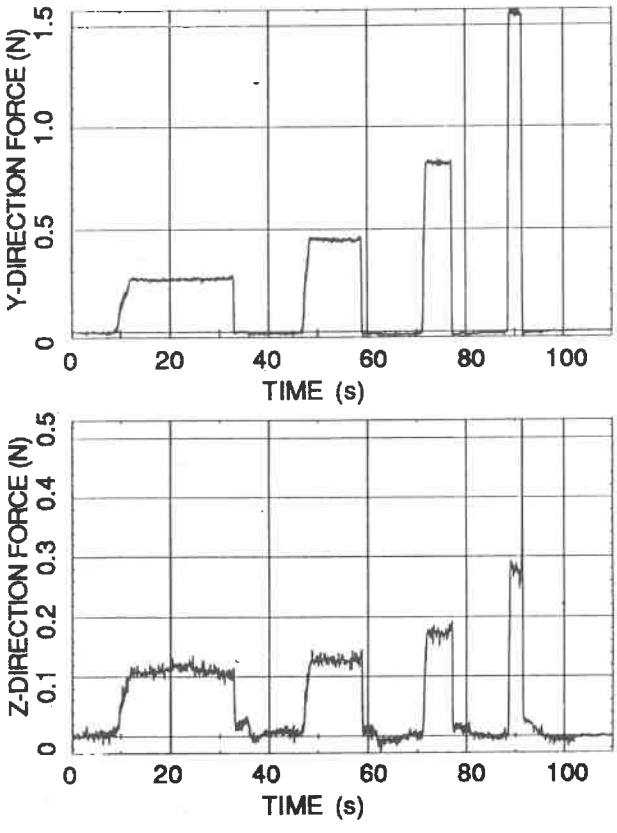

Figure 2: Example data file of force components for four feedrates of 0.32, 0.64, 1.27, and 2.54$\mu m/rev$

Each of the four cuts removed the same volume of material. Therefore the first of the four cuts is the slowest infeed and takes the longest time.

Model Development

Tool forces can be modeled simply as in Figure 3 which is a planar schematic of the orthogonal cutting process [2]. In this view there are two pairs of normal and tangential force components. One pair acts on the tool rake face and the other at the tool edge. Assuming uniformity along the tool edge, the forces acting at the edge should scale linearly with the length of contact (dimension out of the plane in Figure 3). It also is reasonable to expect the forces at the rakeface to be dependent on both cutting depth and edge length. Both tangential force components can be related to the respective normal forces by a coefficient of friction.

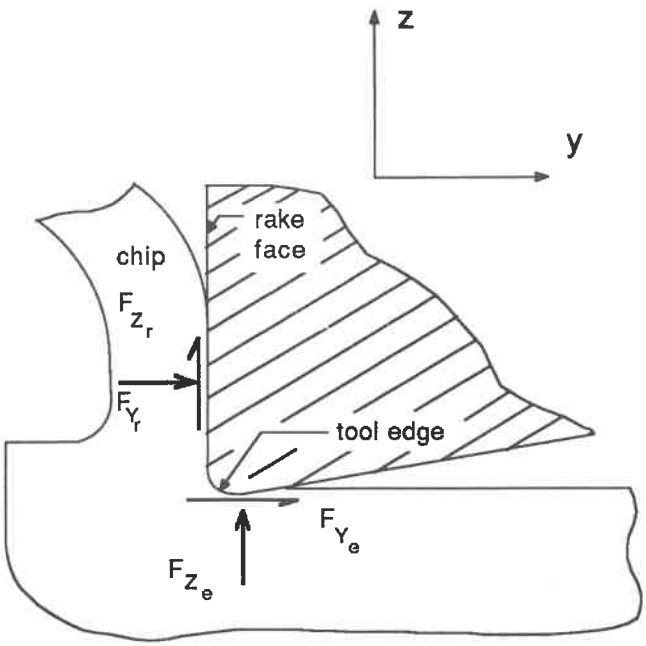

Figure 3: Components of tool forces in DT

	d($\mu m/rev$)											
	0.32			0.64			1.27			2.54		
l(μm)	F_y	F_z	ϕ	F_y	F_z	ϕ	F_y	F_z	ϕ	F_y	F_z	ϕ
635	0.39	0.16	22°	0.70	0.22	17°	1.32	0.33	14°	2.52	0.53	12°
508	0.30	0.12	22°	0.54	0.18	18°	1.06	0.31	16°	2.06	0.63	17°
381	0.22	0.09	22°	0.41	0.14	19°	0.80	0.22	15°	1.50	0.38	14°
254	0.15	0.07	25°	0.28	0.09	18°	0.53	0.15	16°	1.02	0.25	14°

Table 1: Example force data (Forces in Newtons)

Table 1 includes typical force values for the parameters covered. The angle ϕ is $tan^{-1}(F_z/F_y)$ where the directions are defined in Figure 3. It is the angle between the cutting direction and the force vector sum which is an indicator of the relative magnitude of tool force components. The measured forces are linear with edge length, l. For example, at $0.64\mu m/rev$, the force, F_y, changes by 250% from $0.28N$ to $0.70N$ as the edge length is increased by 250% from 254 to $635\mu m$. However these same forces are not exactly linear with infeed rate, d, which is equal to the cutting depth for this geometry. Table 1 shows that at an edge length of $508\mu m$, the force increases by 690% from 0.30 to $2.06N$ as the infeed rate increases 800% from 0.32 to $2.54\mu m/rev$. A model to relate measured forces can be written as follows.

$$F_y = C_1 l d^n + \mu C_2 l \qquad (1)$$

$$F_z = \mu C_1 l d^n + C_2 l \qquad (2)$$

Both forces in this model have a linear dependance on the edge length, l. The exponent on the depth of cut, d, indicates the nonlinearity of forces with this parameter. The first terms in Equations (1) and (2) correspond to the rake face components of Figure 3. The second term in each equation corresponds to the normal and tangential forces exerted at the tool edge.

Results

For the tools used, force data similar to Table 1 was acquired at different stages of wear. The wear was measured in terms of total cutting distance. Each group of data was used to calculate the model parameters, C_1, n, μ, and C_2, which gave the best correspondence between measured forces and those calculated with Equations (1) and (2). The variation in these parameters from tool to tool and over the useful life of each tool was analyzed.

C_1 corresponds to a flow stress. For the copper used, this value was $1.61GPa$ with a variation of $\pm 7\%$ for all tools and stages of wear. C_1 was therefore relatively independent of tool edge condition. The exponent, n, was near but in all cases less than 1.0. It varied between 0.93 and 0.98

The coefficient of friction, μ, should also be independent of edge condition since lubrication, tool material, and work material are not changed. However, this parameter remained constant only after the initial wear-in period. For the newly lapped tools, μ was 0.195 $\pm 8\%$. After the initial wear, μ was consistantly between 0.120 to 0.150.

C_2 is the parameter which is the biggest indicator of the tool edge condition. It has units of stress $\times$ length and the length included in

C_2 is that of the tool contact in the cutting direction. This parameter changed by more than 500% as the tools became dulled.

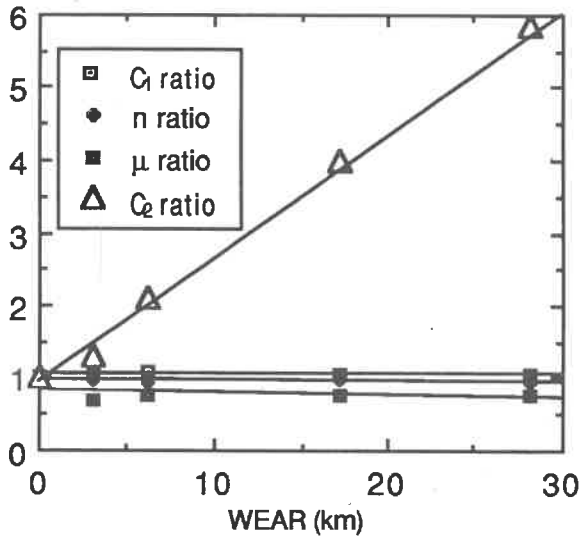

Figure 4: Changes in force model parameters with tool wear

Figure 4 is a graph showing the changes in model parameters over the tool life. The ratios of the values calculated at each stage of wear to the original values, calculated for the new tool, give the percentage change in the parameters. These ratios are plotted against wear distance.

Conclusions

A model is given for orthogonal tool forces in diamond turning of copper which agrees with measured forces over a wide range of cutting conditions. The model includes four parameters. These are:

- C_1, a flow stress;
- n, an exponent to account for the non-linearity of forces with cutting depth;
- μ, a coefficient of friction;
- C_2, a factor relating force at the tool edge to the length of contact at the edge.

C_1, n, and μ remain relatively constant for different tools at different stages of wear. C_2, however, changes by more than 500% as the tool wears. C_2 is therefore directly related to the edge condition of a diamond tool and this condition can be found quantitatively by measuring tool forces. Since surface quality degrades along with tool edge condition, tool forces are related directly to the diamond turned surface.

References

[1] D.L. Decker; "Tailoring of the optical properties of diamond-machined optical surfaces", *Proc. SPIE*, Vol.433; 1983; pp 96-103

[2] J.D. Drescher, T.A. Dow; "Tool force model development for diamond turning", *Precision Engineering*, Vol.12 No.1; 1990; pp 29-35

HYSTERESIS IN PIEZOELECTRIC ACTUATORS: IMPLICATIONS FOR PRECISION SERVO DESIGN

J Duduch* and A E Gee

Cranfield Institute of Technology, (CoM/70)
Cranfield, Bedford, MK43 0AL, UK

* On leave from Dept Engenharia Mecanica, Univ Sao Paulo, Sao Carlos, SP, 13560, Brazil

1 Introduction: Hysteresis in Micropositioning

In the design and choice of components for precision micropositioning systems, efforts have been made to eliminate the causes of non-linearities in the output/input characteristics of 'divided reset' form incurred with backlash and hysteresis generally. In the operation of actuators and mechanical drive trains, such effects may be buried within noise levels and not apparent at coarser levels of measurement. However, as improvements in precision are called for (with reduced specified resoluble minimum displacement increment and noise level), such non-linearities become increasingly manifest, ultimately limiting the potential for improvement of a system.

In machine-tools, for example, these effects become increasingly apparent as the size of cut (and thence required actuator motion reversals) become smaller. They may be incurred due to lost motion on reversal of drive-forces at mechanical interfaces, such effects being well-known in gears, worm/wheel faces, linear transmission linkages and leadscrew/nut actuators. Similarly classified effects occur where a sub-range of reduced stiffness and changed displacement characteristics is apparent following a reversal of the input signal.

These effects can be ameliorated to a certain extent by careful adjustment or increase of retention forces; the latter is often incompatible with ultra-precise positioning. Other strategies include high frequency dither and the limitation of command signals so as to be unidirectional (permissible in tracking or machine-profiling type tasks).

2 Feedback Control Loops

For many of the highest precision applications, a fine motion actuator is incorporated with a high precision position-transducer as the principal components of a feedback control system; the resultant 'microservomechanism' is required to be both dynamically fast-acting and statically precise. Such control design requirements favour high loop-gain at the upper end of the frequency response spectrum and forward path (mathematical) integration of the measured error signal to ensure effectively infinite loop-gain (and zero average error) at the lower end.

In the case of feedback control-systems exhibiting solely linear transfer characteristics, techniques based on harmonic frequency response analysis enable designs to be optimised. Where a system manifests non-linear characteristics, it is axiomatic that an understanding of their effects is necessary if the full potential (possibly even adequate performance) is to be achieved.

3 Piezoelectric Actuators

For fine positioning over ranges below about 100um, the piezoelectric actuator has many advantages. Operating through a fundamental dimensional change effect, it does not require sliding interfaces and oil films.

Figure 1 shows a typical piezoelectric actuator characteristic in which lost-motion is manifest. However, measured over a single traversal range and about a particular set-point, the plot is valid only for that condition. The need for precise information about variational aspects of reversal non-linearities (with respect to both amplitude and set position) does not seem to have been generally appreciated.

A local feedback loop around the actuator may be employed to improve the linearity of an element. In effect this forces the characteristic toward that of the measuring transducer employed, any difference being essentially proportional to the achieved loop gain. Such systems can be stabilised by low pass filtering and, measured at near-zero frequencies, the linearity is often excellent. Incorporated into a larger system, it is desirable that the required overall system frequency response bandwidth be constrained to an order less that of the local (actuator) loop.

When considering the effects of reversal non-linearities, it is useful to normalise output/input amplitude plots to unity gain (slope) sensitivity for comparison; any correction to this can be treated as a cascaded (series) ideal amplifier.

4 Effects of Hysteresis on Closed Loop Systems

Piecewise linear approximations, as shown in Figure 2(a), may be employed for analysis (tending only to introduce errors associated with higher frequency harmonics). The resultant output displacement/time response to one particular sinusoidal input amplitude is shown in Figure 2(b) together with the response fundamental harmonic. Since feedback systems are invariably optimised to operate close to the upper mechanical frequency capability, only the first harmonic of the response is significant, higher harmonics being filtered out.

5 Principal Types of Hysteresis: Variational Effects of Amplitude

5.1 'Backlash'

Backlash is a classical reversal non-linear effect where, irrespective of the input signal amplitude (ie the traversal history), an invariant quantum of displacement is 'lost' on reversal; the (divided) forward and reverse plots for all amplitudes will respectively lie on two parallel lines as shown in Figure 3. However, if the normalised output/input amplitude ratio is considered, as the input amplitude is decreased, the effect of the lost motion is to occupy an increasing proportion of the required output displacement so the gain tends toward zero and the phase toward 90°arc; when the input motion falls below the level of lost motion, all output motion is lost.

In any mechanical system, the decribing equations, of second (or higher) order, incur (at least) two variable phase-lags, increasing respectively with frequency from 0 toward 90°arc. Adding the further phase-lag of up to 90°arc due to backlash, the system has the potential to incur 180°arc phase lag or more with finite gain,

leading to oscillatory instability. With an integrator (of a further 90°arc delay) in the loop, the occurrence of 'hunting' in systems with backlash should not so much be considered remarkable as very likely.

Although backlash is not observed as being intrinsic in piezoelectric devices, it may be found in associated attachments and containments used in the construction of an actuator.

5.2 Lost Motion as a Function of Amplitude (including 'Constant-characteristic' Hysteresis)

If the lost motion diminishes with amplitude, a different situation will prevail; a set of nested characteristics will be obtained as shown in figure 4. Further, if the lost motion reduces proportionally with input amplitude then, normalised to the input, the characteristic will be invariant **ie the non-linearity will have constant effect at all amplitudes.** For analysis, this requires only a single mathematical model (for all amplitudes); for design purposes, it can be modelled as an element with constant gain and phase-delay.

It follows that, if, normalised to the input amplitude, the lost motion is seen to reduce with amplitude, then, unlike the effects of backlash (which become increasingly deleterious as the input amplitude is reduced), the effects of such a non-linearity diminish. If a system can be designed to exhibit adequate gain and stability at the largest anticipated amplitude, then its performance at low amplitudes is likely to be superior. (With reduced attenuation at low amplitude, there is an effective gain increase to be borne in mind but, as this becomes manifest in finer motion reversals, the destabilising phase-lag is also decreased).

6 Conclusions

In order to assess the potential utility of a particular piezoelectric actuator whose characteristics manifest divided-reset non-linearity, it is necessary to measure its output/input displacement characteristics over a range of amplitudes and set-points.

Whereas backlash of constant amplitude causes a major limitation in a system, diminishing hysteresis is much less detrimental. The case of 'constant-characteristic' hysteresis is particularly interesting; although fundamentally non-linear, it can legitimately be treated as a linear element manifesting fixed values of attenuation and phase-lag.

Modelling and optimisation of a feedback control system containing a piezoelectric actuator element are particularly facilitated by multiple amplitude measurements (until now seldom published).

Figure 1
Typical PZT Characteristic

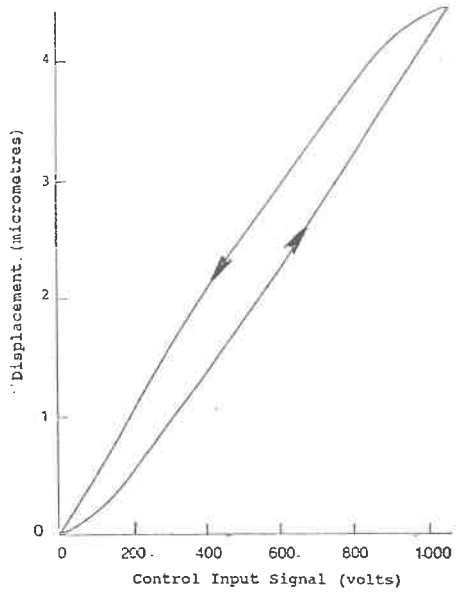

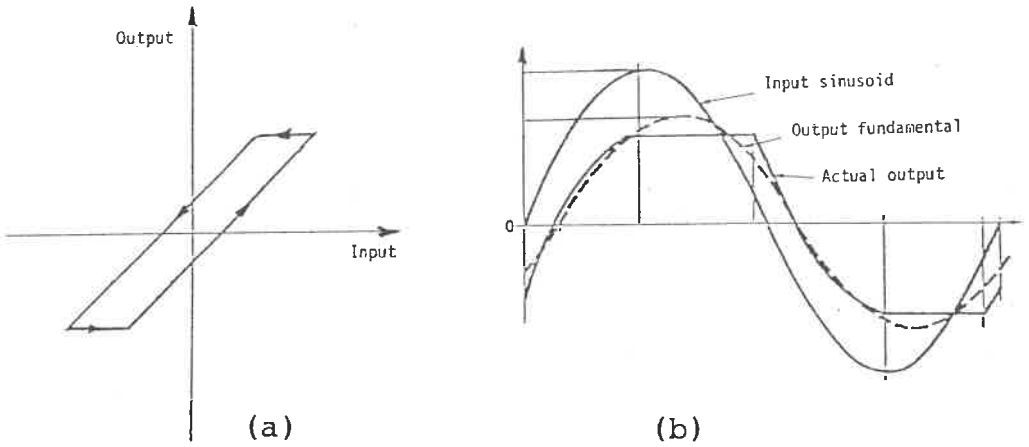

Figure 2 Single Amplitude Characteristic (a)
and Response to Sinusoid (b)

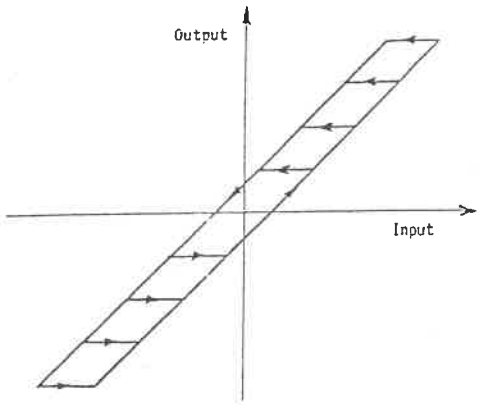

Figure 3 Backlash Characteristics
for Different Amplitudes

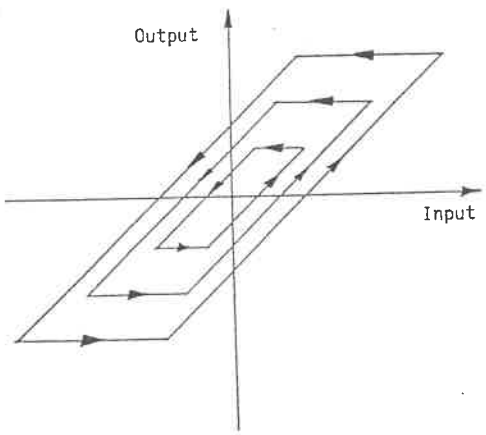

Figure 4 'Constant' Hysteresis
at Different Amplitudes

NANOMETER POSITIONING USING MICRO-DYNAMICS OF ROLLING GUIDE

Shigeru FUTAMI and Akihiro FURUTANI
Yoshida Nano-Mechanism Project, ERATO, JRDC
5-9-9 Tohkohdai, Tsukuba, Ibaraki 300-26, JAPAN

Introduction

Precise position control is a basic and important technology for which ever higher performance is always required. Positioning methods with high resolution and long stroke have previously been designed by using hybrid mechanical structures and coarse and fine control. Such hybrid mechanisms with coarse and fine control have two disadvantages; the structure of the mechanism becomes intricate and the size of the mechanism becomes large.

In this paper, a nanometer position control system is proposed using a stage mechanism driven by an AC linear motor and guided by a rolling ball guide. The nanometer-order dynamic characteristics of the guide are different in different displacement regions. We demonstrate that the stage with a single mechanism works both as a long stroke stage with a high velocity and a nanometer positioning stage by changing the control mode.

Configuration of the system

The experimental system consists of the following: (1) a one-axis stage mechanism (Fig. 1) comprising an AC linear motor, a rolling guide mechanism and two position sensors, coarse and fine, (2) power amplifiers, (3) controllers and (4) a data processing computer.

Microdynamics of the rolling guide

The force to displacement relationship of the rolling guide and the dynamic models of the stage are shown in Fig. 2. The dynamic property of the guide changes with the displacement:

Region 1; in a displacement of less than 100 nm, the force is proportional to the displacement which means that the group of balls acts as a spring element,

Region 2; in a displacement between 100 nm and 100 μm, the balls act as a nonlinear spring,

Region 3; in a displacement over 100 μm, normal rolling takes place and the force saturates.

The dynamic property in region 1 is suitable for fine position control and the dynamic property in region 3 is suitable for long-stroke coarse position control.

Figures 3 and 4 show the relationship between the displacement and force for the reference inputs in which the displacement response was partly reversed. The whisker-shape responses correspond to the transition between the three regions. From these measurement, the characteristics in region 1 and 2 are considered not to vary with position changes.

Coarse position control

The stage dynamics in region 3 are that of a simple mass system acted on by the rolling friction force as shown in Fig. 2. The coarse position control is designed as a combination of a proportional position control and a proportional-integral velocity control. The velocity is obtained from the coarse position signal using a frequency-to-voltage converter. The one-pulse (100 nm) step response is shown in Fig. 5. The stage position followed the reference and no backlash was observed. A maximum velocity of 200 mm/s was achieved in the control as shown in Fig. 6. This value was limited by the maximum pulse rate of the coarse sensor.

Fine position control

The stage dynamics in region 1 are of the simple mass-spring system as shown in Fig. 2. The fine position control is designed as a simple integral control with a cascaded second order lag filter to stabilize the control system. The one-nanometer step response is shown in Fig. 7. The stage position precisely followed the reference and no backlash was observed. The bandwidth of the fine control was higher than 100 Hz.

Switching from coarse to fine positioning control

It was found that the dynamic property transition from region 3 to 2 and 1 easily takes place when the motor force is released. Using this phenomenon, a long-stroke and fine resolution positioning can be obtained by the following sequence:

(1) carry out long and coarse positioning from the starting point to the reference position,

(2) release the deformation of the balls just after the coarse positioning is completed,

(3) this release causes a dynamic property transition from region 3 to 2 then 1

in that order,

(4) after that, activate the fine position control and adjust the coarse positioning error.

Conclusions

A nanometer position control system has been constructed using a single stage mechanism driven by an AC linear motor and guided by a rolling guide mechanism. By using the microdynamics of the rolling guide, a nanometer positioning of better than 1 nm resolution, 200 mm/s maximum velocity and 250 mm stroke is achieved.

Reference

1) Futami S, Furutani A and Yoshida S : Nanometer Positioning and its Micro-Dynamics, Nanotechnology 1 (1990)

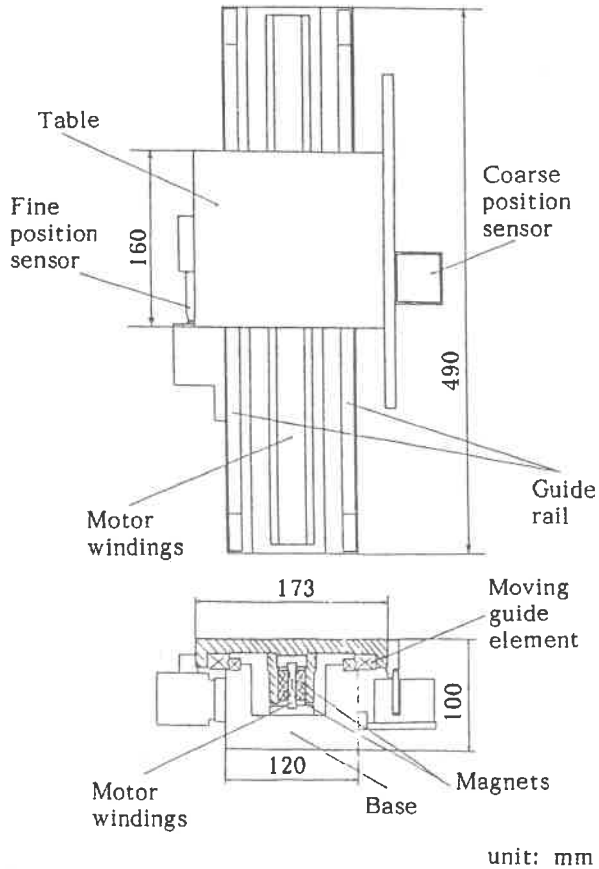

Fig. 1 Structure of the stage mechanism using an AC linear motor and a rolling guide.

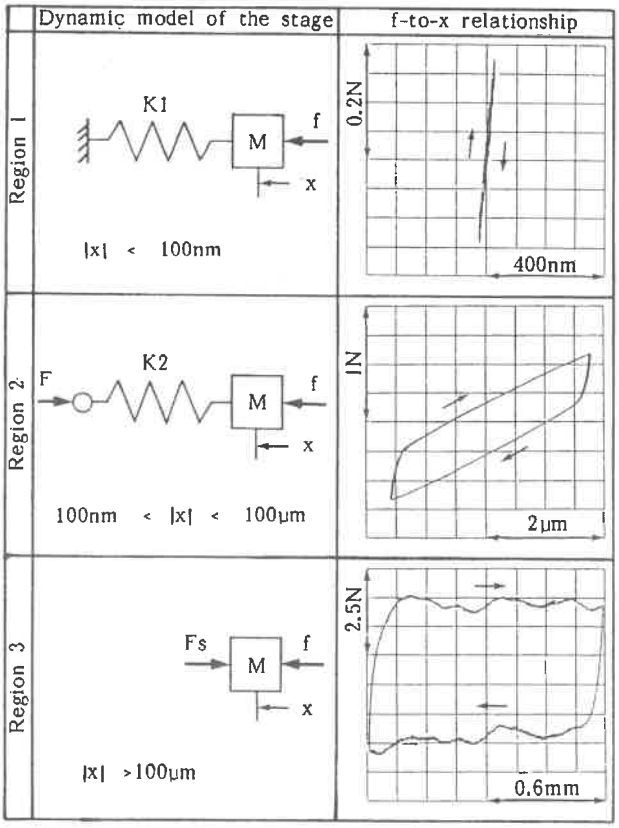

Fig. 2 Dynamic models and measured force-to-displacement relationships of the stage.

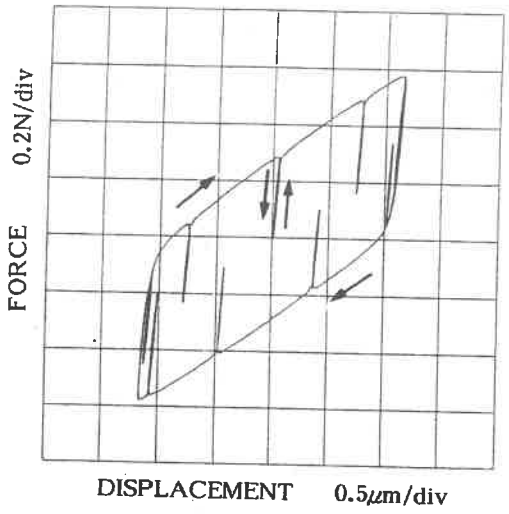

Fig. 3 Force-to-displacement transition response between regions 2 and 1.

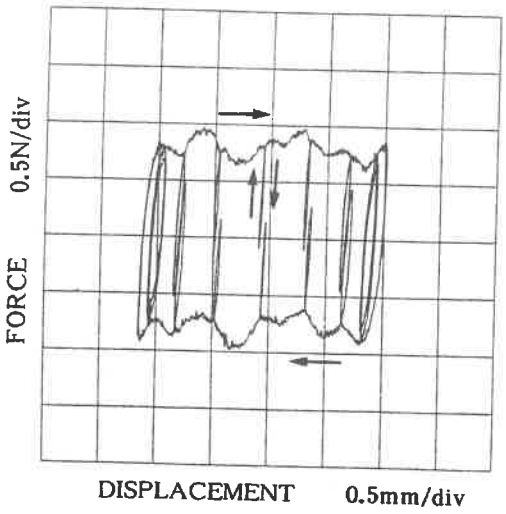

Fig. 4 Force-to-displacement transition response between regions 3 and 2.

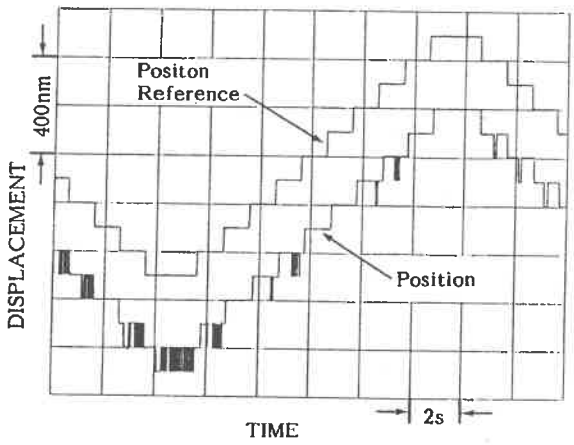

Fig. 5 One-pulse (100 nm) step response of the coarse position control.

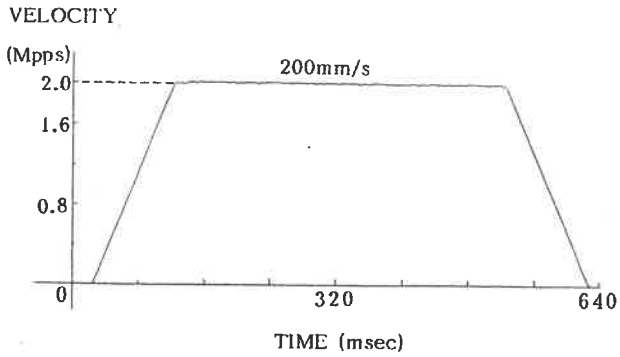

Fig. 6 Maximum velocity response of the coarse position control.

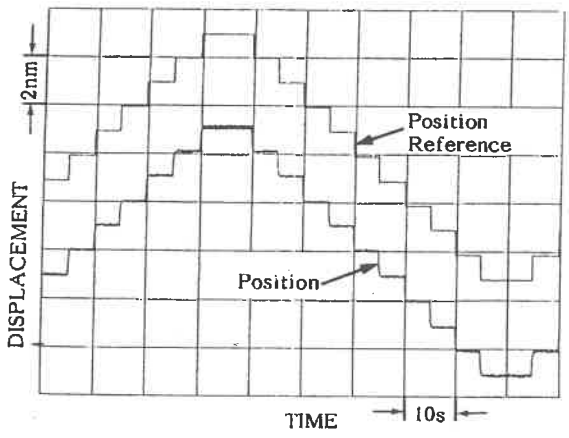

Fig. 7 One-nanometer step response of the fine position control.

CIRCUMFERENTIAL AND INNER DIAMETER METROLOGY FOR THE ADVANCED X-RAY ASTROPHYSICAL FACILITY (AXAF) OPTICS

Thomas E. Gordon
Hughes Danbury Optical Systems, Inc.
100 Wooster Heights Rd.
Danbury, Ct. 06810

Summary

The Advanced X-Ray Astrophysical Facility (AXAF) is part of NASA's Great Observatory program, and is scheduled for launch in the late 1990's. A Wolter Type I grazing incidence telescope, it is planned to study high energy astronomical phenomena which emit in the x-ray spectrum from 0.1-10 KeV (.124 - 1.24 Å). The telescope consists of 6 nested, confocal parabola/hyperbola pairs, with the conic figure polished on the inside surfaces of cylindrical substrates. The 12 cylindrical elements are 1 meter in length and range in diameter from 0.5 - 1 meter.

The specifications for the AXAF optics place strict requirements on the metrology instrumentation used to guide the fabrication process; in general, the accuracy of the measurements must be an order of magnitude better than the quality of the finished product. This is true for each of the measured parameters, which include axial figure, circumferential figure, inner diameter, and surface microroughness. Axial figure, circumferential figure, and inner diameter data are used to form maps of the inside surface of the optics, and form the basis for the subsequent fabrication cycle. Surface microroughness is used to determine the scattering performance of the system. This paper describes the facility used for the measurement of circumferential figure and inner diameter. This facility, the Circularity and Inner Diameter Station (CIDS), measures inner diameters of over 40 inches to within 70 microinches and acquires circularity data which is accurate to better than 1 microinch rms after averaging and the removal of systematic errors.

Design

The CIDS is used to acquire data on the inside surfaces of the AXAF optics throughout the entire fabrication process, from the initial grind to the final polish. It is located in an acoustically isolated enclosure which also has thermal control of better than +/- 0.5 ° F. The instrumentation is placed on a 2.5 foot thick granite table, which is in turn supported by 6 isolation legs. A 50,000 pound rotary/X/Y air bearing assembly and a Precision Metrology Mount (PMM) are used to support, maneuver, and align the AXAF optics once they are loaded into the station. At the center of the Rotary Table Assembly (RTA) is the Circularity and Inner Diameter Instrument (CIDI), with which all data is acquired. The basic design concept and preliminary layout drawings of the CIDI were developed at Hughes Danbury Optical Systems (HDOS), and the detail design and fabrication were carried out by Cranfield Precision Engineering Ltd.

Figure 1 shows a schematic of the CIDI. The instrument uses a pair of diametrically opposed air bearing probes to measure both inner diameter and circularity at 2 axial positions. In the inner diameter mode, an Invar reference standard of known length is used to calibrate the system before the optic is measured. In the circularity mode, a precision air bearing rotates the instrument, with the air bearing probes in light contact with the AXAF substrate.

The main assembly consists of two steel support columns. One column carries two measurement units and the other lends symmetry and structural stiffness to the design. This structure rotates on a standard Cranfield bearing which employs two opposed hemispherical air bearings for tilt stability. Each of the two measurement units has two radial probe axes and is also driven axially to allow access to different areas of the optic. All seven control axes (4 radial, 2 axial, and 1 rotational) are driven via a standard Cranfield motion controller, which in turn receives direction from HDOS station computer software.

Each radial axis includes a double pass laser interferometer displacement system for high resolution (5 nm) measurement of probe position. As shown in Figure 2, the optical system uses two quarter-wave plates on either side of a rotary interface, such that the light is circularly polarized between them. This maintains linear polarization at each measurement axis during rotation, allowing the laser source and the accompanying thermal loads to be separated from the instrument itself.

Polarization nonlinearities are introduced into the interferometer axes from a number of sources, yielding changes in path length measurements which must be accounted for in order to meet the performance requirements of the station. One source of polarization nonlinearities is the laser beam itself. While very close to being linearly polarized, it is slightly elliptical even as it exits the laser head. Another source of polarization effects is the pair of quarter-wave plates, which introduce slight changes in the polarization characteristics of the beam. Both the laser and the quarter-wave plates are common to all interferometer axes, and their effects vary with the rotation angle of the instrument. The interferometers themselves are the final source of polarization nonlinearities, as they are comprised of polarization beamsplitters and quarter-wave plates, each with its own imperfections. The result of all of these effects combined gives each interferometer axis a unique signature. This signature is carefully characterized and the results are removed from subsequent raw circularity data.

Given the cone angle of the AXAF elements (up to 2.5 degrees), a critical parameter for inner diameter metrology is the axial position at which the measurement is taken. A number of precautions have been taken, both in the design of the instrument and in the measurement scenario, to assure that this location is well known. First, the axial encoder scales for each measurement unit are mounted on an Invar spar in order to reduce thermal effects and give a stable datum. The encoder heads themselves are mounted on the measurement carriages, which are in turn coupled to the steel support column. In this configuration any thermal growth of the structure affects the measurement carriage and encoder head, but the motion is detected and corrected by way of the stable encoder scale assembly.

With independent measurement units and encoder scales, a means of determining the relative axial positions of the probe measurement axes is needed. This is accomplished using a 33 inch axial reference bar made of Invar, whose length was carefully calibrated to better than 50 microinches. One probe on each carriage is brought into contact with the bar, and the two carriages are moved axially in 1 micron steps until each probe extends past the edge of the bar. The same procedure is carried out with the opposed pair of probes, and the average of the two measurements gives the axial separation at the center of the two carriages. A similar scenario is used with the actual AXAF elements to determine the datum position during station initialization.

Measurement Scenario

A typical measurement begins with the alignment of the station rotary axis to gravity to within 5 arcseconds. An AXAF optic is then loaded into the station through overhead doors, "floated" on the Precision Metrology Mount (PMM) , and aligned to the station axis to within 50 μm of decenter and 7 arcseconds of tilt. The PMM consists of 18 support points, and has instrumentation that assures proper support of the optic in a "gravity free" configuration.

Station initialization is performed to accurately determine the datum position before beginning measurements. Inner diameter data is then taken at the nominal clear aperture of the optics. The measurement carriages first access and datum in the Invar reference bars, then move down into the optic to measure the inner diameter. 3-5 circularity scans are acquired, using all four probes, at the same axial positions. During a circularity scan, a data point is taken every 3.6 arcseconds, which corresponds to a spatial period of < 25 μm. The scans are then averaged together to yield a single scan from each probe.

In order to pinpoint errors due to improper loading of the PMM, the optic is raised off of the PMM and the refloated, after which the measurement process is repeated. After three independent 'floats' of the optic, differences between the resulting averages are analyzed for PMM induced figure distortions. If no appreciable errors are found, all of the scans are averaged together to yield one set of circularity profiles.

A similar set of data is acquired with the optic rotated by 180 degrees. The two sets are analyzed using the Donaldson Reversal technique to determine the systematic spindle errors of the instrument , which are then backed out of the data. The end result is a single scan for each axial position, where the systematic errors have been removed, and the random errors have been reduced by a factor of 5 through averaging. High frequency noise is then removed from the data using various filtering algorithms, the filters themselves changing depending on the spectrum of the noise present and the particulars of the next grinding/polishing operation.

Grey Noise

Due to the large amplitude microroughness which exists on the ground surface, the air bearing probes tend to 'skip' on the surface, resulting in relatively high frequency, unidirectional spikes in the data. Since ground surfaces are commonly termed 'grey', we call this 'grey noise'. This source of noise is particularly dependent on two factors; surface quality and profile velocity. Table 1 shows the band-limited rms amplitudes for the single scan repeatability achieved under different surface conditions and profile velocities. This data shows a dramatic decrease in the level of noise, both as the surface of the substrate improves and as the profile velocity decreases. Figures 3 and 4 show the polar plot and the PSD representation of the lowest of these noise limits, achieved on a 5 microgrit surface scanned at 0.6 degrees/sec. The random noise level is expected to continue decreasing with the improvement of the substrate microroughness. The flattening of the PSD curves in the high frequency regime (> 0.5 cycles/degree) is a result of the physical characteristics of the probe, where the inertia of the probe is too high to respond to the high frequency microroughness of the surface. In this regime, electronic and laser gauge noise dominate and result in a well behaved white noise spectrum.

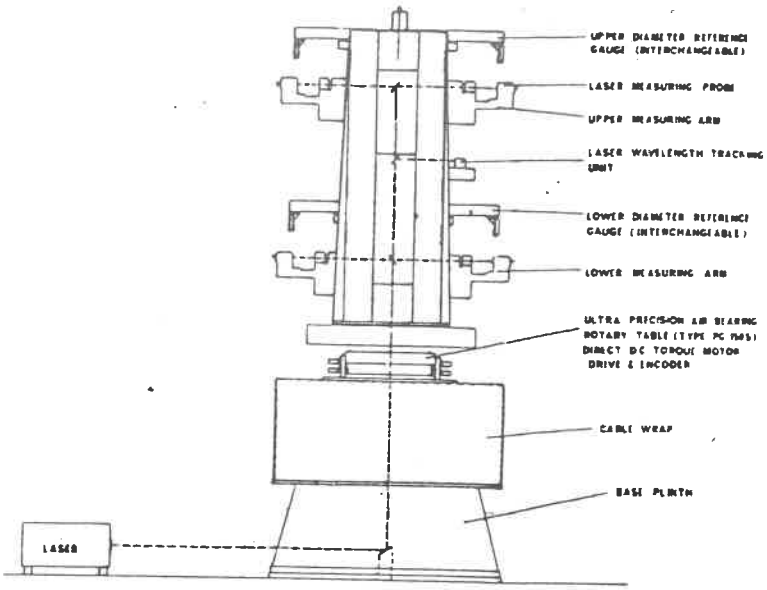
UPPER DIAMETER REFERENCE GAUGE (INTERCHANGEABLE)
LASER MEASURING PROBE
UPPER MEASURING ARM
LASER WAVELENGTH TRACKING UNIT
LOWER DIAMETER REFERENCE GAUGE (INTERCHANGEABLE)
LOWER MEASURING ARM
ULTRA PRECISION AIR BEARING ROTARY TABLE (TYPE PC 7565) DIRECT DC TORQUE MOTOR DRIVE & ENCODER
CABLE WRAP
BASE PLINTH
LASER

Figure 1. CIDI Schematic

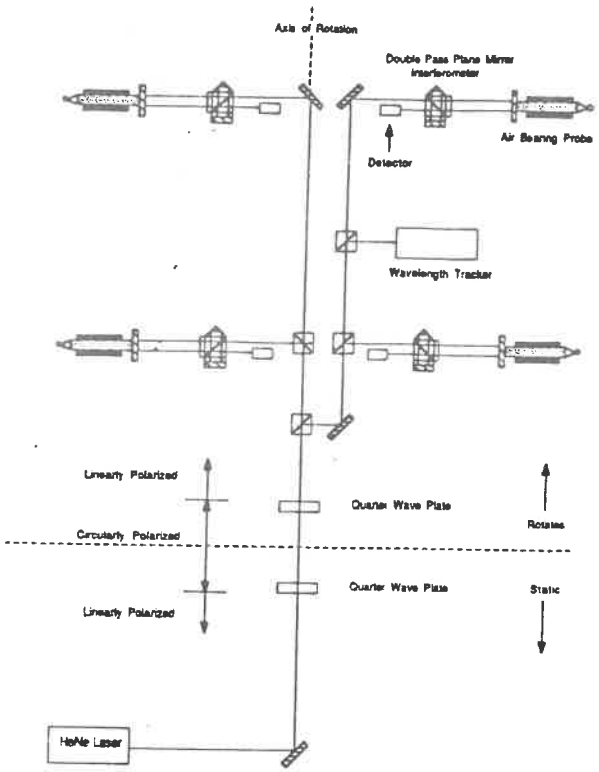

Figure 2. CIDS Optical Schematic

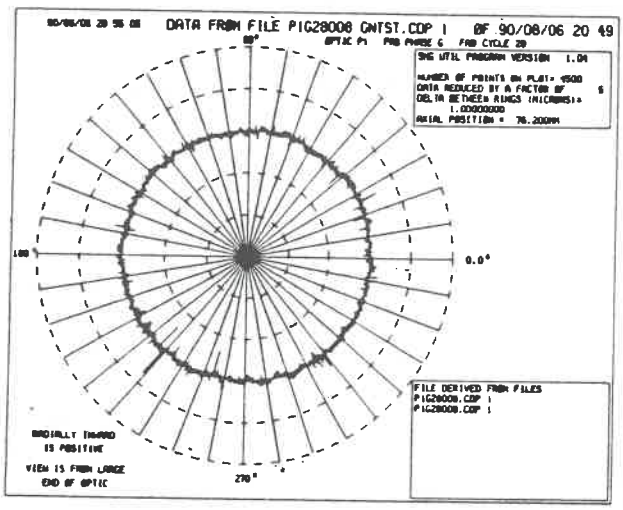

Figure 3. Single Scan Noise - Polar Plot : 1 µm per Division

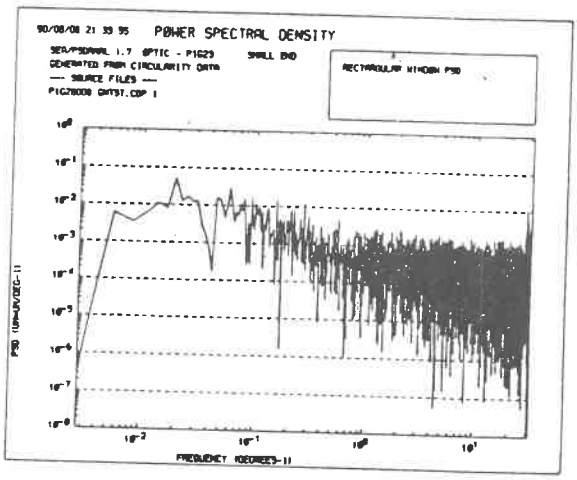

Figure 4. Single Scan Noise - Power Spectral Density

	Bandwidth (cycles/degree)			
	0.003 - 0.1	0.1 - 1.0	1.0 - 10.0	10.0 - 31.0
12 µgrit, 1.2 degrees/sec	0.081	0.198	0.250	0.324
5 µgrit, 1.2 degrees/sec	0.040	0.128	0.189	0.187
5 µgrit, 0.6 degrees/sec	0.022	0.023	0.038	0.052

Table 1. Single Scan Repeatability vs Surface Quality and Profile Velocity
Bandlimited RMS Amplitude (microns)

ULTRA PRECISION ASPHERICAL LENS PROCESSING MACHINE
-ULTRA PRECISION LOCUS CONTROL BY MEANS OF A LINEAR MOTOR-

K. Kubo, H. Nagano, S. Kubota, S. Mochida, M. Takahashi, K. Matsumura, and S. Ueda

Matsushita Electric Industrial Co., Ltd.
Production Engineering Laboratory,
2-7 Matsuba-cho, Kadoma, Osaka, 571 JAPAN

1. Introduction

With the recent increasing demand for smaller-size and higher functional audio and visual apparatus, request for optical lens from conventional spherical lenses to aspherical lenses has also been accelerated. However, grinding of the aspherical surface with high accuracy and speed is not an easy task compared with that of the spherical surface.

With the use of ceramic hydrostatic airslide stage and a linear motor, a high speed ultra precision aspherical lens processing machine was developed. The grinding process was carried out by a two-stage grinding (of rough and fine grindings) with a diamond wheel, and final finishing was performed by a polishing process. Assuring the contour accuracy was accomplished by a grinding process in this processing machine.

2. Machine Configuration

The major specification of ultra precision aspherical lens processing machine developed this time consists of the following; Maximum diameter of lens blank, ϕ50 mm; Speed of main spindle rotation, 1,000 rpm; Speed of grinding stone rotation, 30,000 rpm; and Minimum travel unit, 5 nm/pulse (on X and Z axes).

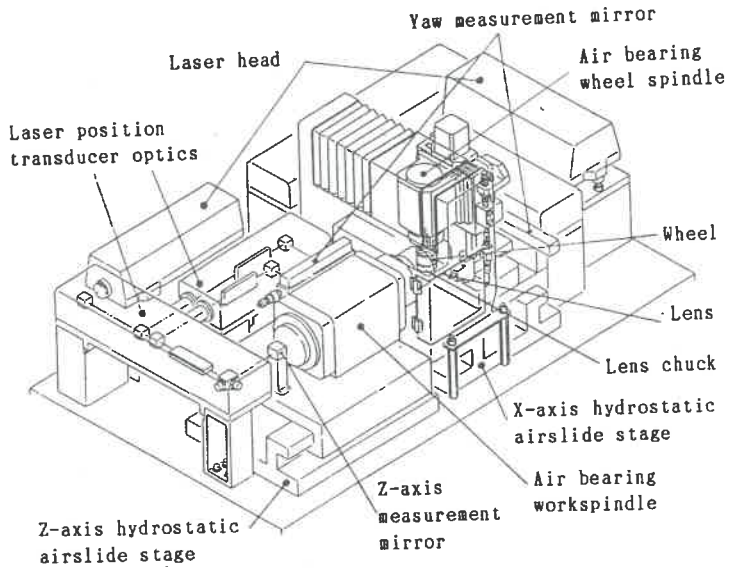

Fig. 1 Mechanism of Ultra Precision Aspherical Lens Processing Machine.

Fig. 1 shows its fundamental configuration and Fig. 2 is an external appearance of the processing machine. The arrangement of slide stage is a T-shape structure, with a grinding stone spindle arranged on an X-axis stage and a work spindle on a Z-axis stage. In order to assure

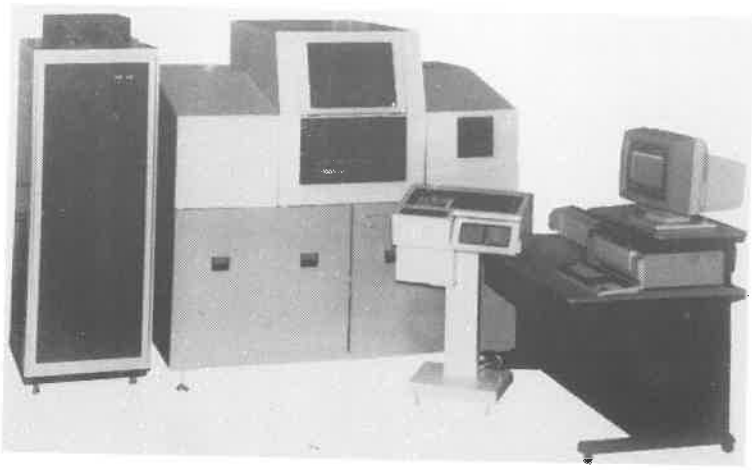

Fig. 2 Apperance of Ultra Precision Aspherical Lens Processing Machine.

necessary accuracy on the relative position between the diamond wheel at a processing point and a workpiece, a mechanical unit was mounted on a cast iron base with a low expansion coefficient, the base of which is supported by an air vibration isolator unit. Each structural component is controlled under temperature deviation within +/- 0.5 oC for pneumatic source, grinding fluid, room temperature, etc., for the purpose of controlling not only static elements but also dynamic elements such as heat, vibration, grinding load, and so forth.

The ability to achieve a higher contour processing accuracy is thus accomplished by conducting a 6-axis compensation control, which compensates errors resulted from a side dislocation and yawing of the stage by detecting positional changes in traveling as well as in a perpendicular direction utilizing HP laser position transducer which has a minimum resolution of 5 nm for measuring the stage positions. The fundamental principle of this 6-axis compensation is based on such a method that, in case side dislocation in the X-axis or yawing error is generated on the stage, correction is made by moving the Z-axis stage and, in the reverse case, correction is made by performing reverse motions of X- and Z-axes. To carry out this 6-axis compensating control, an NC controller was newly developed for an exclusive use of the purpose above. The NC controller performs these calculations in 1 msec, and outputs the results to a D/A converter.

A high speed processing for rough and fine grindings is achieved by using a wheel spindle of high speed rotation, mounting two diamond wheels of ultra abrasive grain which are slidable in a direction of rotation axis, and simultaneously switching the processing grinding stones.

Highly sensitive and accurate velocity detectors are required for highly accurate locus control. However, there have not been conventional linear velocity detectors which satisfy the requirements of locus control with high accuracy. To achieve highly accurate locus control, a linear optical tachometer was developed by us with no phase lag and less ripple error component using two sine wave signals having a 90o different phase in a linear encoder.

The velocity signal from the optical tachometer developed this time is not influenced by the magnitude of two sine wave signals. A linear encoder produced by Heidenhain with a slit pitch of 10 um was used for this optical linear tachometer, and

detection of mechanical origin point is also carried out with the reference mark on its glass scale.

A configuration of the optical tachometer developed this time is shown in Fig. 3. In this conventional method of velocity detection velocity signal has been obtained by the following process as shown in Fig. 4.

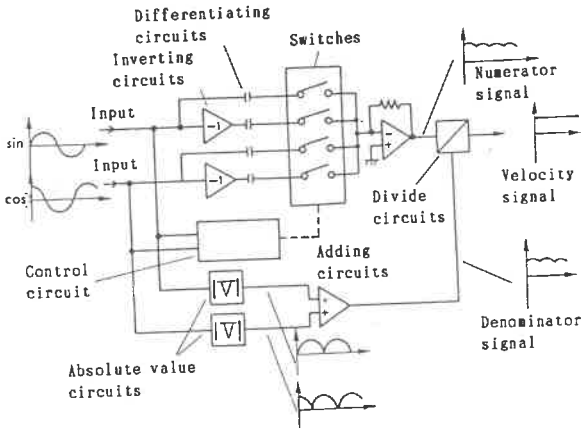

Fig. 3 Structure of optical tachometer.

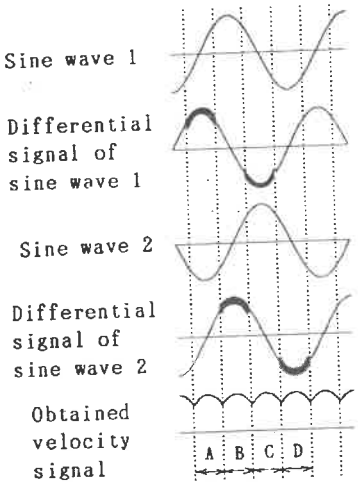

Fig. 4 Conventional method of velocity detection

In region A, differentiated signal of sine wave 1 is selected, then differentiated signal of sine wave 2 selected in region B. In region C, differentiated signal of 1 is selected and inverted its polarity, then differentiated signal of sine wave 2 is selected and inverted its polarity in region D. Those four signals thus selected are successfully connected by switching. Thus, velocity signal is obtained. However, in this conventional method due to ripple error component of differentiated signal, velocity detection errors will result.

Therefore, in this development, these problems are resolved with this configuration by inputting to the numerator of divider the signal from the encoder which is differentiated and at the same time inputting to the denominator of divider the signals from the encoder, and by finally obtaining the results of division as a form of velocity signal. Fig. 5 shows the results of velocity signals thus detected, in which an decrease in ripple component from 29.4 % to 5.1 % can be seen.

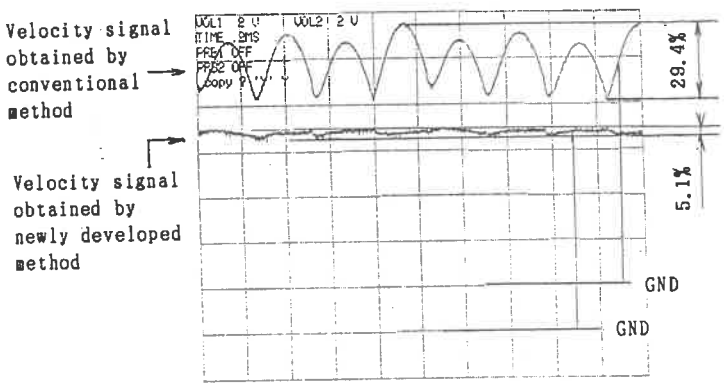

Fig. 5 Result of velocity detection measurenemt.

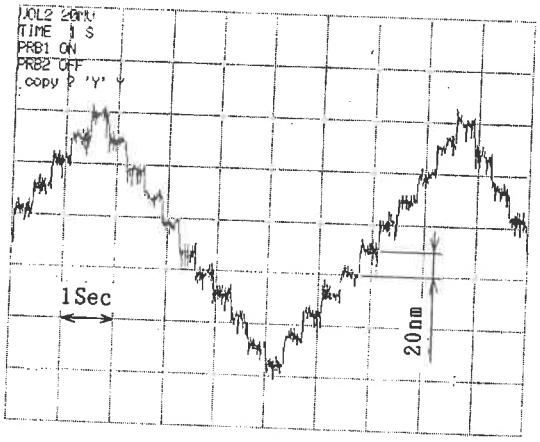

Fig. 6 Result of positioning accuracy measurement.

In order to make sure that the positioning accuracy of the slide stage is sufficiently enough, the results obtained by a 20 nm step feed are shown in Fig. 6. This gives us assurance of our obtaining the sufficient positioning accuracy, with a minimum travel resolution of less than 20 nm.

3. Conclusions

With the configuration as described above, a high speed ultra precision aspherical lens processing machine was developed which shortened by 1/6 the processing time so far taken with the conventional machine and which was also capable of flexibly processing a wide range of aspherical lenses with contour accuracy of 0.25 um (p-p).

References

1) S. Mochida et al.: Flexible Manufacturing System for Aspherical Glass Lenses, National Tech. Report. 36, No. 2, P. 32 (1990)

A PORTABLE NON-RECIRCULATING TEMPERATURE ENCLOSURE

Dan E. Luttrell
Senior Development Engineer

Rank Taylor Hobson Inc
P.O. Box 543, Precision Park
Keene, NH 03431

Dimensional stability in ultra-precision machining and metrology is an important requirement achieved primarily by keeping temperature variations around the equipment to a minimum. This is usually achieved by constructing special rooms in a building or assembling enclosures that provide a constant flow of controlled temperature air around the equipment.

Typically these enclosures recirculate air and make adjustments to temperature by first cooling and then reheating the air in a controlled fashion. It is in the reheating loop that the final fine control of the air temperature is accomplished. This is usually done by a liquid-air heat exchanger with a proportioning valve or with electric heaters. Banks of incandescent light bulbs have also been successfully used for this purpose.

Enclosure Description

To meet the needs of an ever changing R&D area, a 10'×12' constant temperature enclosure was constructed so that it could be easily rolled from one machine to another. This enclosure provides approximately 2000 SCFM of air which flows from the top through perforated ceiling tiles, over the equipment and out at floor level. Vinyl curtains form the enclosure walls and provide easy access. These curtains stop 12" from the floor and this provides the opening for air to flow out of the enclosure.

A portable 36,000 BTU air conditioner takes 2000 SCFM of room air, cools it about 10°F and supplies it to the top of a 14" high plenum above the entire enclosure. Electric heaters are located at the inlet of the plenum for the reheat loop.

This enclosure does not recirculate air as most facilities do, but is of a simpler, single pass design. This enables the enclosure to be constructed so duct work is minimized and portability enhanced. The penalty of such a design is added difficulty in controlling the temperature. Environmental changes outside the enclosure have a greater impact on temperature variations in this type of design.

Temperature Control

Experiments with a number of different control schemes where conducted. It was found that a time delay was the major obstacle to improving temperature stability in the enclosure. Source of this delay was found to be the electric heaters. They had a time constant much longer than expected and therefore added a destabilizing effect to the system.

The problem was overcome by adding a set of damper valves in the supply duct that mixed hot and cold air supplied by the condenser and evaporator sections of the air conditioning unit. A DC

motor actuated these valves and a personal computer was used to read temperature sensors and generate a control signal.

Because the valves could be moved very quickly, a change in the supply air temperature to the enclosure of several degrees could be made within a few seconds. Using just the electric heaters that were installed, this same change took well over a minute. It was this difference in response time that reduced temperature variations from $\pm 0.25°F$ with the electric heaters to $\pm 0.03°F$ with the damper valves – almost an order of magnitude improvement.

A control signal for the damper was generated based on measurements from one thermistor sensor in the supply duct just downstream from the damper valve and one inside the enclosure. Damper valve position was controlled by a proportional loop based on the supply duct sensor. The set point of this loop was adjusted by the enclosure sensor and thus formed an outer control loop. This simple combination proved to be very effective in maintaining short and long term temperature stability.

Temperature Measurements

Temperature recordings taken in the enclosure have shown variations to be within $\pm 0.03°F$ when the room variations were as much as $\pm 1.5°F$. Figure 1 is a plot of room and enclosure temperature taken over a period of two hours. Measurements were taken at one second intervals with a moving average of these measurements over 10 samples recorded at one minute intervals. Maximum and minimum values of the one second measurements were also recorded for each one minute interval to catch any short term transients. However, no significant difference was noted between these values and the moving average values.

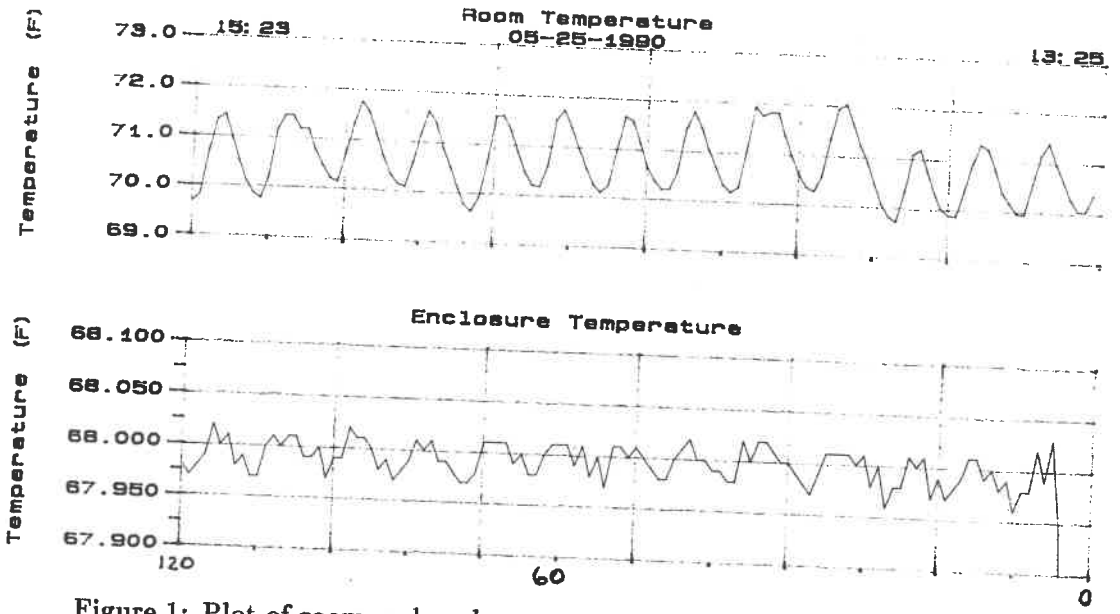

Figure 1: Plot of room and enclosure temperature over a two hour period.

Summary

This project has shown that an inexpensive non-recirculating temperature enclosure can provide a stable environment for precision machine and metrology equipment. Most constant temperature facilities can cost anywhere from $50,000 and up, but this enclosure was built for less than $20,000. Temperature variations in this enclosure can be kept within $\pm 0.03°F$ even when it is located in a rapidly changing thermal environment.

The problem of time delay in the control of air temperature enclosures was found to be the limiting factor in reducing temperature variations. This problem was overcome with the use of a fast acting damper valve that mixed cold and hot air in the supply duct. This quick mixing of hot and cold air is the key to this system and produced almost an order of magnitude reduction in temperature variations when compared to the case where electric heaters were used for control.

A b s o l u t e L a s e r r e f r a c t o m e t e r

Dr. D. Frölich, H.-P. Meiser, D. Frerking
Spindler & Hoyer GmbH
Göttingen, Germany

Laser interferometers are widely used for accurate determination of length and for the calibration of precision length - measuring equipment and tooling machines. The accuracy of an interferometer is determined in part by the uncertainty of the wavelength of the laser light, which is determined by the uncertainties of the laser frequency and the refractive index, n, of the air. In most applications the uncertainty of n is 1 - 2 orders of magnitude larger than the uncertainty of the frequency. Due to this fact, a more precise determination of n will result in a significant increase in the accuracy of the interferometric measurement.

Up to now the following methods have been established for the determination of the refractive index of air:

1. The refractive index depends on temperature, pressure and the composition of the air. The so called Edlén formula expresses the dependence on temperature, pressure, and humidity, and is widely used for the calculation of n. This method has the disadvantage of a long time constant due to the temperature measurement and it does not take the generally unknown composition of the air into account.
2. A tracking refractometer determines the change of n during a given time. The absolute starting value of n has to be measured separatly. This method typically uses a highly stable interferometer whose measurement arm is floated with the air to be measured. A variation of the refractive index changes the optical pathlength in the interferometer which is used to calculate the change of n.

3. An absolute measuring refractometer is used for high precision measurement of n. It consists of a stable interferometer whose measurement arm has to be evacuated for each measurement. Because of its technical enviroment (vacuum pump) it is only used under laborotory conditions by calibration institutes.

We present a new absolute measuring refractometer which allows the determination of n whithout a vacuum pump. The refractometer is a compact device which can also be used in the industrial enviroment.

The basic principle is outlined in Fig 1 and shows the vacuum cell with variable length. There are two interferometers (1 and 2) which are used simultaneously to measure the refractive index. The inner interferometer, 1, measures the length variation of the vacuum cell using the vacuum wavelength of the laser. An actuator moves the window F_2 over a distance L while the window F_1 is held at a fixed position. The number of fringes measured by the interferometer 1 is :

$$N_1 = \frac{2L}{\lambda_0} \qquad (1)$$

λ_0 being the vacuum wavelength of the laser.

Moving the window F_2 produces a replacement of air by vacuum over the length L in the outer interferometer 2. This change in optical path length results in a fringe count :

$$N_2 = \frac{2nL}{\lambda_0} - \frac{2L}{\lambda_0} \qquad (2)$$

Using (1) and (2) n can be expressed as :

$$n = 1 + \frac{N_2}{N_1} \qquad (3)$$

This method has the following features :

- The refractive index is directly determined by the two fringe counts N_1 and N_2. Asuming that the value of n for air under normal conditions is appr. 1.00027, the relation N_2/N_1 takes on a value of appr. 1/3700. Using a simple counter for N_1 and precise zero crossing detection for N_2, this ratio is easily determined.

- Using L = 6 mm an accuracy of 5×10^{-7} is easily achieved.

- The actuation of the vacuum cell allows measuring rates > 1 Hz. This large data rate can be used to analyze fluctuations in the refractive index. The averaging time can be freely chosen and adapted to the fluctuations.

- A very compact design is possible because no vacuum pump is needed. Thus the refractometer can be placed near the measurement volume of the interferometer and can also be used in an industrial enviroment.

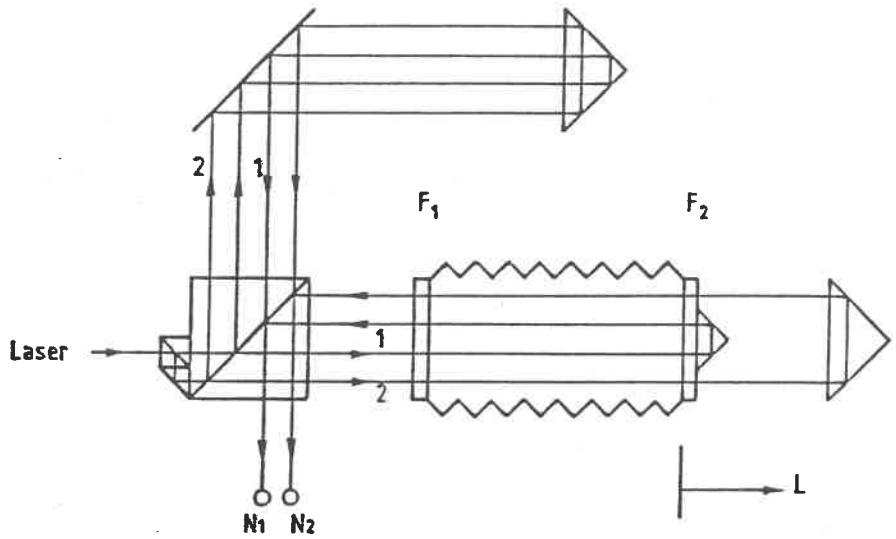

Fig. 1

FAST TOOL SERVO IMPLEMENTATION FOR DIAMOND TURNING

Michele H. Miller
Thomas A. Dow
Precision Engineering Center
North Carolina State University

1 Introduction

Diamond turning has traditionally been limited to rotationally symmetric surfaces. By adding a third axis in the form of a high bandwidth piezoelectric Fast Tool Servo (FTS), features can be machined within each spindle revolution. Potential applications for this technology are: diamond turning off-axis sections of conic surfaces on axis [1], machining shallow letters or figures into a surface [2], compensating for Z slide vibrations [3].

For non-axisymmetric cutting, the Z coordinate has two components: an axisymmetric component assigned to the Z slide and a high frequency non-axisymmetric component produced by the FTS (Z'). The controller for any axis has several tasks which include reading inputs, calculating a reference point, and sending an output voltage to the axis driver. However, the demands on a computer controller are significantly higher for controlling a low amplitude, 2000 Hz bandwidth servo than a large amplitude, 10 Hz bandwidth axis. The FTS, for instance, requires a cycle time on the order of 50 μsec $(1/(10 \times 2000\ \text{Hz}))$ to do closed loop control of its dynamics. A fast cycle time is also necessary to machine accurate non-axisymmetric surfaces at typical cutting speeds. At 1000 rpm, for example, a 50 μsec cycle time translates into 1200 reference points per revolution. A controller architecture which can accommodate the computation and I/O requirements for both types of axes has been developed. In addition, reference point generation schemes which minimize the computation and I/O requirements have been devised and implemented for two types of non-axisymmetric surfaces.

2 Controller Architecture

A parallel processing architecture, Heterogenous Hierarchical Architecture for Real-Time (H^2ART), has been developed at the Precision Engineering Center and adapted to control the Center's diamond turning machine [4]. The DTM H^2ART node consists of an Intel 80186 node controller, two Texas Instruments TMS320C25 digital signal processors (DSP's), and digital and analog I/O boards. The node controller downloads programs to the DSP's, initializes the DSP's, and allows communication between DSP's. The DSP's control the I/O boards and perform high speed calculations. One of the DSP's controls the X and Z slides while the other controls the fast tool servo.

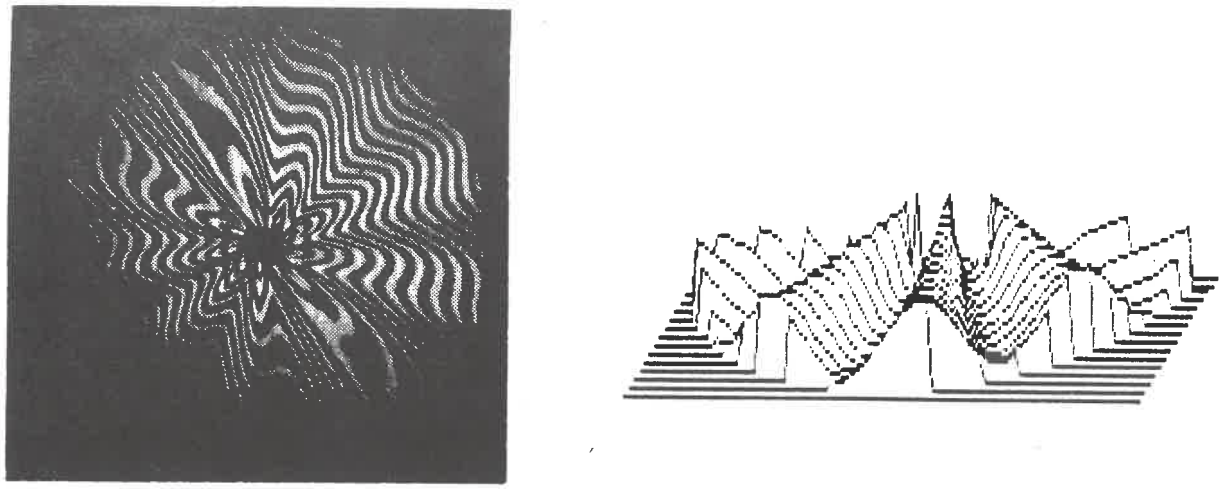

Figure 1: Zygo Mark IV images of circumferential sine waves

3 Reference Point Generation for Non-Axisymmetric Surfaces

For axisymmetric parts the axial dimension, Z, is a function only of the radial dimension, X. For example, the reference generation equation, $Z = X^2$, would produce a paraboloid. For non-axisymmetric parts Z has angular dependence. An example of a surface with angular but no radial dependence is $Z = \sin n\theta$. For this surface the Z reference point is calculated based on angular position provided by a spindle encoder. An example of a surface with both angular and radial dependence is $Z = X \sin n\theta$. In this case, Z is calculated based on angular position as well as X position from a laser interferometer.

Trigonometric Functions

Because non-axisymmetric optical surfaces are represented by expressions which include trigonometric functions, it is important to develop a method for evaluating them quickly. Because only a finite number of angular positions can be discerned with a spindle encoder, complete tables for each trigonometric function in the reference generation equation can be developed which require no interpolation between values. The FTS and H^{2}ART have been used to machine surfaces of the form $Z = a \sin n\theta$. Figure 1 shows an inteferogram and topographical plot of 0.6 μm P-V sine waves machined with a frequency of 10 cycles/rev at a cutting speed of 500 rpm. To machine this surface a table of DAC output values was prepared off-line and inserted into the DSP control program. During cutting the DSP output the next table value each time it received a new pulse from the encoder. Every tenth of a spindle revolution the control program returned to the beginning of the table.

Constant Depth Features

Assuming a constant feedrate and spindle speed, any surface with both radial and angular dependence can be converted into a surface with only angular dependence by using the linear relationship between R and θ. Since the tool traverses a spiral path with respect to the workpiece, R (or X) is

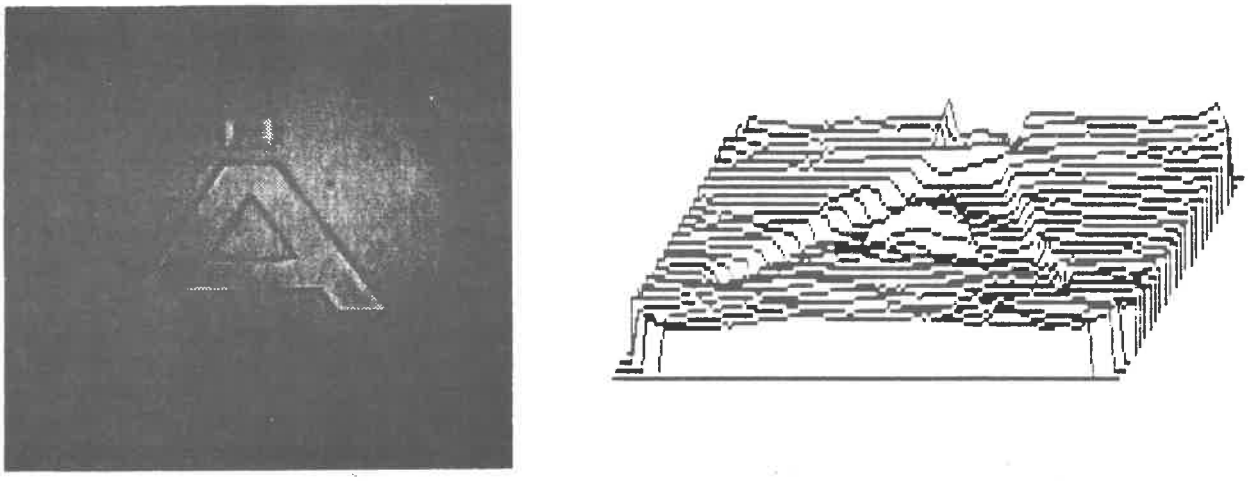

Figure 2: Zygo Mark IV images of 0.25 μm deep angstrom symbol

related to θ by

$$X = R_{wp} - \frac{f}{s}\theta \tag{1}$$

where,

$$\begin{aligned} R_{wp} &= \text{radius of workpiece} \\ f &= \text{feedrate} \\ s &= \text{spindle speed} \\ \theta &= \text{no. of revolutions since start of cut} \end{aligned}$$

The advantage of removing the radial dependence is that the FTS DSP does not have to read the X laser interferometer every controller cycle. The disadvantage is that tool centering errors and X slide following error introduce errors into the surface. To explore the limitations of this method, figures of constant depth were machined. For this type of cut only two tool positions (cutting depths) are used. The tool moves in or out where the cutting spiral intersects line segments which define a figure. The unique θ values corresponding to each intersection point can be found off-line and downloaded as an array to the DSP. During cutting the DSP counts encoder pulses, compares the count to the next number in the array, and increments or decrements the voltage to the FTS when appropriate. Figure 2 shows an interferogram and topographical plot of an angstrom symbol which was machined at 500 rpm.

Effect of Centering Errors Some of the initial cuts produced skewed figures caused by tool centering errors. The effects of Y and X centering errors were determined analytically and simulated. An error in the Y direction warps a square figure as shown in Figure 3(a). An error in the X direction causes figure edges to bow as shown in Figure 3(b). Both effects were observed in cut parts.

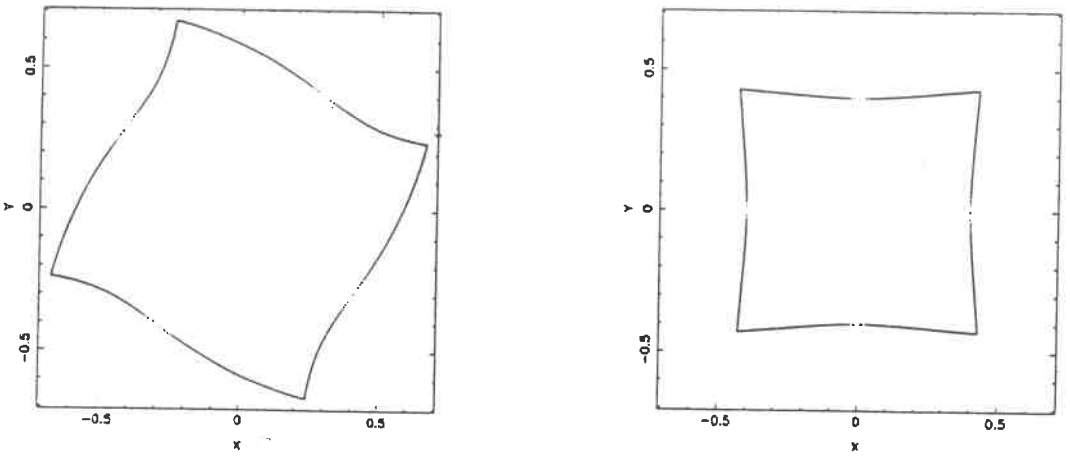

Figure 3: (a) Effect of Y direction tool centering error; (b) Effect of X direction tool centering error

4 Future Stages of FTS Implementation

The surfaces machined thus far required only encoder feedback. Exploiting the full potential of the FTS will require more on-line input conversion and computation. The FTS can be implemented in stages as outlined in the table below.

Application	Ref. Generation Equation	Inputs Required
Non-axisymmetric surfaces without radial dependence	$Z' = f(\theta)$	spindle encoder
Non-axisymmetric surfaces	$Z' = f(X, \theta)$	spindle encoder, X axis position
Z slide error correction	$Z' = f(Z)$	Z axis position
Closed loop control	$Z' = f(..., Z')$	FTS capacitance gage

References

[1] Gerchman, M. C., "An Exact Description of Far Off-Axis Conic Surfaces for Non-Rotationally Symmetric Surface Generation," ASPE Preprints, 1989.

[2] Falter, P. J., "Diamond Turning of Nonrotationally Symmetric Surfaces," *PhD Dissertation*, North Carolina State University, 1990.

[3] Fawcett, S. C., "Small amplitude vibration compensation for precision diamond turning," *Precision Engineering*, Vol. 12, No. 2, April, 1990.

[4] Fornaro, R. J., Garrard K. P., Taylor, L. W., "Architecture and Algorithms for Computer Control of High Precision Machine Tools," ASPE Preprints, 1990.

MICRO GRINDING AT AN ULTRA-HIGH SPEED REGION

S. Mochida, M. Takahashi, and S. Ueda

Matushita Electric Industrial Co., Ltd.
Production Engineering Laboratory,
2-7, Matsuba-cho, Kadoma, Osaka, 571 JAPAN

1. Introduction

It is well-known that even the optical glass and ceramics as one of brittle materials exhibit ductile as well as plastic behaviors, provided working conditions of a cutting edge is set up in a way that those materials are subjected to a stress field of less than the critical fracture stress 1)2)3).

For the purpose of achieving ultra-high precision grinding for aspherical optical lenses and ceramic mirror for an X-ray use, a trial was made for creating a model of grinding at the region described above, and then grinding was tried out by a single-point diamond with ultra-high speed of 5,600 m/min.

From the characteristics analysis on a single-point diamond grinding grooves, a possibility was found out in realizing a crack-free finished surface under high speed conditions, and thereby the report was compiled here.

2. Grinding Theory in a High Speed Region

In a single-point diamond grinding of glass as one of brittle materials, consideration is given to the conditions under which a processed surface is generated in a ductile mode. When a tool having a relative speed is given a forced depth of cut against the workpiece, the following phenomena are considered to be brought about in the grinding point:

(1) The workpiece heats up and softens due to deformation and friction with a tool.4)5)

(2) The neighborhood of the tool becomes high in pressure, thereby making it impossible to neglect the Bridgman effect.

(3) With an increase in strain rate, the fracture strain becomes decreased.

In general, glass as one of brittle materials is lower in heat conductivity by 1 - 2 orders compared with metal materials and the like, and therefore it is expected that the influence on softening from heat will decrease with the interaction of tool at high speed region. Therefore, it is considered that a behavior will be exhibited that governs the effect of decreasing the

fracture strain.

3. Experiment in Single-point Grinding of Glasses

3.1 Experimental method

In order to confirm a grinding behavior of optical glasses as a brittle material, a single-point grinding experiment of optical glasses was carried out with the use of a pyramid diamond stylus. Fig. 1 shows a schematic of the experiment.
Hydrostatic air spindle was used for a rotary disc with stylus. Work-pieces were mounted with a little inclination in order to continuously vary a depth of cut on hydrostatic air slide table, and was allowed to slide in a direction of stylus rotating axis at high speed and to form a single point grinding groove at every one rotation of the stylus.

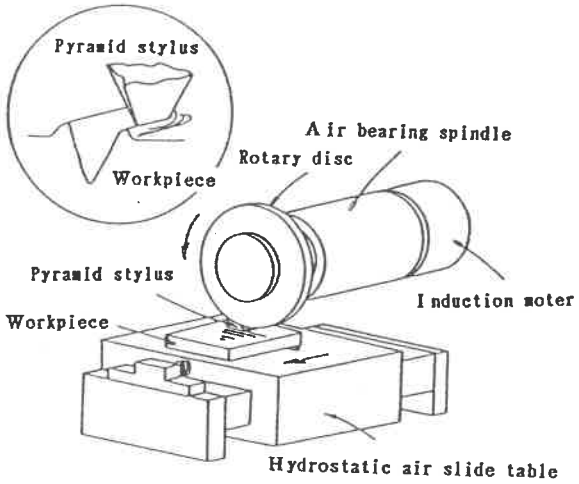

Fig. 1 Schematic of single point diamond grinding

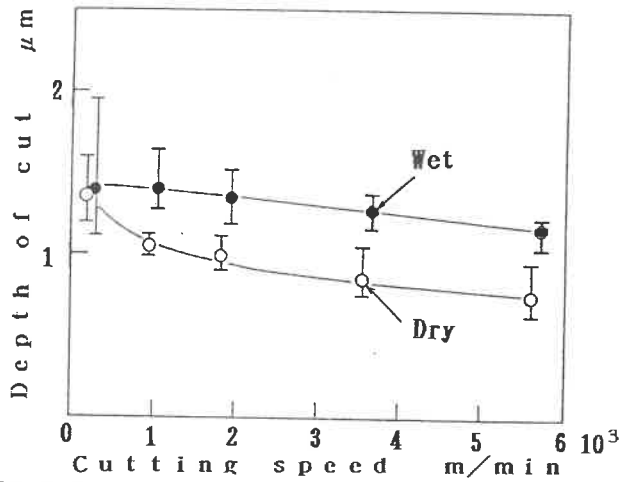

Fig. 2 Relation between cutting speed and depth of cut with BK7 by wet and dry

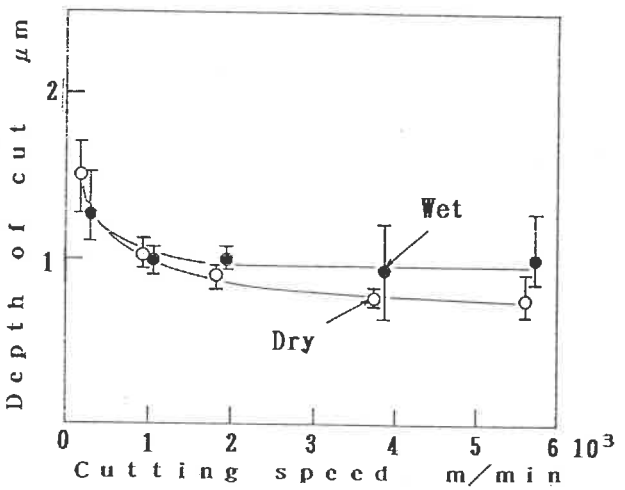

Fig. 3 Relation between cutting speed and depth of cut with SF6 by wet and dry

3.2. Experimental Results

Relations between critical depth of cut and cutting speed are shown in Fig. 2 and Fig. 3 in relation to ductile and brittle behaviors of workpieces BK7 and SF6, respectively. In a dry method, with an increase of cutting speed, the critical depth of cut is decreased, while in a wet method, no remarkable change is shown in a cutting speed region of up to 5,600 m/min. Also a wet method has a greater critical depth of cut

compared with a dry method.

Furthermore, Fig. 4 shows results of characteristics of observation on a single-point diamond grinding grooves which show a ductile behavior and also results of measurements on ductile pile-up condition around grooves for respective BK7 and SF6. No crack was observed on both workpieces, with favorable grinding grooves formed by a ductile behavior. The workpiece SF6 shows a greater ductile pile-up height by about 1.5 times, due to its lower hardness compared with BK7.

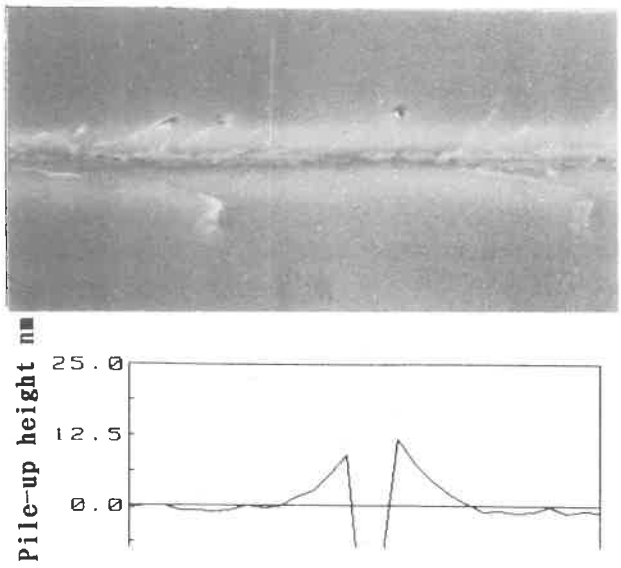

(a) BK7, cutting speed=5600m/min, wet

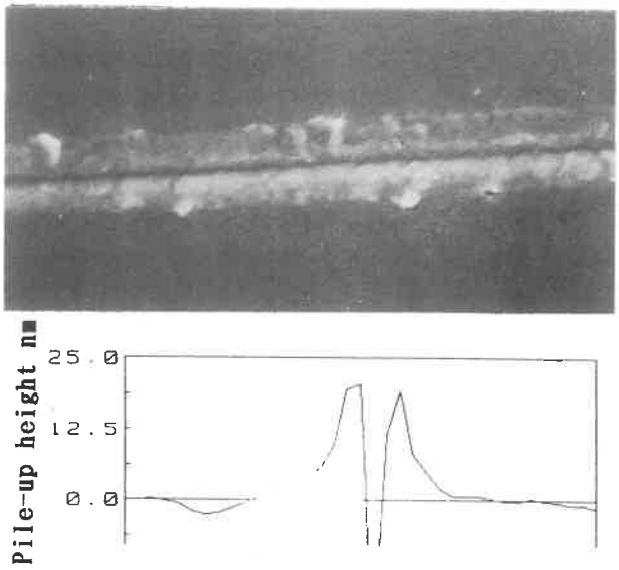

(b) SF6, cutting speed=5600m/min, wet

Fig. 4 Ductile cut surface on optical-glasses by SEM and measurement of pile-up height by WYKO

4. Discussion

(1) Dependency of grinding speed on critical depth of cut

The critical depth of cut decreases with a higher grinding speed. It is considered that a strain rate increases with a grinding speed, and then followed by a decrease in fracture strain. In a slow speed region, it is considered that sufficient heat transfer is achieved due to friction with stylus and material deformation, thus making the critical depth of cut greater.

(2) Influence of wet method on the critical depth of cut

In a wet method, it is considered that the critical depth of cut becomes smaller due to friction with stylus and a heat generation by material deformation in a slow speed region as described above.
However, in a high speed region, it is considered that a smooth

ductile behavior is exhibited owing to a decrease in friction resistance with the help of a lubricating effect of grinding fluid which makes it easy for cut chips to be flown out, thus providing expectation of a greater critical depth of cut.

(3) Microscopic observation on a single-point grinding groove by materials

It is considered that SF6 is easily subjected to plastic flow of material and, therefore, shows a greater ductile pile-up height because of its inherent lower hardness and higher fracture toughness compared with those of BK7.

Furthermore, in this experiment, it is also assumed that the above-mentioned results were exhibited remarkably due to the fact that a grinding groove was formed in a direction of one edge of the pyramid stylus.

5. Conclusions

For the purpose of achieving ultra-high precision grinding for aspherical glass lenses and X-ray ceramics mirror, an analysis on the shape of grinding grooves and discussion were made by creating a model of grinding in a high speed grinding region and a grinding with a single-point diamond. In consequence, conclusions were obtained as follows;

1) The critical depth of cut has the grinding speed dependency, and decreases with an increase in grinding speed.

2) With the supply of grinding fluid, the critical depth of cut in a high speed region is greater compared with that of a dry method.

3) There are difference in volume of ductile pile-up height depending on mechanical properties of the material.

References

1) N. Taniguchi: Material and Process, (1974), 83
2) R. R. Donaldson: Preliminary print for Spring Meeting of JSPE, (1988) 735
3) S. Ueda, etal: Preliminary print for Autumn Meeting of JSPE, (1984) 221
4) T. Sugita, etal: Possibility for Removing of Brittle Deformed type in Micro Cutting of Brittle Materials, J. JSPE. Vol 53, (1988) 2138
5) E. Usui: Cutting and Grinding Engineering, Vol 1, (1968) 31

Application of a Novel Two Step Digital Control Algorithm for Precision Actuation

Hakan Ozisik, Thomas G. Bifano, Thomas A. Dow
North Carolina State University
Precision Engineering Center
Raleigh, NC 27695

A two step, open loop, digital control scheme is implemented in a precision positioning process to minimize residual oscillations of an underdamped second order dynamic system. The control effort is delivered through the sequential application of two distinct output steps. Transient oscillations induced by an initial step are canceled by the application of a delayed second step. The net result is dead-beat a response time equivalent to one half of the system's natural period. Theoretical development of the method is given along with experimental verification for microinch step positioning.

When a precision process is coupled with dynamic response times on the order of the natural period of a structure, a system no longer behaves as a rigid body. Positioning operations in these time frames will result in residual vibrations of the system which can limit the achievable accuracy of a process. An appropriate method of system control must therefore be developed and incorporated into the dynamic process.

The present investigation is a method of open loop control which takes advantage of such conditions to produce a high speed, low amplitude, stable step response for systems with second order dynamic characteristics. The experimental fixture used to test this digitally implemented control scheme consists of a piezoelectric (pzt) actuator coupled to a fixed-fixed beam. The dynamic characteristics of the system are identified, a system model is developed using a lumped analysis and step response control is established through implementation of a two step algorithm. The equation of motion is expressed mathematically in standard form as

$$\ddot{x}(t) + 2\zeta\omega_n\dot{x}(t) + \omega_n x(t) = F(t)$$

The natural frequency of the system is $\omega_n = \sqrt{k/m}$ and $\zeta = c/2m\omega_n$ represents the damping ratio. The system is subjected to an external forcing function represented by $F(t) = A\omega_n^2 (1 - e^{-t/\tau})$, with $A\omega_n^2$ being the amplitude of the applied force. This particular form of the forcing forcing function is necessary to model the the first order dynamic behavior of the piezoelectric actuator. The time constant τ, embedded in the exponential,

takes into account a phase lag created by the capacative nature of the piezoelectric material. The solution to x(t) is written in closed form as follows

$$x(t) = e^{-\zeta\omega_n t} \{ A_o\cos(\omega_d t) + B_o\sin(\omega_d t) \} + A \{ 1 - Be^{-t/\tau} \}$$

where

$$B = \frac{\omega_n\tau^2}{1 - 2\zeta\omega_n\tau + \omega_n^2} \qquad A_o = A \{ B - 1 \} \qquad B_o = \frac{AB \{ \zeta\omega_n\tau - 1 \} - A\zeta}{\tau\omega_d}$$

The solution to x(t) mathematically models the uncontrolled response of the system to the input F(t). This response results in ringing and overshoot, which are not desirable characteristics for a precision positioning operation.

The control problem is addressed implementing a two step corrective algorithm. The first step begins by applying an actuating force at time t=0. A second step in force is then applied after predetermined amount of time. The net effect is dead-beat response of the system in a time equal to one half of the period of the free oscillations. Control is accomplished by taking advantage of the fact that the free response decays periodically at a single frequency in a deterministic manner.

Experimental verification of two step control for high speed precision positioning, tests were conducted on a flexible steel beam with fixed-fixed supports, axially positioned using a piezoelectric actuator. Parameters for the damping ratio, natural frequency, the time constant are experimentally determined to be 0.02, 1860 Hz, and 136 microseconds, respectively.

The beam is then experimentally excited with a 15 microinch step to observe the uncontrolled response. The output response of the beam to this step is seen in an oscilloscope trace in Figure 1. The frequency of oscillation is marked by the dotted cursor lines is approximately 1869 Hz. With a correct model developed the two step method can be applied to control transient oscillations resulting from application of a step input.

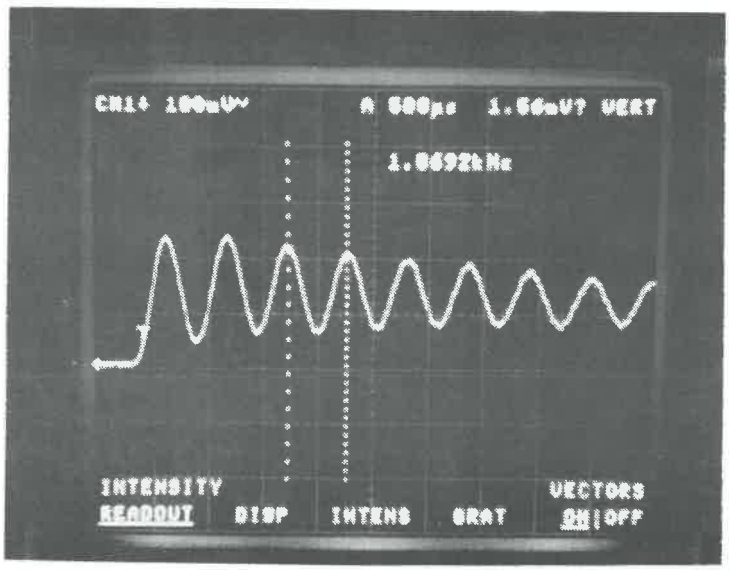

Figure 1 Uncontrolled output response

In order to produce a 20 microinch step response, a first step of 10 microinches is applied followed by a delayed second step of slightly lesser amplitude to account for damping in the system. For an undamped system the amplitude of the first and second steps would be identical. The amplitude of the second step, applied at time equal to one half the natural period, is determined through the amount of damping present in the system. Figure 2 is a simulation of the effectiveness two step control. An initial step of 10 microinches is applied at time t=0 and the uncontrolled response is plotted using dashed lines. The response to a second step of amplitude 9.3 microinches, applied at time t=0.269 milliseconds, is superimposed on to the free oscillation of the first step. The net response of two step loading is plotted as a solid line. The steady state amplitude is slightly less than 20 microinches and the time to reach 90 percent of this value is around 0.5 milliseconds. The simulation illustrates controlled low amplitude motion on the order of the structural natural period (0.537 milliseconds).

Experimental verification of the procedure was then implemented. The timing and voltage levels of the the applied two steps are controlled using a high speed D/A board at a 20 kHz sample rate. The signal is amplified using a Burleigh PZ-70. Axial output motion of the beam detected using a capacitance probe. Final displacement output is recorded on a digital oscilloscope. The input signal generated by the D/A board, shown in the lower trace of Figure 3, consists of two steps in voltage. The application The controlled response of the beam is seen in the upper trace resulting in a 20 microinch amplitude and a rise time of around 0.5 milliseconds.

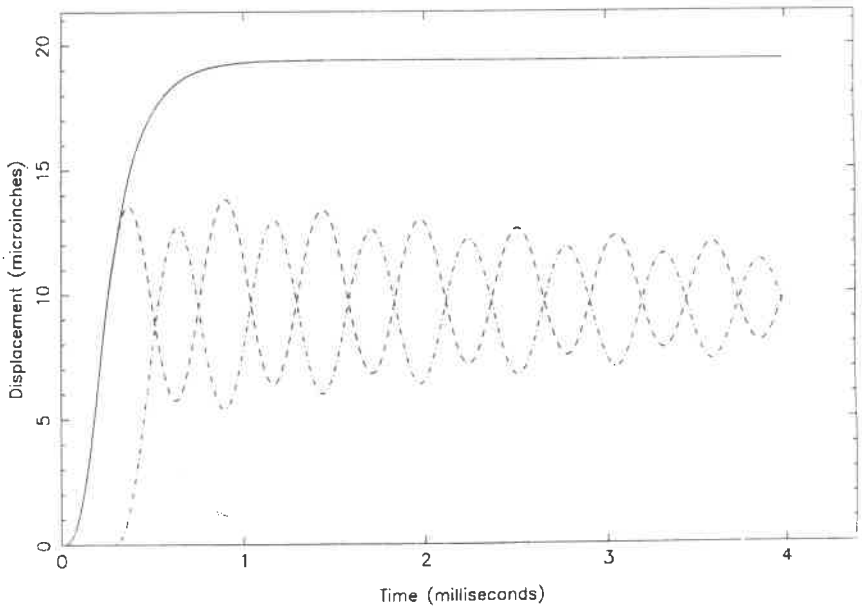

Figure 2 Simulation of Two Step control

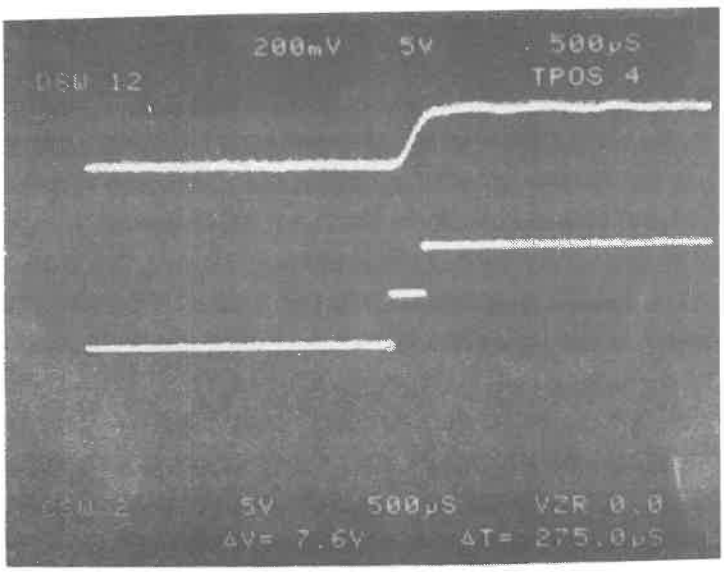

Figure 3 Experimental application of Two Step control

References

H. Ozisik and R.F. Keltie, "Development and Implementation of a High Speed Open Loop Control Technique for Micropositioning of Mechanical Structures", **Journal of Precision Engineering**, Vol. 11, No.4, October 1989, p.225

Hiroshi IIDA, Toshitaka OONO, Akiyoshi TAMURA, Kyosuke ONO, "High Speed Positioning Control of a Flexible System", **Bulletin of JSME**, Vol.29, No. 257 November 1986, p.3899

D.E Luttrell and T.A. Dow , "Development of a High Speed System to Control Dynamic Behavior of Mechanical Structures ", **Journal of Precision Engineering**, Vol. 9, No.4, October 1987,

PRECISION ENGINEERING ASPECTS OF THE PATS PROJECT

Richard Rhorer
Los Alamos National Laboratory
Los Alamos, New Mexico

and

Wayne Hobson, Jeff Jarosz
Moore Special Tool Company
Bridgeport, Connecticut

EXTENDED ABSTRACT

Introduction

The manufacturing of precision components for nuclear weapons systems involves handling toxic and radioactive materials. One of the efforts by the US Department of Energy (DOE) to add "modern" high precision equipment when replacing worn-out equipment, is the Precision Flexible Manufacturing Systems (PFMS) program. The goal of the PFMS program is to develop manufacturing systems that will minimize the exposure of workers to toxic and radioactive materials, and, by having the entire manufacturing process under control, minimize environmental impact and waste. An overview of the PFMS program is presented in a Los Alamos National Lab brochure.[1]

One of the projects within the PFMS program is specifically aimed at designing an unmanned, or automatic, system for the manufacture of high precision hemispherical shells. This system is called the Precision Automated Turning System (PATS). Early in the program it was determined that we could not simply purchase a turning system to meet the needs of the PATS system; therefore, a development effort was initiated for PATS. This development effort included selecting a commercial partner by a competitive bid process. Moore Special Tool Co. was selected by this process to work with the DOE in developing PATS.

Error Budgets

The PATS project has emphasized using a precision engineering approach, including the use of an error budget. An error budget relates to the final precision of a design as the "dollar budget" of a project relates to the overall cost of the project. To allow us to design the PATS by subsystems

and insure that the overall system would meet the precision requirements, we are using an error budget approach.

The authors first learned about error budgets for machine tool design from reports and discussions by Bob Donaldson.[2] The idea is fairly straight forward, and as Chris Evans states about error budgets "it seems that recent work in the area is, in essence, a formal description of a well established (perhaps largely intuitive) process."[3]

For the work here we distinguish between error budgets and error analysis. A physical system can be analyzed, or experimentally studied, to determine the contribution to a total system error of different components, or variable changes, in the system. An error budget can be more or less arbitrarily specified such that a certain amount of error is planned for any one subsystem or variable change. A error budget can be specified without knowing the design details of the system, whereas to perform an error analysis the system or design has to be well known. For example, we can specify in the error budget that we want no more than 5 micrometers error due to temperature changes. The role of the designers is then to determine what would have to be done to either control the environment, or design with low coefficient materials, to meet the required error budget allocation. (In real life situations the error budget might then have to be revised if the dollar budget doesn't allow enough to meet the design proposal or if it is physically impossible to meet the error budget allocation.)

The PATS Error Budget

The PATS system is required to manufacturer a variety of different shell components of different materials -- hence the need for flexibility. The most precise component considered is a thin walled stainless steel shell with a tolerance of plus or minus 12.5 micrometers on size and shape. We have specified a preliminary PATS error budget with the following subcomponents and error allocations:

Component	Budgeted error (micrometers)
Machine tool -- tool path	3.0
Tool set	4.0
Tool size and shape	5.0
Fixture, size, and location	3.0
Part transfer	3.0

The budgeted error amounts can be added to obtain a total of 18.0 micrometers, although it is not clear that the numbers would be added if we were doing an error analysis of an existing system. The total part tolerance of 25 micrometers would allow a larger error budget total, but to be conservative, we have considered an initial budget smaller to allow for uncertainties such as part material stability.

The component of the error budget for "tool path error" is a combined error for all the aspects of the machine tool that are involved in causing the tool to follow a prescribed path. The test commonly used to test for tool path accuracy is the disk check or ball bar which determines how precisely a machine tool can produce a circular tool path. The error budget item for tool path therefore includes all machine geometry errors for straightness, squareness, positioning, etc. Our budgeted error of 3.0 micrometers for tool path guides those designing the basic machine tool subsystem of PATS how precise a design to work toward. For comparison, commercially available diamond turning machines can achieve a tool path accuracy of 1 to 2 micrometers.

The tool set error component of the budget includes how precisely the PATS can automatically locate the cutting edge of the cutting tool with respect to the machining spindle. For PATS we will consider several tool set methods, including a prefinish-cut/part-measurement cycle. Our precision engineering goal is to "build-in" the precision and not have to adjust before a final cut. Our development program has not reached the stage of designing the tool set method to meet our prescribed error budget.

The errors in both the size of the tool and the truth-of-radius of the tool will contribute to the part error and therefore have to be considered. Again, our design goal is to achieve the error budget specification without adjustment; however, a tool mapping and corrected tool path may be used to allow a less stringent requirement to be placed on the tool bit manufacturer.

The fixturing error contribution may be the most difficult for the PATS as compared to previous man operated systems. In our conventional manufacturing systems we can place a fixture on a machine spindle and "indicate it in" by hand, or even take a clean-up cut after mounting a fixture. For the PATS our goal is to automatically locate a new fixture in place on the machine spindle. The location error, and any size error of the fixture, contribute to the final part error in the PATS; therefore, we

need to develop a relocating mount system that does not distort the part holding fixture and meets the error budget specification.

The error contribution for transferring the part from the outside surface machining operation to the inside machining operation is difficult to predict. To study the part transferring schemes a test bed has been built, which will help us develop a transfer method that with a goal of meeting the error budget precision.

Conclusions

The error budget approach is being used as an aid in designing the Precision Automated Turning System. The separate components of the error budget are allowing the design tasks to be separated and still maintain the overall precision goals for the system.

References

1. "U.S. Department of Energy Precision Flexible Manufacturing Systems (PFMS) Program," Los Alamos National Laboratory, LALP-89-40, February 1990.

2. Donaldson, R. R. "Error Budgets" in "Technology of Machine Tools; Vol. 5, Machine Tool Accuracy," edited by Robert J. Hocken, UCRL-52960-5, 1980.

3. Evans, C., Precision Engineering: An Evolutionary View, Cranfield Press, 1989, pg. 36.

Evaluation of Silicon Wafer Polishing Pads

——Rheological Behavior of Polishing Pads and Improvement of Wafer Flatness ——

Yamato SAMITSU[1], Takahumi YOSHIDA[2], Nobuo YASUNAGA[1], Takashi OHMOTO[2], Sadamu HORIE[2]

1)Electronics R & D Laboratories, Nippon Steel Corporation
1618 Ida, Nakahara-Ku, Kawasaki, Kanagawa 211 JAPAN

2)NSCE Electron Corporation
3434 Shimada, Hikari, Yamaguchi 743 JAPAN

We have developed some new easy-to-use equipment for measuring quantitatively the rheological deformation characteristics of the polishing pads. The main results, using the measuring equipment, are as follows : (1)With the processing time, the elastic value of the deformation becomes higher at the peripheral region of the polishing table compared with the center[1], (2) The four-element rheology model showed good agreement with the experimental results. (3) A new parameter, which is derived from the four-element model and is related to the elastic modulus, was found to be significant for the wafer flatness. We could select appropriate pads for improving the flatness using this parameter.

1) Introduction.

The recent highly-integrated IC requires very flat Si wafers. The Local Thickness Variation(LTV) required for 4M DRAM is less than 0.8 μm for a 15X15mm chip. To achieve this flatness, it is essential to choose appropriete polishing pads. Although it is known that the pads are deformed rheologically[2], there is no reproducible method for the pad characterization in an actual polishing process. We report a new equipment for rheological deformation measurement and a new parameter based on four-element model to evaluate pads. We have achieved the flatness for 4M DRAM by these method.

2) Experimental Procedures.

(1) Rheological characteristics measurement.

The set-up of the equipment for measuring the rheological characteristics of the polishing pads is shown in Fig.1. Weight ⑤ is set to move vertically by the weight holder ⑦, which is driven by a motor ⑥. When the weight is set on Aluminum plate ①,

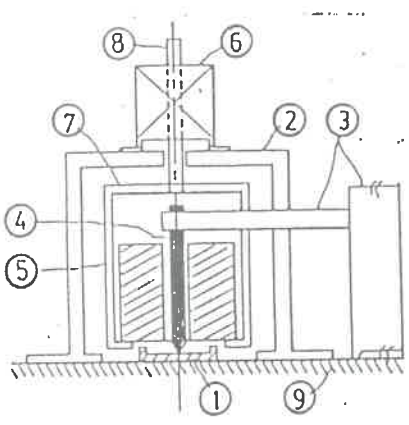

Fig.1 Set up for rheological characteristics measurent

which is placed on pad⑨, the pad deforms. The pad deformation can be indirectly detected mesuring the plate's displacement by electric micrometer④ .

(2) Pad deformation process.

The typical pad deformation process is shown by a solid line in Fig.2. In this experiment, the step load of 190g/cm² was applied to the Al plate. The weight loading time t_1 was set to 10 seconds, when the increasing ratio of the deformation becomes constant. After 20 seconds of the unloading time t_2, the deformation is saturated as seen in Fig.2.

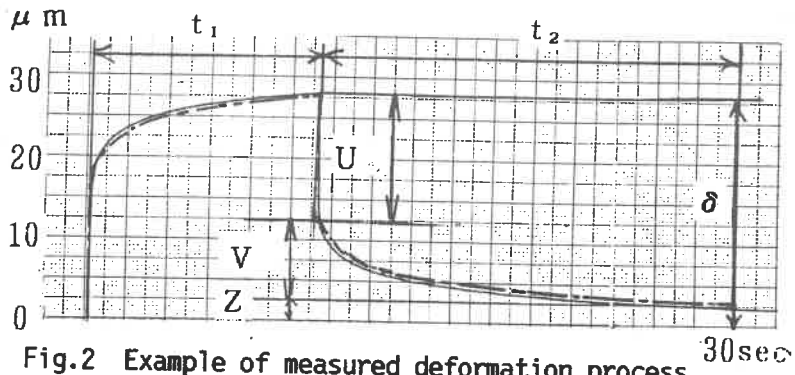

Fig.2 Example of measured deformation process

(3) Polishing experiments.

The diameter of the table of the polishing machine used, which has 4 heads, is 1200mmϕ. At each head, 5 pieces of 5" wafers are fixed by wax. The table was rotated at 60 rpm. A slurry of KOH-solution mixed with SiO_2 powder was used. The PH value of the slurry was kept to between 10.5~11.0 . One batch took 20 minutes to polish.

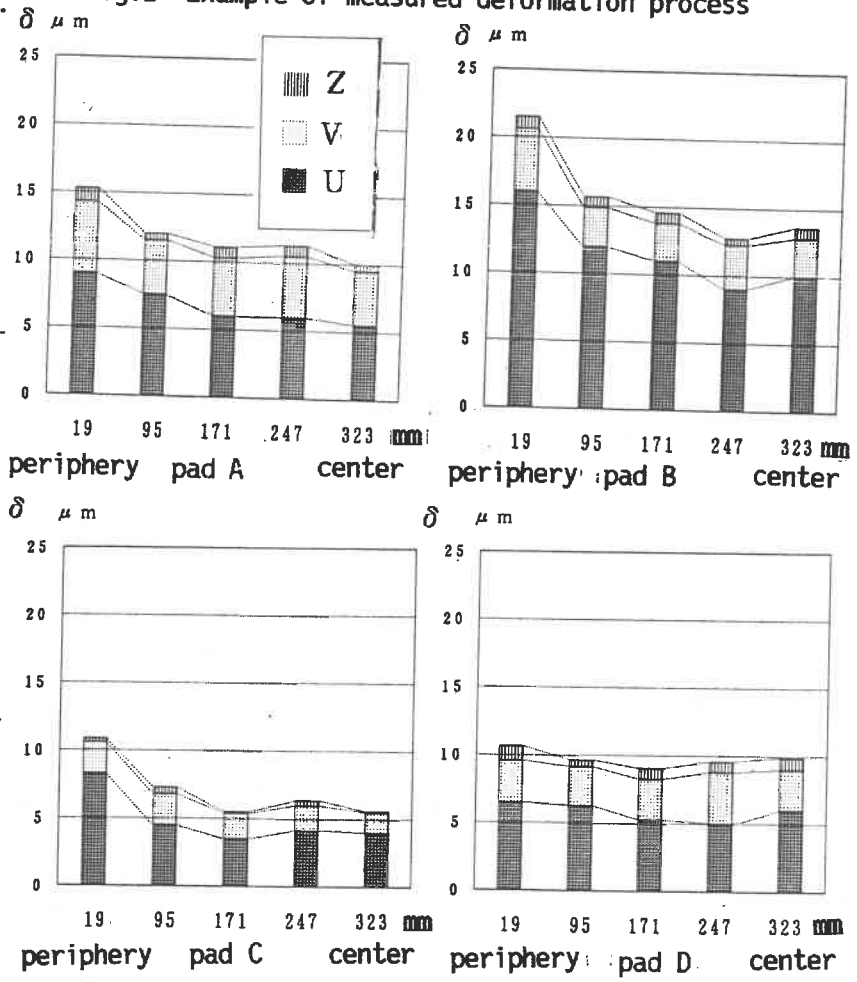

Fig.3 Rheological characteristics of 4 different kinds of pads(Comparison between periphery side and center side)

3) Results and Discussion.

Rheological characteristics of 4 different kinds of pads after 10 batches were ploished are shown in Fig.3. U,V,and Z indicate instantanous elasticty , retarded elasticty and permanent deformation, respectively. Total deformation δ (U+V+Z) is largest in pad B, and becomes smaller in order ,pad A, pad D, and pad C. The differences of δ on the peripheral side and the center are large in pad A, pad B

and pad C. These differences are clearly influenced by U.

(1) Four-element model.

The solid line in Fig.2 shows a typical rheological phenomenon which can be approximately represented by four-element model.The four-element model consists of the combination of the Maxwell and Voigt models as indicated in Fig 4. We can obtain the coefficients of elasticty and viscosity of pads from this model and Timoshenko's theory of elasticity, as follows:

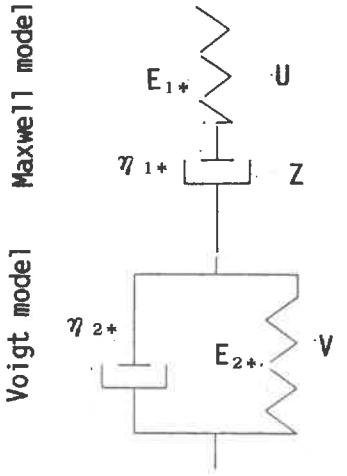

Fig.4 Four-element model

$$\delta = U + V + Z \qquad \text{①}$$

$$2aU = (1-\nu^2)\, P / E_{1*} \qquad \text{②}$$

$$2aV = (1-\nu^2)\, P / E_{2*}\, (1-\exp(-E_{2*} \times t_2 / \eta_{2*})) \qquad \text{③}$$

$$2aZ = (1-\nu^2)\, P \times t_1 / \eta_{1*} \qquad \text{④}$$

where E_{1*}: Coefficient of elasticity of Maxwell model

E_{2*}: Coefficient of elasticity of Voigt model

η_{1*}: Coefficient of viscosity of Maxwell model

η_{2*}: Coefficient of viscosity of Voigt model

a : Radius of Al plate(10mm)

ν : Poisson's ratio(0.4)

P : Load which was given to Al plate(0.42kgf)

t_1 : Time to be loaded

t_2 : Time to be unloaded

We can obtain E_{1*} by substituting the value of U measured from Fig.2 into equation ②. When t_2 is infinite, equation③ can be written as follows:

$$2aV = (1-\nu^2)\, P / E_{2*} \qquad \text{⑤}$$

Fig.2 shows that V becomes almost constant,after t_2 is 20 seconds. Therefore E_{2*} can be obtained from equation ⑤ using the value of V at t_2 =20 sec. $\eta_{2*}$is obtained by substituting t_2 and V into equation③ , after E_{2*} is calculated from equation ⑤. Z can be read off from Fig.2. Consequently η_{1*} is obtained from equation④. The deformation which was calculated from these processes is shown as a dotted line in Fig.2. It agrees well with the solid line obtained from the experiment.

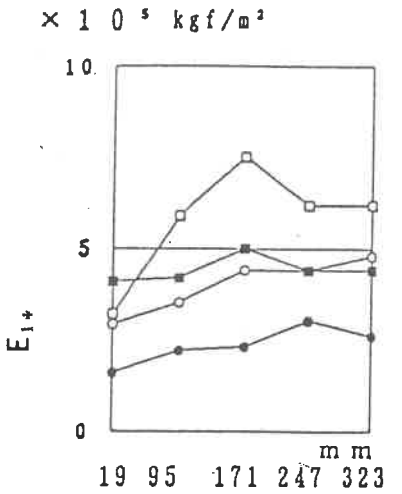

Fig.5 Comparison of E_{1*}

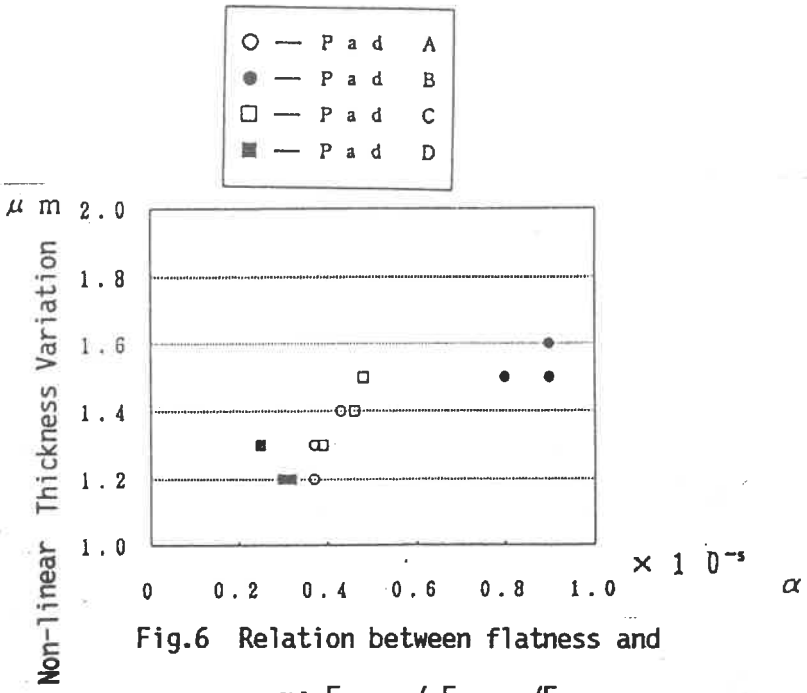

Fig.6 Relation between flatness and α: $E_{1*MAX}/E_{1*MIN}/E_{1*AVE}$

(2) Discussion.

We have calculated coefficients for each pad according to the equations ①~⑤. For example the values of E_{1*} are shown in Fig.5. The E_{1*} of pad D is relatively large and constant, compared with the others. The E_{1*} of pad C is large at the center, but is small on the peripery, that is, E_{1*} varies widely across the table.

Here, we have introduced a new parameter α, which is suitable for evaluating the wafer flatness, shown as follows:

$$\alpha = E_{1*MAX}/E_{1*MIN}/E_{1*AVE}$$

where E_{1*MAX} is the maximum value of E_{1*} and E_{1*MIN} is the minimum value. E_{1*MAX}/E_{1*MIN} indicates the degree of scattering of E_{1*}. E_{1*AVE} is the average value of E_{1*}, which is the mean hardness of the pad.

The relation between α and the flatness is shown in Fig.6. The Non-linear Thickness Variation(NTV) decreases when the α decreases. As to the other coefficients E_{2*}, η_{1*} and η_{2*}, no clear relation with flatness was found.

4) Conclusions.

We have developed new rheological characteristics measuring equipment. By analyzing the pad's deformation with a four-element model, a suitable parameter α which is significant for evaluating Si wafer flatness, was found.

Reference

1) T.Yoshida et al., Proc.Spring Meeting of Japan Soc.Prec.Engg., p211(1989)
2) M.Ikeda et al., Proc.Spring Meeting of Japan Soc.Prec.Engg., p341(1978)

CHIP FORMATION IN SINGLE POINT DIAMOND TURNING

M. C. SHAW, ARIZONA STATE UNIVERSITY
H. G. SHAFER AND M. ADLER, CORNING, INC., CORNING, N.Y.

It has been well established (Blake, 1988 for exmple) that in single point diamond turning (SPDT), the quality of the finished surface is dependent on the undeformed chip thickness when machining a brittle material such as glass. In order to produce a surface free of cracks and of excellent surface finish, it is necessary to use an extremely small undeformed chip thickness. This is achieved in diamond turning by use of a sharp tool having a large nose radius, a small depth of cut and a small feed per revolution such that several revolutions are required to remove all of the material in the depth of cut.

The fact that a diamond hardness indentation may be made in the surface of very brittle materials without any sign of fracture provided the force on the indenter is small and hence the deformed volume beneath the indenter is also small (see for example Fig. 1 and Shaw, 1984 for further discussion) naturally suggests that the good finish obtained is a result of ductile chip formation provided the undeformed chip thickness is sufficiently small. As a result, the term ductile-regime cutting has come into rather wide use. It is the purpose of this presentation to suggest that in the SPDT of a very brittle material the chip forming process is very much concerned with microcrack formation and fracture but in such a manner that the finished surface is of high integrity provided the undeformed chip thickness is small enough.

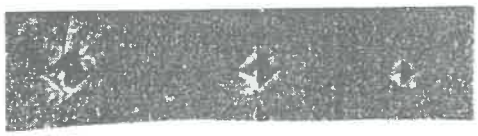

Fig. 1. Impressions made in marble with a diamond indenter under loads of a) 15 gm, b) 10 gm, and c) 5 gm (after Shaw, 1954)

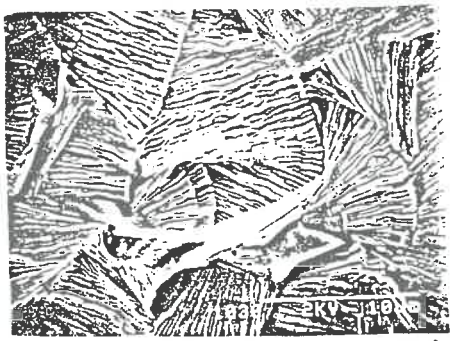

Fig. 2. SEM of SPDT chip of germanium produced under dry "ductile-regime" cutting conditions (after Blake, 1988, p 65)

Figure 2 shows an SEM of some chips produced in SPDT of germanium under "ductile-regime" cutting (Blake, 1988). The fact that these chips have a similar appearance to the segmental chips frequently obtained when ductile metals such as copper are cut in SPDT has been presented as further evidence that chip formation in SPDT in the so-called "ductile regime" is free of fracture. However, fracture followed by gross slip on the plane of fracture and rewelding plays an important role in chip formation even in the case of ductile materials. The fact that the SPDT chip of Figure 2 resembles segmental chips frequently found when ductile metals are cut with relatively large depth of cut should be considered as evidence that fracture was involved in their formation instead of the opposite. This is because chip segmentation is a result of localized fracture, gross slip and rewelding.

Pure titanium provides a large scale model of what happens during chip formation with a brittle material on a very much smaller scale. Figure 3 shows photomicrographs of commercially pure titanium chips produced under identical conditions except for cutting speed. At a very low cutting speed (Fig. 3a) fracture occurs periodically followed by gross slip and then rewelding since the chip is continuous and not a series of disconnected fragments. Fracture occurs at defects of unusually high stress concentrations and extends all the way across the chip resulting in a saw-toothed appearance.

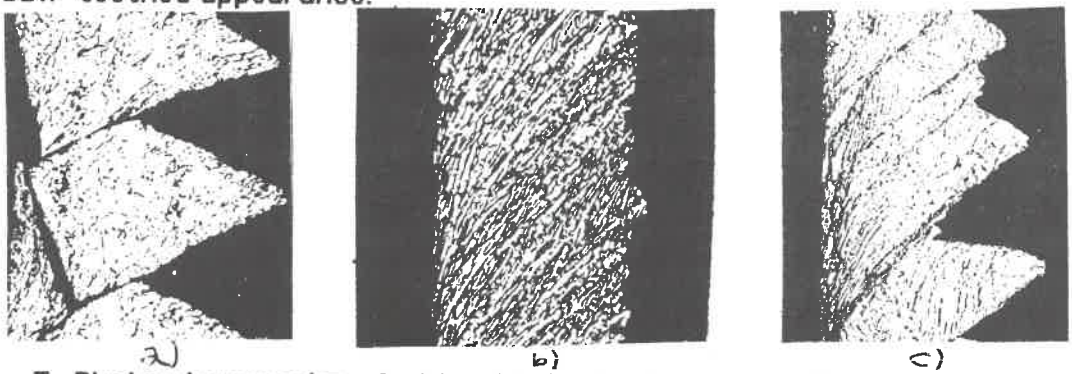

Fig. 3. Photomicrographs of chip obtained when pure titanium is cut dry under identical conditions except for cutting speed V
a) V = 1 ipm = 0.25 m/min; b) V = 50 fpm = 15 m/min;
c) V = 175 fpm = 53 m/min (after Shaw et al. 1954)

The chip of Fig. 3c is similar to 3a except there are more fracture planes and evidence of thermal softening on either side of the fracture planes. This has been termed adiabatic shear and is typical of materials having low thermal diffusivity such as titanium and stainless steel. The

segmentation in this case is not due to the spacing of unusually strong defects causing periodic fracture but due to the fact that once a material starts deforming in shear at high speed, the heat generated causes thermal softening so that slip continues at the point where it initiates for a relatively long time. The action is akin to that at the surface of a heavily loaded friction slider that exhibits subsurface shear flow.

The chip in Figure 3b was formed at an intermediate speed which was not sufficient to result in adiabatic shear but sufficient to thermally activate more defects of lesser intensity that would be inactive at room temperature. This results in a typical continuous chip. It still involves localized fracture, gross slip and rewelding as in Figure 3a but with three important differences:

- There are many more fracture planes and hence less deformation on each one.

- The fracture planes do not extend clear across the width of the chip but only over a fraction of the width. Hence the back of the chip is merely rough instead of being sawtooth-like.

- The strain is relatively homogeneous so that continuum mechanics which is inadmissible for the cyclic behavior of Figures 3a and 3c represent a reasonable first approximation. However, it is important to note that since microfracture and not just flow is involved in continuous chip formation, as is perfectly clear from the appearance of the back of the chip, the Tresca or von Mises constitutive equations cannot be used. It is well known that unlike flow stress, fracture stress is greatly influenced by hydrodrostatic (normal) stress

Since SPDT chips have the appearance of Figures 3a or 3c both of which involve fracture (low temperature shear fracture in the case of Figure 3a and hot shortness-like shear fracture in the case of Figure 3b), it does not appear advisable to consider these chips to be formed by a fractureless flow type mechanism.

Detailed study of chip formation for titanium alloys (such as Ti-6Al-4V) reveals that chip formation is cyclic but on a finer scale than that of Figures 3 since there are then many more defects of uniform

intensity in the form of second phase particles. Chip formation then resembles the deformation of an inclined pack of cards (Fig. 4). The fracture surface consists of an initial tensile crack from A to B which shifts to an inclined shear crack from B to C a short distance from the tool tip. The specific cutting energy and the normal stress at the tool tip increases exponentially as the undeformed chip thickness decreases. It would appear the direction and extent of the initial tensile fracture surface is what determines surface quality and not the absence of fracture in chip formation. Apparently, as the undeformed chip thickness decrases and the hydrostatic stress at the tool tip increases, the initial tensile fracture tends to be more horizontal or to be inclined slightly upward so that subsequent burnishing by the clearance face results in a sound surface of excellent smoothness.

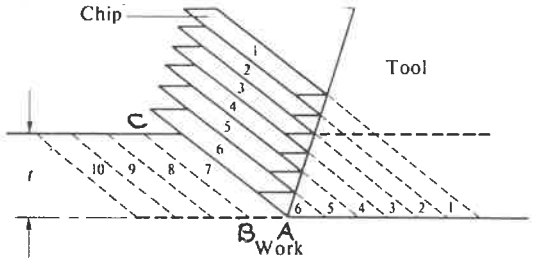

Fig. 4. Piispanen's idealized model of the cutting process (after Piispanen, 1937)

References:

Blake, P.N., 1988, "Ductile Regime Diamond Turning of Germaium and Silicon", PHD Dissertation, N.C. State University, Raleigh, N.C.

Piispanen, V., 1937, Eripaines Teknilliseala Aikakauslehdesla, Vol 27, 315

Shaw, M. C., Dirke, S.O., Smith, P. A., Cook, N. H., Loewen, E. G., and Yang, C.T., 1954, "Machining Titanium", Report to the Air Force at WPAFB, Dayton, OH.

Shaw, M.C., 1954, Proc. Nat. Acad. Sci.,, U.S.A., Vol 46,, 394

Shaw, M.C., 1984, Metal Cutting Principles, Oxford Clarendon Press, pp 93-95

Use of Lasers in Nanomaterial Synthesis

Peter R. Strutt and Kenneth E. Gonsalves
The University of Connecticut

Introduction

A recent National Materials Advisory Board Report by Kear et. al. [1] states that the development of methodologies for the synthesis of ultrafine-structure materials is an important national need. In general, the potential importance of materials constituted from grains (or particles) of only a few nanometers diameter is twofold. Firstly, reduction to such a fine scale is required for achieving isotropic properties in materials used in highly minimized components. Secondly, nanophase materials possess unique basic properties [1,2], that in several instances, have significant technological implications. Conceptually, for example, the theoretical mechanical strength may be realized in biphase alloys formed by the agglomeration of coated nanophase particles. This possibility was originally suggested by Louat [3], where he pointed out the desirability of synthesizing a biphase nanostructure, where the original coating-phase forms the matrix of a dispersion strengthened material.

Various methodologies are required for the synthesis of ultrafine, or nanoscale, materials, since each potential field of application has its own requirements. Physical methods, for instance, although capable of producing high-purity material, involve inherently slow processes. Although this may be perfectly acceptable in electronic application, for instance, alternatives need to be sought for nanomaterials required in structural applications. For this reason, chemical methods become attractive, in view of high attainable reaction rates and a natural amenability to scale-up for industrial processing.

Recent studies at the University of Connecticut [4,5] have shown the potential of producing nanoparticle ceramic and metallic powders in significant amounts, via chemical processing. This is achieved by laser conversion of a liquid metal-organic compound, termed a molecular precursor. The precursor studied most extensively is a silazone monomer $(CH_3SiHNH)_x$, with x=3 or 4. Structurally, as shown in Fig.1, it consists of attennate silicon and nitrogen atoms arranged in a ring. In essence, laser processing involves partial elimination of ligands, i.e. hydrogen atoms and methyl groups (CH_3). It also involves cross-linking between the laser-modified monomer to form solid nanoparticles. These pre-ceramic nanoparticles can undergo subsequent thermal conversion into silicon nitride (Si_3N_4).

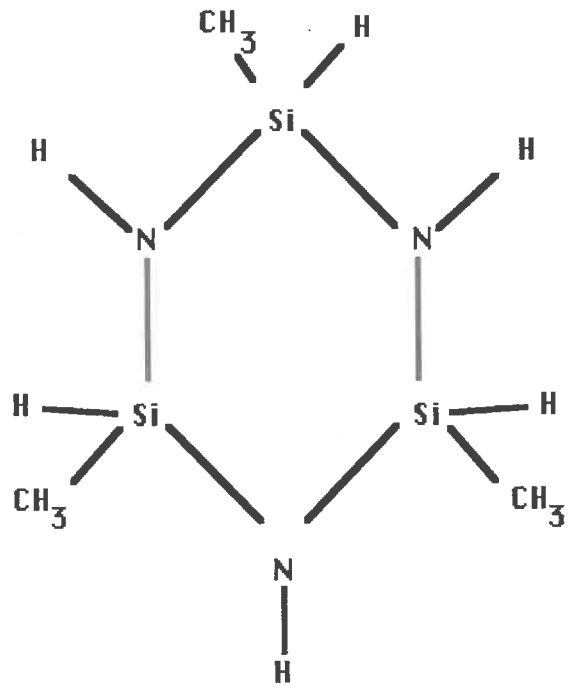

Figure 1

Experimental Methods

A. Liquid precursor and properties.

The silazone monomer precursor was prepared by the ammonolysis of methyldichlorosilane [5]. As revealed by infrared spectroscopy, an important feature of the precursor is a strong absorption peak in the 10.6 micron wavelength region. This ensures strong energy transfer when a precursor aerosol is injected into the beam of a CO_2 laser, see Fig. 2.

B. Laser Pyrolysis Processing

Processing is carried out within a stainless steel controlled environment chamber. A part on the top of the chamber provides access for a convergent beam of an industrial CW CO_2 laser. Prior to laser irradiation, the processing chamber is evacuated to ~ 10^{-4} torr, flushed with nitrogen, and then backfilled with nitrogen to ~ 760 torrs. The chamber is then continuously fed with ammonia and helium gas with the pumping rate of 150 sccm and 100 sccm for ammonia and helium respectively.

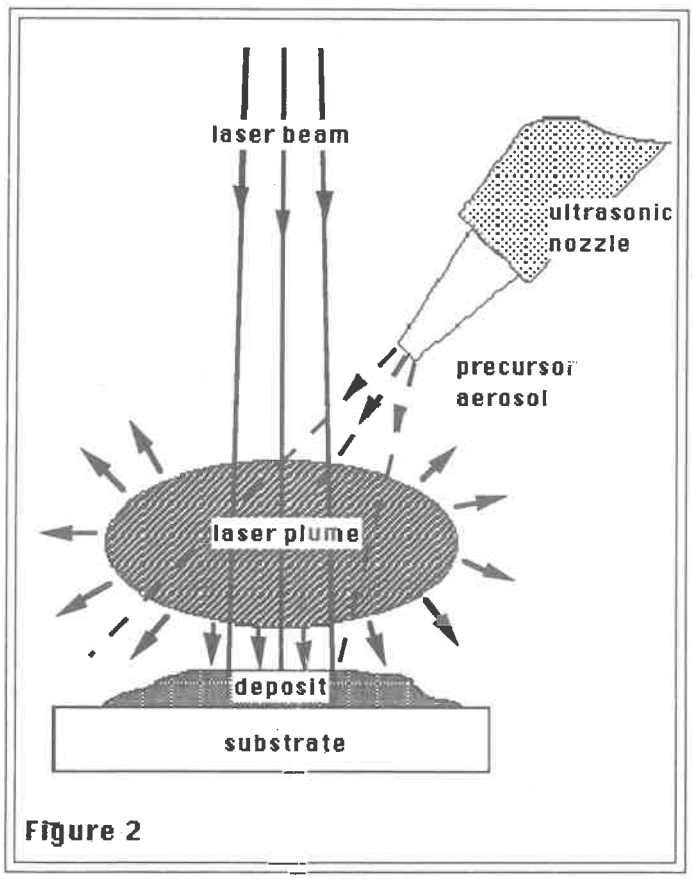

Figure 2

As shown in Fig. 2, the process involves using an ultrasonic nozzle to disperse the precursor liquid into an aerosol. This is achieved by using a Son-Tek system. Strong energy coupling between the laser beam and the injected aerosol droplets results in their rapid evaporation, and the formation of a plume (or plasma). The precursor molecular groups formed by the process rapidly cool as they emerge from the plume. They then condense to form solid pre-ceramic particles, which under the conditions used in current experiments, have a ~ 50 nm diameter. An interesting aspect of the process is that nanoparticles collected on a laser-heated substrate (Fig. 2) undergo coalescence to form a deposited layer. Coalescence (or sintering) is driven by the high surface area of the nanoparticles, and processes involving very short diffusion distances. Consequently, as depicted in Fig. 2, consolidation as well as synthesis can occur in an integrated process, thus obviating the need to handle the nanoparticle powder. However, the method may be used expressly for powder synthesis. This is accomplished by collecting the condensed nanoparticles on a cold substrate surrounding the laser plume. Based on a preliminary trial, a rate of powder production of ~ 100 grams per hour has been achieved.

Results and Discussion

A serendipitous discovery, with important implications, is that molecular species condensing from the beam undergo rapid 3-dimensional cross-linking to form the pre-ceramic nanoparticles. This particularly rapid polymerization process, it should be noted, does not occur in conventional chemical processing. Furthermore, an attractive feature is that 70 wt.% of the liquid precursor is converted into nanoparticle powder. Structural examination of powders using NMR, FTIR spectroscopy, and differential scanning calorimetry reveals a partial elimination of ligand groups with evidence of strong cross-linking. Transmission electron microscopy shows the particles are highly transparent and display no evidence of porosity, (see Fig. 3). Thermogravimetric analysis has revealed that these particles only undergo a ~ 10 wt. % loss, during subsequent thermal processing to form silicon nitride.

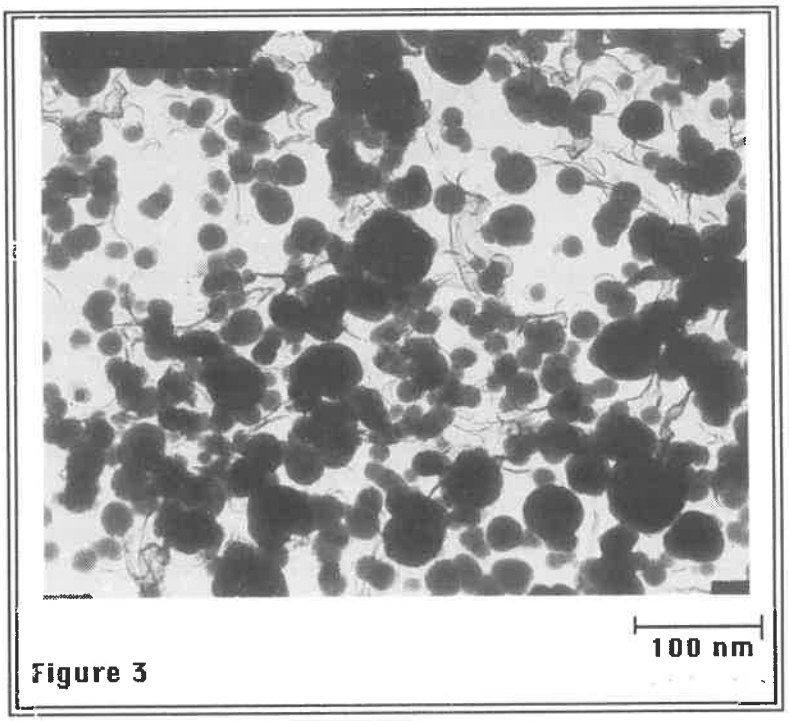

Figure 3

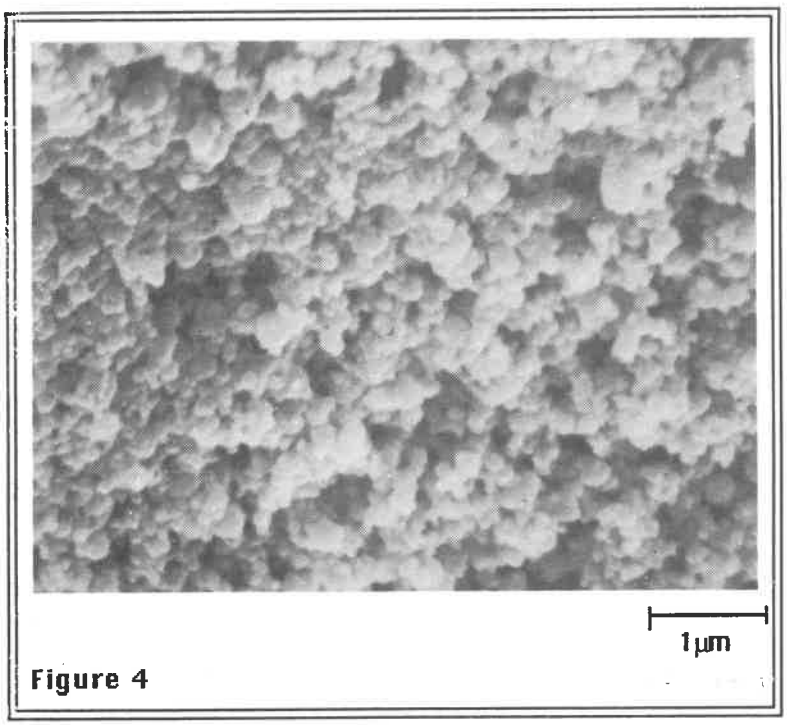

Figure 4

The method depicted in Fig.4 may be used expressly for powder synthesis. This is accomplished by collecting the condensed nanoparticles on a cold substrate surrounding the laser plume. Based on a preliminary trial, a rate of powder production of ~100 grams per hour has been achieved. Currently, a study is in progress for determining the reliability of achieving a rate of 1 kg. per hour by scale-up, and by optimizing the conversion process efficiency. This requires studying the effect of precursor injection rate and beam power density, process parameters that control, for instance, the structure and chemistry of collected nanoparticle powders. Such a study would be particularly valuable where large amounts of polymeric particle powders are required for subsequent die extrusion into component preforms. In this case, the use of minimal laser irradiation per particle would optimize the production volume.

In using the method to form surface deposits, nanoparticles are collected on a laser-heated substrate (Fig. 3). These undergo coalescence, or sintering. this process facilitates both surface-particle bonding and interparticle bonding. Coalescence is driven by the high surface area of the nanoparticles, and processes involving very short diffusion distances. Consequently, as depicted in Fig. 3, consolidation as well as synthesis can occur in an integrated process, thus obviating the need to handle the nanoparticle powder. A high magnification scanning electron micrograph (Fig. 4) reveals the sintered particle structure in a surface deposit.

References

1. B. H. Kear et al, Research Applications for Materials with Ultrafine Microstructures, National Materials Advisory Board - 454 (National Academy Press, Washington, D.C., 1989).

2. R. W. Seigel, et al, J. Mat. Res., 4 (3), 1989, p.704.

3. N. Louat, Acta Metal 33(1), 1985, p. 59.

4. T.D. Xiao, R.R. Strutt & K.E. Gonsalves, Mat. Res. Soc. Symp. 155, 1989, Pittsburgh, PA, p. 247.

5. P. R. Strutt, with A. P. Magee and K. E. Gonsalves, Chemistry of Materials, 2(3), 1990, p. 232. See also T.D. Xiao, P.R. Strutt, and K.E. Gonsalves, Mat. Res. Soc. Symp. 168, 1990, Pittsburgh, PA, p. 199.

Study on the Polishing of Diamond by Metallic Plate

Hitoshi Tokura, Cheng-Feng Yang and Masanori Yoshikawa
Tokyo Institute of Technology
2-12-1, O-okayama, Meguro-ku, Tokyo 152, Japan

1. Introduction

Nowadays diamond is known as an important engineering material. It has also known as a hard-working material. Usually it has been worked by mechanical method with diamond powders except for a cutting or a hole-making case by laser beam. By the way, we experience that diamond cutting tools wear hard on cutting steels. In this study, we examined to apply this phenomenon to polishing diamonds.

2. Experimental

Heating experiments were carried out in order to see whether diamond can be worked or not by contacting with metal at high temperature. As shown in Fig.1, metallic wire of 0.35mm diameter was put on a single natural diamond and they were heated at over 800C by W-filament set above the diamond in hydrogen atmosphere for 3 hours. After heating, it was observed that the wire sank into the diamond and formed a groove. SEM photographs of the diamond which was heated at about 1000C using a nickel wire is shown in Fig.2. Grooves were obtained with iron wire instead of nickel wire. This is clear from above that diamond can be worked by contacting with the metal at high temperature.

Next, the experimental polishing apparatus shown in Fig.3 was manufactured. The internal view of the apparatus is shown in Fig.4. Diamond workpiece slides on a heated metallic plate in a low speed. The temperature of the polishing plate is measured by a thermocouple. The sliding speed and the applied pressure are extremely small comparing with conventional polishing method using diamond powders.

The experimental conditions are shown in Table1. Materials of the polishing plates are iron, cast iron, nickel and molybdenum, and the range of heating temperature is from 700C to 950C. In addition to vacuum, hydrogen, nitrogen, helium and argon is used as the atmospheric gas. Diamond film synthesized by microwave plasma CVD method was selected as a workpiece. Polishing rate is evaluated by polished area/whole area of a diamond film.

3. Results

Effect of polishing plate materials on polishing rate is shown in Table2. Iron and nickel have high polishing rate in comparison with cast iron and molybdenum. Effect of polishing atmospheres on polishing rate is shown in Table3. In vacuum highest value of the polishing rate is obtained and in almost cases the rate with iron are higher than that with nickel. The higher of the plate temperature, the high of the polishing rate as shown in Fig.5. Polishing process of a diamond film is shown in Fig.6 and Fig.7. A rough surface becomes a smooth surface. As another application of this polishing method, SEM photograph of the polished interface between CVD diamond and sintered diamond is shown in Fig.8.

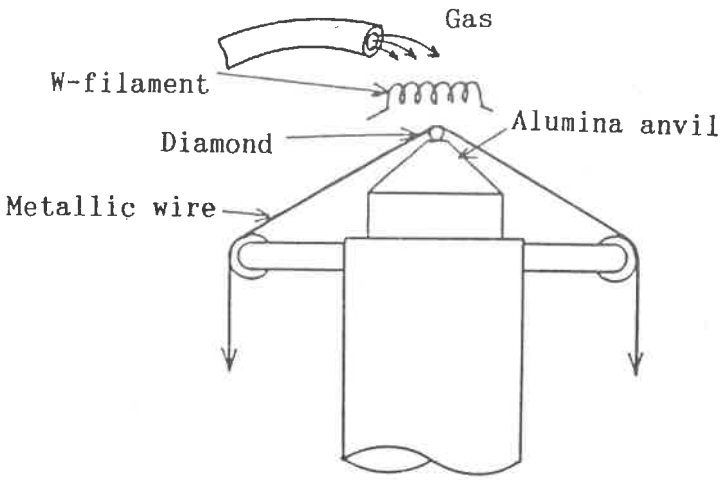

Fig.1 Experimental set-up for heating diamond contacting with metallic wire

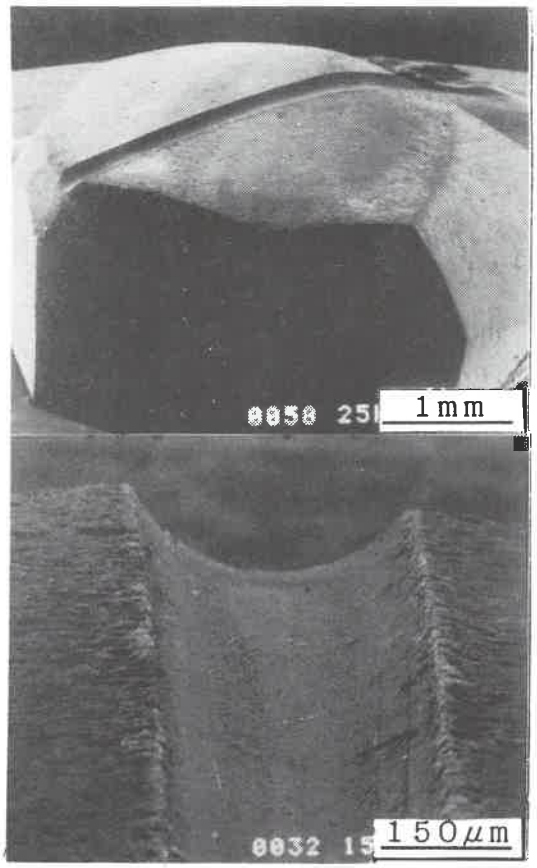

Fig.2 SEM photos of the groove on diamond surface

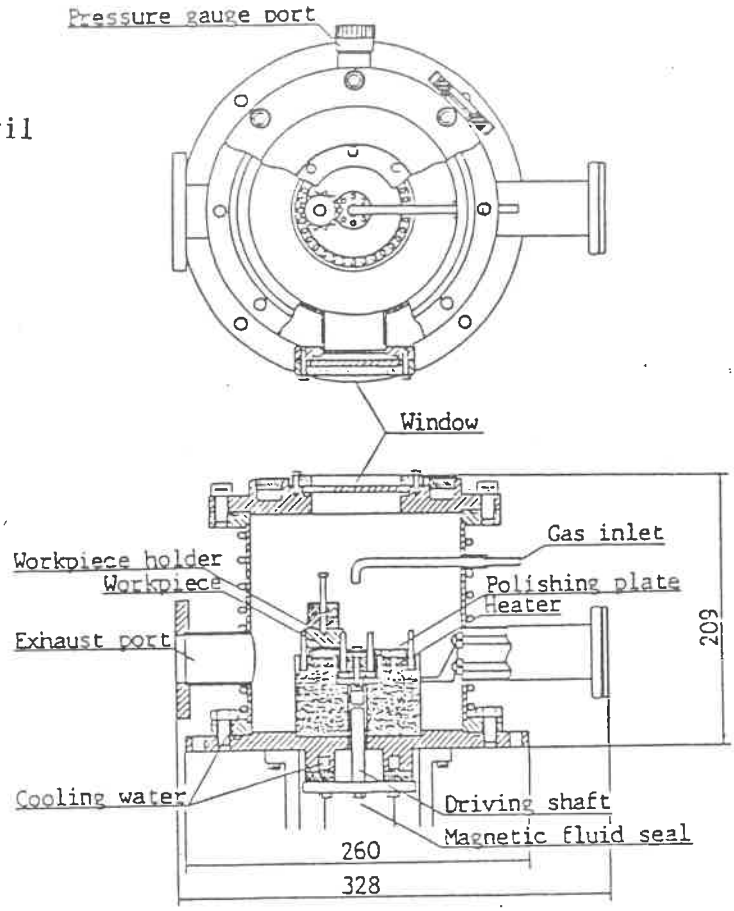

Fig.3 Structural drawing of the polishing apparatus

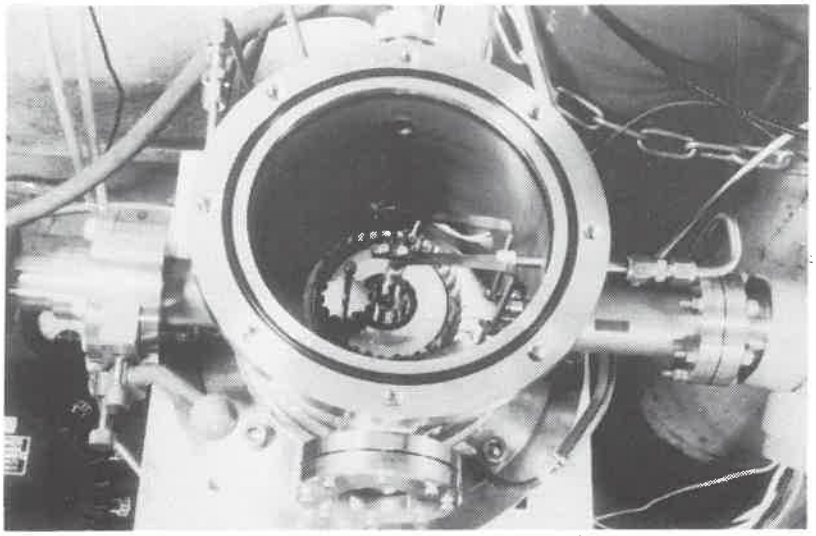

Fig.4 Photograph of the polishing apparatus

Table 1 Polishing conditions

Polishing plate	Iron,Cast iron,Nickel,Molybdenum
Temperature	700,750,800,850,900,950 °C
Atmospheric gas	Vacuum,H_2,N_2,He,Ar
Gas flow rate	100 (when gas is used) SCCM
Atmospheric pressure	<1(vacuum),5300(the others) Pa
Applied pressure	15, 40 kPa
Sliding speed	0, 2.8, 7.0 mm/s

Table 2 Effect of polishing plate materials

Temperature : 900 °C		Polishing pressure: 15 kPa	
Atmospheric gas : hydrogen		Sliding speed : 2.8 mm/s	
Gas flow rate : 100 SCCM		Time : 30 min	
Atmospheric pressure: 5.3 kPa			

Polishing plate	Iron	Nickel	Cast iron	Molybdenum
Polished area %	55	45	0	0

Table 3 Effect of atmospheric gases

Polished area % / Polishing condition / Polishing plate	Temperature : 900 °C Atmospheric pressure:<1(vacuum),5300Pa Applied pressure : 15 kPa Sliding speed : 2.8 mm/s Time : 30 min				
	vacuum	H_2	He	Ar	N_2
Iron	100	55	35	35	22
Nickel	60	45	35	38	20

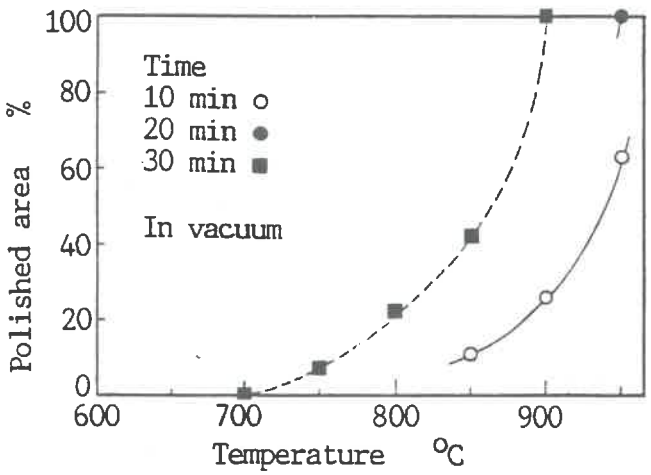

Polishing plate : Iron
Atmospheric pressure: <1Pa
Applied pressure : 15 kPa
Sliding speed : 2.8 mm/s

Fig.5 Effect of temperatures

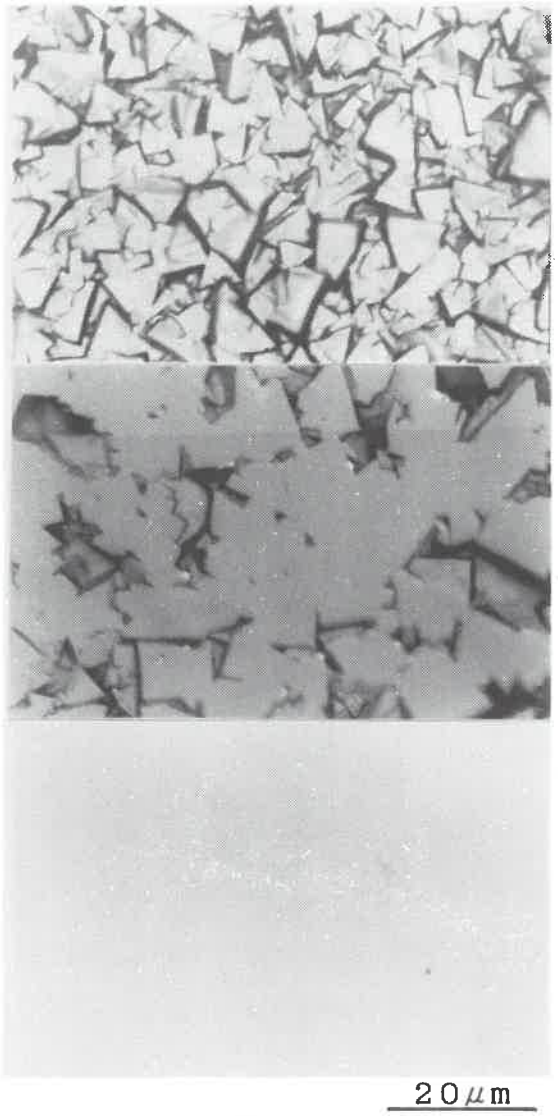

Fig.6 Microphotographs of the polishing process
(a) As deposited
(b) In the course of polishing
(c) Finished

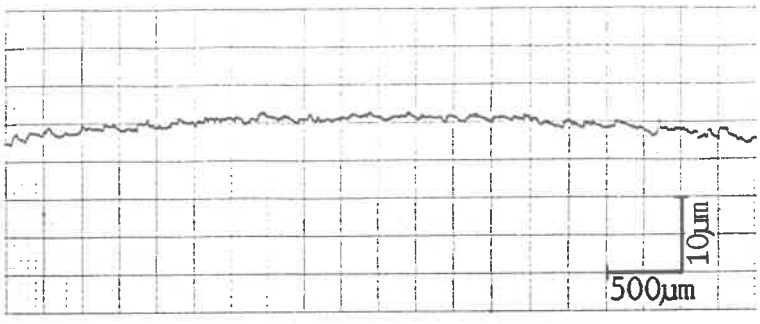

(a) Before polishing

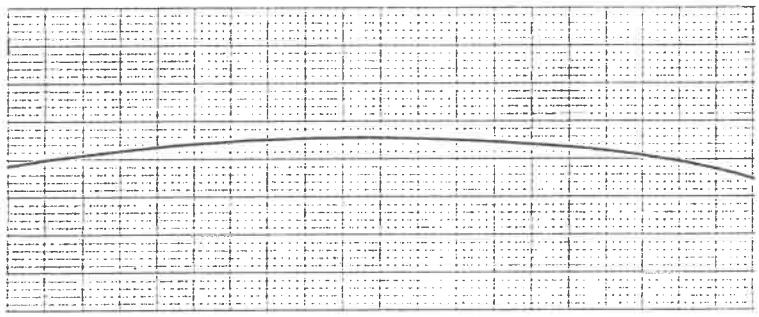

(b) After polishing

Fig.7 Surface profile change by polishing

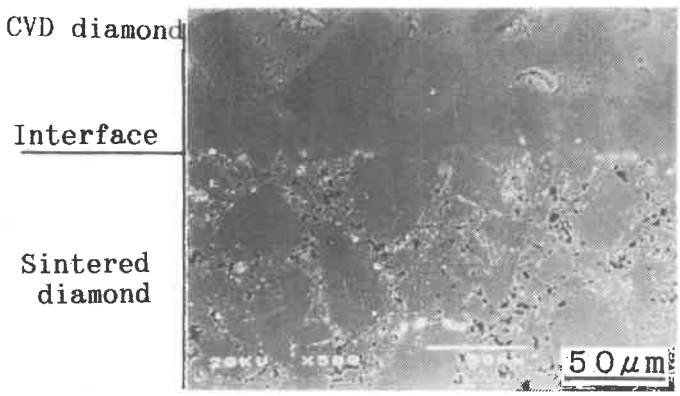

Fig.8 SEM photograph of the polished interface between CVD diamond and sintered diamond

Measurement and Compensation of Guideway Errors by a Laser Doppler Displacement Meter

Charles Wang

Optodyne, Inc.

1180 Mahalo Place

Compton, CA 90220

High accuracy linear slides and XY-tables are needed for various applications, such as IC manufacturing, video inspection and precision machine tools. Accurate and high-resolution linear encoders, such as a grating scale, a holographic scale, a laser interferometer and a Laser Doppler Displacement Meter (LDDM)[1], are available to achieve high linear accuracy. However, because of the guideway error which causes the angular pitch, yaw and roll motion, the accuracy of most linear slides, XY-tables, and coordinate measuring machines (CMM) are not limited by the accuracy of the encoders, but rather by Abbe error. Furthermore, the thermal gradients or their changes will cause the structure to twist and bend, which leads to additional angular motions. These effects are often magnified by the fact that the point of action is nearly always some distance removed from the axis around which bending or twisting takes place. This magnifying effect is called Abbe offset error[2].

For a single-axis linear slide (Fig. 1), there are six degrees of freedom affecting its position accuracy. There are three rotations along the x-axis (roll), the y-axis (pitch) and the z-axis (yaw), two linear deviations from the straight line of travel, z, vertical straightness (or straightness), y, horizontal straightness (or flatness), and finally, the linear position error, x. Two fundamental errors are generated by a single-axis slide -- cosine error and Abbe error. With careful alignment, the cosine error is negligible.

The goal of any XY-table or CMM design is to deliver accurate movement at the work piece. Abbe

error appears when the axis of measurement is offset from the plane of the work piece and when there is pitch or yaw angle due to the guideway errors. As shown in Fig. 2, the Abbe error is equal to the angle measured in radians multiplied by the Abbe offset, d.

For typical ways, the pitch and the yaw angles are +/- 10 arcsec, and typical air bearings, the pitch and yaw angles are +/- 2 arcsec. For large XY-tables or CMM, the Abbe offset d is large, hence the positioning error due to pitch or yaw angles may be very large. For example, when d = 20 inches, a guideway pitch angle of

+/- 2 arcsec will cause a positioning error of +/- 200 microinches.

Based on current development in laser radar technology, a new technique, Laser Doppler Displacement Meter (LDDM) has been developed[1]. The LDDM is an electro-optical device, which uses the Doppler shift of a laser frequency caused by a moving target to measure displacement accurately over a few meters. As shown in Fig. 3, the LDDM consists of a laser head, a retrorefletor, a processor and a display. Using the latest microelectronics, electro-optics, and optical heterodyne, the LDDM provides a high precision and compact alternative in submicron positioning. To measure both linear displacement and pitch angle simultaneously, a dual-beam laser head is developed. As shown in Fig. 4, the dual-beam laser head emits two laser beams, which are reflected by a dual-retroreflector and received by two photo-detectors. The linear displacement of the top retroreflector is measured by the first photo-detector and the linear displacement of the top retro-reflector minus the linear displacement of the bottom retroreflector is measured by the second photo-detector. This output divided by the distance between the two retroreflectors is the pitch angle. After processed by the processor module, there are two outputs, one is the displacement and the other is the pitch angle of the dual-reflector. The linear resolution is 1 microinch and the angular resolution is 0.2 arcsec.

Using a dual-beam LDDM, the guideway pitch and yaw angles can easily be measured. There are two applications of the dual-beam LDDM. One is to measure the linear position accuracy, pitch and yaw angle along each axis of motion, then feed this information to a computer to compensate these errors. Hence higher positioning accuracy can be achieved. However, because of the wearing, the thermal gradient and the structure changes, the guideway errors (pitch and yaw angle) may not be repeatable.

Hence, the second application of the dual-beam LDDM replaces the linear encoder by a dual-beam LDDM on each axis of motion. The linear displacement and angle can be measured simultaneously.

The linear displacement data can be used for the position servo control and the angular data can be used to compensate any Abbe error at the work plane or the measuring point. Higher positioning accuracy can be obtained. The major advantages of this application are 1) no need for periodical calibraiton, update the error map or the compensation file, 2) not affected by any thermal gradient, or structure changes, hence relax the requirement on the environment and temperature control, and 3) positioning accuracy is not affected by the load factor. This technique can also be applied for the accurate positioning of linear measurement machines, XY-tables, and CMMs.

Figure Captions

1) A schematic of a single-axis slide
2) Abbe error due to yaw angle
3) A schematic of the Laser Doppler Displacement Meter
4) A photo of a dual-beam laser head and a dual-retroreflector for both linear and angular measurement.

References

1) C.P. Wang, "Laser Doppler Displacement Measurement". **Lasers and Optronics**, Vol. 6, No. 9, p. 69-71 (Sept 1987).

2) Erwin G. Laewen, "Structural Integrity in Optical Systems". **Applied Optics**, Vol. 29, No. 13, p. 1842-1843 (May 1990).

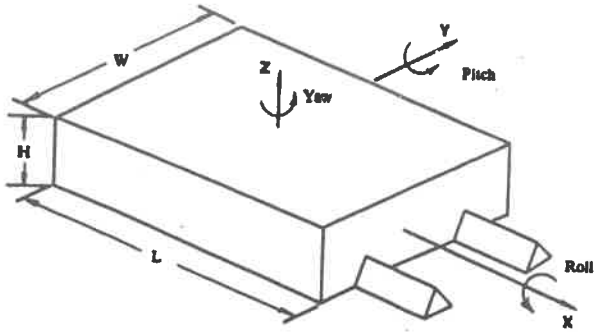

1) A schematic of a single-axis slide

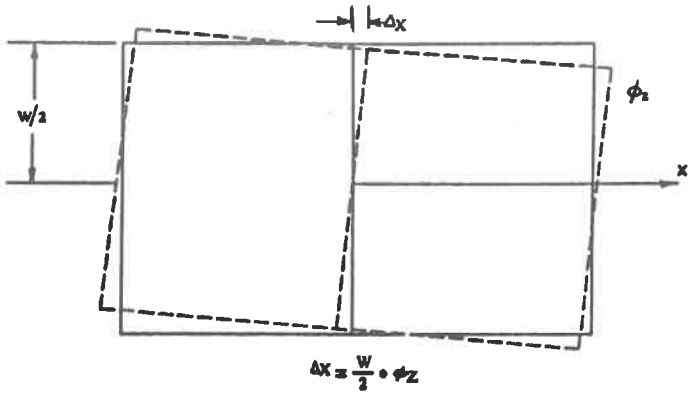

2) Abbe error due to yaw angle

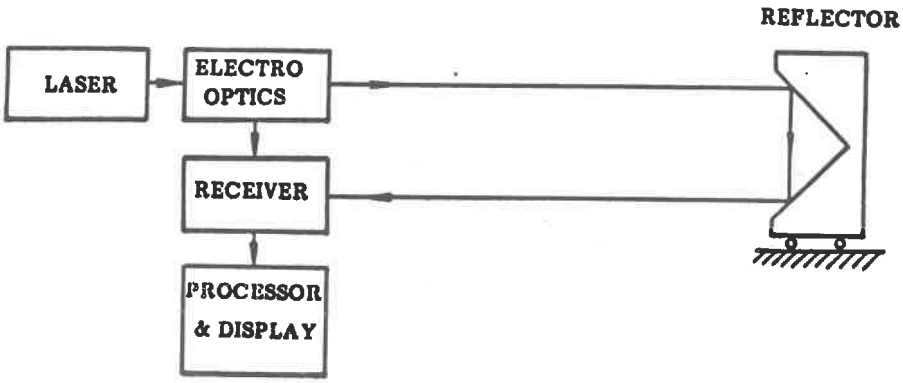

3) A schematic of the Laser Doppler Displacement Meter

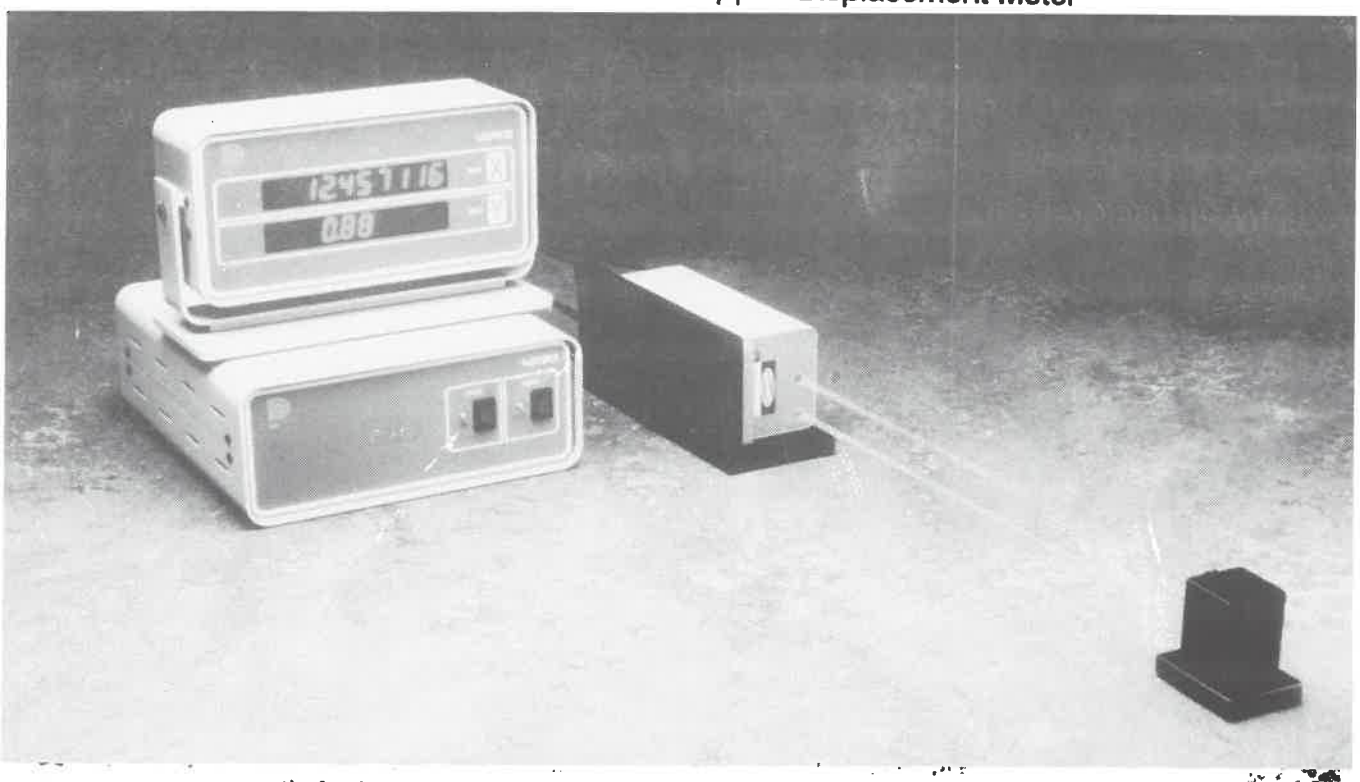

4) A photo of a dual-beam laser head and a dual-retroreflector

STIFFNESS CHARACTERISTICS OF EXTERNALLY PRESSURIZED GAS BEARINGS

Wang, J.M., Schellekens P.H.J. and A.C.H. van der Wolf
Eindhoven University of Technology, The Netherlands

INTRODUCTION

Externally pressurized gas (EPG) bearings have found their positions in the field of the precision engineering, not only as the motion support elements but also the actuators. This is due to their qualified characteristics, such as low and constant friction coefficient and error-average effect etc. The stiffness of EPG bearings govern the stability limits and determine the grade of accuracy. Many researches have been done on the enhancing static stiffness, as summarized in [1]. The stiffness characteristics as whole has rarely concerned, at least in the publications, which is the motivation of this paper.

In the paper, the principle to increase the stiffness, stiffness capacity, dynamic natural stiffness and stiffness loss are discussed. Authors will be very delightful if the information presented could help the use of EPG bearings in the precision engineering.

COMPENSATION METHODS AND STIFFNESS OF BEARINGS

The EPG bearings are generally compensated in three ways, fixed restriction compensation(fig. 1a and 1c), variable-restriction compensation (fig. 1b and 1d to 1h) external displacement compensation. The fixed restriction compensation stands for the bearings with rigid restrictor and rigid bearing surfaces. The stiffness of the fixed restriction compensation bearings can be expressed as the following from:

$$S = - dW/dh \qquad (1)$$

The variable restriction compensation bearings employ a changeable restriction parts or device, i.e. the bearing surface or flexible restrictor (flow) surface. The external displacement compensation bearings stands for the bearing with an extra device to generate a displacement to

cancel the bearing displacements. The stiffness for the last two compensation bearings is modified by the equivalent displacement or external displacement, say h_e,

$$S = dW/(dh-dh_e) \qquad (2)$$

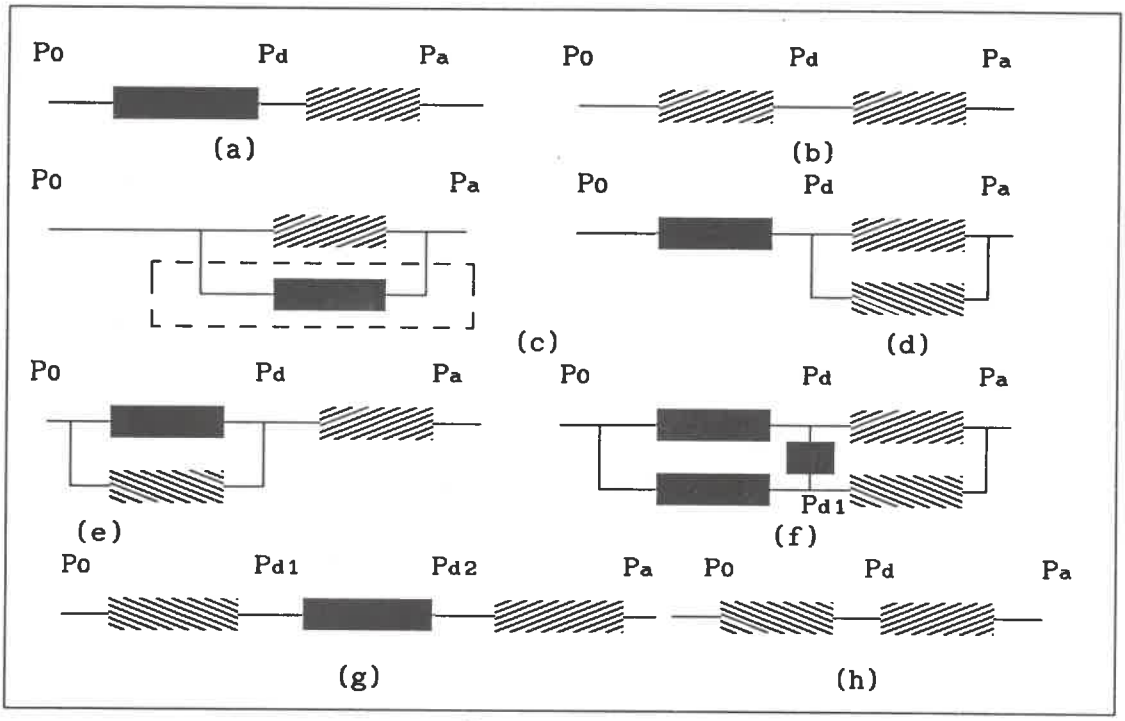

▒ : changeable restrictor; ▮ : fixed restrictor

▒ : bearing gap controlled restrictor

a and c: basic design in which only gap height changes with load change in a working condition (fixed restriction compensation);
d to h: variable restrictioncompensation examples in which there is at least one variable restriction

Fig. 1. Some possible arrangement of the restriction elements

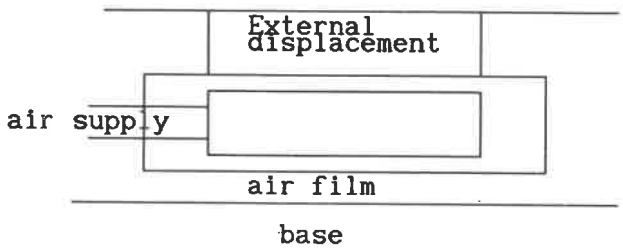

Fig. 2. EPG bearings with external displacement device

STIFFNESS CAPACITY

In order to understand the inside of characteristics of bearing stiffness, a term called stiffness capacity is introduced, which is defined as the integral of stiffness distribution over the all possible working gap, i.e.

$$Sc = -\int_{hmin}^{hmax} dW/dhw\ dhw$$
$$= W(h_{min}) - W(h_{max}) \qquad (3)$$

This formula tell us that in order to increase the stiffness in all the possible working gap height the load capacity must increase. If load capacity does not increase, the stiffness increase will have the decrease either load capacity or the range of working gap height. It reveals the facts that the infinite stiffness bearings with the constant supply pressure could have negative stiffness counter parts. In general, it may state that the range of the working gap decreases with increasing the absolute value of stiffness.

DYNAMIC NATURAL STIFFNESS

For the convenience, a new term called dynamic natural frequency is introduced to judge the stability of bearing system by reviewing the the close-looped servo model of EPG bearings [2]. In the closed-loop, the frequency response of mass supported by EPG bearings is the main loop with transfer function of $M(j\omega) = -1/M\omega^2$ and the response of equivalent springs is the feedback loop with a transfer function $K(j\omega)$ - the stiffness characteristic of the EPG bearings. For such a system, the stability can be evaluated by the Nyquist criterion i.e. (for frequency responsae, $s = j\omega$), the product plot

$$S(j\omega) = -\frac{1}{\omega^2}\{Re[K(j\omega)] + Im[K(j\omega)]\} \qquad (4)$$

is located on the right-hand of the point (-1,0) in the complex plan. It also implies that

$$Re[K(j\omega_1)/M\omega_1^2 < \text{or} > 1 \text{ when } Im[K(j\omega_1] = 0 \qquad (5)$$

or $$\{Re[K(j\omega_1)/M\}^{1/2}/\omega_1 < \text{or} > 1 \text{ when } Im[K(j\omega_1] = 0$$

If ω_1 represents that a cross-over frequency, the stability means that when Im[K(jω)] equals zero the ratio of Re[K(jω_1)] over cross-over-frequency, $\{Re[K(j\omega_1)]/m\}^{1/2}/\omega_1$, should be larger than unit if the curve goes from π to $-\pi$ with frequency increase and smaller than unit if it goes from $-\pi$ to π with frequency increase. Combining these two conditions, the stability of bearing systems means that the point (-1,0) will be not situated in the frequency region in which imaginary part of S(jω) is non-negative. The term, $\{Re[K(\omega_1)]/M\}^{1/2}$, is defined as the dynamic natural frequency and Re[K(ω_1)] is defined as dynamic natural stiffness.

STIFFNESS LOSS

Stiffness of EPG bearing, or generally speaking any kind of fluid film bearings, will have great loss when a weak connection is used, especially in the cases of higher film stiffness. The bar connection is a common "element" to connect the pad to a structure, such as carriages. From the Hook law, $\sigma = E\,\varepsilon$, ,for axial loaded bars the stress is simply expressed as $\sigma = Q/A$ and the strain can be expressed as elongation over the original length, $\Delta L/L$, therefore the stiffness expression reads

$$S_b = AE/L = \pi d^2 E/L \qquad (6)$$

where

A : section area of bar (m^2), L : bar length (m)

E : Elasticity model of bar material, for steel E = 208 GN/m^2

If a bar is made of steel with 3 mm radius and 18 mm length, the stiffness of this bar is 312 MN/m. If a bearing with 100 MN/m stiffness is connected to a structure by this bar, the overall stiffness of the system is only 75 % of the pad stiffness. Good care on the connection should be taken in the design of precision machines with EPG bearings.

REFERENCES

[1] J. M. Wang "On the principle and possible methods to improve aerostatic bearing stiffness" Master thesis, TUE (1987)

[2] J. M. Wang and P. H. J. Schellenkens " Dynamic Natural Frequency and Stability of Bearing Systems" STLE 1990 Annual Meeting, Dever,

DYNAMIC SIMULATION AS A DESIGN TOOL FOR PRECISION MACHINE TOOL INSTALLATIONS

BY

Gerald P. Hegarty
Scott A. Woodward

FABREEKA INTERNATIONAL, INC.
Stoughton, MA.

Keywords: Dynamic environment, steady-state vibration, transient vibration, mechanical shaker.

ABSTRACT

The operation of precision machine tools requires consideration of the environment in which they shall operate.

One environmental element to consider is vibration. Tests can establish whether the dynamic environment (vibration level) is within guidelines set forth by the equipment manufacturer. A problem arises, however, if on-line precision machine tools are subjected to a change in the dynamic environment. This occurs frequently when manufacturing equipment (presses, compressors, deburring equipment, etc.) is relocated within close proximity to precision machine tool operations. The effect that the introduction of a potential source of disruptive vibration (manufacturing equipment) will have on the accuracy of the precision machine tool is difficult to predict.

The following report is a discussion of the Dynamic Simulation Technique and is highlighted with a recent case history. This technique allows a future environment to be predicted, simulated, quantified, and analyzed with respect to its effect on the Precision Engineering operations.

INTRODUCTION

Environmental considerations such as structural vibration play an important role in a successful precision machine tool operation. The effect of vibration on machine tool tolerances is usually a degenerative one. The more vibration a machine tool is subjected to during operation, the less "precision" it can achieve. It is standard practice to measure the levels of vibration before a typical precision machine tool installation. A quick comparison between existing vibration levels and the manufacturers' specifications allow a judgement to be made

relative to the effect vibration will have on equipment performance. A problem arises if the dynamic environment in which the machine tool operates changes subsequent to the installation date. The increased levels of vibration can be caused by the installation of new equipment (such as an air compressor, punch press, deburring equipment, etc.) near the existing precision machine tool site. It becomes a problem when the tolerance of the machine tool is reduced and if its workpiece quality is sacrificed. In the worst scenario, the precision equipment may have to be relocated to a "quieter" location. Any solution to this problem may involve down time, impaired performance, and costly facility modifications.

A technique has been developed where the levels of vibration expected by the installation of new equipment can be predicted and simulated. This technique is viable in cases when there is precision equipment presently in operation and the introduction of a new piece of equipment is judged to be a possible source of unwanted vibration.

The dynamic simulation technique has three main components:

1 - The computation of the expected dynamic forces which will be created by the equipment in question.

2 - Dynamically simulating these forces at the proposed installation site.

3 - Measuring, observing, and analyzing the effects of this vibration on precision machine tool performance.

Dynamic forces and frequencies are easily computed from available equipment specifications. The on site simulation of steady state and transient vibration can be accomplished with various shaker/shock machines. Once the proper force generator is chosen, it is installed at the proposed equipment site and operated. The effect of the simulated forces can be observed and measured on the neighboring precision machine tools. Part quality can be quantified and evaluated after which the feasibility of the proposed equipment relocation can be assessed. Facility and equipment relocation efforts can be very expensive. This dynamic simulation technique can help the facility engineer make a proper decision thus insuring expected machine tool precision.

The remainder of this paper discusses a recent case history and the far reaching implications of its findings.

CASE HISTORY

A highly regarded aircraft engine manufacturer was experiencing severe manufacturing and inspection problems caused by vibration emanating from an old Deburring machine. Nearby precision equipment such as grinders, milling machines, machining centers, and finishing machines showed the detrimental effects of this unwanted vibration in the quality of their workpieces.

The design of the old Deburring machine was such that a vibration isolation system could not be utilized. An alternate solution to this problem was to purchase a new, less disruptive machine. This was the most favorable option due to the economics of relocating a precision machine tool facility. Some doubt remained as to whether the new machine, while less disruptive, would still cause similar problems as the old machine. In order to eliminate this doubt, a dynamic simulation of the incoming equipment was proposed. The aircraft engine manufacturer, assured that this simulation would add a high degree of confidence to the decision, quickly authorized the test.

The first step was to obtain all relevant information on the incoming machine and calculate the dynamic forces which would be transmitted to the machine foundation. The opportunity arose to confirm the calculated dynamic forces with those generated from the actual machine in operation at a different site. Vibration measurements showed a high correlation between calculated and actual dynamic forces.

The maximum generated acceleration attained by the system is 1.5G in a frequency range between 900 and 1800 rpm. After calculating the input force characteristics a decision was made to dynamically simulate the incoming machine by means of a mechanical shaker.

The shaker was secured to the foundation at the proposed installation site and set at various outputs during the tests. The first setting was at the Deburring machine's calculated output force of 270 lbs. at an operating speed of 15 Hz. (900 rpm). On the next test, the force was held constant but the operating speed was increased to a maximum of 30 Hz. (1800 rpm). The final test of the shaker was with an output force of 540 lbs., (double the calculated output force) and an operating speed of 30 Hz. This last test was used to insure a comfortable factor of safety.

During the field tests, a two channel vibration analyzer was used to establish a baseline of background noise and to quantify vibration levels on the precision machine tool in question.

Several test sites were chosen at key neighboring precision equipment locations in the facility to perform the vibration measurements. Data was collected on each machine tool which quantified the levels of vibration imposed on it by shaker operation. Along with this data, operators of each group of machinery were requested to determine if the vibration caused any problems in workpiece quality.

RESULTS AND CONCLUSIONS

The results of the dynamic simulation showed that even at double the expected force input, the quality of neighboring precision machine tool operation was not impaired. Based on these results, the decision was made to replace the old Deburring machine.

In summary, the dynamic simulation tests removed any doubt as to the feasibility of the new Deburring machine installation. This technique is an economical means of guaranteeing that hostile equipment does not disrupt the operation of nearby precision machine tools.

REFERENCES

1. Harris C.M., Shock and Vibration Handbook, Third Edition, McGraw-Hill Book Company, New York, New York, 1988.

2. Broch, Jens Trampe, Mechanical Vibration and Shock Measurements, Second Edition, K. Larsen & Son N/S. Glostrup, Danmark.

3. Randall, R.B., Frequency Analysis, Third Edition, K. Larsen & Son N/S. Glostrup, Danmark.

Newly developed electron-beam lithography system for fabricating high accuracy concentric circle patterns with large diameter

Y.Yamazaki* , K.Nakamura* , T.Sasaoka* and M.Mitsui*
H.Murao** , T.Maeda** , H.Goto** , S.Ogata** and T.Yamashita**
* Manufacturing Technology R&D Laboratory,
** Central R&D Laboratory,
OMRON Corporation, Nagaokakyo-city,Kyoto,617 Japan 075-951-5111

Introduction

With the progress of small optical instruments, fabrication of micro optical elements for example micro fresnel lens are paid attention. The way of fabricating fine pitch concentric circle patterns have become important. Concentric circle patterns are generally fabricated using electron-beam lithography system[1][2][3]. However only small diameter circle patterns with the diameter of ϕ0.5mm and discontinuous patterns could be fabricated, because of limitations of electron-beam deflection and point-to-point irradiation of electron-beam. Also concentric circle patterns are generally fabricated using a diamond turning machine[4]. However only rough pitch patterns could be fabricated, because of the diamond tool shape.

In this paper, newly developed electron-beam lithography system is to be presented. This system has fine linear motion and fine rotary motion. Without beam deflection, high accuracy concentric circle patterns with large diameter can be fabricated. The concentric circle patterns accuracy of 0.1μm and the circle patterns diameter of ϕ60mm have been obtained. In the following, the concept of lithography, features of this system and experimental result are described.

The concept of lithography

Figure 1 shows the concept of lithography. Specimen stage consists of X-Y stage and rotary stage. Electron-beam is always fixed. When electron-beam is irradiated to the specimen on the rotary stage, one circle pattern is fabricated. After some distance travel in X-axis direction of X-Y stage, this irradiation is repeated. In this way concentric circle patterns are fabricated.

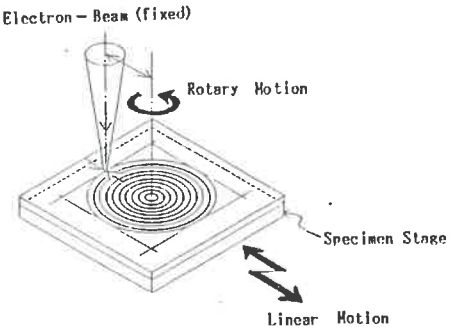

Fig.1 The Concept of Lithography

Features of this system

Figure 2 shows the construction of specimen stage. Figure 3 shows the block diagram of this system. The features of this system are as follows:

1) To achieve high speed, high accuracy positioning, the X-Y stage consists of the coarse positioning stage and the fine positioning stage[4]. The rotary stage is mounted on the center of the fine positioning stage.
2) To avoid the deflection of electron-beam by magnetic noise from the actuator, piezoelectric inch worm motor is used for driving the coarse positioning stage and piezoelectric ceramic actuator is used for driving the fine positioning stage.
3) To guide the fine positioning stage precisely in the X and Y directions, flexible hinge springs are used.
4) To achieve fine rotary motion under vacuum, air bearing spindle with non-contact vacuum labyrinth seal is used for the rotary stage.
5) To achieve high accuracy measurement, the position of X-Y stage is measured by ZYGO laser measurement system with the resolution of 1.25nm and the rotation angle of rotary stage is measured by the built-in rotary encoder with the resolution of 0.01 degree.
6) To turn on and off electron-beam irradiation according to lithography patterns, high speed beam blanking function with the rise time of 25nsec is prepared in this system.
7) The position and rotation of specimen stage is controlled by 68000 CPU connected to host computer through GP-IB.
8) To achieve high accuracy patterns, this system is placed in a class 10000 clean room with constant temparature of 23±0.1℃. This specimen stage is placed on vibration-free stands of the air-support type.

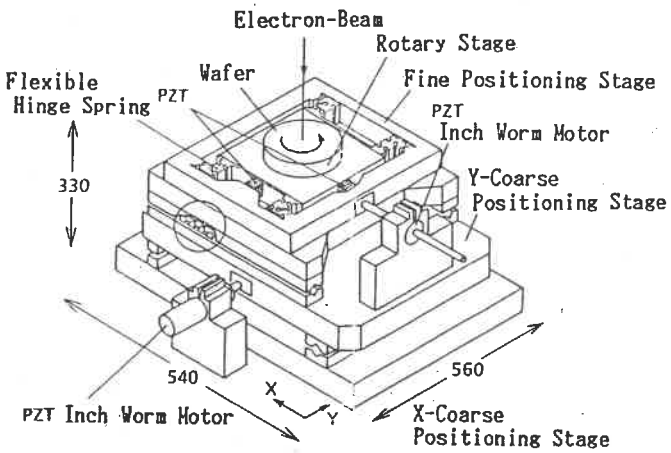

Fig.2 Construction of Specimen Stage

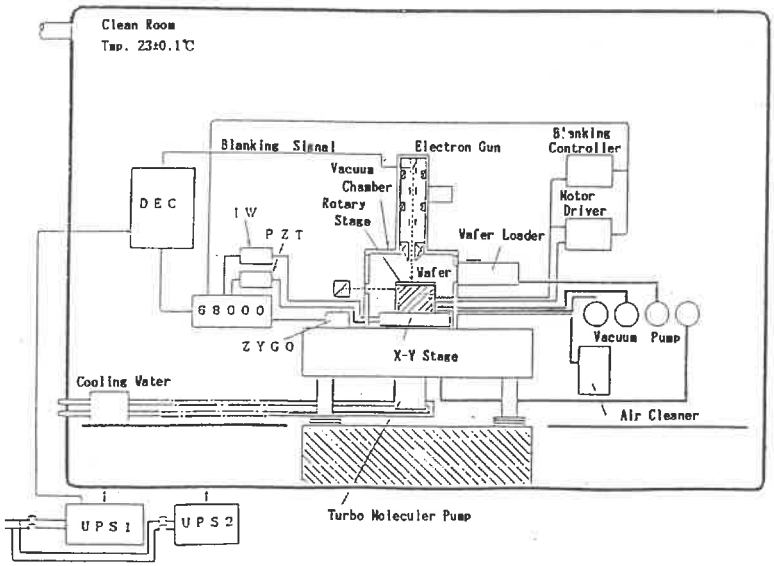

Fig.3 Electron-Beam Lithography System

Figure 4 shows the positioning waveform when displacement instructions of 0.1μm are given to the X-Y stage. The X-Y stage is set within $\pm$0.01μm of the target position 40ms after the start of the operation. That is, high speed and high accuracy positioning operation is achieved. Figure 5 shows the rotation characteristics of the rotary stage when it turns at 300r.p.m. under vacuum. The rotation error is within $\pm$0.05μm. That is, fine rotary motion under vacuum is achieved.

The basic characteristics of this new electron-beam lithography system are;

electron-beam stability	:	0.1μm / 0.5hour
minimum diameter of beam spot	:	0.05μm
positoning accuracy of X-Y stage	:	$\pm$0.01μm
rotation error of rotary stage	:	$\pm$0.05μm
vacuum pressure	:	2×10^{-5}Pa

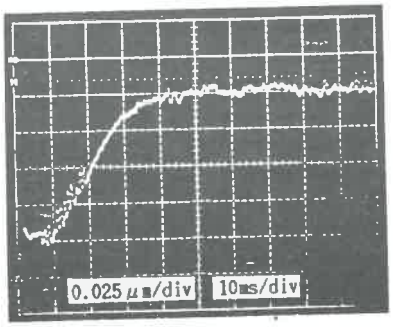

Fig.4 Positioning Characteristics

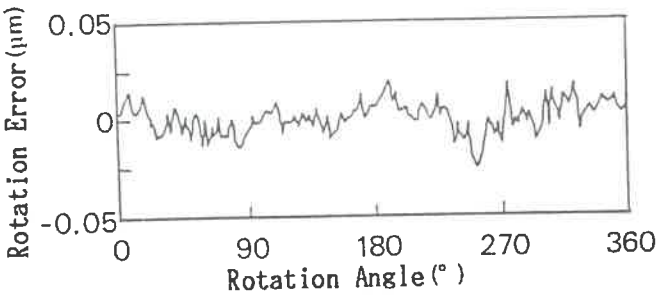

Fig.5 Rotation Characteristics

Experimental result

Figure 6 shows 1μm pitch concentric circle patterns fabricated by this system. As a result with measurement of pattern pitch by SEM, it is ascertained that the concentric circle patterns accuracy of 0.1μm have been obtained. Judging from the construction of specimen stage, the circle patterns diameter of ϕ60mm is obtained. Figure 7 shows rotary encorder disk patterns fabricated by this system using beam blanking function. Fabricating concentric circle patterns using beam blanking function, broken concentric circle patterns are obtained. Taking advantage of it, rotary encoder disk patterns (diameter ϕ15mm,slits 30000pulses/rev,slit pitch 1.57μm) can be fabricated.

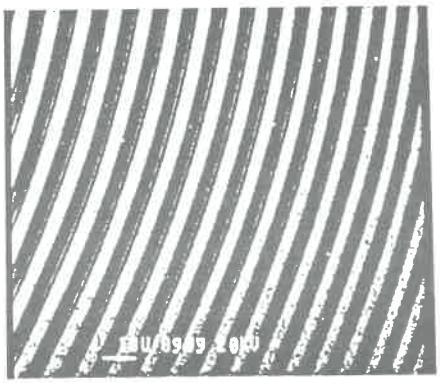

Fig.6 Concentric Circle Patterns

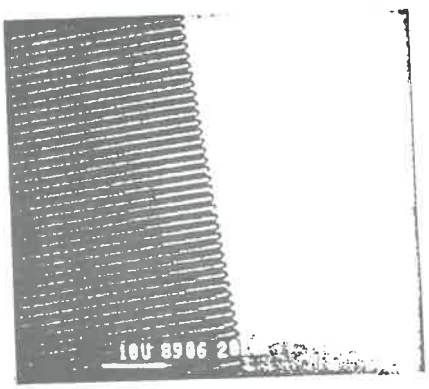

Fig.7 Rotary Encorder Disk Patterns

Conclusions

Electron-beam lithography system that has fine linear motion and fine rotary motion has been developed. The concentric circle patterns accuracy of 0.1μm and the circle patterns diameter of ϕ60mm have been obtained.

In comparision with conventional beam deflection lithography, this continuous irradiation system is well characterized as follows;

1) high accuracy concentric circle patterns with large diameter can be fabricated.
2) the shortening of lithography time can be done.

Using this system, high accurate and large-sized micro fresnel lenses and rotary encoder disks with fine pitch patterns can be fabricated.

References

(1) S.Aoyama et al., Fabrication of Micro Fresnel Lens by Electron-Beam Lithography, OQE 88-118,P49(1989)

(2) G.Hatakoshi et al., Off-axis Grating Lenses Fabricated by EB Lithography, Technical Digest, Fourth International Conference on Integrated Optics and Optical Fiber Communication, Paper 29A2 (IECE,Tokyo,1983)

(3) T.Fujita et al., Fabrication of Micro Lenses Using Electron Beam Lithography, Opt. Lett., 6 (1981) 613

(4) K.Goto et al., Plastic Grating Collimating Lens, Japanese Journal of Optics, 364 (1989)

(5) H.Goto et al., XY Stage Capable of Positioning in Submicron Order, J. Rob. Mech. Vol.1, 333 (1989)

Authors Index

Adler, M. 212
Auriemma, R. Anthony 147
Belak, James F. 76
Bietry, Joseph 147
Bifano, Thomas G. 162, 200
Blackley, S. 68
Bogy, D.B. 96
Bottger, U. 72
Bruning, John H. 9
Cao, Lin-xiang 110
Carr, Jeffrey W. 55
Caskey, G 151
Ceglio, N.M. 67
Chen, K. 151
Choi, H.S. 155
Church, E.L. 103
Colby, Roy S. 97
Cook, Lee M. 47
Creath, Katherine 159
Daito, M. 143
Day, Robert 11
DePiero, Douglas 162
Demarest, F. 35
Donmez, A. 80
Dow, Thomas A. 92, 135, 166, 192, 200
Drescher, J.D. 166
Duduch, J. 170
Falter, Peter J. 92
Fawcett, Steven C. 135
Feger, Claudius 55
Ferrell, T.L. 106
Fornaro, Robert J. 27
Frerking, D. 189
Frolich, D. 189
Furutani, Akihiro 174
Futami, Shigeru 174
Garrard, Kenneth P. 27
Gavin, R. 80
Gee, A.E. 170
Gonsalves, Kenneth E. 216
Gordon, Thomas E. 178
Goto, H. 236
Grant, John 88
Grenville, A. 43
Hari, Y. 151
Hartman, A.W. 63
Hashimoto, F. 143
Hegarty, Gerald P. 232
Hobson, Wayne 204
Hocken, Robert J. 88, 119, 151
Hoose, John 131
Horie, Sadamu 200
Hsieh, R.L. 43
Jarosz, Jeff 204
Jeon, J.U. 155
Jeong, H.D. 155
Johnson, C.E. 106
Kanai, A. 143
Katayama, Kazuyoshi 39
Keltie, R.F. 139
Ketelsen, D.A. 19
Kiely, Aaron B. 110
Kittrell, W.C. 19
Kubo, K. 182
Kubota, S. 182
Leadbeater, P.B. 114
Lettieri, Thomas R. 110
Loewen, Erwin 131
Lucca, Don A. 51
Luttrell, Dan E. 31, 186
Maeda, T. 236
Marion, J.E. 127
Markle, D.A. 43
Matsumura, K. 182
McKeown, P.A. 114
Meiser, H. 189
Miller, Jimmie A. 119
Miller, Michele H. 192
Mitsui, M. 236
Miyashita, M. 143
Mochida, S. 182, 196
Moyer, P.J. 106
Murai, Nobuyoshi 39
Murao, H. 236
Nagano, H. 182
Nakamura, K. 236
Ogata, S. 236
Ohmoto, Takashi 208
Ohtake, Naoto 123
Olson, Jeffrey 131
Owen, G. 43
Ozisik, Hakan 139, 200
Paesler, M.A. 15, 106
Palanivelu, D. 151
Parks, R.E. 119
Patten, John 88
Pease, R.F.W. 43
Pyra, M. 59
Reddick, R.C. 106
Rhorer, Richard L. 51, 204
Ro, Paul I. 97
Rudder, F. 80
Russell, Philip 11
Samitsu, Yamato 208
Sasaoka, T. 236
Scattergood, R.O. 68
Schellekens, P.H.J. 228
Scott, Paul J. 84
Shafer, H.G. 212
Shao, Lianzhen 19
Shaw, M.C. 212
Smythe, R.A. 35
Sparks, R.G. 15
Spreybroeck, Leon Van 118

Stowers, Irving F. *76*
Strutt, Peter *216*
Takacs, P.S. *103*
Takahashi, M. *182, 196*
Takahashi, Yoshinori *39*
Tan, C.P. *23*
Taylor, J.S. *127*
Taylor, Lauren W. *27*
Tezuka, Shinichi *123*
Theye, Lonnie A. *11*
Tokura, Hitoshi *220*
Trimmer, William *38*
Tullar, Paul *88*
Ueda, S. *182, 196*
Venkatesh, V.C. *23*
Vorburger, T.V. *63, 80, 110*
Wang, Charles *224*
Wang, J.M. *228*
Warmack, R.J. *106*
Weck, M. *59, 72*
Wiley, Robert *131*
Wills-Moren, W.J. *114*
Wilson, R. *151*
Wilson, Timothy J. *101*
Woodward, Scott A. *232*
van der Wolf, A.C.H. *228*
Yamashita, T. *236*
Yamazaki, Y. *236*
Yang, Cheng-Feng *220*
Yang, J. *151*
Yasunaga, Nobuo *208*
Yee, K. *80*
Yim, N.B. *155*
Yoshida, Takahumi *208*
Yoshikawa, Masanori *123, 220*
Yoshioka, J. *143*
Yu, H.S. *155*
Zheleznyak, Semyon *131*